Modeling of galactic cosmic rays in the heliosphere

M.D Ngobeni

13161229

Thesis submitted for the degree *Philosophiae Doctor* in Space Physics (specialising Physics) at the Potchefstroom Campus of the North-West University

Promoter: Prof MS Potgieter

February 2015

Abstract

The modulation of galactic cosmic ray (GCR) Carbon in a north-south asymmetrical heliosphere is studied, using a two-dimensional numerical model that contains a solar wind termination shock (TS), a heliosheath, as well as particle drifts and diffusive shock re-acceleration of GCRs. The asymmetry in the geometry of the heliosphere is incorporated in the model by assuming a significant dependence on heliolatitude of the thickness of the heliosheath. As a result, the model allows comparisons of modulation in the north and south hemispheres during both magnetic polarity cycles of the Sun, and from solar minimum to moderate maximum conditions. When comparing the computed spectra between polar angles of 55^o (approximating the Voyager 1 direction) and 125^o (approximating the Voyager 2 direction), it is found that at kinetic energies $E <\sim 1.0$ GeV/nuc the effects of the assumed asymmetry in the geometry of the heliosphere on the modulated spectra are insignificant up to 60 AU from the Sun, but become increasingly more significant with larger radial distances to reach a maximum inside the heliosheath. In contrast, with $E >\sim 1.0$ GeV/nuc, these effects remained insignificant throughout the heliosphere even very close to the heliopause (HP). However, when the enhancement of both polar and radial perpendicular diffusion coefficients off the equatorial plane is assumed to differ from heliographic pole to pole, reflecting different modulation conditions between the two hemispheres, major differences in the computed intensities between the two Voyager directions are obtained throughout the heliosphere. The model is further improved by incorporating new information about the HP location and the relevant heliopause spectrum for GCR Carbon at $E < 200$ MeV/nuc based on the recent Voyager 1 observations. When comparing the computed solutions at the Earth with ACE observations taken during different solar modulation conditions, it is found that it is possible for the level of modulation at the Earth, when solar activity changes from moderate maximum conditions to solar minimum conditions, to exceed the total modulation between the HP and the Earth during solar minimum periods. In the outer heliosphere, reasonable compatibility with the corresponding Voyager observations is established when drifts are scaled down to zero in the heliosheath in both polarity cycles. The effects of neglecting drifts in the heliosheath are found to be more significant than neglecting the enhancement of polar perpendicular diffusion. Theoretical expressions for the scattering function required for the reduction of the drift coefficient in modulation studies are illustrated and implemented in the numerical model. It is found that when

this scattering function decreases rapidly over the poles, the computed $A < 0$ spectra are higher than the $A > 0$ spectra at all energies at Earth primarily because of drifts, which is unexpected from a classical drift modeling point of view. Scenarios of this function with strong decreases over the polar regions seem realistic at and beyond the TS, where the solar wind must have a larger latitudinal dependence.

Keywords: Cosmic rays, galactic Carbon, heliosphere, heliopause, termination shock, heliosheath, solar modulation, solar activity, particle drifts.

Opsomming

Die modulasie van galaktiese kosmiese strale (GKS) Koolstof in 'n noord-suid asimmetriese heliosfeer is bestudeer. 'n Twee-dimensionele numeriese model is gebruik wat 'n sonwind terminasieskok en 'n helioskede bevat, asook deeltjiedryf en diffuse skokversnelling vir die herversnelling van GKS. Die geometriese asimmetrie van die heliosfeer is in die model ingesluit met die aanname van 'n betekenisvolle afhanklikheid van heliobreedtegraad vir die breedte van die helioskede. Die model maak dit sodoende moontlik om 'n vergelykende studie van modulasie te doen vir die noordelike en suidelike hemisfere gedurende beide magnetiese siklusse van die Son, asook van minimum tot matige maksimum sonaktiwiteit. Numeriese berekenings van spektra by poolhoeke van 55^o (ongeveer die Voyager 1 rigting) en 125^o (ongeveer die Voyager 2 rigting) is gedoen. Vergelykings van die spektra vir kinetiese energie van $E <\sim 1.0$ GeV/nukleon toon aan dat die effek van 'n asimmetriese heliosfeer weglaatbaar is tot by 60 AU vanaf die Son maar betekensvol word met toenemende afstande om 'n maksimum effek te bereik binne die helioskede. Daarenteen, vir $E >\sim 1.0$ GeV/nukleon, bly die effek onbelangrik dwarsdeur die heliosfeer, selfs naby aan die heliopause (HP). Groot verskille tussen die twee Voyager se rigtings word egter verkry as beide die poolwaartse en radiale loodregte diffusie koeffisiënte aanvaar word om te verskil weg van die ekwatoriale vlak, van pool-tot-pool. Hierdie aanvaarding gee modulasie toestande weer wat verskil tussen die twee hemisfere. Die model is verbeter deur die byvoeging van die nuutste inligting oor die posisie van die HP en die relevante spektrum by die heliopause vir GKS Koolstof met $E < 200$ MeV/nukleon soos gebaseer op die Voyager 1 waarnemings. 'n Vergelyking van numeriese berekenings met die model en waarnemings van die ACE satelliet gedurende verskillende modulasie toestande toon aan dat dit moontlik is vir die wisselvlak van modulasie van maksimum tot minimum sonaktiwiteit om groter te wees by die Aarde as die totale vlak van modulasie tussen die HP en die Aarde. In die buitenste heliosfeer is redelike ooreenstemming gevind tussen die model en toepaslike waarnemings van Voyager 1 wanneer deeltjiedryf gedurende albei magnetiese sonsiklusse na nul afgeskaal word in die helioskede. Die effekte van die afskaling van deeltjiedryf in die helioskede is meer betekenisvol as die verwaarlosing van die vergroting van poolwaartse loodregte diffusie. Teoretiese uitdrukkings vir die verstrooiingsfunksie wat benodig word vir die afskaling van deeltjiedryf in modulasie studies word illustreer en is in die numeriese model bygevoeg en gebruik. Die bevinding is dat wanneer hierdie funksie na die heliosferiese pole afneem, die berekende A < 0 spektra hoër is as die A > 0 spektra by die

Aarde vir alle energieë, wat nie inpas in die klassieke dryfmodel benadering nie. Senarios met hierdie verstrooiingsfunksie wat afneem oor die pole blyk realisties te wees by, en stroom-af, van die TS waar die sonwind se turbulensie 'n sterker breedtegraadse afhanklikheid behoort te hê.

Sleutelwoorde: Kosmiese strale, galaktiese Koolstof, heliosfeer, heliopouse, terminasieskok, helioskede, sonmodulasie, sonaktiwitiet, deeltjiedryf.

Nomenclature

1D	One-dimensional
2D	Two-dimensional
3D	Three-dimensional
ACR	Anomalous cosmic ray
ADI	Alternating direction implicit
AU	Astronomical unit ($1\ \text{AU} = 1.49 \times 10^8$ km)
eV	Electron volt ($1\ \text{eV} = 1.6 \times 10^{-19}$ J)
GCR	Galactic cosmic ray
HCS	Heliospheric current sheet
HD	Hydrodynamic
HMF	Heliospheric magnetic field
HPS	Heliopause spectrum
ISMF	Interstellar magnetic field
LISM	Local interstellar medium
MHD	Magnetohydrodynamic
PDE	Partial differential equation
QLT	Quasilinear theory
TPE	Transport equation
TS	Termination shock

Contents

Chapter 1

Introduction

Galactic cosmic rays (GCRs) that enter our heliosphere encounter an outward flowing solar wind which carries a turbulent magnetic field. The main boundaries of the heliosphere are the solar wind termination shock (TS) and the heliopause (HP). Of importance in modulation studies of GCRs is the interaction between GCRs as energetic charged particles and the interplanetary medium. This interaction causes the intensities of these particles to change as a function of position, energy and time, a phenomenon called the heliospheric modulation of cosmic rays (CRs). The numerical modeling of GCR modulation in the heliosphere is described by the *Parker* (1965) transport equation and depends on assumptions made about the elements of the diffusion tensor, the heliopause spectra (HPS, usually referred to as the local interstellar spectra), and the heliospheric geometry in addition to the solar wind and the heliospheric magnetic field (HMF).

The knowledge about the geometrical structure of the heliosphere has been enhanced by the crossing of the solar wind TS by both Voyager 1 and Voyager 2 spacecraft at different positions. These different positions of the TS confirm the dynamic and cyclic nature of the shock's position. The recent Voyager 1 observations (*Stone et al.*, 2013; *Krimigis et al.*, 2013; *Burlaga et al.*, 2013) indicate that it has crossed the HP into the very local interstellar medium at a radial distance of $\sim$ 122 AU in August 2012 (*Gurnett et al.*, 2013). The crossing of the HP is indeed a milestone and a giant step towards understanding the very local interstellar space, providing both the intensity and spectral shape for various species of GCRs in the interstellar medium down to a few MeV/nuc.

Inside the heliosheath, observations of CRs and plasma flows from the two Voyager spacecraft indicate significant differences between them (*Richardson*, 2013; *Caballero-Lopez et al.*, 2010; *Webber et al.*, 2009; *Stone et al.*, 2008), suggesting that apart from the dynamic nature caused by the changing solar activity there also may exist a global asymmetry in the north-south (meridional or polar) dimensions of the heliosphere (*Opher et al.*, 2009; *Pogorelov et al.*, 2009), in addition to the expected nose-tail asymmetry. This relates to the direction in which the heliosphere is moving in interstellar space and its orientation with respect to the interstellar magnetic field

(ISMF). See also the review by *Potgieter* (2013).

The purpose of this study is to extend the two-dimesional (2D) shock acceleration numerical model developed by *Langner* (2004), based on the transport equation (*Parker*, 1965), to compute the distribution of GCR Carbon in a north-south asymmetrically shaped heliosphere. This asymmetry is incorporated in the model by using, as a first approach, a heliosheath width that has a significant latitude dependence; both the TS and the HP positions are made asymmetrical.

The structure of this thesis is as follows:

Chapter 2 introduces the study of CRs and the heliosphere. It starts with a brief discussion of the Sun, the solar wind, the HMF, the heliospheric current sheet (HCS), solar cycle variations, the geometry of the heliosphere and charged particles in the heliosphere in particular GCRs. It closes with a concise discussion of selected spacecraft missions, which provide valuable observations for comparison with numerical models.

The transport processes that affect and determine the transport of CRs throughout the heliosphere, as combined in the transport equation (*Parker*, 1965), as well as a discussion of the diffusion tensor, used in this work, is given in **Chapter 3**. The expressions for the elements of the diffusion tensor are based on the work of *Burger et al.* (2000) and *Burger et al.* (2008). A mathematical description of GCR re-acceleration at the solar wind TS through diffusive shock acceleration is also given in this chapter.

Chapter 4 introduces the mathematical description of the transport equation in an asymmetrically modeled heliosphere together with a brief history of numerical models. The numerical method for solving the transport equation in an asymmetrical heliosphere is also given here. This model is based on earlier models developed by *Langner* (2004) and *Langner and Potgieter* (2005). The asymmetrical modulation model is then applied to illustrate the effects of this north-south asymmetry in the geometry of the heliosphere on the modulation of the GCR Carbon between the north (Voyager 1 direction) and south (Voyager 2 direction) hemispheres. This is done for both the two magnetic polarity cycles and also as solar activity changes from solar minimum to moderate maximum conditions.

Chapter 5 focuses on illustrating the effects on GCR Carbon of asymmetrical modulation conditions combined with a heliosheath thickness that has a significant dependence on heliolatitude as described in **Chapter 4**. To reflect different modulation conditions between the two heliospheric hemispheres in the numerical model, the enhancement of both polar and radial perpendicular diffusion off the ecliptic plane is assumed to differ from heliographic pole to pole. This is done in the context of illustrating how different values of the enhancement of both polar and radial perpendicular diffusion between the two hemispheres contribute to causing differences in GCR Carbon modulation during solar minimum and moderate maximum con-

ditions in both magnetic polarity cycles.

Observations of GCR Carbon in the heliosphere provide a useful tool with which a comprehensive description of the global modulation of GCRs both inside and outside off the solar wind TS can be made. This is, in part, because GCR Carbon is not contaminated by anomalous cosmic rays as is the case for Oxygen, Helium and Hydrogen. In **Chapter 6**, the numerical model is improved to incorporate the new HPS at kinetic energy $E <\sim 200$ MeV/nuc and the HP location in the Voyager 1 direction. This HPS is derived from observations made by the Voyager 1 spacecraft of GCR Carbon at a radial distance of ~ 122 AU from the Sun. The model is used first to study modulation from solar minimum to moderate maximum activity at the Earth. Second, the model is applied to study the contribution of drifts and the enhancement of polar perpendicular diffusion in the heliosheath to the total modulation in the heliosphere for both polarity cycles of the magnetic field during solar minimum conditions. The modeling results are compared with observations from various spacecraft.

To improve the understanding of particle drifts in the modulation of GCRs in the heliosphere, the effects of different scenarios of the scattering parameter $\omega\tau$ on the drift coefficient in the modulation of GCR Carbon in the heliosphere are studied in **Chapter 7**. This is illustrated with and without the enhancement of the perpendicular polar diffusion for the two solar magnetic field polarities during solar minimum conditions. Of particular interest is how the relation between the four scenarios of the drift scale and polar perpendicular diffusion influences differences in spectra between the $A > 0$ cycle and $A < 0$ cycles for modulation in the equatorial plane and at a heliolatitude of Voyager 1.

Chapter 8 gives a summary and the conclusions of this study.

Extracts from this work were published in peer reviewed journals. See *Ngobeni and Potgieter* (2010), *Ngobeni and Potgieter* (2011), *Ngobeni and Potgieter* (2012) and *Ngobeni and Potgieter* (2014).

Chapter 2

Cosmic rays and the heliosphere

2.1 Introduction

This chapter introduces the basic concepts that are important to the study of CR propagation in the heliosphere. It starts with a brief discussion of the Sun, the solar wind, the HMF, the HCS, solar cycle variations, the heliosphere and charged particles in the heliosphere, in particular GCRs as fully ionized particles with kinetic energy $E > 1.0$ MeV/nuc. It closes with a concise discussion of selected spacecraft missions, which provide valuable $in\ situ$ observations and insight for modulation studies.

2.2 The Sun and solar activity

The Sun is the nearest rotating magnetic star that forms the basis of the solar system, situated at about one astronomical unit (AU) from the Earth (one astronomical unit = 1.49×10^8 km, the average distance between the Sun and Earth) and with radius $r_\odot \sim 0.005$ AU. It is mainly composed of Hydrogen ($\sim 90\%$) and Helium ($\sim 10\%$) with traces of heavier elements such as Carbon, Nitrogen and Oxygen. The visible solar surface over the convective zone is called the photosphere. Visible on the photosphere of the Sun are sunspots which are dark regions, usually appearing in groups, that have a lower temperature than their surroundings and contain intense magnetic fields. The formation of the sunspots on the solar surface is one of the important properties of the Sun from CR point of view (see e.g. *Hathaway*, 2010; *Usoskin*, 2013). Detailed records of the sunspot numbers, which are a direct indication of the level of solar activity, are shown in Figure 2.1 from 1750 up to 2012 as a function of time in years (data from: `ftp://ftp.ngdc.noaa.gov`). From these observations of monthly averaged values of the sunspot numbers, it is evident that the Sun has a quasi-periodic ~ 11 year cycle called a solar activity cycle. Every 11 years the Sun moves through a period of fewer and smaller sunspots called solar minimum followed by a period of larger and more sunspots called solar

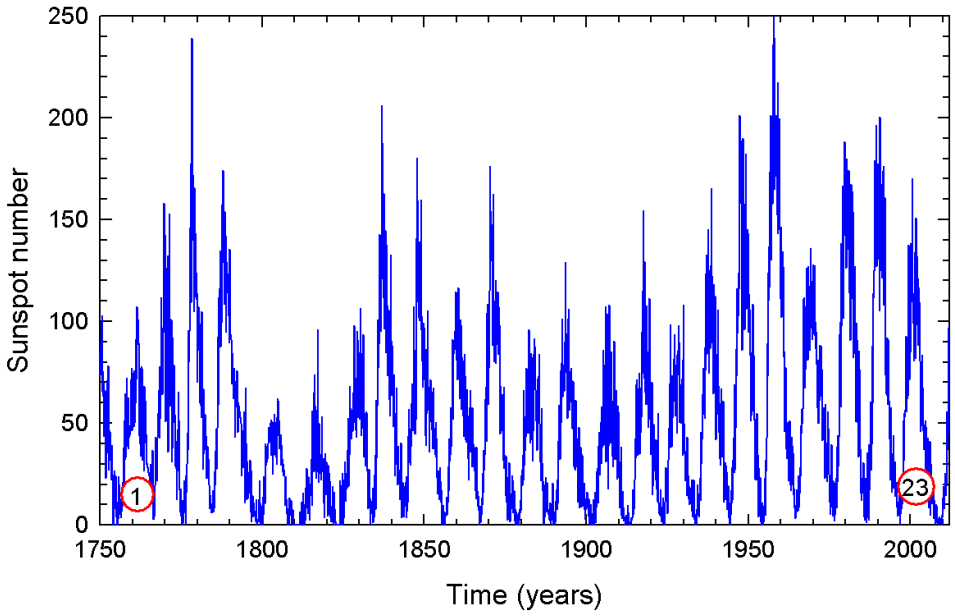

Figure 2.1: Monthly averaged sunspot numbers from 1750 to 2012, as a proxy for solar activity. The red circled 1 and 23 denote the first official solar cycle and the 23^{rd}. Data from: ftp://ftp.ngdc.noaa.gov.

maximum. The importance of the Sun from a CR point of view will be discussed in the next sections.

2.3 The solar wind

The plasmatic atmosphere of the Sun constantly blows away from its surface to maintain equilibrium (*Parker*, 1958). This plasmatic atmosphere is called the solar wind, which flows through interplanetary space and past the Earth with a velocity of several hundred kilometres per second. The source of the solar wind is the Sun's hot corona. The temperature of the corona is so high that the Sun's gravity cannot hold on to it (see e.g. *Hansteen and Leer*, 1995). Solar wind particles have been detected by space probes and the discovery of the solar wind was one of the first astronomical measurements made by the space programme. Before the solar wind was discovered, its possible existence was suggested. The behaviour of the tails of the comets that always pointed directly away from the Sun regardless of their position, when they were close to the Sun, could be understood if they were continuously bombarded by a stream of electrically charged particles emitted by the Sun (*Biermann*, 1951, 1957). For a review, see *Fichtner* (2001) and references therein.

The latitudinal dependence of the solar wind speed V has been confirmed by Ulysses spacecraft observations (e.g. *Phillips et al.*, 1994, 1995). These observations have revealed that V is not uniform over all heliolatitudes and can be divided into the fast and slow solar wind. The

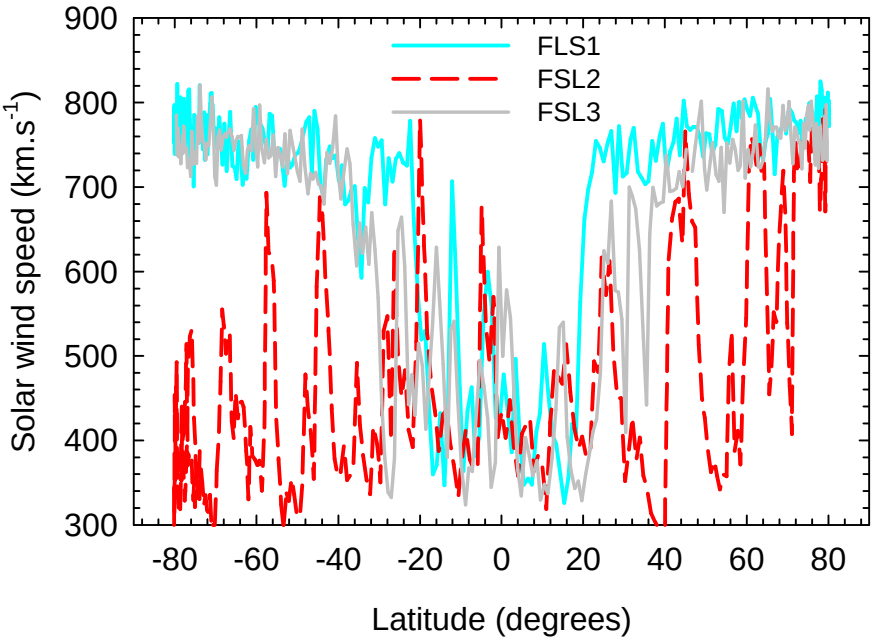

Figure 2.2: The solar wind speed as a function of heliolatitude with 0 degrees the equatorial plane as measured by Ulysses during the three fast latitude scans (FLS), represented by FLS1 (cyan line, July 1994 - July 1995), FLS2 (red line, October 2000 - September 2001) and FLS3 (grey line, February 2007 - January 2008). The FLS1 and FLS3 occurred during solar minimum periods but FLS2 was during solar maximum period. Data from: http://cohoweb.gsfc.nasa.gov.

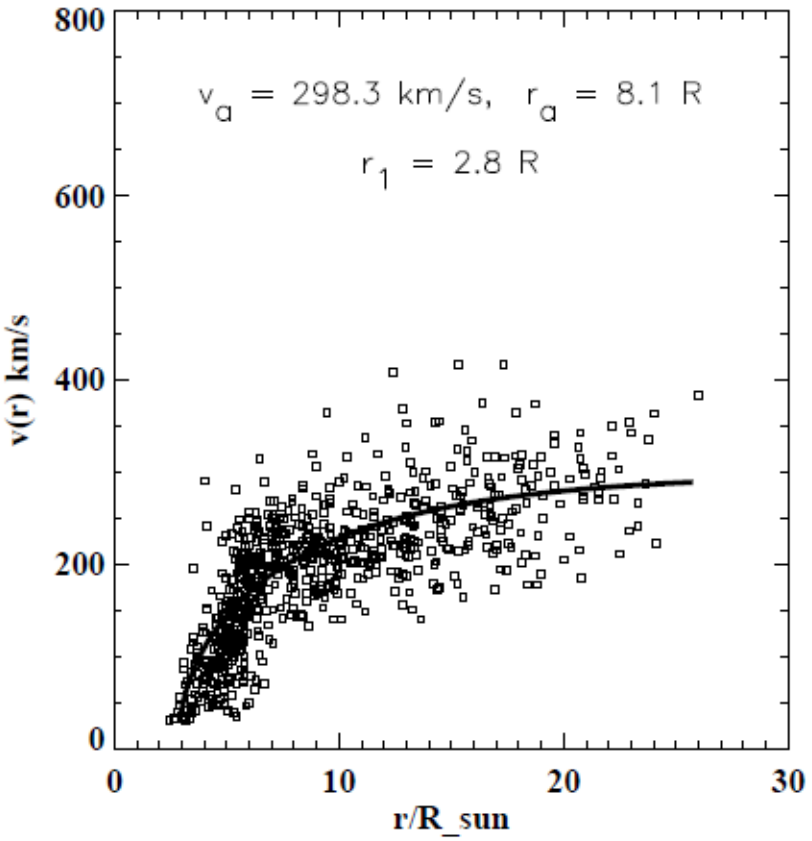

Figure 2.3: Radial solar wind speed for 65 individual moving density enhancements in the slow solar wind stream as a function of $r/r_{\odot}$. The figure shows that the speed of these enhancements tends to cluster along a quasi-parabolic path. The solid line is the best fit to the data points. Note that R_sun in the figure denotes $r_{\odot}$. Adapted from *Sheeley et al.* (1997).

basic reason is that the Sun's magnetic field dominates the original outflow of the solar wind. If the solar magnetic field is perpendicular to the radial outflow of the solar wind it can prevent the outflow. This is usually the case at low solar latitudes where the near Sun magnetic field lines are parallel to the Sun's surface. These field lines are in the form of loops which begin and end on the solar surface and stretch around the Sun to form the streamer belts. These streamer belts are regarded as the most plausible sources of the slow solar wind speed which have typical values of ~ 400 km.s^{-1} (*Schwenn*, 1983; *Marsch*, 1991). Other indications are that the slow solar wind speed may arise from the edges of large coronal holes or from smaller coronal holes (e.g. *Schwenn*, 2006; *Wang*, 2011). In regions where the solar magnetic field is directed radially outward, such as at the solar polar regions, the magnetic field will assist rather than oppose the coronal outflow. The fast solar wind with a characteristic average speed of up to ~ 800 km.s^{-1} emanates from the polar coronal holes that are located at the higher heliographic latitudes (e.g. *Krieger et al.*, 1973; *McComas et al.*, 2002). An example of the latitude dependence of V as measured by Ulysses is shown in Figure 2.2 during the three fast latitude scan (FLS) periods, represented in the figure as FLS1 (cyan line), FLS2 (red line) and FLS3 (grey line). The FLS1 and FLS3 occurred during solar minimum periods but FLS2 was during solar maximum period. Evident from Figure 2.2 are significant variations of V with heliolatitude, particularly the existence of the fast and slow solar wind during solar minimum conditions. In contrast, for solar maximum activity no well-defined latitude dependence of V is observed (e.g. *Richardson et al.*, 2001; *McComas et al.*, 2002).

The radial dependence of V between 0.1 AU and 1.0 AU was studied by e.g., *Kojima et al.* (2004) and *Sheeley et al.* (1997). They have found that both the low and high speed winds accelerate within 0.1 AU of the Sun and become a steady flow beyond 0.3 AU. An example is shown in Figure 2.3 where the radial solar wind speeds for 65 individual moving density enhancements in the slow solar wind stream are shown as a function of $r/r_\odot$ taken from *Sheeley et al.* (1997), with r representing the radial distance in AU. It follows from this figure that the speeds of these enhancements tend to cluster along a quasi-parabolic path (solid line) showing the radial dependence of V in this region.

To model the solar wind velocity, $\mathbf{V}$, on a global scale, thus neglecting smaller scale variations, in modulation models it is assumed that

$$\mathbf{V}(r,\theta) = V(r,\theta)\mathbf{e}_r = V_r(r)V_\theta(\theta)\mathbf{e}_r, \tag{2.1}$$

where θ is the polar angle with $\mathbf{e}_r$ the unit vector in the radial direction. The latitude dependence $V_\theta(\theta)$ during solar minimum conditions (e.g. *Hattingh*, 1998) is given as,

$$V_\theta(\theta) = 1.5 \mp 0.5 \tanh\left[\frac{2\pi}{45}(\theta - 90^o \pm \varphi)\right], \tag{2.2}$$

where $0^o \leq \theta \leq 90^o$, the northern hemisphere and $90^o \leq \theta \leq 180^o$, the southern hemisphere respectively with $\varphi = 35^o$. For solar maximum the solar wind speed is assumed independent

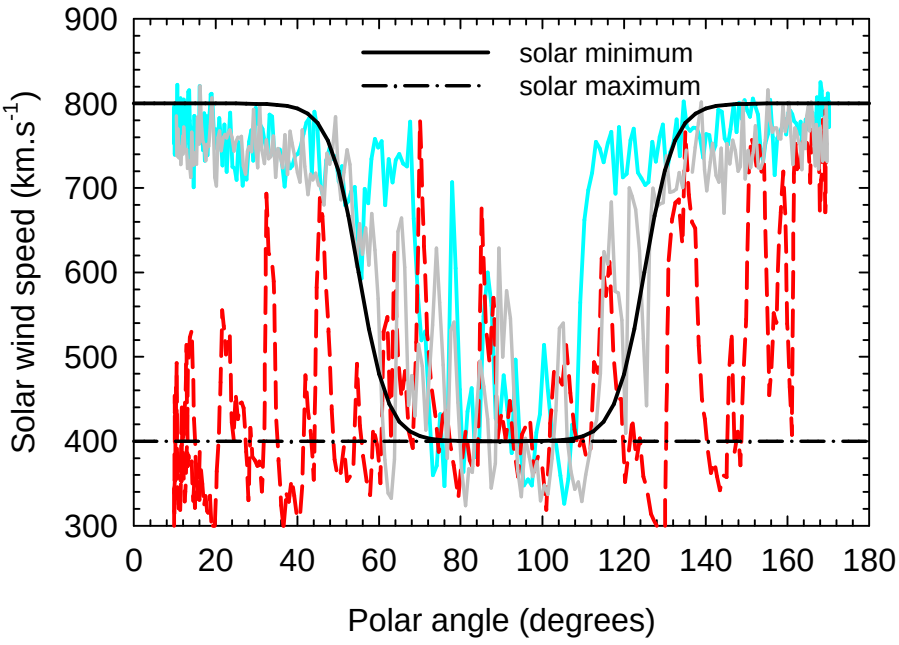

Figure 2.4: The assumed global latitude dependence of the solar wind speed as a function of polar angle θ during solar minimum (black solid line given by Equation 2.2) and solar maximum conditions (dash-dot line given by Equation 2.3). The modeled solar wind profiles are compared with Ulysses solar wind speed measurements given in Figure 2.2.

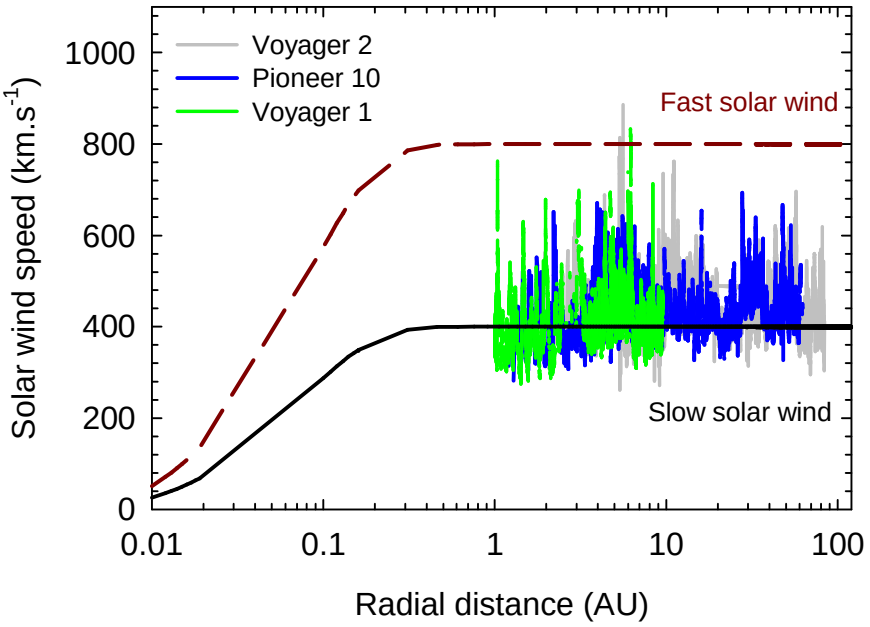

Figure 2.5: The radial dependence of the solar wind speed as modeled by Equation 2.4 for a slow solar wind stream (black solid line) and a fast solar wind stream (dark-red dashed line). Radial solar wind speed data from Pioneer 10 (blue line), the Voyager 1 (green line) and the Voyager 2 (grey line) are shown for comparison. Data from: http://cohoweb.gsfc.nasa.gov.

of latitude so that

$$V_\theta(\theta) = 1.0. \tag{2.3}$$

Figure 2.4 shows the globally modeled latitude dependence of V as given by Equations 2.2 and 2.3 for solar minimum and solar maximum conditions respectively. The black solid line shows solar minimum while the dash-dot line shows solar maximum conditions. The modeled V profiles are compared with Ulysses solar wind speed measurements described in Figure 2.2. For solar minimum there is a slow solar wind speed of ∼400 km.s^{-1} in the equatorial regions which increases in the polar regions to ∼800 km.s^{-1}. For solar maximum conditions no latitudinal dependence is assumed, so that under these conditions the solar wind speed on average is assumed 400 km.s^{-1} for all latitudes.

The globally modeled radial dependence, based on what was shown in Figure 2.3, $V_r(r)$ of the solar wind inside off the termination shock is given as

$$V_r(r) = V_0 \left(1 - \exp\left[\frac{40}{3}\frac{(r_\odot - r)}{r_0}\right]\right), \tag{2.4}$$

with $r_0 = 1$ AU, $V_0 = 400$ km.s^{-1} and $r_\odot = 0.005$ AU. Figure 2.5 shows the modeled radial dependence of both the slow and fast solar wind speed profiles, as given by Equation 2.4, compared with the solar wind measurements from Pioneer 10, Voyager 1 and Voyager 2 taken inside off the TS. It follows from this figure that $V_r(r)$ has a strong radial dependence below 0.3 AU but then becomes almost constant beyond 0.3 AU. The effects of the solar wind TS on the radial dependence of V are discussed below in Section 2.6.1.

2.4 The heliospheric magnetic field

Due to the small resistivity of the solar wind plasma, the HMF is frozen-in so that it is carried with the solar wind throughout the heliosphere. The rotation of the Sun causes the HMF to have a spiral structure in and away from the Sun's equatorial plane. Furthermore, the HMF is directed outward from the Sun in one of its hemispheres (north) and inward in the other (south). However, during extreme solar activity (every ~ 11 years) the direction of the HMF changes and as a result a 22 year magnetic polarity cycle is formed. The HMF plays an important role in the transport of cosmic rays in the heliosphere. Charged particles, such as GCRs, follow and gyrate along the HMF so that the magnetic field irregularities, due to turbulence, cause pitch angle scattering of these particles.

A standard choice for the HMF is a Parker spiral field (*Parker*, 1958),

$$\mathbf{B} = B_0 \left(\frac{r_0}{r}\right)^2 (\mathbf{e}_r - \tan\psi \mathbf{e}_\phi), \tag{2.5}$$

where $\mathbf{e}_\phi$ is the unit vector component in the azimuthal direction, B_0 is the HMF magnitude at

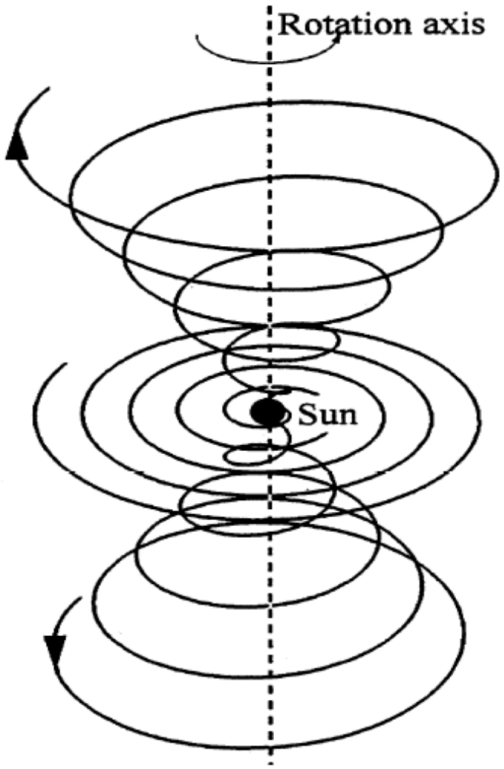

Figure 2.6: A graphical illustration of a 3D representation of the Parker HMF spiral structure with the Sun at the origin. The spirals rotate around the polar axis $\theta = 45^o$, $\theta = 90^o$ and $\theta = 135^o$. The arrows show the direction of the HMF. Adapted from *Hattingh* (1998).

the Earth and

$$\tan\psi = \frac{\Omega(r - r_\odot)\sin\theta}{V}. \tag{2.6}$$

Here Ω is the average angular rotation speed of the Sun and ψ is the spiral angle defined as the average angle between the radial and the average HMF at a certain position. An example of the three-dimensional (3D) HMF spiral structure taken from *Hattingh* (1998) is shown in Figure 2.6. The magnitude of the HMF, B_m, is given by

$$B_m = B_0 \left(\frac{r_0}{r}\right)^2 \sqrt{1 + \left(\frac{\Omega(r - r_\odot)\sin\theta}{V}\right)^2}, \tag{2.7}$$

or equivalently

$$B_m = B_0 \left(\frac{r_0}{r}\right)^2 \sqrt{1 + \tan^2\psi}. \tag{2.8}$$

Over the years many modifications of this Parker HMF have been proposed with varying level of complication (see e.g. *Jokipii and Kóta*, 1989; *Moraal*, 1990; *Smith and Bieber*, 1991; *Fisk*, 1996). Below, discussion on the modifications of the Parker HMF is given, but limited to the work done by *Jokipii and Kóta* (1989) and *Fisk* (1996). The *Smith and Bieber* (1991) modification was studied in detail by *Raath* (2014).

2.4.1 The Jokipii-Kóta modification of the Parker spiral

At high latitude the geometry of the HMF is not just an ordinary Parker spiral as argued by *Jokipii and Kóta* (1989). This argument is based on the fact that the solar surface near the poles is not a smooth surface, but a granular turbulent surface that keeps changing with time. Consequently, this turbulence may cause the field lines to wander randomly, creating transverse components in the field, thus causing temporal deviations from the smooth Parker geometry (*Jokipii and Kóta*, 1989; *Forsyth et al.*, 1996). The effect of the more turbulent magnetic field at the polar regions is to increase the mean magnetic field strength compared to pure Parker model. The modification of the Parker spiral suggested by *Jokipii and Kóta* (1989) is such that Equation 2.7 becomes

$$B_m = B_0 \left(\frac{r_0}{r}\right)^2 \sqrt{1 + \left(\frac{\Omega(r - r_\odot)\sin\theta}{V}\right)^2 + \left(\frac{r\delta(\theta)}{r_\odot}\right)^2}. \tag{2.9}$$

Here the modification $\delta(\theta)$ is given by

$$\delta(\theta) = \frac{\delta_m}{\sin\theta}, \tag{2.10}$$

with $\delta_m = 8.6 \times 10^{-5}$, so that $\delta(\theta) = 0.002$ near the poles and $\delta(\theta) \sim 0$ in the equatorial plane. The original modification, as proposed by *Jokipii and Kóta* (1989), had $\delta(\theta)$ equal to a constant so that the subsequent $\mathbf{B}$ was not divergence free. Equation 2.9 remains divergent free (see *Steenberg*, 1998; *Langner*, 2004). Measurements of the HMF by Ulysses spacecraft in the polar regions qualitatively support this modification (*Balogh et al.*, 1995; *Heber and Potgieter*, 2006). The Jokipii-Kóta modification to the pure Parker HMF is used in this study.

2.4.2 The Fisk field model

An alternative model for the HMF geometry has been proposed by *Fisk* (1996) based on the argument that the Sun does not rotate rigidly, but rather differentially with solar poles rotating $\sim 20\%$ slower than the solar equator (e.g. *Snodgrass*, 1983). Due to this differential rotation of the Sun, the foot points of the HMF on the solar surface also undergo differential rotation. According to the Fisk model the field lines will move through a coronal hole due to the differential rotation and experience a subsequent non-radial expansion from the solar surface. This results in large excursions of the field lines with heliographic latitude and hence the magnetic field lines at high latitudes can be connected directly to corotating regions in the solar wind at lower latitudes.

When the foot point trajectories on the source surface can be approximated by circles offset from the solar rotation axis with an angle β_A, the three components of the Fisk field are ob-

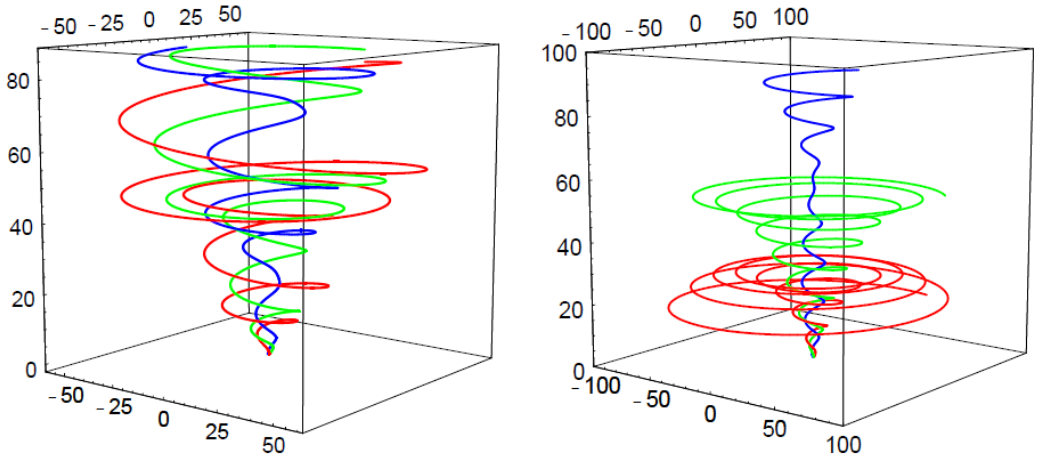

Figure 2.7: A graphical illustration of the HMF lines of the type I Fisk field (left panel) and type II Fisk field (right panel). The field lines originate from 30^o co-latitude, but at different longitudes. Radial distances are in AU, with the Sun at the centre. Adapted from *Burger and Hattingh* (2001).

tained (*Zurbuchen et al.*, 1997):

$$
\begin{aligned}
B_r &= B_0 \left(\frac{r_0}{r}\right)^2, \\
B_\theta &= B_r \frac{(r - r_{ss})\omega'}{V} \sin\beta_A \sin\left(\phi + \frac{\Omega(r - r_{ss})}{V}\right), \\
B_\phi &= B_r \frac{(r - r_{ss})}{V}\left(\omega' \sin\beta_A \cos\theta \cos\left(\phi + \frac{\Omega(r - r_{ss})}{V}\right) + \sin\theta(\omega' \cos\beta_A - \Omega)\right),
\end{aligned}
\tag{2.11}
$$

where r_{ss} is the radius of the solar source surface, ω' is the differential rotation rate and ϕ is the azimuthal angle. The Fisk model includes a meridional component of **B** which is not present in the Parker model. With $\beta_A \neq 90^o$ and $\beta_A = 90^o$ respectively, Equation 2.11 describes what *Burger and Hattingh* (2001) called a type I and type II Fisk field. Graphical representations of both types of the Fisk fields are shown in Figure 2.7.

The HMF given by Equation 2.11 leads to a more complicated form of transport equation and the implementation of this 3D field geometry in numerical models lies beyond the scope of this work. For more information from a cosmic ray point of view the reader is referred to *Kóta and Jokipii* (1997); *Giacalone and Jokipii* (1999); *Burger and Hattingh* (2001); *Burger and Hitge* (2004); *Krüger* (2005); *Engelbrecht* (2008) and *Sternal et al.* (2011).

2.5 Heliospheric current sheet

A major three dimensional corotating structure of the HMF of importance to CR modulation is the HCS, which divides the solar magnetic field into two hemispheres of opposite polarity. The HCS is tilted by an angle α because of the fact that the magnetic equator of the Sun does not coincide with the heliographic equator, because the magnetic axis of the Sun is tilted relative

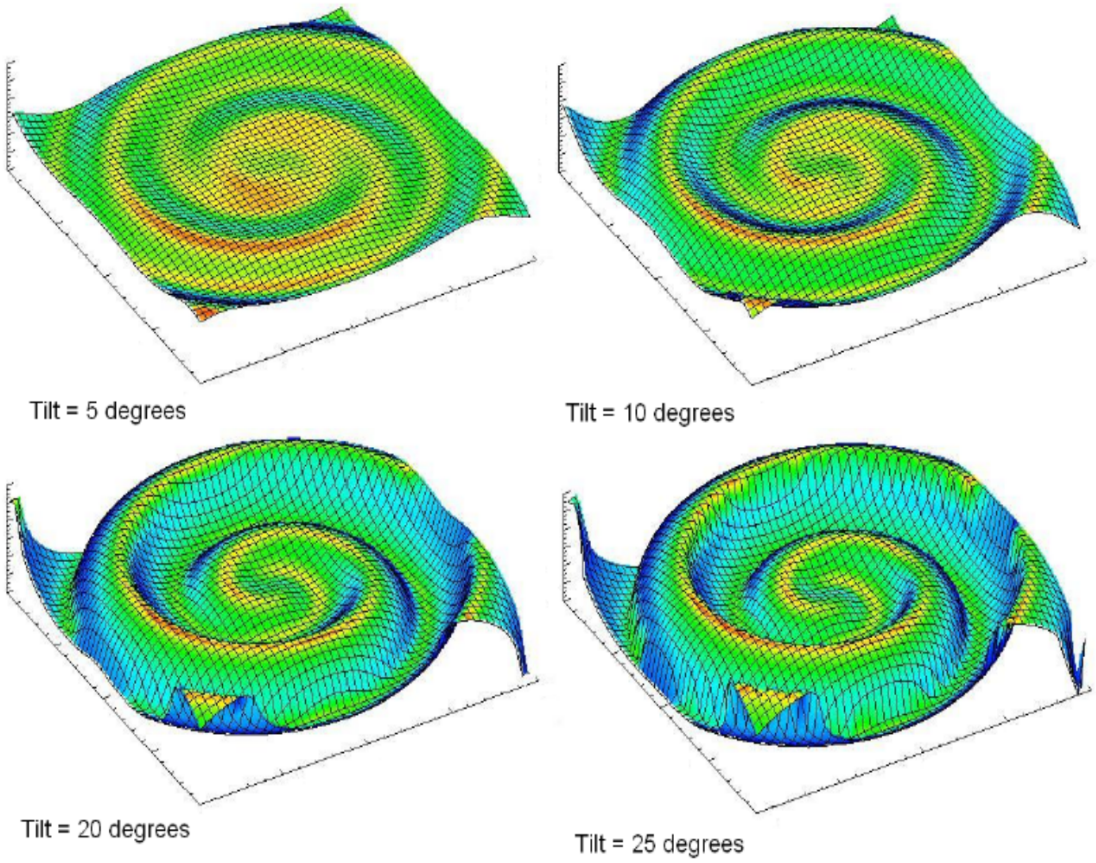

Figure 2.8: A graphical representation of the wavy heliospheric current sheet to a radial distance of 10 AU with a tilt angle of $\alpha = 5^o$ (top, left panel), $\alpha = 10^o$ (top, right panel), $\alpha = 20^o$ (bottom, left panel) and $\alpha = 25^o$ (bottom, right panel). The Sun is at the centre. Adapted from *Strauss* (2010).

to the rotational axis. Thus the HCS has a wavy structure as it is convected with the solar wind outward to the outer heliosphere. Since the Sun has typically an 11-year activity cycle, the waviness of the HCS correlates with solar activity of the Sun. This indicates that during solar maximum conditions the angle between the Sun's magnetic and rotational axis, known as the tilt angle α, increases to more than 70^o. While during periods of lower solar activity the rotation and magnetic axis of the Sun become nearly aligned, causing relatively small neutral sheet waviness $\sim 5^o - 10^o$. Figure 2.8 illustrates an example of a 3D idealization of four HCS configurations, taken from *Strauss* (2010), for distances up to 10 AU when $\alpha = 5^o$ (top, left panel), $\alpha = 10^o$ (top, right panel), $\alpha = 20^o$ (bottom, left panel) and $\alpha = 25^o$ (bottom, right panel). For details on the HCS see e.g. *Smith* (2001); see also *Strauss et al.* (2012), *Strauss* (2013) and *Raath* (2014) for the 3D modelling of the HCS.

For a constant and radial solar wind speed an expression for the latitudinal extent of the HCS is given by *Jokipii and Thomas* (1981) as,

$$\theta' = \frac{\pi}{2} + \sin^{-1}\left(\sin\alpha \sin\left[\phi + \frac{\Omega(r - r_0)}{V}\right]\right), \tag{2.12}$$

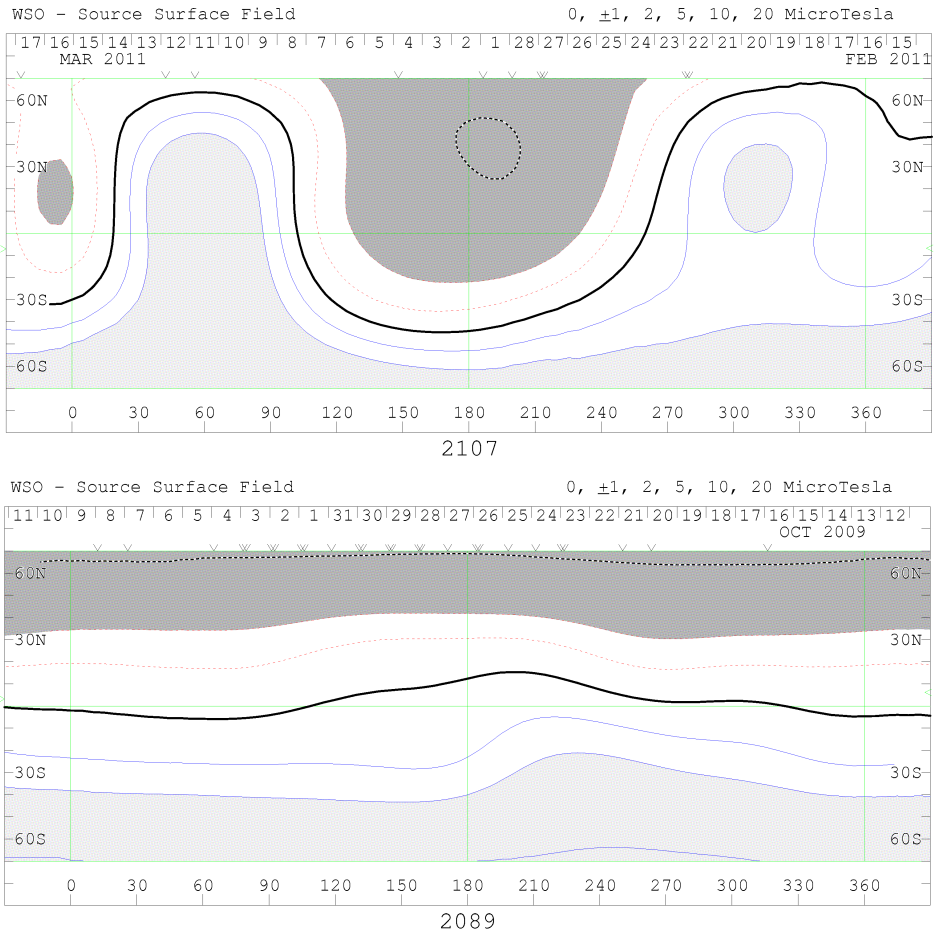

Figure 2.9: Contour plots of the coronal magnetic field computed using the Potential Field Source Surface (PFSS) model (*Schatten et al.*, 1969) on a source surface at $2.5r_{\odot}$. These contour plots are for the October 2009 solar minimum (lower panel) and for an increased solar activity in February 2011 (upper panel). The thick black line in both panels corresponds to the neutral line which is the origin of the wavy HCS. The magnetic polarities of each solar hemisphere are represented by light grey (magnetic field directed inwards to the Sun) and dark grey (magnetic field directed away from the Sun) shades. Below and above the neutral lines opposite polarities are seen, in this case corresponding to an $A < 0$ HMF polarity cycle. Images from http://wso.stanford.edu.

where θ' is the polar angle of the HCS. For smaller values of α the above equation reduces to,

$$\theta' \cong \frac{\pi}{2} + \alpha \sin\left[\phi + \frac{\Omega(r - r_0)}{V}\right]. \tag{2.13}$$

Figure 2.9 displays a clear indication of the existence of the HCS, which shows contour plots of the coronal magnetic field, computed using the Potential Field Source Surface (PFSS) model (*Schatten et al.*, 1969), on the source surface located at $2.5r_{\odot}$. These contours show the magnetic field strength and polarity in the northern and southern hemispheres during low solar activity (lower panel) and high solar activity (upper panel) periods. The HCS can be identified on each panel as the black line separating regions of opposite polarity, shown as shades of grey colour. The wavy structure of the HCS is also readily observed, especially during high levels of solar activity (larger values of α), indicating that it varies with solar activity.

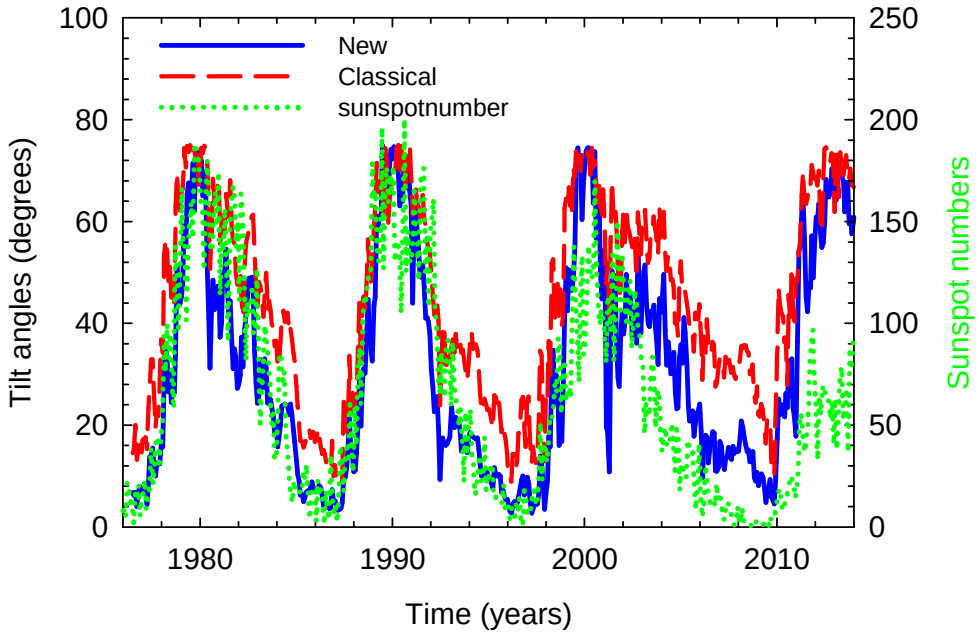

Figure 2.10: The two different model tilt angle α, namely "classical" (red solid line) and "new" (blue dashed line) are shown as a function of time from 1977 until 2014. Both the tilt angles are compared to the yearly sunspot number (green dotted line). Tilt angle data from: http://wso.stanford.edu and yearly sunspot data from:ftp://ftp.ngdc.noaa.gov.

Figure 2.10 shows the averaged HCS tilt angles as a function of time computed with the "classic" and "new" models (*Hoeksema*, 1992). Both tilt angle models are compared to the yearly sunspot number. It is evident that α varies from small to a larger value between solar minimum ($\alpha \sim 3 - 10^o$) and solar maximum ($\alpha \sim 75^o$) tracing out an ~ 11 year solar cycle.

The waviness of the HCS plays an important role in CR modulation and it is regarded as a good proxy for solar activity. However, it is not known how the waviness is preserved throughout the outer heliosphere, especially what happens to it in the heliosheath (see e.g. *Opher et al.*, 2009; *Florinski*, 2011; *Pogorelov et al.*, 2013; *Strauss*, 2013; *Luo et al.*, 2013).

To include the polarity of the HMF, Equation 2.5 is modified so that it becomes,

$$\mathbf{B} = AB_0 \left(\frac{r_0}{r}\right)^2 (\mathbf{e}_r - \tan\psi \mathbf{e}_\phi)\,[1 - 2H(\theta - \theta')]. \tag{2.14}$$

Here $A = \pm 1$ is a constant determining the polarity of the HMF which alternates every 11 years. Periods when the HMF in the northern hemisphere is pointed away and towards the Sun in the southern hemisphere are called the $A > 0$ polarity cycles with $A = +1$. For the $A < 0$ polarity cycles, $A = -1$ and the direction of the HMF reverses. The $H(\theta - \theta')$ is the Heaviside step function and is given by,

$$H(\theta - \theta') = \begin{cases} 0 & \text{when } \theta < \theta' \\ 1 & \text{when } \theta > \theta'. \end{cases} \tag{2.15}$$

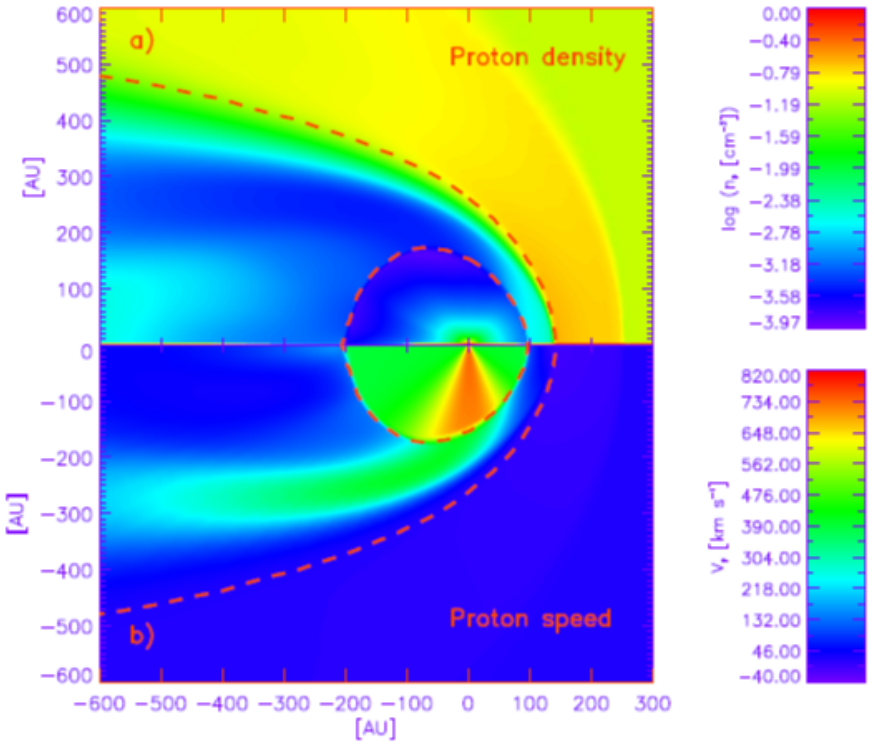

Figure 2.11: Contour plot of a HD simulated heliosphere showing the computed proton number density (top) and proton speed (bottom). Shown by the dashed lines are the positions of the TS (dashed circle) and the HP. From *Scherer and Ferreira* (2005).

This function causes the HMF to change polarities across the HCS. If this function is used directly in the numerical modulation model, the discontinuity causes severe numerical problems. To overcome this problem the Heaviside function is approximated (*Hattingh*, 1998; *Langner*, 2004) by

$$H'(\theta) \approx \tanh\left[2.75(\theta - \theta')\right]. \tag{2.16}$$

2.6 The heliosphere and its geometry

The heliosphere can be defined as the region around the Sun filled by the solar wind and its embedded magnetic field. The heliosphere moves through the local interstellar medium (LISM) with a speed of $\sim$ 25 km.s^{-1} so that a heliospheric interface is formed caused by the interaction of the solar and interstellar plasmas. The solar wind and the HMF push back the interstellar field and plasma to prevent them from flowing into the heliosphere. Eventually, the solar wind pressure is balanced by LISM pressure at a location called the heliopause. The HP is defined as the outer boundary of the heliosphere that separates the solar and interstellar plasmas. As the heliosphere moves through the LISM, it becomes asymmetrical with respect to the Sun, with the tail region much more extended than the nose region, the direction in which

it is moving. An example of a hydrodynamically (HD) simulated heliosphere is shown in Figure 2.11 as a contour plot with the computed proton number density (top) and proton speed (bottom) for an anisotropic solar wind taken from *Scherer and Ferreira* (2005). Since the proton number density varies over several orders of magnitude, a logarithmic scale is assumed. The results are shown in the rest frame of the Sun, where its motion relative to the LISM appears as an interstellar wind blowing from right to left. The dashed lines indicate the position of the solar wind TS and the HP. The main boundaries of the interaction between the solar and interstellar flows are the TS, the HP and perhaps also a bow shock (BS); see also *Scherer and Fichtner* (2014). As shown in Figure 2.11, both the TS and HP positions are functions of polar angle and are elongated along the Sun's polar axis (see e.g. *Fahr et al.*, 2000; *Zank and Muller*, 2003; *Scherer and Ferreira*, 2005). Furthermore, it follows from Figure 2.11 that there is no well defined distance to the HP in the tail direction.

A new view of the geometrical shape of the heliosphere from magneto-hydrodynamic (MHD) models includes a north-south asymmetry caused by the external pressure resulting from the ISMF (see e.g *Opher et al.*, 2009; *Pogorelov et al.*, 2009; *Strauss*, 2013; *Luo et al.*, 2013). This aspect is discussed in more detail in Chapter 4.

2.6.1 The solar wind termination shock

The supersonic solar wind, originating on the Sun, must merge with the LISM surrounding the heliosphere. It must, however, first undergo a transition from a supersonic into a subsonic flow at the TS in order for the solar wind ram pressure to match the interstellar thermal pressure. The TS was first suggested by *Parker* (1961) and can be considered as the first heliospheric boundary away from the Sun. The TS can be described as a collision-less shock wave, i.e., a discontinuous transition from a supersonic to subsonic flow speed. Various instabilities can be generated in the TS so that it is highly dynamic in both structure and location (see e.g. *Scherer and Ferreira*, 2005; *Snyman*, 2007). The dynamic TS was confirmed when the Voyager 1 and 2 spacecraft crossed it at $r \sim 94$ AU and ~ 84 AU respectively (see *Stone et al.*, 2005; *Decker et al.*, 2005; *Stone et al.*, 2008; *Richardson et al.*, 2008). The difference in the TS positions between the Voyager 1 and 2 directions is further discussed in Chapter 4.

For the modeled heliosphere that includes the TS, the radial dependence of V decreases from the upstream value $V_1(\theta)$ across the shock according to:

$$V_r = \frac{V_1(\theta)\,(s_k+1)}{2s_k} - \frac{V_1(\theta)\,(s_k-1)}{2s_k}\tanh\left(\frac{r-r_{TS}}{L}\right), \tag{2.17}$$

with r_{TS} the radial position of the TS, $s_k = 2.0$ the shock compression ratio at all latitudes and $L = 1.2$ AU the shock precursor scale length (*le Roux et al.*, 1996; *Langner et al.*, 2003). This means that up to the shock, V decreases by $0.5s_k$ starting at L, then abruptly as a step function

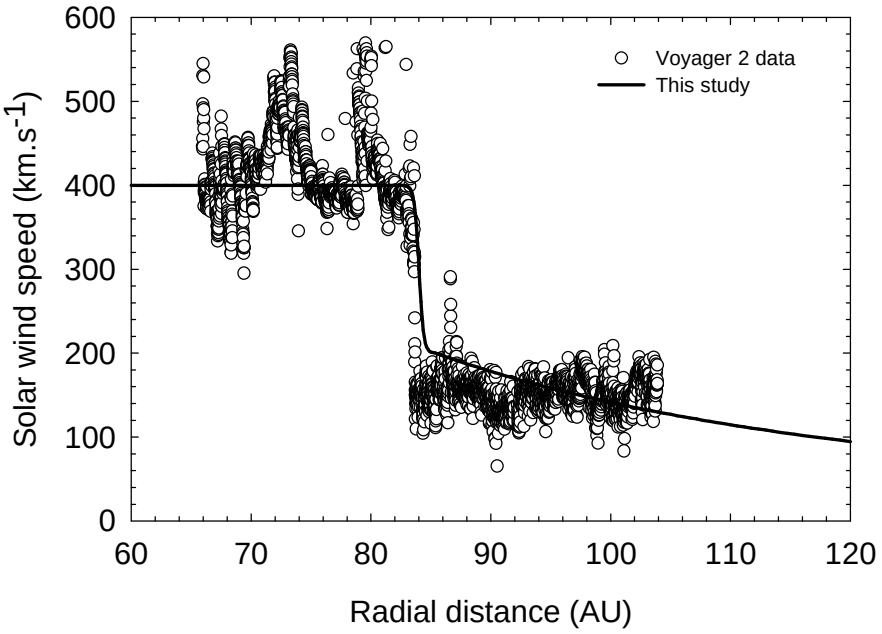

Figure 2.12: Radial component of the solar wind speed V modeled as a function of radial distance for $r \geq 60$ AU compared to solar wind speed observations from Voyager 2 taken before the TS crossing and in the heliosheath. The TS position is placed at 84 AU with $s_k = 2.0$ and the HP position at 120 AU. Solar wind data from: http://cohoweb.gsfc.nasa.gov.

to the downstream value, in total to a value of V/s_k. The HMF thus increases by a factor s_k at the TS. The assumed value of s_k is consistent with Voyager 1 and 2 observations (*Stone et al.*, 2005; *Richardson et al.*, 2008). However, the value of s_k may change when the shock moves out and also as a function of latitude (*Ngobeni and Potgieter*, 2008; *Strauss*, 2010).

Beyond the TS, $r > r_{TS}$, it is assumed in this study that V_r decreases up to the HP simply as

$$V_r \propto r^{-2}. \tag{2.18}$$

For an illustration of possible various radial dependence of V_r in the heliosheath, see *Langner et al.* (2006); *Strauss* (2010). Figure 2.12 depicts how the computed V_r slows down from in front to behind the TS and how it then decreases proportional to r^{-2} beyond the TS to the HP. The modeled V_r is compared with the solar wind speed measurements from Voyager 2, emphasising what happens close to the TS. Take note that in the heliosheath, the solar wind deviates from its original radial flow and hence its radial profile is expected to be different to the approach given by Equation 2.18. At ~ 84 AU the Voyager 2 measurements show a sudden decrease in speed, which corresponds to the TS crossing (*Stone et al.*, 2008; *Richardson et al.*, 2008).

2.6.2 The heliosheath

The region between the TS and the HP is the inner heliosheath, simply referred to as the heliosheath in CR modulation literature, that contains hot shocked plasma of solar origin that is deflected from its initial radial expansion and forms an extended heliotail in the downwind direction. In the inner heliosheath the wind is slower, hotter and denser as it interacts with the surrounding interstellar matter. The HMF is still frozen into the solar wind plasma and increases in proportion to the increase in plasma density in the inner heliosheath. The LISM plasma assumingly also undergoes a weak shock transition at the BS ahead of the heliopause. The LISM flow is diverted around this obstacle in the region behind the BS forming the outer heliosheath. The outer heliosheath is unlikely to have significant effects on GCRs, although different opinions exist about what may happen in this region e.g. *Strauss et al.* (2013a); *Kóta and Jokipii* (2014) and *Guo and Florinski* (2014). The inner heliosheath is different from the region up-wind of the TS and it is rather complex but very interesting (see a review by *Potgieter*, 2008).

Observation made by Voyager 1 in the heliosheath confirmed earlier predictions that the dominant part of the modulation of GCRs at lower energies occur in the heliosheath (*Webber et al.*, 2013). This aspect is revisited in Chapter 6.

2.7 Charged particles in the heliosphere

Cosmic rays are energetic charged particles. They were discovered by Victor Hess during the historic balloon flights in 1911 and 1912, where it was shown that the origin of these particles is outside the Earth's atmosphere. See the review by *Carlson* (2012). As charged particles, CRs travel through interstellar space and the heliosphere, filter through our atmosphere to be detected at ground level. In the heliosphere four main populations of CRs are found. They are GCRs, anomalous components of cosmic rays (ACRs), Jovian electrons and solar energetic particles (SEPs). All these types of CRs are briefly discussed below but the last three are disregarded for the purpose of this study.

2.7.1 Galactic cosmic rays

Galactic CRs originate from far outside our solar system. It is believed that the energy transfer processes during supernova explosions in the galaxy are probably the major sources of these particles (see e.g. *Casadei and Bindi*, 2004; *Kobayashi et al.*, 2004). When arriving at the Earth, these particles are composed of $\sim 98\%$ nuclei (mostly protons), fully stripped of all their orbital electrons, and $\sim 2\%$ electrons, fewer positrons and anti-protons. On their way to Earth these particles are to some extent reaccelerated at the solar wind TS (e.g. *Jokipii et al.*, 1993). Modeling

the modulation of GCRs, in particular Carbon, in the heliosphere is the research topic for this study.

2.7.2 Anomalous cosmic rays

The ACRs were discovered by *Garcia-Munoz et al.* (1973). *Fisk et al.* (1974) recognized that these elements were originally interstellar neutral atoms that got singly ionized in the heliosphere by charge exchange with the solar wind ions, electron collisions, or photo-ionization. These singly ionized atoms are then picked up by the solar wind and convected outwards towards the outer heliosphere, where they are accelerated at, or beyond, the TS through various processes. Prior to Voyager 1 TS crossing, the principal acceleration mechanism at the TS was considered to be the diffusive shock acceleration. The acceleration of ACRs to higher energies is still a topic of considerable debate because no direct evidence of this process occurring at the location of the TS observed by Voyager 1 and 2 spacecraft (*Stone et al.*, 2005; *Decker et al.*, 2005; *Stone et al.*, 2008). For alternative acceleration processes of ACRs in the heliosheath see discussions by *Fisk and Gloeckler* (2009); *Strauss* (2010); *Strauss et al.* (2010b) and *Giacalone et al.* (2012).

2.7.3 Jovian electrons

It was discovered with the Jupiter fly-by of the Pioneer 10 spacecraft in 1973 that the Jovian magnetosphere, situated at ~ 5 AU in the ecliptic plane, is a relatively strong source of electrons with energies up to at least ~ 30 MeV (see e.g. *Simpson et al.*, 1974). These electrons, when released into the interplanetary medium, dominate the low energy electron intensities within the first ~ 10 AU away from the Sun (see *Haasbroek*, 1997; *Ferreira et al.*, 2001b,a; *Ferreira*, 2002; *Strauss et al.*, 2013b; *Potgieter and Nndanganeni*, 2013).

2.7.4 Solar energetic particles

Solar energetic particles are of solar origin. They are accelerated mainly by solar flares, coronal mass ejections and shocks in the interplanetary medium. SEPs may have energies up to several hundred MeV but are usually observed at Earth only for several hours mainly during solar maximum activity when occurring. For a review, see *Cliver* (2008).

2.8 Space missions

One of the most important aspects in the study of the heliospheric modulation of the CRs is the accumulation of data from $in\ situ$ observations. In this section the Voyager, Ulysses and Advanced Composition Explorer space missions are briefly discussed.

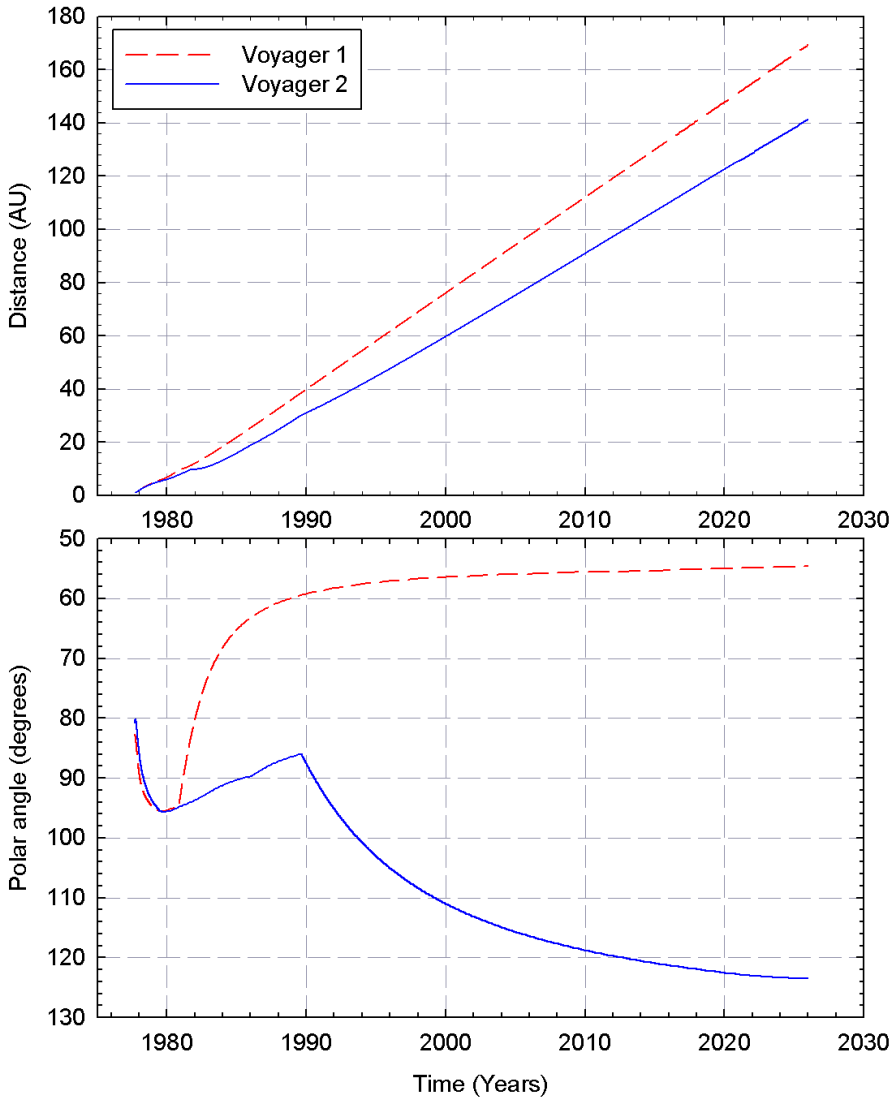

Figure 2.13: The trajectory of the Voyager 1 (red dashed lines) and Voyager 2 (blue solid lines) spacecraft in terms of radial distance from the Sun (top panel) and polar angle θ (bottom panel) as a function of time in years. The equatorial plane is at $\theta = 90^o$. Data from: http://cohoweb.gsfc.nasa.gov.

2.8.1 Voyager mission

The Voyager program consisted of a pair of unmanned scientific probes, Voyager 1 and Voyager 2, launched in 1977. They were sent to study Jupiter and Saturn and their satellites and magnetospheres. Voyager 2 also examined Uranus and Neptune. The two Voyager spacecraft were set to explore the Sun's environment from different heliographic latitudes simultaneously by sending Voyager 1 to the north while Voyager 2 was sent to the southern hemisphere both in the general direction of the nose of the heliosphere. Voyager 1 is currently at $\sim 34.4^o$ above the equatorial plane, while Voyager 2 is situated at $\sim 28.8^o$ below the equatorial plane. Both missions revealed large amounts of information about the HMF, solar wind and CRs. This information has been used to study the spatial and temporal variation of CRs at distances now

extending beyond 128 AU.

Voyager 1 and 2 are travelling at the speeds of ~ 3.6 and ~ 3.1 AU per year respectively. Voyager 1 crossed the TS in December 2004 (*Stone et al.*, 2005; *Decker et al.*, 2005) and the HP in 2012 (*Stone et al.*, 2013; *Krimigis et al.*, 2013; *Burlaga et al.*, 2013). While Voyager 2 crossed the TS in 2007 (*Stone et al.*, 2008; *Richardson et al.*, 2008) with the HP position along its trajectory still an unknown distance ahead. Figure 2.13 shows the heliospheric positions of both Voyager 1 (red dashed lines) and Voyager 2 (blue solid lines) as a function of time, in years, in terms of radial distance (top panel) and polar angle (bottom panel). At present, Voyager 1 is at 129 AU and Voyager 2 at 106 AU. Dramatic discoveries have unfolded when Voyager 1 crossed the HP (*Stone et al.*, 2013; *Krimigis et al.*, 2013; *Gurnett et al.*, 2013; *Burlaga et al.*, 2013) and when Voyager 2 crosses it more discoveries are expected that will give additional information of the HP structure, the ISMF and interstellar spectra for GCR species.

2.8.2 Ulysses mission

The Ulysses spacecraft was launched on 6 October 1990. This was the first spacecraft to undertake measurements far from the ecliptic plane and over the polar regions of the Sun, thus obtaining first hand knowledge concerning the high latitudes of the inner heliosphere ($r <\sim 5$ AU).

After its launch, the spacecraft stayed close to the ecliptic plane to reach Jupiter (at ~ 5 AU), from where it started to move to higher latitudes south of the ecliptic plane. In mid-1994 the highest southern latitude was reached at minimum solar activity. From there, Ulysses moved to the northern polar region which was reached in mid 1995 and returned to the equatorial plane again in 1998. After ∼1998 Ulysses started the second out-of-ecliptic orbit moving into the southern heliospheric polar regions. It crossed the equatorial plane in May 2001, and on 5 February 2004 the spacecraft was again closest to Jupiter. The Ulysses mission finally ended its exploration of the heliosphere on the 30th June 2009 after 18.8 years lifetime (see e.g. *Smith*, 2011).

The Ulysses mission was highly successful and had contributed significantly to the current knowledge regarding the inner heliosphere and CRs modulation. See the following publications for an overview: *Simpson et al.* (1996); *Marsden* (2001); *Heber and Potgieter* (2006); *Heber* (2011); *Smith* (2011).

2.8.3 Advanced Composition Explorer

Advanced Composition Explorer (ACE) was launched in August 1997 and it is located in orbit about the inner Sun-Earth Lagrangian (1.5×10^6 km sunward from the Earth). On board the

ACE spacecraft is the Cosmic Ray Isotope Spectrometer (CRIS) measuring the charge, energy and mass of GCRs for elements ranging from Boron to Nickel in the energy range $\sim 50 - 550$ MeV/nuc (e.g. *Lave et al.*, 2013). See also http://srl.caltech.edu/ACE/ASC/level2 for more details. In this study, measurements of energy spectra for GCR Carbon from CRIS are used as 1 AU observations when comparison is made with the modeled solutions.

2.9 Summary

In this chapter a basic and brief overview was given of the concepts used in the numerical modeling of heliospheric modulation of CRs. These concepts include the nature of CRs, the heliosphere and its geometry, the solar wind, the HMF, the solar cycle and the HCS. The Voyager, Ulysses and ACE space missions were briefly discussed.

In the next chapter an overview of modulation theory is given, particularly a discussion regarding the transport equation and the diffusion tensor.

Chapter 3

The transport equation and the diffusion tensor

3.1 Introduction

Galactic CRs enter the heliosphere from all directions and then propagate toward the Sun. Once inside the heliosphere they interact with the convective solar wind and its embedded turbulent magnetic field. The understanding of this global interaction is currently based on four major modulation processes: (1) convection with the solar wind, (2) diffusive random walk along and across the HMF, (3) adiabatic energy changes, and (4) drift motions due to gradients and curvatures in the HMF or any abrupt changes in the field direction, e.g. the HCS. Combined, these interplaying processes cause the intensity of GCRs to decrease toward the Sun and to change significantly over its 11-year activity cycle, exhibiting also a clear 22-year cycle. These four major modulation processes were combined by *Parker* (1965) into a transport equation (TPE) and cause the GCR intensities to decrease toward the Sun as a function of position, energy and time relative to their interstellar values. See e.g. the review on solar modulation by *Potgieter* (2013).

In this chapter a discussion of the heliospheric transport processes as they occur in the TPE is given, together with the corresponding spatial and rigidity dependence of CR diffusion and drift coefficients as they are implemented in the numerical model.

3.2 The Parker transport equation

The modulation processes outlined above were combined by *Parker* (1965) into a time-dependent TPE which is given by:

$$\frac{\partial f}{\partial t} = -\left(\mathbf{V} + \langle \mathbf{v}_d \rangle\right) \cdot \nabla f + \nabla \cdot \left(\mathbf{K_S} \cdot \nabla f\right) + \frac{1}{3}(\nabla \cdot \mathbf{V}) \frac{\partial f}{\partial \ln P} + Q. \tag{3.1}$$

Here t is the time, P is the rigidity, $\mathbf{V}$ is the solar wind velocity, $\mathbf{K_S}$ is the symmetric diffusion tensor and $\langle \mathbf{v}_d \rangle$ the pitch angle averaged guiding center drift velocity (e.g. *Burger et al.*, 2000; *Stawicki*, 2005a) for a near isotropic distribution function $f(\mathbf{r}, P, t)$, with $\mathbf{r}$ the heliocentric position vector. The differential intensity j is related to f by $j = P^2 f$, with P defined as the momentum per charge for a given particle i.e $P = \frac{pc}{q}$ with p the particle's momentum, q the charge and c the speed of light. This TPE includes the following modulation mechanisms:

- The term on the left describes the change in the CRs distribution with time.
- The first term on the right side describes the outward directed particle convection caused by the radially expanding solar wind.
- The second term on the right side describes the gradient and curvature drifts of CRs including any abrupt changes in the HMF direction such as the HCS.
- The third term on the right side describes the spatial diffusion parallel and perpendicular to the average HMF.
- The fourth term on the right side describes energy changes in the form of adiabatic cooling ($\nabla \cdot \mathbf{V} > 0$) or heating and acceleration of particles at the shock ($\nabla \cdot \mathbf{V} < 0$).
- The last term is a source function Q that could represent any local source inside the heliosphere e.g., the Jovian magnetosphere as source of low-energy electrons (e.g. *Ferreira et al.*, 2001b; *Potgieter and Nndanganeni*, 2013) or the pick-up ion source for the ACRs (e.g. *Langner*, 2004; *Strauss*, 2010; *Strauss et al.*, 2010b)

The relative contribution of these processes change with the solar cycle (time-dependence) and also spatially inside the heliosphere (including the heliosheath).

For clarity on the roles of the major modulation processes, the time-dependent TPE is written in spherical coordinate system rotating with the Sun as,

$$\begin{aligned}
\frac{\partial f}{\partial t} &= \left[\frac{1}{r^2}\frac{\partial}{\partial r}(r^2 K_{rr}) + \frac{1}{r\sin\theta}\frac{\partial}{\partial \theta}(K_{\theta r}\sin\theta) + \frac{1}{r\sin\theta}\frac{\partial K_{\phi r}}{\partial \phi} - V\right]\frac{\partial f}{\partial r} \\
&+ \left[\frac{1}{r^2}\frac{\partial}{\partial r}(rK_{r\theta}) + \frac{1}{r^2\sin\theta}\frac{\partial}{\partial \theta}(K_{\theta\theta}\sin\theta) + \frac{1}{r^2\sin\theta}\frac{\partial K_{\phi\theta}}{\partial \phi}\right]\frac{\partial f}{\partial \theta} \\
&+ \left[\frac{1}{r^2\sin\theta}\frac{\partial}{\partial r}(rK_{r\phi}) + \frac{1}{r^2\sin\theta}\frac{\partial K_{\theta\phi}}{\partial \theta} + \frac{1}{r^2\sin^2\theta}\frac{\partial K_{\phi\phi}}{\partial \phi} + \Omega\right]\frac{\partial f}{\partial \phi} \\
&+ K_{rr}\frac{\partial^2 f}{\partial r^2} + \frac{K_{\theta\theta}}{r^2}\frac{\partial^2 f}{\partial \theta^2} + \frac{K_{\phi\phi}}{r^2\sin^2\theta}\frac{\partial^2 f}{\partial \phi^2} + \frac{2K_{r\phi}}{r\sin\theta}\frac{\partial^2 f}{\partial r \partial \phi} \\
&+ \frac{1}{3r^2}\frac{\partial}{\partial r}(r^2 V)\frac{\partial f}{\partial \ln P} + Q,
\end{aligned} \tag{3.2}$$

where K_{rr}, $K_{r\theta}$, $K_{r\phi}$, $K_{\theta r}$, $K_{\theta\theta}$, $K_{\theta\phi}$, $K_{\phi r}$, $K_{\phi\theta}$ and $K_{\phi\phi}$ are the elements of the generalized diffusion tensor $\mathbf{K}$ including the particle drift term, Ω the average angular rotational speed of the

Sun and V the solar wind speed already encountered in Chapter 2. The position $\mathbf{r}$ is described in terms of radial distance r, polar angle θ, and the azimuthal angle ϕ. The components of the drift velocity are given in Section 3.5.3.

If azimuthal symmetry ($\frac{\partial}{\partial\phi} = 0$) is assumed, then Equation 3.2 reduces to

$$\begin{aligned}\frac{\partial f}{\partial t} &= \left[\frac{1}{r^2}\frac{\partial}{\partial r}(r^2 K_{rr}) + \frac{1}{r\sin\theta}\frac{\partial}{\partial\theta}(K_{\theta r}\sin\theta) - V\right]\frac{\partial f}{\partial r} \\ &+ \left[\frac{1}{r^2}\frac{\partial}{\partial r}(rK_{r\theta}) + \frac{1}{r^2\sin\theta}\frac{\partial}{\partial\theta}(K_{\theta\theta}\sin\theta)\right]\frac{\partial f}{\partial\theta} \\ &+ K_{rr}\frac{\partial^2 f}{\partial r^2} + \frac{K_{\theta\theta}}{r^2}\frac{\partial^2 f}{\partial\theta^2} + \frac{1}{3r^2}\frac{\partial}{\partial r}(r^2 V)\frac{\partial f}{\partial \ln P} + Q.\end{aligned} \tag{3.3}$$

Equation 3.3 is a partial differential equation (PDE) of the form

$$\frac{\partial f}{\partial t} = a_0\frac{\partial^2 f}{\partial r^2} + b_0\frac{\partial^2 f}{\partial\theta^2} + c_0\frac{\partial f}{\partial r} + d_0\frac{\partial f}{\partial\theta} + e_0\frac{\partial f}{\partial \ln P} + Q \tag{3.4}$$

with coefficients

$$\begin{aligned}a_0 &= K_{rr} \\ b_0 &= \frac{K_{\theta\theta}}{r^2} \\ c_0 &= \frac{1}{r^2}\frac{\partial}{\partial r}(r^2 K_{rr}) + \frac{1}{r\sin\theta}\frac{\partial}{\partial\theta}(K_{\theta r}\sin\theta) - V \\ d_0 &= \frac{1}{r^2}\frac{\partial}{\partial r}(rK_{r\theta}) + \frac{1}{r^2\sin\theta}\frac{\partial}{\partial\theta}(K_{\theta\theta}\sin\theta) \\ e_0 &= \frac{1}{3r^2}\frac{\partial}{\partial r}(r^2 V).\end{aligned}$$

A theoretical challenge in modulation studies remains to determine the elements of the diffusion tensor as a function of rigidity, position and time from first principles. In Chapter 4, the numerical solution of Equation 3.4 is given and discussed in detail.

3.3 The diffusion tensor

The generalized diffusion tensor $\mathbf{K}$ is the combination of the symmetric diffusion tensor $\mathbf{K_S}$ and the asymmetrical drift tensor $\mathbf{K_D}$, and is usually defined in terms of the HMF aligned coordinate system as

$$\begin{aligned}\mathbf{K} &= \mathbf{K_S} + \mathbf{K_D} \\ &= \begin{bmatrix} K_{||} & 0 & 0 \\ 0 & K_{\perp\theta} & K_T \\ 0 & -K_T & K_{\perp r}\end{bmatrix}.\end{aligned} \tag{3.5}$$

With

$$\mathbf{K_S} = \begin{bmatrix} K_{||} & 0 & 0 \\ 0 & K_{\perp\theta} & 0 \\ 0 & 0 & K_{\perp r} \end{bmatrix}, \tag{3.6}$$

and

$$\mathbf{K_D} = \begin{bmatrix} 0 & 0 & 0 \\ 0 & 0 & K_T \\ 0 & -K_T & 0 \end{bmatrix}. \tag{3.7}$$

In Equation 3.5, $K_{||}$ is the diffusion coefficient parallel to the mean HMF, $K_{\perp\theta}$ and $K_{\perp r}$ denote the diffusion coefficients perpendicular to the mean HMF in the polar and radial direction respectively and the anti-symmetric K_T, describes particle drifts which include gradient, curvature and HCS drift in the large scale HMF. The HMF aligned coordinate system is related to the spherical coordinate system through the HMF spiral angle ψ as,

$$\begin{aligned} \mathbf{e}_{||} &= \cos\psi \mathbf{e}_r - \sin\psi \mathbf{e}_\phi \\ \mathbf{e}_{\perp\theta} &= \mathbf{e}_\theta \\ \mathbf{e}_{\perp r} &= \sin\psi \mathbf{e}_r + \cos\psi \mathbf{e}_\phi. \end{aligned} \tag{3.8}$$

Here one axis $\mathbf{e}_{||}$ is parallel to the mean HMF, the second axis $\mathbf{e}_{\perp\theta}$ perpendicular to $\mathbf{e}_{||}$ in the polar direction, $\mathbf{e}_{\perp r}$ perpendicular to $\mathbf{e}_{||}$ in radial direction, while $\mathbf{e}_r$, $\mathbf{e}_\theta$ and $\mathbf{e}_\phi$ are the unit vectors in the spherical polar coordinate system.

The generalized diffusion tensor $\mathbf{K}$ must be transformed into the same coordinate system as the TPE in Equation 3.2, by specifying the appropriate transformation matrix, to obtain the solution of CR transport in the heliosphere. In spherical coordinate system, $\mathbf{K}$ is thus obtained by using the transformation matrix $\mathbf{T}$ given by

$$\mathbf{T} = \begin{bmatrix} \cos\psi & 0 & -\sin\psi \\ 0 & 1 & 0 \\ \sin\psi & 0 & \cos\psi \end{bmatrix}. \tag{3.9}$$

Consequently $\mathbf{K}$ can be written as

$$\begin{aligned} \begin{bmatrix} K_{rr} & K_{r\theta} & K_{r\phi} \\ K_{\theta r} & K_{\theta\theta} & K_{\phi\phi} \\ K_{\phi r} & K_{\phi\theta} & K_{\phi\phi} \end{bmatrix} &= \mathbf{T}\mathbf{K}\mathbf{T}^{\mathsf{T}} \\ &= \begin{bmatrix} \cos\psi & 0 & \sin\psi \\ 0 & 1 & 0 \\ -\sin\psi & 0 & \cos\psi \end{bmatrix} \begin{bmatrix} K_{||} & 0 & 0 \\ 0 & K_{\perp\theta} & K_T \\ 0 & -K_T & K_{\perp r} \end{bmatrix} \begin{bmatrix} \cos\psi & 0 & -\sin\psi \\ 0 & 1 & 0 \\ \sin\psi & 0 & \cos\psi \end{bmatrix} \\ &= \begin{bmatrix} K_{||}\cos^2\psi + K_{\perp r}\sin^2\psi & -K_T\sin\psi & (K_{\perp r} - K_{||})\cos\psi\sin\psi \\ K_T\sin\psi & K_{\perp\theta} & K_T\cos\psi \\ (K_{\perp r} - K_{||})\cos\psi\sin\psi & -K_T\cos\psi & K_{||}\sin^2\psi + K_{\perp r}\cos^2\psi \end{bmatrix}. \end{aligned} \tag{3.10}$$

The superscript T above denotes the transpose of the orthogonal matrix. The elements of $\mathbf{K}$ of special interest to this study after equating terms in Equation 3.10 are:

$$\begin{aligned} K_{rr} &= K_{||}\cos^2\psi + K_{\perp r}\sin^2\psi \\ K_{\theta\theta} &= K_{\perp\theta} \\ K_{\theta r} &= K_T\sin\psi, \end{aligned} \tag{3.11}$$

with K_{rr} and $K_{\theta\theta}$ the effective diffusion coefficients in the radial and polar direction respectively, and $K_{\theta r}$ the diffusion coefficient caused by particle drifts. It is important to note that K_{rr} is the combination of both $K_{||}$ and $K_{\perp r}$. For a Parkerian type HMF, $\psi \longrightarrow 90^o$ for $r > 20$ AU in the equatorial plane so that K_{rr} is dominated by $K_{\perp r}$ although it is assumed to be $\sim 2\,\%$ of $K_{||}$. In the inner and polar heliospheric regions K_{rr} is dominated by $K_{||}$. If a non-Parkerian type of HMF is assumed, expressions in Equation 3.11 become very complicated (see e.g. *Effenberger et al.* (2012), *Sternal et al.* (2011) and *Burger et al.* (2008) for a detailed discussion). In modeling the modulation of CRs in the heliosphere, specifying $K_{||}$, $K_{\perp r}$, $K_{\perp\theta}$ and K_T in terms of their spatial and rigidity dependence is an important requirement.

3.4 Turbulence

Turbulence in the solar wind is generally regarded as waves (*Schlickeiser*, 1988) or as dynamical turbulence (e.g. *Bieber and Matthaeus*, 1991). However, the common understanding is that in the presence of turbulence, the HMF can be written as the sum of uniform background magnetic field with magnitude B_m, taken to be directed along the Z-axis of the right-handed Cartesian coordinate system, and some fluctuating component $\delta\mathbf{B}$. As a result, the HMF can be written as

$$\mathbf{B} = B_m\mathbf{e}_z + \delta\mathbf{B}(x,y,z), \tag{3.12}$$

with the average $\langle\delta\mathbf{B}\rangle = 0$ after some averaging process. The root mean square amplitude of the fluctuating component in the present study is represented as δB, while δB^2 represents the total energy in the fluctuations and it is known as the magnetic field variance. The properties of this fluctuating components depend on which turbulence model is utilized (see e.g. *Bieber and Matthaeus*, 1991; *Bieber et al.*, 1994, 1996; *Matthaeus et al.*, 1995, 2003).

The total turbulence is commonly expressed as a sum of slab or one dimensional (1D) and 2D components (*Bieber et al.*, 1994; *Matthaeus et al.*, 1995) as,

$$\delta\mathbf{B} = \delta\mathbf{B}_{slab}(z) + \delta\mathbf{B}_{2D}(x,y). \tag{3.13}$$

Here $\delta\mathbf{B}_{slab}(z)$ represents the slab turbulence where the magnitude of fluctuations are only along the mean HMF, while $\delta\mathbf{B}_{2D}(x,y)$ represents 2D turbulence where fluctuations are assumed to reside in planes orthogonal to the mean field. In this composite turbulence model, for

axisymmetric turbulence with respect to the mean HMF direction, the total variance (*Matthaeus et al.*, 1995) is then given as

$$\begin{aligned} \delta B^2 &= \delta B^2_{slab}(z) + \delta B^2_{2D}(x,y) \\ &= 2\delta B^2_{slab,x}(z) + 2\delta B^2_{2D,x}(x,y). \end{aligned} \tag{3.14}$$

In this study a composite model for turbulence is used with 20% slab and 80% 2D similar to *Bieber et al.* (1994) and *Burger et al.* (2000, 2008). The slab and 2D magnetic field variance components are then written as,

$$\delta B^2_{slab}(z) = 0.2\delta B^2 \tag{3.15}$$

and

$$\delta B^2_{2D}(x,y) = 0.8\delta B^2. \tag{3.16}$$

Assumptions about the values of $\delta B^2_{slab}(z)$ and $\delta B^2_{2D}(x,y)$ are important for determining the diffusion coefficients in this study. This aspect is further shown below.

3.5 Cosmic ray modulation processes in the transport equation

In this section, a theoretical background on certain aspects of CR diffusion, drifts and shock acceleration processes, as they are modeled in the TPE, is given without going into the detailed theory.

3.5.1 Parallel diffusion

The diffusive transport of charged particles in the heliosphere is determined by the parallel and perpendicular diffusion coefficients. The parallel diffusion coefficient describes the transport of the CRs along the HMF lines. This process can be described by quasi-linear theory (QLT) (see e.g. *Jokipii*, 1966; *Hasselmann and Wibberenz*, 1970; *Earl*, 1974; *Teufel and Schlickeiser*, 2002), with the pitch angle averaged parallel mean free path, $\lambda_{||}$, given by

$$\lambda_{||} = \frac{3v}{8}\int_{-1}^{1}\frac{(1-\mu^2)^2}{D_{\mu\mu}(\mu)}d\mu. \tag{3.17}$$

Here μ is the cosine of the particle's pitch angle, v is the particle speed and $D_{\mu\mu}$ is the pitch angle Fokker-Plank coefficient. Note that, in general, mean free paths λ are related to the coefficients K of the diffusion tensor as

$$K = \frac{v}{3}\lambda, \tag{3.18}$$

Therefore, in the present case, the relationship between $\lambda_{||}$ and $K_{||}$ is given by

$$K_{||} = \frac{v}{3}\lambda_{||}. \tag{3.19}$$

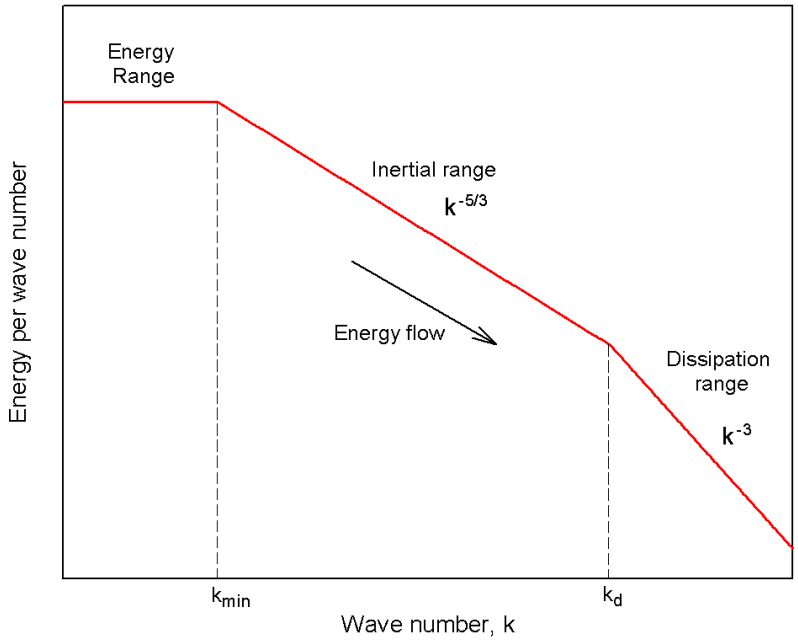

Figure 3.1: A schematic representation of a turbulence power spectrum (*Bieber et al.*, 1994; *Goldstein et al.*, 1995; *Teufel and Schlickeiser*, 2003). The dotted vertical lines represent k_{min} the spectral break point between the inertial and energy range and k_d the spectral break point between inertial and dissipation range. Note that k_{min} in the figure denotes k_{min}.

The calculation of $D_{\mu\mu}$ in Equation 3.17 needs as input the power spectrum of the magnetic field fluctuations. Hence, $D_{\mu\mu}$ depends on the turbulence model and the theory adopted. Figure 3.1 shows as an example a power spectrum of the magnetic fluctuations which can be divided into three ranges (see *Bieber et al.*, 1994; *Goldstein et al.*, 1995; *Teufel and Schlickeiser*, 2003). It can be seen from this figure that the energy range depicts the region where the power spectrum variation is independent of the wave number k, the inertial range where it is proportional to $k^{-5/3}$, and a dissipation range where it is proportional to k^{-3}. The spectral break between the energy and the inertial range is represented as k_{min} and that between the inertial and the dissipation range is represented as k_d. *Horbury et al.* (1996), *Engelbrecht* (2008) and *Perri et al.* (2010) showed that k_{min} depends on radial distance away from the Sun.

Figure 3.2 compares $\lambda_{||}$ derived from observations (filled and open symbols represent results derived from electrons and protons respectively) with that predicted by the standard QLT (represented by the dotted line; Equation 3.17). The shaded area shows the Palmer consensus range of values (*Palmer*, 1982), which places $\lambda_{||}$ in a range of 0.08 AU $\leq \lambda_{||} \leq 0.3$ AU for $P \leq 5$ GV at the Earth. When the dissipation range is neglected, QLT predicts that $\lambda_{||} \propto P^{\frac{1}{3}}$ for $P \leq 10$ GV and $\lambda_{||} \propto P^{1.5}$ for $P > 10$ GV. In contrast to QLT prediction, $\lambda_{||}$ derived from observations is rigidity independent for $P \leq 5$ GV. Clearly, the predicted $\lambda_{||}$ is too small at low rigidities when the dissipation range is neglected as done in Figure 3.2. However, for low

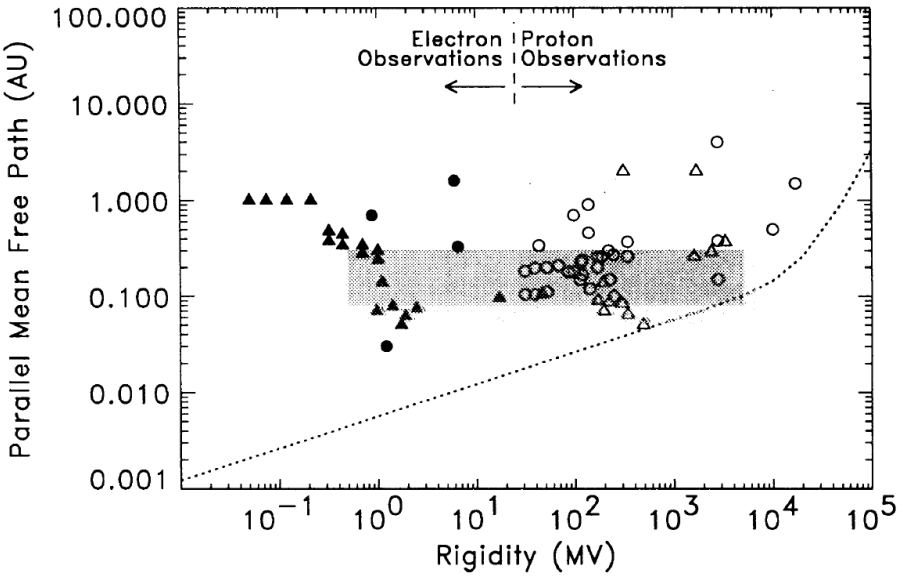

Figure 3.2: Parallel mean free path, $\lambda_{||}$, as a function of rigidity. Filled and open symbols denote results derived from electron and proton observations respectively. The shaded area represents the observational consensus of *Palmer* (1982). The dotted line represents the prediction of standard QLT without the dissipation range. From *Bieber et al.* (1994).

energy proton modulation in the heliosphere, similarly for Carbon, the $\lambda_{||}$ derived without the dissipation range is applicable because the CR proton undergoes significant adiabatic energy changes below $\sim$ 300 MeV. The proton modulation appears unaffected by $\lambda_{||}$ variations for these lower energies (see *Potgieter*, 1996; *Ferreira*, 2002).

In this study the expression for $\lambda_{||}$ used in this work is taken from *Burger et al.* (2008) and *Engelbrecht* (2008) based on expressions derived by *Teufel and Schlickeiser* (2003) using quasilinear theory and a random sweeping model for composite dynamical turbulence. Neglecting the effects of the dissipation range similar to the approach of *Engelbrecht and Burger* (2013) and *Engelbrecht* (2013), $\lambda_{||}$ is given by

$$\lambda_{||} = \frac{B_m^2}{\delta B_{slab,x}^2} \frac{3s}{\pi(s-1)} \frac{R^2}{k_{min}} \left[\frac{1}{4} + \frac{2R^{-s}}{(2-s)(4-s)} \right], \tag{3.20}$$

with B_m as discussed in Chapter 2 (see Equation 2.9), $s = 5/3$ is the spectral index in the inertial range and $R = k_{min} R_L$ with R_L the gyro-radius. Furthermore, k_{min} given by *Burger et al.* (2008) is used in this study similar to studies done by *Strauss* (2010) and it is given by

$$k_{min} = 32 \left(\frac{r}{r_0} \right)^{-0.5} \text{ AU}^{-1} \quad \text{for } r \leq r_{TS}, \tag{3.21}$$

where $r_0 = 1$AU and r_{TS} is the position of the solar wind termination shock (TS). For $r > r_{TS}$ the behaviour of k_{min} is unclear, as a result a constant value is assumed in this region similar to *Strauss* (2010).

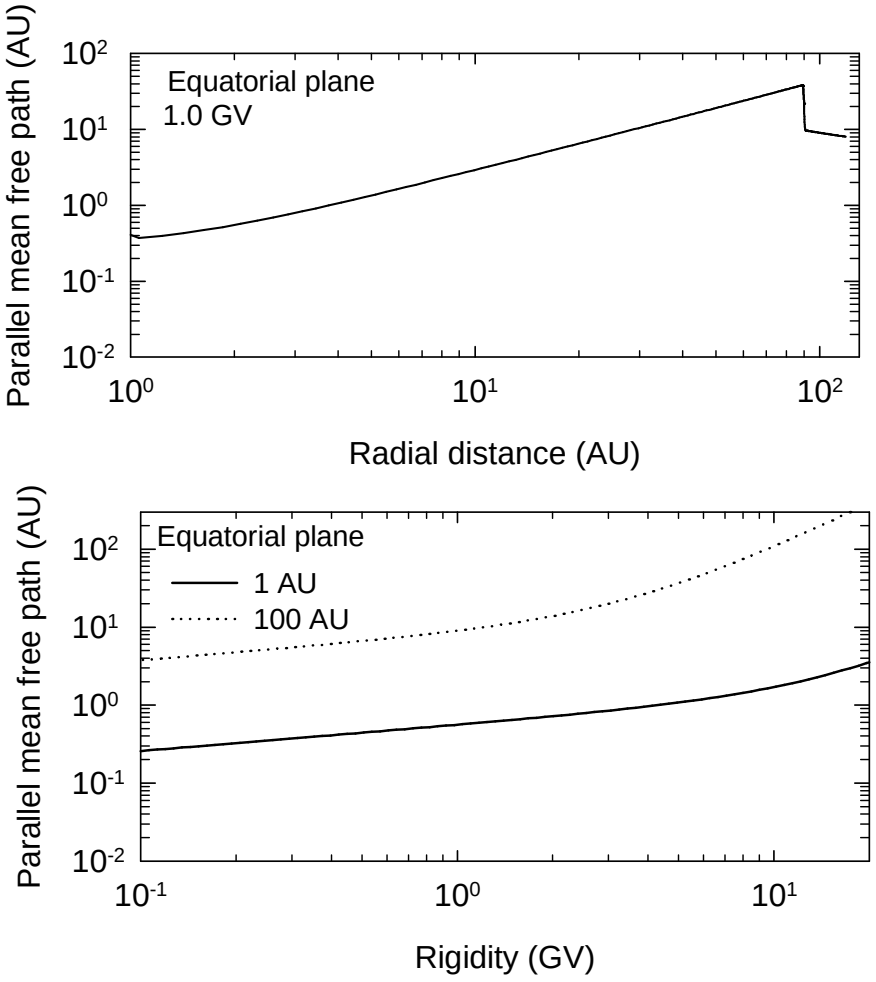

Figure 3.3: The top panel shows the parallel mean free path ($\lambda_{||}$) as a function of radial distance in the equatorial plane ($\theta = 90^o$) for solar minimum conditions ($\alpha = 10^o$) for 1.0 GV GCR Carbon. The TS is placed at 90 AU. The bottom panel shows the $\lambda_{||}$ as a function of rigidity at radial distances of 1 AU (solid line) and 100 AU (dotted line) in the equatorial plane also with $\alpha = 10^o$.

The expression for the slab component of the variance is given as

$$\begin{aligned} \delta B^2_{slab,x} &= 0.2\delta B^2 \\ &= 0.2\left[25\left(\frac{r_0}{r}\right)^{2.7}\right] \text{ nT}^2 \quad \text{for } r < r_{TS}. \end{aligned} \tag{3.22}$$

Again the slab component is not clear in the region $r > r_{TS}$, hence an assumption $\delta B^2_{slab,x} = B^2_m$ is invoked. The motivation for the use of these analytical expressions to represent turbulence quantities is given by *Burger et al.* (2008). For a detail discussion of turbulence quantities based on $ab\ initio$ turbulence model see *Engelbrecht and Burger* (2013) and *Engelbrecht* (2013). Since a turbulence transport theory for the heliosheath has not been developed, these assumptions are considered adequate for this type of global modulation study.

Figure 3.3 shows the radial dependence of $\lambda_{||}$ for GCR Carbon, as used in this study, at a rigidity of 1.0 GV (top panel) as well as the rigidity dependence at radial distances of 1 AU and

100 AU (bottom panel) in the equatorial plane during solar minimum conditions ($\alpha = 10^o$). It follows from the top row of this figure that $\lambda_{||} \propto r$ inside off the TS and also that it drops by a factor s_k^2 (with $s_k = 2.0$ the compression ratio of the TS) across the TS to decrease further in the heliosheath. In the bottom panel, it is evident that the rigidity dependence of $\lambda_{||}$ is a combination of two power laws with $\lambda_{||} \propto P^{1/3}$ for $P < 5$ GV and $\propto P^2$ for $P \geq 5$. Note also that $\lambda_{||}$ as a function of rigidity has typical values between 0.2 AU – 1.7 AU at the Earth for GCR Carbon for $P < 10$ GV which is in good agreement with those values for GCR Protons that have been given by *Engelbrecht and Burger* (2013) and *Engelbrecht* (2013).

3.5.2 Perpendicular diffusion

The theory of perpendicular diffusion is much more complicated (e.g. see a discussion by *Matthaeus et al.*, 2003; *Stawicki*, 2005b; *Shalchi*, 2010), but can be described by the field line random walk limit of QLT (*Jokipii*, 1966) or the non-linear guiding center (NLGC) theory of *Matthaeus et al.* (2003). Both these processes which CRs experience are combined in the TPE via a perpendicular diffusion coefficient $K_\perp$ describing the diffusion of particles perpendicular to the average HMF. The perpendicular diffusion coefficient can thus be subdivided into two possibly independent coefficients, one in the polar direction $K_{\perp\theta}$ and the other in the radial direction $K_{\perp r}$.

The important role of $K_\perp$ has become better understood especially in the inner heliosphere, though inadequate $ab\ initio$ theoretical work still exists due to its complexity. It was realized that $K_\perp$ should be assumed to be anisotropic (*Kóta and Jokipii*, 1995; *Potgieter*, 1996, 2000; *Ferreira et al.*, 2000; *Heber and Potgieter*, 2006) to establish better compatibility with Ulysses observations. The Ulysses spacecraft revealed that the latitudinal dependence of CR Protons is significantly less than predicted by the then classical drift models (see a concise review on this topic by *Heber and Potgieter*, 2006). A reasonable phenomenological consensus for the global description of CR modulation in the heliosphere was reached, i.e, $K_{\perp\theta} > K_{\perp r}$ away from the equatorial region and $K_{\perp\theta} = K_{\perp r}$ in the equatorial region (*Potgieter*, 1996, 2000; *Burger et al.*, 2000; *Ferreira*, 2002; *Langner*, 2004; *Moeketsi*, 2004; *Ngobeni*, 2006; *Strauss*, 2010). In this study, the expressions for the rigidity and spatial dependences of $K_{\perp r}$ and $K_{\perp\theta}$ are based on a steady state model derived by *Burger et al.* (2000) and are given respectively as:

$$K_{\perp r} = k_e \frac{\delta B_{2D,x}^2}{B_m^2} K_{||} \left(\frac{P}{P_0}\right)^\gamma \tag{3.23}$$

and

$$K_{\perp\theta} = F(\theta) \frac{\delta B_{2D,x}^2}{B_m^2} K_{||} \left(\frac{P}{P_0}\right)^\gamma . \tag{3.24}$$

Where

$$F(\theta) = \left(\frac{k_p + k_e}{2}\right) \mp \left(\frac{k_p - k_e}{2}\right) \tanh\left[\frac{1}{\Delta\theta}(\theta - 90^o + \theta_F)\right], \tag{3.25}$$

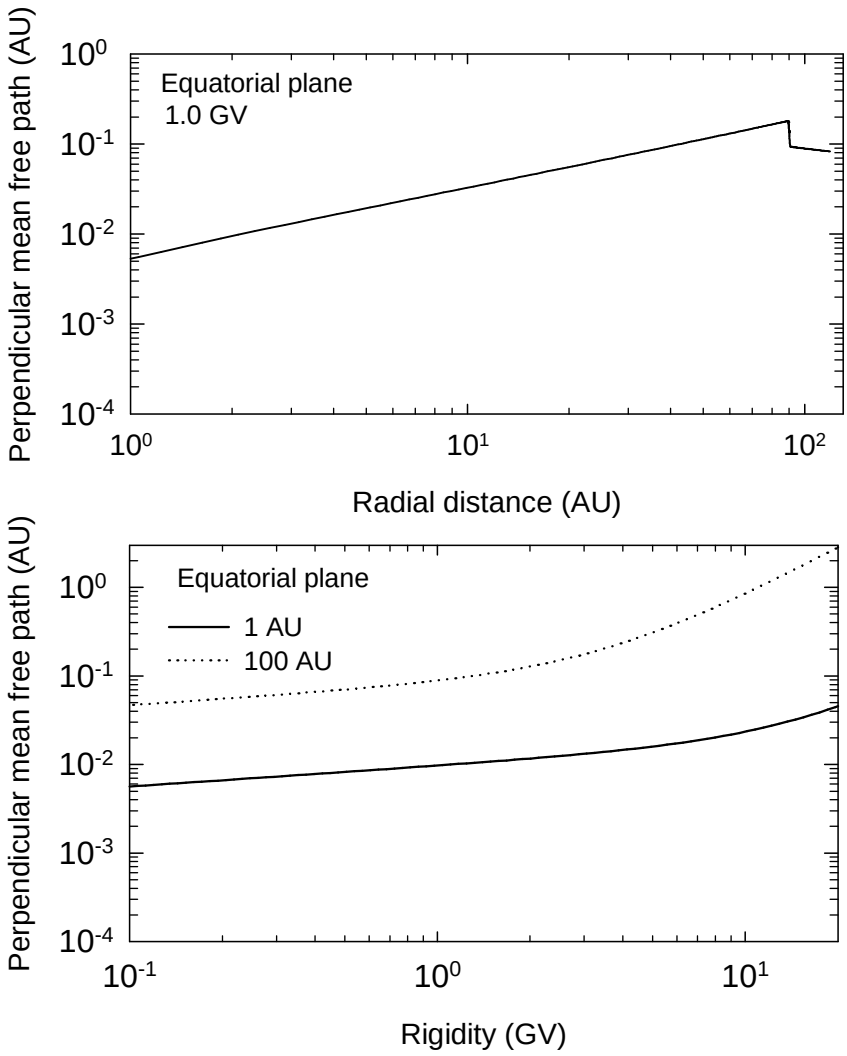

Figure 3.4: The top panel shows the perpendicular mean free path ($\lambda_\perp$) as a function of radial distance in the equatorial plane ($\theta = 90^o$) for solar minimum conditions ($\alpha = 10^o$) for 1.0 GV GCR Carbon. The bottom panel shows the $\lambda_\perp$ as a function of rigidity at radial distances of 1 AU (solid line) and 100 AU (dotted line) in the equatorial plane also with $\alpha = 10^o$.

and

$$\delta B^2_{2D,x} = 4\delta B^2_{slab,x}, \tag{3.26}$$

with $P_0 = 1.0$ GV, $\Delta\theta = \dfrac{1}{8}$, $\theta_F = 25^o$ and where the upper signs are valid for polar angles $\theta \leq 90^o$ and the lower signs for $\theta > 90^o$. The quantities γ, k_e and k_p are dimensionless and the function $F(\theta)$ enhances $K_{\perp\theta}$ by a factor ~ 7.1 towards the polar regions with respect to its value in the equatorial plane by assuming $k_p = 0.185$ and $k_e = 0.026$; this enhancement is an implicit way of reducing drift effects by changing CR intensity gradients in the heliosphere. The quantity $\gamma = -0.1$ changes the rigidity dependence of $K_\perp$ with respect to that of $K_{||}$. These assumptions mean that $K_\perp = K_{\perp\theta} = K_{\perp r}$ in the equatorial plane. Note that the latitude dependence of $F(\theta)$ is further discussed in Chapter 5 in the context of inherent asymmetric

modulation conditions of GCRs between the northern and southern hemispheres.

The top panel of Figure 3.4 shows the assumed radial dependence of the perpendicular diffusion coefficients at a rigidity of 1.0 GV in the equatorial plane ($\lambda_\perp = \lambda_{\perp r} = \lambda_{\perp\theta}$). Also shown in the bottom panel of this figure is the rigidity dependence of $\lambda_\perp$ at radial distances of 1 AU and 100 AU in the equatorial plane for $\alpha = 10^o$. The radial dependence of $\lambda_\perp$ is similar to that of $\lambda_{||}$ shown in Figure 3.3. It can be noted that typical values as a function of rigidity for $\lambda_{\perp r}/\lambda_{||}$ and $\lambda_{\perp\theta}/\lambda_{||}$ at the Earth in this model are between $0.02 - 0.04$. Away from the equatorial plane at 1 AU these values change for $\lambda_{\perp\theta}/\lambda_{||}$ to become $0.14 - 0.28$ due to the enhancement of $\lambda_{\perp\theta}$. In general these values are in good agreement with those values which have been given by *Burger et al.* (2000); *Langner* (2004); *Strauss* (2010) and *Engelbrecht and Burger* (2013).

3.5.3 Particle drifts

Although particle drifts were included in the original TPE they had been neglected until *Jokipii et al.* (1977) pointed out that the inclusion of drifts could alter modulation, especially since drifts are sensitive to the polarity of the HMF leading to a charge asymmetry. The smooth global or background HMF affects the CR transport by contributing drift motions associated with the gradients in field magnitude, the curvature of the field and any abrupt changes in the field direction, such as the HCS. The components of the average drift velocity as they appear in Equation 3.3 in two dimensions are:

$$\begin{aligned} \langle \mathbf{v}_d \rangle_r &= -\frac{A}{r\sin\theta}\frac{\partial}{\partial\theta}(K_{\theta r}\sin\theta)\mathbf{e}_r, \\ \langle \mathbf{v}_d \rangle_\theta &= -\frac{A}{r}\frac{\partial}{\partial r}(rK_{r\theta})\mathbf{e}_\theta, \end{aligned} \tag{3.27}$$

where A determines the drift direction of the charged particles in the heliosphere. In the present case only nuclei are studied and hence A becomes

$$A = \begin{cases} +1 & \text{if } A > 0 \\ -1 & \text{if } A < 0. \end{cases}$$

Alternatively Equation 3.27 can be written as

$$\langle \mathbf{v}_d \rangle = \nabla \times K_T \mathbf{e}_B, \tag{3.28}$$

with $\mathbf{e}_B = \dfrac{\mathbf{B}}{B_m}$ a unit vector in the direction of magnetic field $\mathbf{B}$ and K_T the generalized drift coefficient.

Equation 3.28 can also be written as

$$\langle \mathbf{v}_d \rangle = \nabla \times K_T \mathbf{e}_B (1 - 2H(\theta - \theta')) + 2\delta_d(\theta - \theta') K_T \mathbf{e}_B \times \nabla(\theta - \theta'). \tag{3.29}$$

Here the first term represents the gradient and curvature drifts due to the Parker HMF and the second term represents particle drifts as a result of the HCS. The Heaviside step function

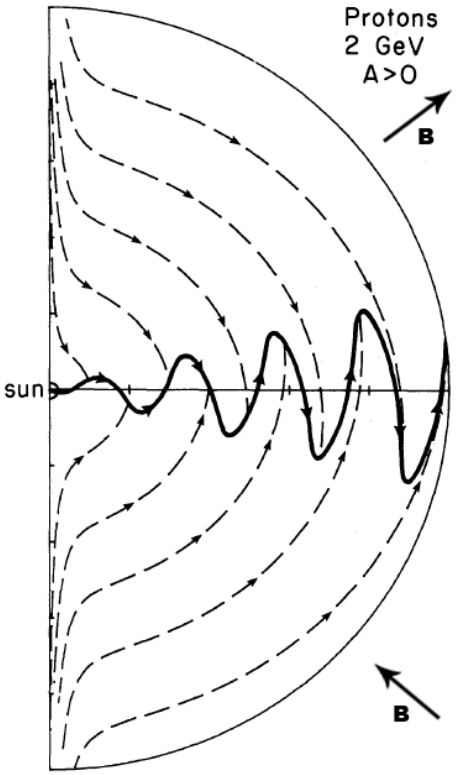

Figure 3.5: Meridional projection of drift trajectories for 2 GeV protons during an $A > 0$ magnetic polarity cycle i.e. when the HMF, indicated by **B**, is directed outward in the northern hemisphere and inwards in the southern hemisphere of Sun. The arrows will change to opposite direction during an $A < 0$ HMF polarity cycle or when electron drifts are considered. From *Jokipii and Thomas* (1981).

is given as H in Chapter 2 and θ' is the polar angle describing the position of the HCS with δ_d the Dirac-Delta function given by,

$$\delta_d(\theta - \theta') = \begin{cases} 0 & \text{if } \theta \neq \theta' \\ \infty & \text{if } \theta = \theta'. \end{cases} \tag{3.30}$$

For the $A > 0$ polarity cycle, positively charged particles drift from the polar region of the heliosphere down to the equatorial regions and they are largely insensitive to the conditions in the equatorial region, e.g. changes in HCS. For $A < 0$ polarity cycle, positively charged particles drift primarily in along the HCS and outwards over the polar regions and are sensitive to changes in the tilt angle of the HCS. An example of these drift directions are shown in Figure 3.5 for protons adapted from *Jokipii and Thomas* (1981). For negatively charged particles the drift direction is the opposite.

Under the assumption of weak scattering, K_T as given by the standard approach becomes

$$K_T = k_A \frac{\beta P}{3B_m}, \tag{3.31}$$

with k_A a dimensionless constant. When $k_A = 1.0$, 0.5, and 0.0 respectively, this equation

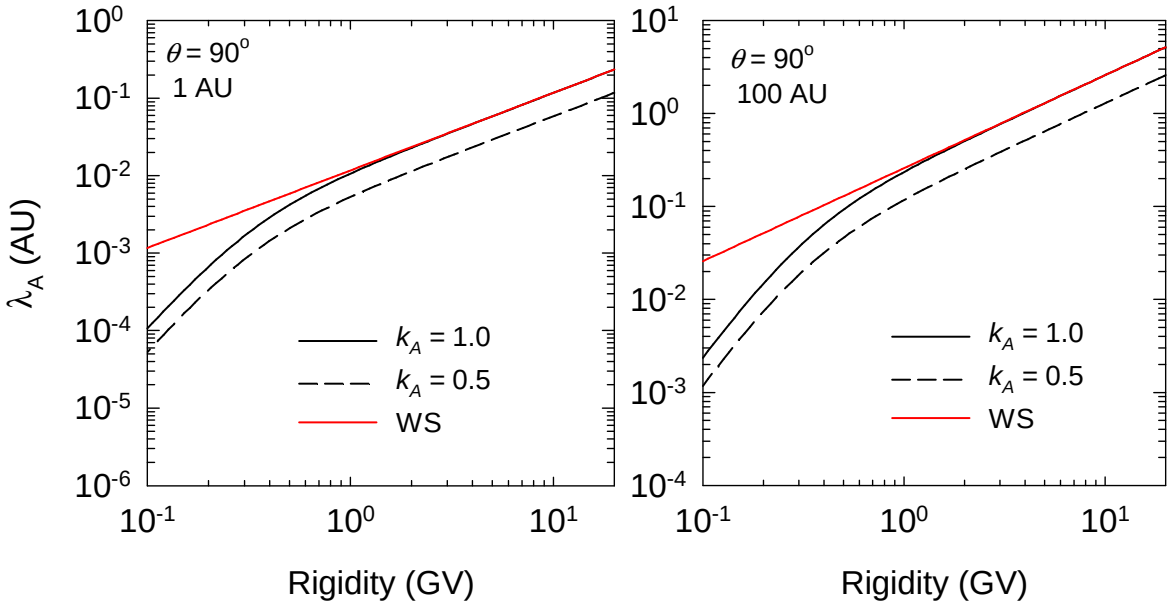

Figure 3.6: The drift scales λ_A, as given by Equation 3.33, are shown as a function of rigidity for different values of k_A at radial distances of 1 AU (left panel) and 100 AU (right panel) in the equatorial plane with $\theta = 90^o$. Shown in red are the corresponding weak scattering values (denoted WS) of λ_A.

describes what *Potgieter et al.* (1989) have called 100% (full drifts), 50% (half drifts) and no-drifts. The suppression of drifts by turbulence (scattering) can be discussed in the context of Equation 3.31 (see *Bieber and Matthaeus*, 1997; *Minnie et al.*, 2007; *Burger and Visser*, 2010). This aspect is studied and discussed further in more detail in Chapter 7.

The drift coefficient used in this study is taken from *Burger et al.* (2000) and takes into account the fact that drifts in the heliosphere are reduced by the presence of turbulence though in a phenomenological approach manner. A simple, but most practical functional form for the drift reduction function that depends only on rigidity is assumed so that K_T is then given by:

$$K_T = k_A \frac{\beta P}{3B_m} \frac{(P/P_0')^2}{1 + (P/P_0')^2}, \tag{3.32}$$

where $P_0' = \dfrac{1}{\sqrt{10}}$ GV. For this work, $k_A = 0.5$ is used unless otherwise stated (see also *Langner et al.*, 2003, 2004). The essence of Equation 3.32 is that below $\sim$ 1.0 GV drifts are reduced with respect to the weak scattering case (see also *Burger et al.*, 2000) when $k_A = 1.0$. These parameters are optimal in order to reproduce a comprehensive set of CR observations (*Burger et al.*, 2000; *Langner et al.*, 2003; *Strauss et al.*, 2010b,a; *Ngobeni and Potgieter*, 2014).

The drift coefficient can be expressed in terms of the drift scale λ_A as,

$$\lambda_A = \frac{3}{v} K_T. \tag{3.33}$$

Figure 3.6 shows λ_A, in AU, as a function of rigidity for different values of k_A at radial distances of 1 AU and 100 AU in the equatorial plane. Also shown is the corresponding drift scale,

represented by red lines and denoted WS, under the assumption of weak scattering i.e. with K_T given by Equation 3.31. For the modified K_T, as given by Equation 3.32, λ_A at 1 AU and 100 AU are indistinguishable to their corresponding weak scattering values above 1.0 GV when $k_A = 1.0$ but this is not the case for $k_A = 0.5$. When $k_A = 0.5$ drifts are also reduced at rigidities $P > 1.0$ GV. However for both values of k_A, the effect of the assumed modification of K_T is to reduce drifts significantly below 1.0 GV at all radial distances.

The HCS is simulated by replacing the 3D drift velocity by a 2D drift field (e.g. *Hattingh and Burger*, 1995; *Burger and Hattingh*, 1995). In this study the 2D wavy current sheet approach of *Langner* (2004) is followed which is an improvement of the current sheet model of *Hattingh and Burger* (1995).

3.5.4 Particle acceleration at the termination shock

In the presence of any jump in plasma bulk velocity, first-order Fermi (Fermi I) acceleration, also known as diffusive shock acceleration, is an unavoidable consequence if particles cross such a jump multiple times and undergo multiple collisions. The basic idea is that since the downward plasma is faster than the plasma upstream of the shock, energetic particles are, in effect, bouncing between two converging "walls", thus continuously gaining energy (see e.g. *Giacalone*, 2005). Such shocks exist in a wide variety of astrophysical plasmas including those associated with supernovae blast waves, coronal mass ejections, and the solar wind TS. The acceleration of particles by shocks has been studied extensively (see earlier reviews by *Jones and Ellison*, 1991; *Drury*, 1983) and the preferred process of acceleration has been believed to be the diffusive shock acceleration (*Axford et al.*, 1977; *Krymski*, 1977; *Bell*, 1978a,b; *Drury*, 1983).

Particle acceleration or re-acceleration at the discontinuity can also be included in the framework of the TPE. In the TS acceleration problem, modeling diffusive shock acceleration mechanism is absorbed into the TPE by noting that the negative divergence of the solar wind at the TS ($\nabla \cdot \mathbf{V} < 0$) can accelerate particles (see e.g. *Jokipii*, 1986; *Potgieter and Moraal*, 1988; *Jokipii et al.*, 1993; *Steenkamp*, 1995; *le Roux et al.*, 1996; *Langner*, 2004; *Strauss*, 2010). In this context, various quantities on one side (upstream region) of the TS are related to those on the other side (downstream region) by specifying certain jump conditions.

Since particles have mobility across the shock, the first condition is that the distribution function f (or the differential intensity) must be continuous across the shock, i.e,

$$f^- = f^+. \tag{3.34}$$

Where the notations '-' and '+' represent the upstream and downstream regions of the shock respectively,

$$f^+ = \lim_{r \leftarrow r_{TS}} f(r) \tag{3.35}$$

and

$$f^{-} = \lim_{r \to r_{TS}} f(r). \tag{3.36}$$

The second condition is that the flux of particles that diverge from the shock must be due to a source of particles on the shock, i.e.,

$$\nabla \cdot \mathbf{S} = Q. \tag{3.37}$$

Where $\mathbf{S}$ is the differential particle current density given as

$$\begin{aligned} \mathbf{S} &= C\mathbf{V}j - \mathbf{K_S} \cdot \nabla j \\ &= -4\pi p^2 \left[\frac{\mathbf{V}}{3} \frac{\partial f}{\partial \ln p} + \mathbf{K_S} \cdot \nabla f \right], \end{aligned} \tag{3.38}$$

with C the Compton-Getting factor (e.g. *Gleeson and Axford*, 1968) given by

$$\begin{aligned} C &= 1 - \frac{1}{3j} \frac{\partial}{\partial p}(pj) \\ &= -\frac{1}{3} \frac{\partial \ln f}{\partial \ln p}. \end{aligned} \tag{3.39}$$

If the flux is perpendicular to the shock face, Equation 3.37 can be written as

$$S^{+} - S^{-} = \lim_{\varepsilon \to 0} \int_{r_{TS}-\varepsilon}^{r_{TS}+\varepsilon} Q dr. \tag{3.40}$$

If it is further assumed that the source of particles on the shock is a delta function in r,

$$Q = Q_{*}(p)\delta(r - r_{TS}), \tag{3.41}$$

the continuity condition, Equation 3.40, reduces to

$$\left(\frac{\partial f}{\partial r} \right)^{-} = \frac{K_{rr}^{+}}{K_{rr}^{-}} \left(\frac{\partial f}{\partial r} \right)^{+} - \frac{V^{-} - V^{+}}{3K_{rr}^{-}} \frac{\partial f}{\partial \ln p} - \frac{K_{r\theta}^{-} - K_{r\theta}^{+}}{r_{TS} K_{rr}^{-}} \frac{\partial f}{\partial \theta} + \frac{Q}{K_{rr}^{-}}. \tag{3.42}$$

Equation 3.42 is referred to as the matching condition at the TS. For $Q = 0$, as done in this study, Equation 3.42 can be written in the same form as Equation 3.4,

$$A_0 \left(\frac{\partial f}{\partial r} \right)^{-} = B_0 \left(\frac{\partial f}{\partial r} \right)^{+} + C_0 \frac{\partial f}{\partial \ln p} + D_0 \frac{\partial f}{\partial \theta}, \tag{3.43}$$

with

$$\begin{aligned} A_0 &= 1 \\ B_0 &= \frac{K_{rr}^{+}}{K_{rr}^{-}} \\ C_0 &= -\frac{V^{-} - V^{+}}{3K_{rr}^{-}} \\ D_0 &= -\frac{K_{r\theta}^{-} - K_{r\theta}^{+}}{r_{TS} K_{rr}^{-}}. \end{aligned} \tag{3.44}$$

Then the TPE, Equation 3.3, is valid in the domain $r_{\odot} \leq r < r_{TS}$ and $r_{TS} < r \leq r_{HP}\ \forall \theta, P$ and Equation 3.42 is valid at the discontinuity $r = r_{TS}\ \forall \theta, P$; with r_{HP} the position of the HP. In the modulation model assumed in this study, the low-energy GCR Carbon are re-accelerated at the TS and the effectiveness of this process depends also on the shock's compression ratio (see e.g., *Potgieter and Langner*, 2004; *Ngobeni and Potgieter*, 2008, 2010).

Another acceleration mechanism of particles can take place in the presence of magnetic field fluctuations. In this acceleration process particles are also scattered back and forth between plasma waves with different velocities in the plasma frame. This leads to a second-order Fermi acceleration (Fermi II), also known as stochastic acceleration, which is also a natural consequence of particle transport. Fermi II is believed to be a viable acceleration process for ACR in the heliosheath (e.g. *Moraal et al.*, 2006; *Ferreira et al.*, 2007; *Strauss et al.*, 2010b). This process is modelled by inserting relevant additional terms to the standard TPE given above (see e.g. *Strauss*, 2010; *Strauss et al.*, 2010b,a, for a detailed discussion on this topic). The acceleration process of ACRs beyond the TS remains a topic of considerable debate since Voyager 1 crossed the TS (e.g. *Stone et al.*, 2005; *Fisk and Gloeckler*, 2009). For this study Fermi II is not relevant because the focus is on global modulation of high rigidity GCR Carbon in the heliosphere.

3.6 Summary

The distribution of CRs inside the heliosphere is a result of four modulation processes namely diffusion, convection, drift and adiabatic energy changes which can be combined into a transport equation (*Parker*, 1965). This equation can be solved numerically in various dimensions to study cosmic ray transport also in the context where CRs are accelerated, or simply re-accelerated, at the solar wind TS. It has been shown that in 2D modulation models four different diffusion coefficients are of particular interest, namely $K_{||}$, $K_{\perp r}$, $K_{\perp \theta}$ and K_T. In this study $K_{||}$ was constructed based on theoretical calculations of *Teufel and Schlickeiser* (2003) without a dissipation range but with slab/2D turbulence according to the work of *Burger et al.* (2008). Because of the complexity in the development of the perpendicular diffusion coefficient from the first principle, expressions for $K_{\perp r}$ and $K_{\perp \theta}$ are extracted from *Burger et al.* (2000) and are scaled as $K_{||}$ but with moderate differences in the rigidity dependence. Furthermore, it was illustrated by *Potgieter et al.* (1997); *Potgieter* (2000); *Burger et al.* (2000); *Ferreira* (2002) and *Langner* (2004) that to produce the correct CR latitude dependence, $K_{\perp \theta}$ needs to enhance toward the poles. This enhancement is an implicit way to reduce particle drifts without changing the drift coefficient. The drift coefficient describes gradient and curvature of the field, and any abrupt change in the field direction such as HCS. The drift directions depend on the HMF polarity sign and influence cosmic ray transport resulting in a 22-year and charge-sign dependent modulation (see e.g. *Potgieter and Moraal*, 1985; *Ferreira*, 2002). The standard weak scattering

drift coefficient is modified based on the arguments given by *Burger et al.* (2000).

At the solar wind TS, in this study, low energy GCR Carbon particles are re-accelerated to higher energies by a process called diffusive shock acceleration or Fermi I. The matching conditions necessary for this re-acceleration process valid at the TS were given and discussed.

In the next chapter the TS model developed by *Langner* (2004) is extended to study modulation of GCR Carbon particles in a north-south asymmetrical heliosphere.

Chapter 4

Numerical solution of the transport equation in an asymmetrical heliosphere

4.1 Introduction

Observations made with the two Voyager spacecraft confirmed that the solar wind decelerates to form the heliospheric TS. Voyager 1 (V1) crossed this TS at a radial distance of ~ 94 AU in 2004, while Voyager 2 (V2) crossed it in 2007 at a different heliolatitude, about 10 AU closer to the Sun. These different positions of the TS confirm the dynamic and cyclic nature of the shock's position. Observations of CRs and plasma flows from the two Voyager spacecraft inside the heliosheath indicate significant differences between them (*Richardson*, 2013; *Caballero-Lopez et al.*, 2010; *Webber et al.*, 2009; *Stone et al.*, 2008), suggesting that apart from the dynamic nature caused by the changing solar activity there also may exist a global asymmetry in the north-south (polar) dimensions of the heliosphere, in addition to the expected nose-tail asymmetry. This relates to the direction in which the heliosphere is moving in interstellar space and its orientation with respect to the ISMF.

The purpose of this chapter is to extend the 2D shock acceleration numerical model developed by *Langner* (2004), based on the TPE, to compute the distribution of GCR Carbon in a north-south asymmetrically shaped heliosphere. This asymmetry is incorporated in the model by using, as a first approach, a heliosheath width that has a significant latitude dependence; both the TS and the HP positions are made asymmetrical. It will be shown how the significance of the effects of a meridional asymmetry in the width of the heliosheath between $\theta = 55^o$ and $\theta = 125^o$ depends on the position of the observer in the heliosphere, particle energy, solar activity and the assumed GCR input spectrum (IS).

The content of this chapter was published by *Ngobeni and Potgieter* (2011).

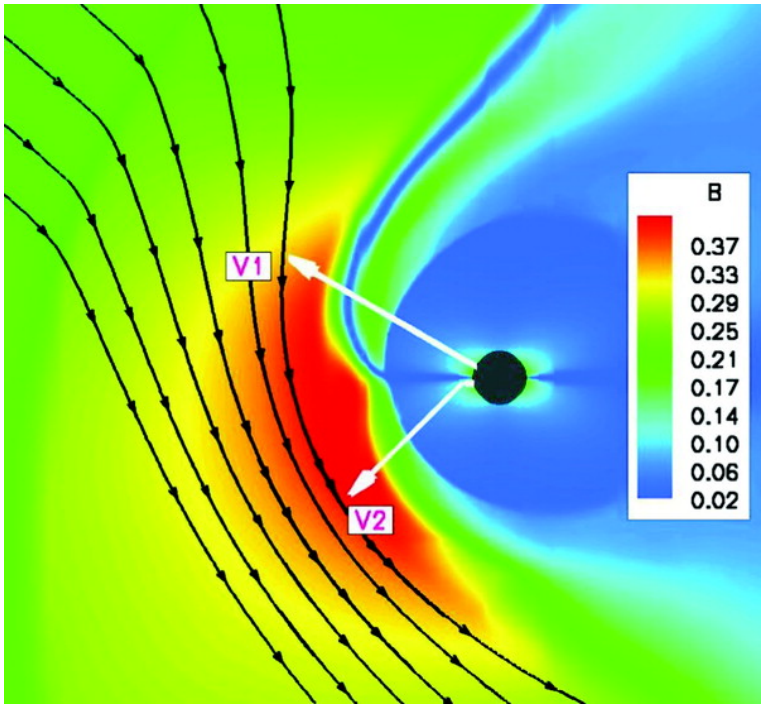

Figure 4.1: The meridional cut of the heliosphere showing the contours of the magnetic field magnitude. The black lines represent the ISMF and the white arrows the trajectories of V1 and V2 respectively. The HCS (dark blue) is deflected northward in the heliosheath. From *Opher et al.* (2006), see also *Strauss et al.* (2013a) and *Luo et al.* (2013).

4.2 Heliospheric asymmetries

It is well known from comprehensive modeling that the global heliosphere has a steady asymmetric geometry (structure) in the nose-tail direction, with the nose region much less extended than the tail direction with respect to the Sun. This is caused by the relative motion of the heliosphere through the interstellar medium (e.g., *Fahr et al.*, 2000; *Zank and Muller*, 2003; *Scherer and Ferreira*, 2005). The predicted ratio of nose-to-tail TS position in the equatorial plane is ∼1:2, while the HP is only well defined in the nose direction and may probably be an open structure in the tail direction (see a discussion by *Scherer and Ferreira*, 2005). It is also generally accepted that the position of the TS at all heliolatitudes changes significantly over an 11-year cycle (e.g., *Washimi and Tanaka*, 1999; *Snyman*, 2007; *Potgieter*, 2010). In addition to this solar cycle related time-dependence, the meridional asymmetry of the TS geometry is enhanced by the increasing latitude dependence of the solar wind velocity and ram pressure during solar minimum conditions over the solar poles (*Scherer and Fahr*, 2003; *Scherer and Ferreira*, 2005). Apart from the large nose-tail asymmetry of the heliosphere and the corresponding moderate non-spherical geometry of the TS, recent MHD models predict additional north-south asymmetries (in the meridional plane) in both the TS and HP positions in the nose region of the heliosphere (*Opher et al.*, 2009; *Pogorelov et al.*, 2009) when considering the influences of both the ISMF and the

HMF. Taking solar cycle dynamical effects into consideration, these asymmetries may result in a significant latitude dependent thickness of the heliosheath. The compression of the HP and the TS by the ISMF on the southern side of the heliosphere has been recently confirmed by IBEX observations (*McComas et al.*, 2012), indicating that the interaction of the LISM and the heliosphere is more complex than earlier thought.

A representation of the north-south heliospheric asymmetries, from MHD modeling results, is shown in Figure 4.1 (adapted from *Opher et al.,* 2006; see also *Strauss,* 2013; *Strauss et al.,* 2013 and *Luo et al.,* 2013). It is a view of the meridional cut of the heliosphere with the contours representing the magnetic field magnitudes. Due to the external pressure resulting from the ISMF, the heliosphere is squeezed in the southern hemisphere when compared to the northern hemisphere causing the positions of the TS and HP to be closer to the Sun in the southern hemisphere. This prediction has, indeed, been confirmed by V1 and V2 observation of the TS position. V1 crossed the TS in 2004 at a radial distance of ~ 94 AU from the Sun and at a polar angle of $\theta =\sim 55^o$ (*Stone et al.*, 2005; *Decker et al.*, 2005). In 2007, V2 also crossed the TS but at a radial distance of ~ 84 AU and at $\theta =\sim 125^o$ (*Stone et al.*, 2008; *Richardson et al.*, 2008). This observation was a milestone of the Voyager mission to interstellar space. It confirmed the dynamic nature of the TS, in particular, that its position with respect to the Sun depends also on the solar cycle (see also *Snyman*, 2007; *Webber and Intriligator*, 2011).

The heliosheath is a prominent feature of the heliosphere that contributes to the overall modulation of GCRs (e.g., *Webber and Lockwood*, 2001; *Langner et al.*, 2003; *Webber*, 2006; *Stone et al.*, 2008), it thus becomes important to investigate the effects on GCR modulation of a north-south asymmetry using, as a first approach, a heliosheath width that is latitude dependent.

In the next sections it will be shown how the north-south asymmetries of the TS and HP positions are incorporated into the TPE to compute the modulation of GCRs in the heliosphere. The modulation effects caused by the north-south asymmetry in the geometry of the heliosphere is therefore new.

4.3 The transport equation in an asymmetrically modeled heliosphere

To incorporate the north-south asymmetries in the heliospheric positions of the TS and the HP, the TPE is solved in a heliospheric geometry other than a sphere, such as meridional (north-south) asymmetric. Thus the cosmic ray distribution function $f(r, \theta, P)$ in the TPE, as shown in Equation 3.1, is transformed to $g(u, v, w)$ using the following coordinate transformation

$$\begin{aligned} u &= r(x + ycos\theta) \\ v &= \theta \\ w &= P. \end{aligned} \tag{4.1}$$

With x and y variables that can be changed to give the desired location of both the TS and the HP at various polar angles. As a result the following relationship between various derivatives of $f(r,\theta,P)$ and $g(u,v,w)$ can be obtained (see also *Haasbroek*, 1997),

$$\begin{aligned}
\frac{\partial f}{\partial t} &= \frac{\partial g}{\partial t} \\
\frac{\partial f}{\partial r} &= \frac{\partial g}{\partial u}\frac{\partial u}{\partial r} \\
\frac{\partial f}{\partial \theta} &= \frac{\partial g}{\partial u}\frac{\partial u}{\partial \theta} + \frac{\partial g}{\partial v} \\
\frac{\partial^2 f}{\partial r^2} &= \frac{\partial^2 g}{\partial u^2}(\frac{\partial u}{\partial r})^2 \\
\frac{\partial^2 f}{\partial \theta^2} &= \frac{\partial^2 g}{\partial v^2} + \frac{\partial^2 g}{\partial u^2}(\frac{\partial u}{\partial \theta})^2 + \frac{\partial g}{\partial u}\frac{\partial^2 u}{\partial \theta^2} + 2\frac{\partial^2 g}{\partial u \partial v}\frac{\partial u}{\partial \theta} \\
\frac{\partial f}{\partial \ln P} &= \frac{\partial g}{\partial \ln w}.
\end{aligned} \tag{4.2}$$

The TPE in an asymmetrically modelled heliosphere is then written in terms of $g(u,v,w)$, instead of $f(r,\theta,P)$, as follows

$$\begin{aligned}
\frac{\partial g}{\partial t} &= \frac{\partial^2 g}{\partial u^2}\left[a_0(\frac{\partial u}{\partial r})^2 + b_0(\frac{\partial u}{\partial \theta})^2\right] + b_0\frac{\partial^2 g}{\partial v^2} + \frac{\partial g}{\partial u}\left[b_0\frac{\partial^2 u}{\partial \theta^2} + c_0\frac{\partial u}{\partial r} + d_0\frac{\partial u}{\partial \theta}\right] \\
&\quad + d_0\frac{\partial g}{\partial v} + 2\frac{\partial^2 g}{\partial u \partial v}\frac{\partial u}{\partial \theta} + e_0\frac{\partial g}{\partial \ln w}.
\end{aligned} \tag{4.3}$$

When simplified Equation 4.3 becomes,

$$\frac{\partial g}{\partial t} = a'\frac{\partial^2 g}{\partial u^2} + b'\frac{\partial^2 g}{\partial v^2} + c'\frac{\partial g}{\partial u} + d'\frac{\partial g}{\partial v} + e'\frac{\partial g}{\partial \ln w} + j'\frac{\partial^2 g}{\partial u \partial v}, \tag{4.4}$$

with

$$\begin{aligned}
a' &= a_0(\frac{\partial u}{\partial r})^2 + b_0(\frac{\partial u}{\partial \theta})^2 \\
b' &= b_0 \\
c' &= b_0\frac{\partial^2 u}{\partial \theta^2} + c_0\frac{\partial u}{\partial r} + d_0\frac{\partial u}{\partial \theta} \\
d' &= d_0 \\
e' &= e_0 \\
j' &= 2\frac{\partial u}{\partial \theta}.
\end{aligned} \tag{4.5}$$

The expressions for a_0, b_0, c_0, d_0 and e_0 are given in Equation 3.4. The numerical solution of Equation 4.4 is the focus of this chapter.

4.4 A brief history of numerical modulation models

The first finite difference numerical model of the TPE was developed by *Fisk* (1971), who solved the TPE numerically by assuming a steady–state and spherical symmetry, i.e. a 1D model with

the radial distance as the only spatial variable. Later the polar angle was included to form a 2D model without drifts (*Fisk*, 1975, 1976). After this, various authors contributed to the development of increasingly sophisticated numerical models, see e.g., *Potgieter* (1984), *Burger* (1987), *le Roux* (1990), *Steenkamp* (1995), *Haasbroek* (1997), *Hattingh* (1998), *Ferreira* (2002) and *Langner* (2004). The first 2D models where the wavy HCS was emulated were developed by *Potgieter* (1984) and *Burger* (1987) (see also *Potgieter and Moraal*, 1985; *Burger and Potgieter*, 1989). This simulation has been improved by *Hattingh and Burger* (1995).

The first 2D time-dependent shock acceleration model was first developed by *Jokipii* (1986) using finite difference method. Almost a decade later *Steenkamp* (1995) developed a 2D time-dependent shock acceleration model with a discontinuous transition of the solar wind at the TS and drifts. A similar model was also developed by *le Roux et al.* (1996) but with a continuous transition of the solar wind at the TS. These models were earlier refined by *Steenberg and Moraal* (1996) and *Haasbroek* (1997), and later by *Langner* (2004).

The first 3D steady-state model including drifts and full wavy HCS was developed by *Kóta and Jokipii* (1983) and later by *Hattingh* (1998). A comparison of the 2D and 3D steady-state models were done by *Hattingh* (1998) and *Ferreira* (1998) to show to what extent they agree. They found that the agreement was excellent and therefore the 2D models, which use less computer time and memory, can be used with great confidence. By including drifts in modulation models the 22-year record of the long-term modulation by neutron monitors could be explained, amongst others; see the review by *Potgieter* (2013).

Recently, several stochastic differential equations (SDEs) that numerically solve the TPE in 3D have been developed (*Zhang*, 1999; *Florinski and Pogorelov*, 2009; *Pei et al.*, 2010; *Strauss et al.*, 2011; *Strauss*, 2013; *Luo et al.*, 2013; *Kopp et al.*, 2014). SDEs have several numerical advantages than finite difference methods, e.g. the propagation times and energy losses of cosmic ray particles can be calculated.

In this study the 2D time-dependent shock acceleration model of *Langner* (2004) and *Langner and Potgieter* (2005) that employs finite difference method with continuous and discontinuous transitions of the solar wind at the TS is extended to obtain a numerical solution of Equation 4.4.

4.5 Numerical method for solving the time-dependent transport equation in an asymmetrical heliosphere

The TPE is a second order linear parabolic partial differential equation (PDE) which can be solved using a Locally One Dimensional (LOD) method for two spatial dimensions and a time dimension in a symmetrical heliosphere. In this case the TPE can be split into a system of three

equations each containing only derivatives in one direction. Each of the solution is obtained by specifying the IS at the HP and starting with an empty heliosphere at time $t = 0$ and stepping in time until sufficient convergence (typically a steady-state) is reached. A detailed discussion of the exact formulation of the LOD method to solve the TPE is given in *Steenkamp* (1995) and *Langner* (2004).

However, for an asymmetrical heliosphere, e.g. north-south asymmetrical heliosphere as done in this study, the LOD method becomes limited due to the term with mixed derivatives appearing in Equation 4.4. However, Equation 4.4 can still be split into a system of two equations instead of three as,

$$\frac{1}{2}\frac{\partial g}{\partial t} = a'\frac{\partial^2 g}{\partial u^2} + b'\frac{\partial^2 g}{\partial v^2} + c'\frac{\partial g}{\partial u} + d'\frac{\partial g}{\partial v} + j'\frac{\partial^2 g}{\partial u \partial v} \tag{4.6}$$

and

$$\frac{1}{2}\frac{\partial g}{\partial t} = e'\frac{\partial g}{\partial \ln w}. \tag{4.7}$$

Equation 4.6 is of parabolic form and thus an Alternating Direction Implicit (ADI) method is used to solve it. Whereas Equation 4.7 is of first-order hyperbolic form and is solved differently. The solution of Equation 4.7 is constant along a set of characteristic curves in (w, t, g) space so that the method of characteristics is used to solve it. A detailed discussion of the exact formulation of the method of characteristics is fully shown in *Steenkamp* (1995) and *Langner* (2004) and is not repeated here. Equations 4.6 and 4.7 are thus referred to as the spatial and the energy equation respectively.

The spatial equation is solved by using the ADI method for two spatial dimensions and a time dimension as given by *Haasbroek* (1997). The ADI method is developed by *Peaceman and Rachford* (1955) and *Douglas* (1955). It is a stable numerical procedure with a discretization error of the second order in both space and time variables. The ADI method is a modification of the Crank-Nicholson finite difference method for two spatial dimensions which computes derivatives at half-way time and/or rigidity intervals on the spatial grid. Applying the ADI method, the spatial equation is solved by firstly stepping implicitly in the radial direction i to obtain a first estimate of g. Then the first estimate of g is used and stepping implicitly in the polar direction j, the final solution is then obtained in terms of g and its estimate. The result is a system of linear equations which can be solved using the Thomas Algorithms (for detailed discussion see *Steenkamp*, 1995; *Haasbroek*, 1997).

However, before a numerical solution of the TPE can be obtained, the exact finite difference method, grid domains, boundary conditions and initial values must be specified.

4.6 The finite difference formulae for the transformed transport equation

The basis of the finite difference method is the Taylor expansion of a function $g(x)$ about an interval Δx. Up to the first three terms the Taylor expansion of $g(x)$ can be approximated as:

$$g(x-\Delta x) = g(x) - g'(x)\Delta x + \frac{g''(x)(\Delta x)^2}{2} \tag{4.8}$$

$$g(x+\Delta x) = g(x) + g'(x)\Delta x + \frac{g''(x)(\Delta x)^2}{2} \tag{4.9}$$

The first order $g'(x)$ and the second order $g''(x)$ derivatives centred around x can be obtained by subtracting and adding Equations 4.8 and 4.9 leading to

$$g'(x) = \frac{g(x+\Delta x) - g(x-\Delta x)}{2\Delta x} \tag{4.10}$$

$$g''(x) = \frac{g(x+\Delta x) - 2g(x) + g(x-\Delta x)}{(\Delta x)^2}. \tag{4.11}$$

The backward and forward first order derivatives can also be calculated easily by truncating Equations 4.8 and 4.9 after the second term,

$$g'(x) = \frac{g(x) - g(x-\Delta x)}{\Delta x} \tag{4.12}$$

$$g'(x) = \frac{g(x+\Delta x) - g(x)}{\Delta x}. \tag{4.13}$$

For the case of the uneven grid, as in this study e.g. the grid in the radial direction u, the derivatives are not as straight forward as above. However, one can still approximate the first and second-order derivatives of function $g(u)$ with accuracy. The first and second-order derivatives of the function $g(u)$ are approximated for an uneven grid in u, that is $\Delta u_1 \neq \Delta u_2 \neq \Delta u_3 \neq \Delta u_4$ (see a detailed discussion by *Steenkamp*, 1995). After assigning the grid index i to distinguish steps in u, the radial direction, the first and second-order derivatives of $g(u)$ become

$$\begin{aligned}
\frac{\partial g}{\partial u} &= g' = \frac{-\Delta u_1}{\Delta u_2(\Delta u_1 + \Delta u_2)} g_{i-1} + \frac{\Delta u_1 - \Delta u_2}{\Delta u_1 \Delta u_2} g_i + \frac{\Delta u_2}{\Delta u_1(\Delta u_1 + \Delta u_2)} g_{i+1} \\
\frac{\partial^2 g}{\partial^2 u} &= g'' = \frac{2}{\Delta u_2(\Delta u_1 + \Delta u_2)} g_{i-1} - \frac{2}{\Delta u_1 \Delta u_2} g_i + \frac{2}{\Delta u_1(\Delta u_1 + \Delta u_2)} g_{i+1},
\end{aligned} \tag{4.14}$$

where

$$\begin{aligned}
g_{i-2} &= g(u - \Delta u_2 - \Delta u_4) \\
g_{i-1} &= g(u - \Delta u_2) \\
g_i &= g(u) \\
g_{i+1} &= g(u + \Delta u_1) \\
g_{i+2} &= g(u + \Delta u_1 + \Delta u_3).
\end{aligned} \tag{4.15}$$

The one sided forward and backward derivatives are respectively approximated as

$$g' = -\frac{2\Delta u_1 + \Delta u_3}{\Delta u_1(\Delta u_1 + \Delta u_3)} g_i + \frac{\Delta u_1 + \Delta u_3}{\Delta u_1 \Delta u_3} g_{i+1} - \frac{\Delta u_1}{\Delta u_3(\Delta u_1 + \Delta u_3)} g_{i+2} \tag{4.16}$$

and

$$g' = \frac{2\Delta u_2 + \Delta u_4}{\Delta u_2(\Delta u_2 + \Delta u_4)} g_i - \frac{\Delta u_2 + \Delta u_4}{\Delta u_2 \Delta u_4} g_{i-1} + \frac{\Delta u_2}{\Delta u_4(\Delta u_2 + \Delta u_4)} g_{i-2}. \tag{4.17}$$

The grid in the polar direction in this study is even, i.e. Δv is a constant. Hence in this case, after assigning the grid index j to distinguish steps in v, the derivatives of the function $g(v)$ are approximated as

$$\begin{aligned} g' &= \frac{g_{j+1} - g_{j-1}}{2\Delta v} && \text{(centred)} \\ g'' &= \frac{g_{j-1} - 2g_j + g_{j+1}}{(\Delta v)^2} && \text{(centred)} \\ g' &= \frac{-3g_j + 4g_{j+1} - g_{j+2}}{2\Delta v} && \text{(forward)} \\ g' &= \frac{3g_j - 4g_{j-1} + g_{j-2}}{2\Delta v}. && \text{(backward)} \end{aligned} \tag{4.18}$$

Where

$$\begin{aligned} g_{j-2} &= g(v - \Delta v_2 - \Delta v_4) \\ g_{j-1} &= g(v - \Delta v_2) \\ g_j &= g(v) \\ g_{j+1} &= g(v + \Delta v_1) \\ g_{j+2} &= g(v + \Delta v_1 + \Delta v_3). \end{aligned} \tag{4.19}$$

The term $\frac{\partial^2 g}{\partial u \partial v}$ consisting of mixed derivatives in Equation 4.4 is approximated as

$$\begin{aligned} \frac{\partial^2 g}{\partial u \partial v} = &\frac{-\Delta u_1}{\Delta u_2(\Delta u_1 + \Delta u_2)} \frac{g_{i-1,j+1} - g_{i-1,j-1}}{2\Delta v} + \frac{\Delta u_1 - \Delta u_2}{\Delta u_1 \Delta u_2} \frac{g_{i,j+1} - g_{i,j-1}}{2\Delta v} \\ &+ \frac{\Delta u_2}{\Delta u_1(\Delta u_1 + \Delta u_2)} \frac{g_{i+1,j+1} - g_{i+1,j-1}}{2\Delta v}. \end{aligned} \tag{4.20}$$

4.7 Grid domains

In this section grid domains for the respective spatial, energy and time grids used to solve Equation 4.4 are specified, as well as the values of the stepping parameters.

4.7.1 Radial grid

Solutions are obtained on a radial grid running from $i = 1$ (representing the inner boundary) to $i = n = 300$ (representing the outer boundary). The respective asymmetric boundary positions

are given by:

$$u_1 = 0.7 \text{ AU} \quad \text{(inner boundary)}, \tag{4.21}$$

$u_n = 140$ AU at $\theta = 0^o, 120$ AU at $\theta = 90^o$and 100 AU at $\theta = 180^o$ (outer boundary).

The radial grid is transformed with uneven grid spacing (for a detail discussion see *Langner*, 2004). This transformation is general and can be used for any value of n and boundary positions including the asymmetric boundary, the focus of this study.

4.7.2 Polar grid

A linear polar grid runs in steps of $\Delta v = 2.5^o$ from $j = 1 \rightarrow m$ with $j = 1 = 0^o$ and $m = 73 = 180^o$.

4.7.3 Rigidity grid

The rigidity grid ($k = 1 \rightarrow 102$) is linear ($\Delta \ln w$ is constant). The rigidity decreases logarithmically from an initial value of $w_{max} = 43$ GV, where modulation is assumed negligible, to a minimum value $w_{min} = 0.1$ GV in steps of $\Delta \ln w = 0.06$.

4.7.4 Time grid

A linear time grid is chosen such that time is incremented from $t = 0$ to 30000 with an amount $\Delta t = 0.02$. When $t = 30000$ sufficient convergence is reached: the difference between two successive solutions becomes sufficiently small.

4.8 Boundary conditions and initial values

1. The heliosphere is taken to be asymmetrical in the meridional plane (meridional implies north-south directions opposing to east-west directions which is interpreted to be a nose-tail asymmetry) with the relevant IS specified at the asymmetric boundary:

$$g_{n,j,k} = g_g, \tag{4.22}$$

   with g_g representing the IS for GCR species.

2. The inner boundary, u_1, is assumed to be an absorbing boundary which implies that particles can enter or leave this boundary.

$$\left[\frac{\partial g}{\partial u}\right]_{\lim u \rightarrow u_1^+} = \left[\frac{\partial g}{\partial u}\right]_{\lim u \rightarrow u_1^-}. \tag{4.23}$$

   The gradient of the distribution function relative to u is the same just outside the boundary and just inside the boundary.

3. The numerical grid was chosen to range from 0^o to 180^o (from pole to pole) with the equatorial plane at 90^o. Hence the boundary conditions at the polar regions are specified as,
$$\left[\frac{\partial g}{\partial v}\right]_{v=0^o,180^o} = 0 \tag{4.24}$$
at these positions in the heliosphere.

4. At the TS the distribution function is assumed to be related by $g^- = g^+$, where '-' represents upstream region and '+' represents downstream region.

4.9 Solving the spatial equation of the TPE using the ADI numerical scheme

Equation 4.6 includes the convection, diffusion and drift terms of the TPE. To solve Equation 4.6 using the ADI method, the following discretization is used

$$g(u, v, w) = g(u_i, v_j, w_k) = g_{i,j,k}. \tag{4.25}$$

Assuming $\Delta u_1(\Delta u_1 + \Delta u_2) = \Delta u_{11}$, $\Delta u_2(\Delta u_1 + \Delta u_2) = \Delta u'_{11}$ and $\Delta u_1 \Delta u_2 = \Delta u_{12}$ in Equation 4.14, the first equation of the finite difference expression for Equation 4.6 is obtained by stepping implicitly in the radial direction i evaluating half of $\frac{\partial g}{\partial u}$ and $\frac{\partial^2 g}{\partial u^2}$ at the current rigidity step k and the other half at $k + 1/2$ to obtain $g^*_{i,j}$:

$$\begin{aligned}
\frac{1}{\Delta t}(g^*_{i,j} - g_{i,j}) &= a'\Big[(\frac{1}{\Delta u_{11}})\, g_{i+1,j} - (\frac{1}{\Delta u_{12}})\, g_{i,j} + (\frac{1}{\Delta u'_{11}})\, g_{i-1,j} + (\frac{1}{\Delta u_{11}})\, g^*_{i+1,j} \\
&- (\frac{1}{\Delta u_{12}})\, g^*_{i,j} + (\frac{1}{\Delta u'_{11}})\, g^*_{i-1,j}\Big] \\
&+ \frac{b'}{(\Delta v)^2}\Big[g_{i,j+1} - 2g_{i,j} + g_{i,j-1}\Big] \\
&+ \frac{c'}{2}\Big[(\frac{\Delta u_2}{\Delta u_{11}})\, g_{i+1,j} + (\frac{\Delta u_1 - \Delta u_2}{\Delta u_{12}})\, g_{i,j} - (\frac{\Delta u_1}{\Delta u'_{11}})\, g_{i-1,j} + (\frac{\Delta u_2}{\Delta u_{11}})\, g^*_{i+1,j} \\
&+ (\frac{\Delta u_1 - \Delta u_2}{\Delta u_{12}})\, g^*_{i,j} - (\frac{\Delta u_1}{\Delta u'_{11}})\, g^*_{i-1,j}\Big] \\
&+ \frac{d'}{2\Delta v}\Big[g_{i,j+1} - g_{i,j-1}\Big] \\
&+ \frac{j'}{2\Delta v}\Big[(\frac{\Delta u_2}{\Delta u_{11}})\, g_{i+1,j+1} - (\frac{\Delta u_1}{\Delta u'_{11}})\, g_{i-1,j+1} - (\frac{\Delta u_2}{\Delta u_{11}})\, g_{i+1,j-1} \\
&+ (\frac{\Delta u_1}{\Delta u'_{11}})\, g_{i-1,j-1} + (\frac{\Delta u_1 - \Delta u_2}{\Delta u_{12}})\, g_{i,j+1} - (\frac{\Delta u_1 - \Delta u_2}{\Delta u_{12}})\, g_{i,j-1}\Big],
\end{aligned} \tag{4.26}$$

where $g_{i,j} = g_{i,j,k}$ and $g*_{i,j} = g_{i,j,k+1/2}$.

Grouping terms in Equation 4.26 that have the same i and j subscript together, yields

$$\begin{aligned} A_{ijk}g^*_{i-1,j} + B_{ijk}g^*_{i,j} + C_{ijk}g^*_{i+1,j} &= -D1_{ijk}g_{i-1,j} - D2_{ijk}g_{i,j} - D3_{ijk}g_{i+1,j} - D4_{ijk}g_{i,j-1} \\ &- D5_{ijk}g_{i,j+1} - D6_{ijk}g_{i-1,j-1} - D7_{ijk}g_{i+1,j-1} \\ &- D8_{ijk}g_{i+1,j+1} - D9_{ijk}g_{i-1,j+1}, \end{aligned} \tag{4.27}$$

where the coefficients are given by

$$\begin{aligned} A &= \frac{a'}{\Delta u_{11}} - \frac{c'}{2}\frac{\Delta u_1}{\Delta u'_{11}} \\ B &= \frac{c'}{2}\frac{\Delta u_1 - \Delta u_2}{\Delta u_{12}} - \frac{1}{\Delta t} - \frac{a'}{\Delta u_{12}} \\ C &= \frac{c'}{2}\frac{\Delta u_2}{\Delta u_{11}} - \frac{a'}{\Delta u_{11}} \\ D1 &= \frac{a'}{\Delta u'_{11}} - \frac{c'}{2}\frac{\Delta u_1}{\Delta u'_{11}} \\ D2 &= \frac{1}{\Delta t} - \frac{a'}{\Delta u_{12}} - \frac{2b'}{(\Delta v)^2} + \frac{c'}{2}\frac{\Delta u_1 - \Delta u_2}{\Delta u_{12}} \\ D3 &= \frac{a'}{\Delta u_{11}} + \frac{c'}{2}\frac{\Delta u_2}{\Delta u_{11}} \\ D4 &= \frac{b'}{(\Delta v)^2} - \frac{d'}{2\Delta v} - \frac{j'}{2\Delta v}\frac{\Delta u_1 - \Delta u_2}{\Delta u_{12}} \\ D5 &= \frac{b'}{(\Delta v)^2} + \frac{d'}{2\Delta v} + \frac{\Delta u_1 - \Delta u_2}{\Delta u_{12}} \\ D6 &= \frac{j'}{2\Delta v}\frac{\Delta u_1}{\Delta u'_{11}} \\ D7 &= -\frac{j'}{2\Delta v}\frac{\Delta u_2}{\Delta u_{11}} \\ D8 &= \frac{j'}{2\Delta v}\frac{\Delta u_2}{\Delta u_{11}} \\ D9 &= -\frac{j'}{2\Delta v}\frac{\Delta u_1}{\Delta u'_{11}}. \end{aligned} \tag{4.28}$$

Equation 4.27 can be represented as a matrix equation using the initial values and boundary

conditions above. Equation 4.27 thus becomes,

$$\begin{bmatrix} B_1 & A_1+C_1 & 0 & .... & 0 & 0 & 0 \\ A_2 & B_2 & C_2 & .... & 0 & 0 & 0 \\ \vdots & \vdots & \vdots & \ddots & \vdots & \vdots & \vdots \\ 0 & 0 & 0 & .... & A_{n-2} & B_{n-2} & C_{n-2} \\ 0 & 0 & 0 & .... & 0 & A_{n-1} & B_{n-1} \end{bmatrix} \begin{bmatrix} g^*_{1,j} \\ g^*_{2,j} \\ \vdots \\ g^*_{n-2,j} \\ g^*_{n-1,j} \end{bmatrix} = \tag{4.29}$$

$$- \begin{bmatrix} D2_1 & D1_1+D3_1 & 0 & .... & 0 & 0 & 0 \\ D1_2 & D2_2 & D3_2 & .... & 0 & 0 & 0 \\ \vdots & \vdots & \vdots & \ddots & \vdots & \vdots & \vdots \\ 0 & 0 & 0 & .... & D1_{n-2} & D2_{n-2} & D3_{n-2} \\ 0 & 0 & 0 & .... & 0 & D1_{n-1} & D2_{n-1} \end{bmatrix} \begin{bmatrix} g_{1,j} \\ g_{2,j} \\ \vdots \\ g_{n-2,j} \\ g_{n-1,j} \end{bmatrix}$$

$$- \begin{bmatrix} D4_1 & D6_1+D7_1 & 0 & .... & 0 & 0 & 0 \\ D6_2 & D4_2 & D7_2 & .... & 0 & 0 & 0 \\ \vdots & \vdots & \vdots & \ddots & \vdots & \vdots & \vdots \\ 0 & 0 & 0 & .... & D6_{n-2} & D4_{n-2} & D7_{n-2} \\ 0 & 0 & 0 & .... & 0 & D6_{n-1} & D4_{n-1} \end{bmatrix} \begin{bmatrix} g^*_{1,j-1} \\ g^*_{2,j-1} \\ \vdots \\ g^*_{n-2,j-1} \\ g^*_{n-1,j-1} \end{bmatrix}$$

$$- \begin{bmatrix} D5_1 & D9_1+D8_1 & 0 & .... & 0 & 0 & 0 \\ D9_2 & D5_2 & D8_2 & .... & 0 & 0 & 0 \\ \vdots & \vdots & \vdots & \ddots & \vdots & \vdots & \vdots \\ 0 & 0 & 0 & .... & D9_{n-2} & D5_{n-2} & D8_{n-2} \\ 0 & 0 & 0 & .... & 0 & D9_{n-1} & D5_{n-1} \end{bmatrix} \begin{bmatrix} g_{1,j+1} \\ g_{2,j+1} \\ \vdots \\ g_{n-2,j+1} \\ g_{n-1,j+1} \end{bmatrix}.$$

Matrix Equation 4.29 is a tri-diagonal system and the Thomas algorithm is used to solve it. Two variables X_i and Y_i are defined as

$$\begin{aligned} X_1 &= \frac{A_1+C_1}{B_1}; \qquad \text{for} \quad i=1 \\ X_i &= \frac{C_i}{B_i - A_i X_{i-1}}; \quad \text{for} \quad i=2,3,...,n-1; \end{aligned}$$

and

$$\begin{aligned} Y_1 &= \frac{D_1}{B_1}; \qquad \text{for} \quad i=1 \\ Y_i &= \frac{D_i - A_i Y_{i-1}}{B_i - A_i X_{i-1}}; \quad \text{for} \quad i=2,3,...,n-1; \end{aligned}$$

where the variables on the right-hand side come from Equation 4.29, and D_1 and D_i are,

$$\begin{aligned} D_1 &= -D2_1 g_{1,j} - (D1_1+D3_1) g_{2,j} - D4_1 g_{1,j-1} - (D6_1+D7_1) g_{g2,j-1} \\ &\quad -D5_1 g_{1,j+1} - (D9_1+D8_1) g_{2,j+1}, \\ D_i &= -D1_i g_{i-1,j} - D2_i g_{i,j} - D3_i g_{i+1,j} - D6_i g_{i-1,j-1} - D4_i g_{i,j-1} \\ &\quad -D7_i g_{i+1,j-1} - D9_i g_{i-1,j+1} - D5_i g_{i,j+1} - D8_i g_{i+1,j+1}. \end{aligned}$$

The solution of $g*_{i,j}$ is then obtained by stepping through all i and j indices using the following relation:

$$g*_{n-i,j} = Y_{n-i} - X_{n-i} g*_{n-i+1,j}; \quad \text{for} \quad i = 1, 2, ..., n-1; \text{ and } \quad j = 1, 2, ..., m.$$

A second solution $h_{i,j,k}$, which is one time-step ahead of $g_{i,j,k}$, in terms of the first solution $g*_{i,j}$ can be obtained by solving Equation 4.6 with the same boundary conditions by stepping implicitly in the $\theta-$ direction j. This is fully shown in *Haasbroek* (1997) and is not repeated here.

The spatial and the energy equations are solved simultaneously together with the matching conditions at the TS given by Equation 3.43. Thus the transformed TPE is solved time dependently as a combined diffusive-shock-acceleration and drift model until an equilibrium solution is reached in order to find the full impact of the TS. This standard approach to studying TS effects (see also *Steenkamp*, 1995; *le Roux et al.*, 1996; *Haasbroek*, 1997; *Langner*, 2004; *Langner and Potgieter*, 2005, 2008; *Potgieter and Ferreira*, 2002; *Strauss*, 2010) does not allow changing all modulation parameters dynamically e.g. updating them with every solar rotation as is done by *Manuel et al.* (2011a) but whose model does not contain TS re-acceleration effects.

4.10 The assumed north-south asymmetry in the TS and the HP positions

In numerical models of the global solar modulation of GCRs, the location of the heliospheric boundary, usually assumed to be the HP, is most relevant (see e.g. *Langner and Potgieter*, 2005; *Nkosi et al.*, 2011; *Manuel et al.*, 2011b). In modeling this boundary is where modulation is assumed to commence, more specifically where the IS's of the various GCR species are specified.

A north-south asymmetry for the heliosheath based on the assumed transformation is given in Figure 4.2, as a function of polar angle, with $\theta = 0^o$ corresponding to a heliolatitude of 90^o N. Clearly the assumed meridional asymmetry in the extent of the heliosheath results in a heliosheath thickness (width) that is latitude dependent. It is wider in the northern hemisphere ($0^o < \theta < 90^o$) than in the southern hemisphere ($90^o < \theta < 180^o$). Respectively, this places the HP and TS at a radial distance $r_{HP} \sim 120$ AU and $r_{TS} \sim 90$ AU in the equatorial plane, at $r_{HP} \sim 131$ AU and $r_{TS} \sim 94$ with $\theta = 55^o$ (approximating the V1 direction) and at $r_{HP} \sim 109$ AU and $r_{TS} \sim 86$ AU with $\theta = 125^o$ (approximating the V2 direction); with r_{TS} and r_{HP} the positions of the TS and the HP respectively. The essence of this assumption is that the thickness of the heliosheath is decreased from ~ 40 AU to ~ 20 AU from heliographic pole to pole, in the nose region of the heliosphere. The subsequent modulation effects and differences that result from this latitude dependent heliosheath thickness are next illustrated.

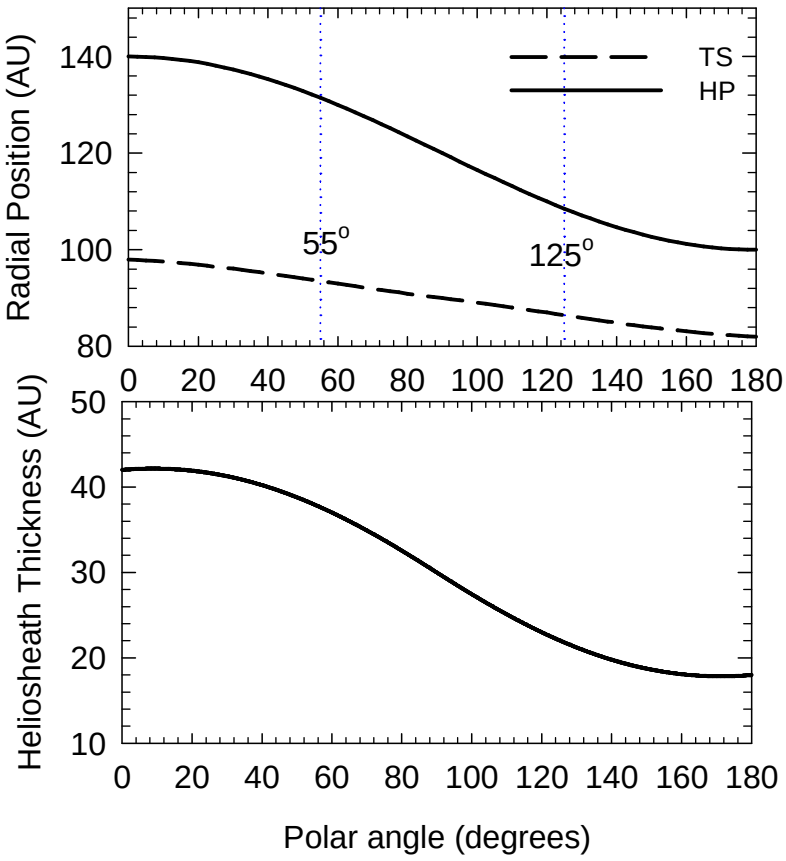

Figure 4.2: In the top panel the assumed heliocentric radial position of the TS (dashed line) and the HP (solid line) is shown as a function of polar angle θ, with the approximated θ for the two Voyager spacecraft trajectories indicated as vertical dotted lines. The bottom panel shows the corresponding polar angle (co-latitude) dependent thickness of the heliosheath from heliospheric pole to pole ($\theta = 0^o$ to $\theta = 180^o$).

4.11 North-south asymmetry of GCR Carbon in the heliosphere

4.11.1 Dependence on the input spectra

The first step is to compare computed spectra with $\theta = 55^o$ (V1 heliolatitude) to those with $\theta = 125^o$ (V2 heliolatitude) for the two different IS's. This is done for the two drift cycles during solar minimum modulation and for the assumed geometric asymmetry of the heliosphere as discussed above. For the GCR Carbon IS, two approaches are followed for intensities below ~ 300 MeV/nuc, the estimated IS of *Webber and Higbie* (2009) as the lowest possibility and the computed IS by *Moskalenko et al.* (2002) as the highest possibility. Above 300 MeV/nuc, the two IS's are identical. (A detailed discussion of the IS of GCR Carbon based on very recent V1 *in situ* observations (*Stone et al.*, 2013) is given in Chapter 6.) The computational results are shown in Figure 4.3 as a function of kinetic energy/nuc; the two top panels for the low IS (*Webber and Higbie*, 2009) and the bottom panels for the high IS (*Moskalenko et al.*, 2002). The

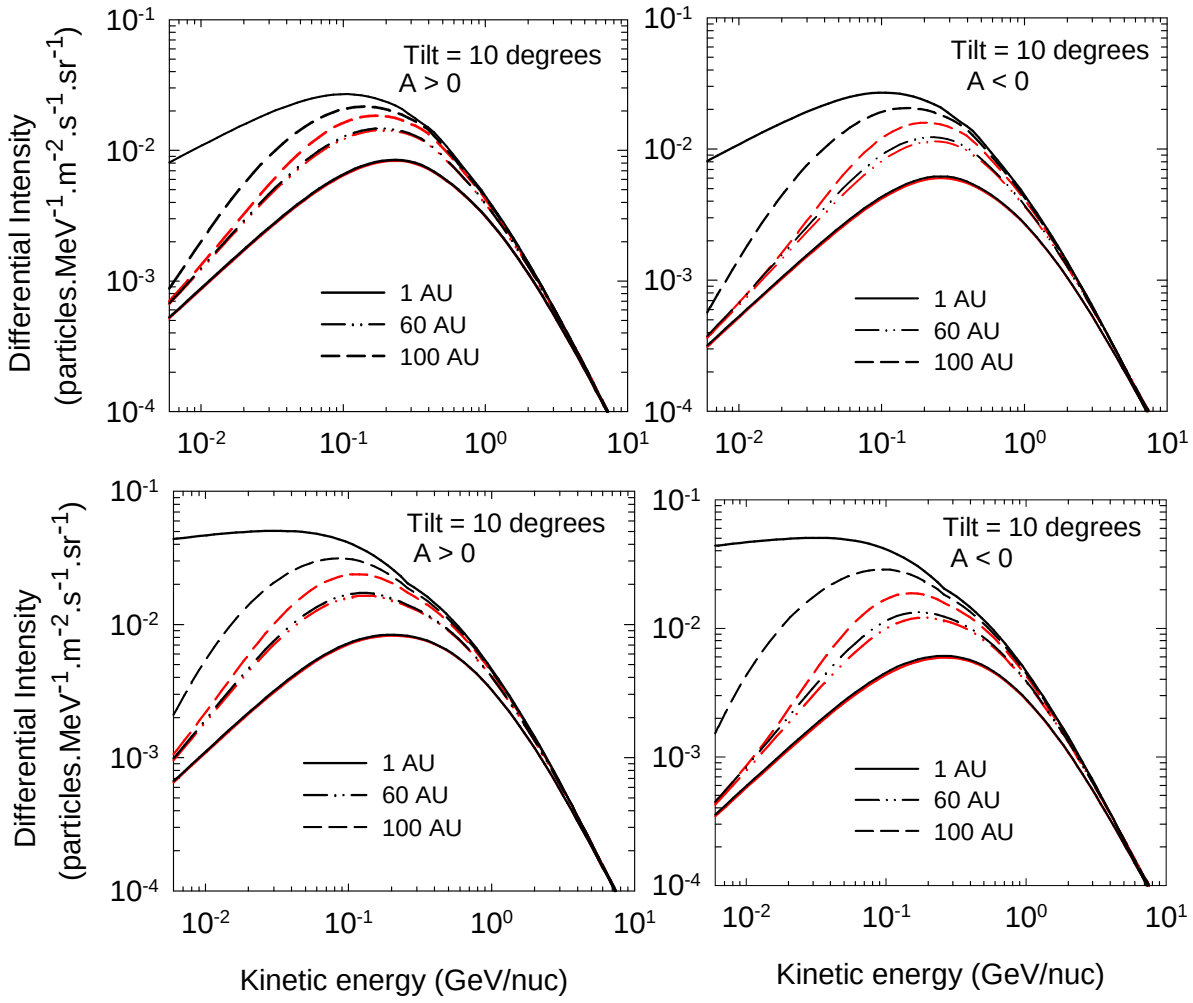

Figure 4.3: Computed differential intensities for GCR Carbon as a function of kinetic energy/nuc at radial distances of 1 AU, 60 AU and 100 AU for both polarity cycles (left panels for A > 0, right panels for A < 0) during solar minimum conditions ($\alpha = 10^o$). Black lines represent solutions at $\theta = 125^o$ and red lines at $\theta = 55^o$. For results in the top row the IS of *Webber and Higbie* (2009) is used at the HP, whereas for the bottom row the IS of *Moskalenko et al.* (2002) is used.

left panels are for the A > 0 polarity cycle and the right panels for the A < 0 cycles. Spectra for GCR Carbon are shown at radial distances of 1 AU, 60 AU and 100 AU, at $\theta = 55^o$ (red lines) and $\theta = 125^o$ (black lines). The differences between the black and red lines illustrate the effect of the assumed meridional asymmetry.

It follows from Figure 4.3 that when the IS of *Webber and Higbie* (2009) is used, the computed spectrum, with kinetic energy $E <\sim 100$ MeV/nuc in the A > 0 cycle, at 100 AU with $\theta = 125^o$ is a factor of ~ 1.4 higher than with $\theta = 55^o$. At 60 AU, in the A > 0 cycle, the differences caused by the assumed north-south asymmetry are negligible. The A < 0 cycle exhibits large differences between the two polar angles, with the computed spectrum becoming a factor ~2.0 higher at 125^o than at 55^o at 100 AU with $E < 100$ MeV/nuc. For the IS from *Moskalenko et al.* (2002) the differences in spectra between $\theta = 55^o$ and $\theta = 125^o$ are larger for both polarity

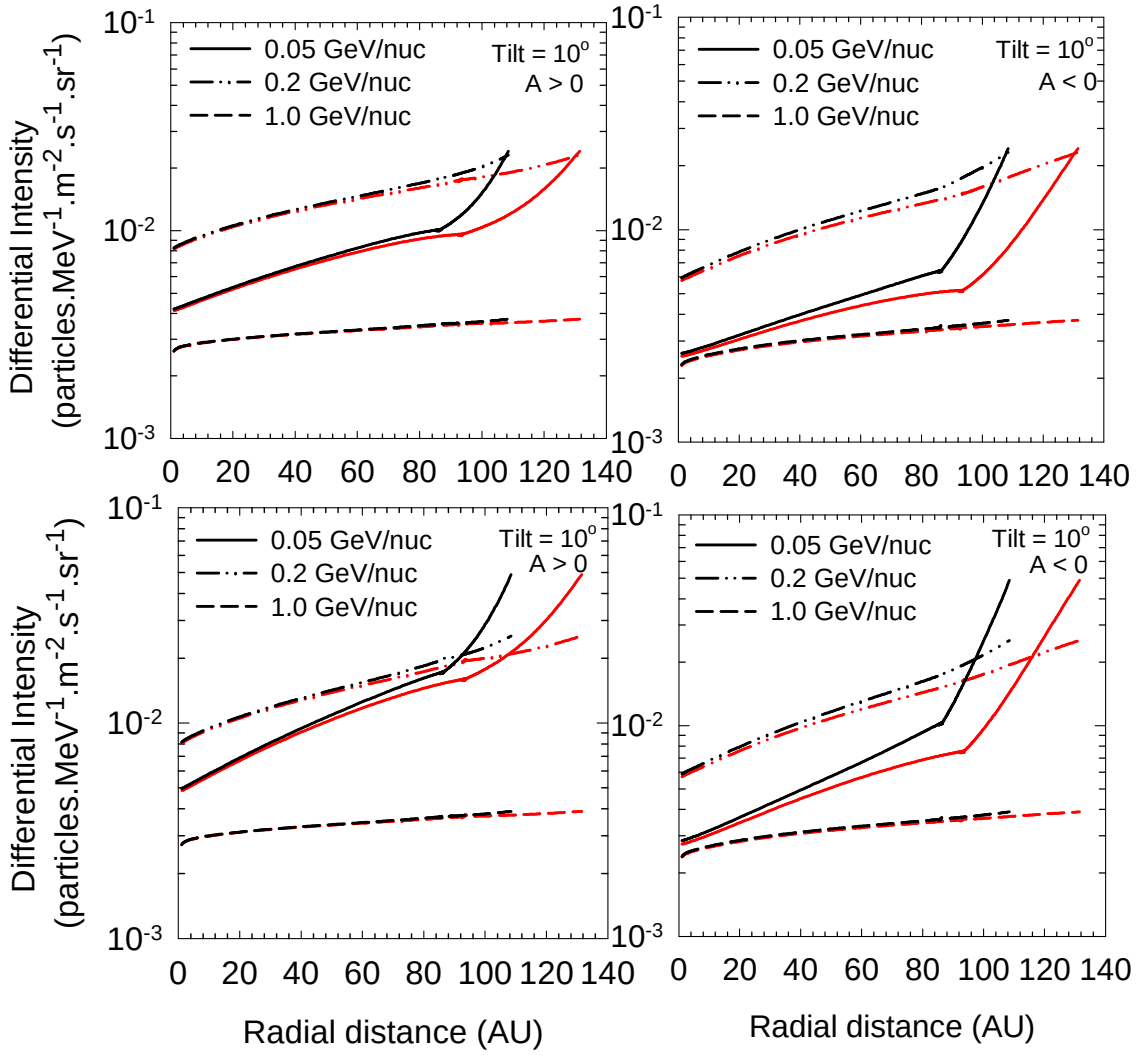

Figure 4.4: Computed differential intensity for GCR Carbon as a function of radial distance at energies of 0.05 GeV/nuc, 0.2 GeV/nuc and 1.0 GeV/nuc for both polarity cycles during solar minimum conditions ($\alpha = 10^o$). In the top row the IS of *Webber and Higbie* (2009) is specified at the HP, whereas in the bottom row the IS of *Moskalenko et al.* (2002) is used. Black lines are solutions at $\theta = 125^o$ ($r_{HP} = 109$ AU and $r_{TS} = 86$ AU) and red lines at $\theta = 55^o$ ($r_{HP} = 131$ AU and $r_{TS} = 94$ AU).

cycles. In the A < 0 cycle, with $E < 50$ MeV/nuc, the difference can be as large as a factor of ~ 4.0. Such a large difference between V1 and V2 should be easily measurable beyond 100 AU in the heliosheath. At 60 AU the differences are again not large enough to be considered significant. As expected, these differences become negligible with increasing energies.

A general result from Figure 4.3 is that the computed spectra at $\theta = 125^o$ are higher than that at 55^o with the differences caused by the assumed meridional asymmetry, quite prominent at 100 AU. These differences vary from insignificant at higher energies to as large as a factor of $\sim$ 2.2 at lower energies in the heliosheath during the A > 0 cycle, whereas during the A < 0 cycle it can be as large as a factor ~ 4.0 at lower energies ($E <\sim 100$ MeV/nuc) but these numbers depend strongly on what is assumed for the IS at these lower energies.

In Figure 4.4 the computed radial intensities at $\theta = 55^o$ (red lines), at energies of 0.05 GeV/nuc, 0.2 GeV/nuc and 1.0 GeV/nuc, are compared to those at $\theta = 125^o$ (black lines). This is done for the two different IS's and the two drift cycles during solar minimum modulation, respectively. The two top panels show solutions obtained with the IS of *Webber and Higbie* (2009) whereas in the bottom panels the IS of *Moskalenko et al.* (2002) was used. The effects of the assumed asymmetry between $\theta = 55^o$ and $\theta = 125^o$ on the radial intensities of GCR Carbon are of interest. The differences (between the black and red lines) clearly increase as a function of radial distance r and become significant in the heliosheath, but only at low energies; compare e.g. the 0.2 GeV/nuc with 1.0 GeV/nuc intensities. With $E >\sim 0.2$ GeV/nuc, it seems that the modulation effects of a north-south asymmetry of the heliosheath are insignificant, even very close to the HP, in both polarity cycles. In the inner heliosphere ($r <\sim$40 AU), these effects on the modulation of GCRs subside at all energies for both drift cycles. Also noteworthy is that with $E = 0.05$ GeV/nuc and $E = 0.2$ GeV/nuc the associated radial gradient will increase beyond the TS but more significantly at $\theta = 125^o$ than at $\theta = 55^o$, resulting from the HP that is much closer to the TS at $\theta = 125^o$ than at $\theta = 55^o$. The computed GCR Carbon intensities obtained with the assumed asymmetry illustrate insignificant differences between 55^o and 125^o in the inner to middle heliosphere but the effect grows with increasing distance, as expected, towards the TS, especially for the A > 0 cycle. Inside the heliosheath larger differences are possible at energies below a few-hundred MeV/nuc. Clearly, with $E = 1.0$ GeV/nuc, the differences are already insignificant.

4.11.2 Dependence on solar activity

The diffusion coefficients given in Chapter 3 are derived to study modulation of GCRs during solar minimum conditions. To represent modulation also for increasing solar activity an adjustment is made to $K_{||}$, with respect to the assumed solar minimum value similar to *Ferreira and Potgieter* (2004), for both polarity cycles given by

$$\left(\frac{10^o}{\alpha}\right)^{\frac{1}{\eta}} K_{||}, \tag{4.30}$$

where α is the HCS tilt angle in degrees and $\eta = 3.25$. The tilt angle is assumed to represent solar minimum conditions with $\alpha = 10^o$ and moderate maximum conditions with $\alpha = 50^o$. (See www.wso.stanford.edu; Wilcox Solar Observatory; courtesy of J.T. Hoeksema). For $\alpha = 50^o$, this adjustment changes $K_{||}$ by a factor of ~ 0.6 as compared to its value when $\alpha = 10^o$, whereas the perpendicular diffusion coefficients $K_{\perp r}$ and $K_{\perp\theta}$ are also increased by a factor of ~ 1.5 from their assumed solar minimum values. These adjustments for increasing solar activity are considered optimal and in accordance with the time dependence of the diffusion tensor (see also *Strauss and Potgieter*, 2010). The difference between minimum and moderate maximum conditions, in this context, is contained in the change of tilt angle from

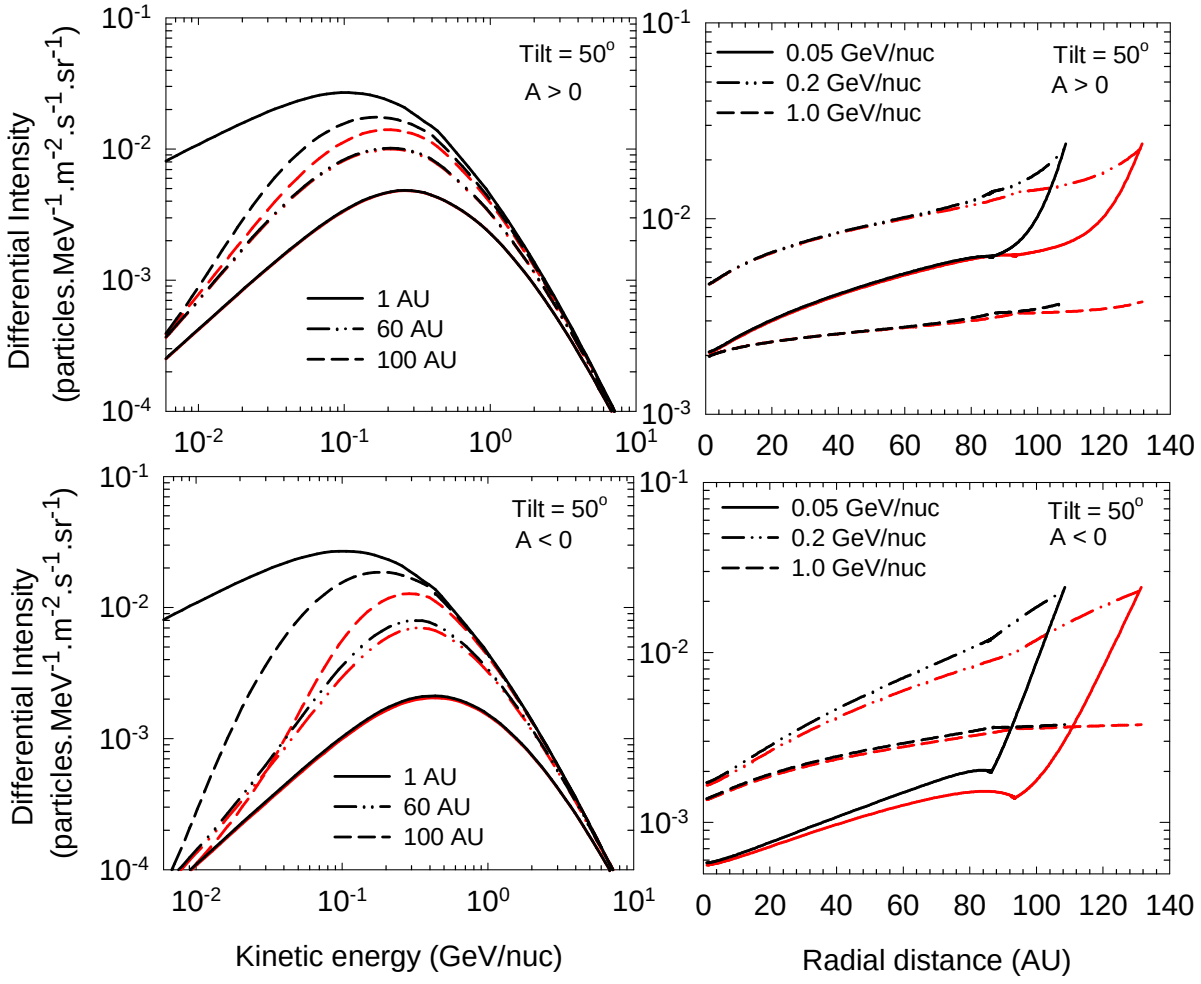

Figure 4.5: Left panels: computed differential intensities for GCR Carbon as a function of kinetic energy/nuc at radial distances of 1 AU, 60 AU and 100 AU for both polarity cycles (top panel for A > 0, bottom panel for A < 0) during moderate solar maximum conditions ($\alpha = 50^o$). Right panels: corresponding differential intensities as a function of radial distance for 0.05 GeV/nuc, 0.2 GeV/nuc and 1.0 GeV/nuc, respectively. Black lines represent solutions at $\theta = 125^o$ and red lines at $\theta = 55^o$. The IS of *Webber and Higbie* (2009) is specified at the asymmetric HP.

10^o to 50^o, the change in the solar wind speed, as indicated in Chapter 2, and changes in $K_{||}$, $K_{\perp r}$ and $K_{\perp \theta}$.

The left panels of Figure 4.5 show the computed differential intensity for GCR Carbon as a function of kinetic energy/nuc for both polarity cycles, A > 0 (top panel) and A< 0 (bottom panel) for moderate maximum conditions represented by $\alpha = 50^o$. The energy spectra are shown at radial distances of 1 AU, 60 AU and 100 AU with respect to the unmodulated spectrum, IS of *Webber and Higbie* (2009). The right panels show the differential intensity as a function of radial distance in AU, at kinetic energy $E = 0.05$ GeV/nuc, 0.2 GeV/nuc and 1.0 GeV/nuc, respectively. Two sets of solutions are shown, with $\theta = 55^o$ (red lines) compared to those with $\theta = 125^o$ (black lines). Differences between black and red lines in this figure thus

illustrate the modulation differences obtained between 55^o and 125^o caused by the assumed geometric asymmetry in the TS and HP positions when solar activity is increased to moderate solar maximum. It follows from Figure 4.5 that during the A > 0 cycle, differences in GCR intensities between $\theta = 55^o$ and $\theta = 125^o$ are insignificant inside the TS but become large in the heliosheath, but only at energies below a few-hundred MeV/nuc. While in the $A < 0$ cycle differences are more pronounced, even inside off the TS but again only at energies $E < 1.0$ GeV/nuc. These differences become larger with increasing tilt angles, showing that the model is more responsive to changes in the tilt angle during this cycle (see also *Langner and Potgieter*, 2004).

The results shown in Figure 4.4 and 4.5 can be interpreted to indicate that V1 and V2 may observe large differences in GCR intensities below a few-hundred MeV/nuc when approaching the asymmetric boundary, if such an asymmetry would exist. Finally, it should be noted that in addition to the asymmetry in the geometry of the heliosphere it is possible that an asymmetry in modulation conditions between the north and south hemispheres can also exist, for example, the HMF turbulence could develop differently. Such an asymmetry, to reflect different modulation conditions, can be simulated in modulation models e.g., by an enhancement of $K_{\perp\theta}$ (*Potgieter*, 1996, 2000) and $K_{\perp r}$ that differs from heliographic pole to pole. This may produce even larger effects when combined with the geometrical asymmetry as discussed above. This aspect is explored in the next chapter.

4.12 Summary and conclusion

In this chapter the numerical method used to solve the 2D time-dependent TPE in an asymmetric heliospheric geometry was given and discussed. This model includes all four major modulation processes and the re-acceleration of GCR particles at the solar wind TS. Thereafter, the modulation of GCR Carbon was investigated using this numerical model with a heliosheath thickness (width) that is asymmetrical in the meridional plane varying from $\sim$ 40 AU to $\sim$ 20 AU, from heliographic pole to pole (Figure 4.2). (Meridional implies north-south directions opposing to east-west directions which is interpreted to be a nose-tail asymmetry.) The effects of this asymmetry on the modulated GCR Carbon spectrum and its radial dependence were studied at 1 AU, 60 AU and 100 AU and at polar angles of $\theta = 55^o$ and $\theta = 125^o$, corresponding to the trajectories of V1 and V2, respectively. The results were shown at energies of 0.05 GeV/nuc, 0.2 GeV/nuc and 1.0 GeV/nuc for both polarity cycles and for solar minimum and moderate solar maximum conditions. The computations were repeated using two IS's for GCR Carbon, one from *Webber and Higbie* (2009) as the lowest option, and the other one as the highest option from *Moskalenko et al.* (2002).

Using the higher IS at the HP, it was found that the differences in computed spectra between

$\theta = 55^o$ and $\theta = 125^o$ caused by the assumed asymmetry vary from insignificant at higher energies ($E >\sim$ 1.0 GeV/nuc) to as large as a factor of $\sim$ 2.2 below $\sim$ 100 MeV/nuc in the heliosheath during the A > 0 cycle, whereas during the A < 0 cycle the factor difference can be as large as $\sim$ 4.0 at this energy. For the lower IS, a difference of a factor of $\sim$ 1.4 was found for the A > 0 cycle and $\sim$ 2.0 in the A < 0 cycle, with $E <\sim$ 100 MeV/nuc in the heliosheath. In the inner heliosphere ($r <$ 40 AU), the effects are insignificant at all energies. These effects were found to enhance when solar activity is increased from $\alpha = 10^o$ to 50^o.

Based on these modeling results, it is concluded that the significance of the effects of a meridional asymmetry in the width of the heliosheath between $\theta = 55^o$ and $\theta = 125^o$ on GCR Carbon intensities depends on the position of the observer in the heliosphere, the particle energy, the location of the HP and the assumed IS. Increasing the IS at $E <\sim$ 300 MeV/nuc enhances asymmetric modulation effects for a given polar angle dependence of the width of the heliosheath. The effects on GCR modulation of this type of asymmetry are insignificant in the inner heliosphere but become increasingly important with increasing distance to reach a maximum effect beyond the TS but only for energies below a few-hundred MeV/nuc. Above 1.0 GeV/nuc the effects subside even inside the heliosheath. The computed modulation differences between the two Voyager positions can be enhanced by assuming: (1) A significantly larger meridional asymmetry. (2) A much higher IS at low energies. (3) A non-isotropic IS and (4) modulation conditions that are globally different between the northern and southern regions of the heliosphere.

Chapter 5

Inherent north-south asymmetric modulation conditions

5.1 Introduction

The cause(s) of the asymmetrical heliospheric modulation of GCRs as observed by V1 and V2 in the heliosheath (e.g., *Webber et al.*, 2009; *Caballero-Lopez et al.*, 2010; *Manuel et al.*, 2011a) is not well established or understood. It is, however, established that GCRs are modulated in anti-phase with solar activity and that this strong anti-correlation seems to exist well into the heliosheath (*Webber et al.*, 2011).

It was shown in the previous chapters that the numerical modeling of GCR modulation in the heliosphere depends on assumptions about the elements of the diffusion tensor, the IS and heliospheric geometry in addition to the solar wind and the HMF. The diffusion coefficients are basically determined by the turbulence properties of the expanding solar wind and the imbedded HMF. Up to now, particularly in numerical modeling, it has simply been assumed that the turbulence and the consequent modulation conditions are symmetrical away from the heliospheric equatorial plane. However, this is not necessarily the case, especially not in the heliosheath. For a review on turbulence theory applicable to the heliosphere, see *Engelbrecht* (2013).

The purpose of this chapter is to investigate the inherent asymmetrical modulation conditions that arise when different enhancements for $K_{\perp\theta}$ and $K_{\perp r}$ between the two hemispheres are assumed. It will be illustrated how differently these assumptions as implemented in the model effect the modulation of GCR Carbon between polar angles of $\theta = 55^o$ (approximating the V1 direction) and $\theta = 125^o$ (approximating the V2 direction). This is done with a simulated heliosphere that already contains a north-south (meridional) asymmetrical geometry as described in Chapter 4. The modeling presented here is done for the two HMF polarity cycles (A < 0 and A> 0), and assuming solar activity increasing from solar minimum conditions, with HCS tilt angle of $\alpha = 10^o$, to moderate solar maximum activity represented by a tilt angle of $\alpha = 50^o$.

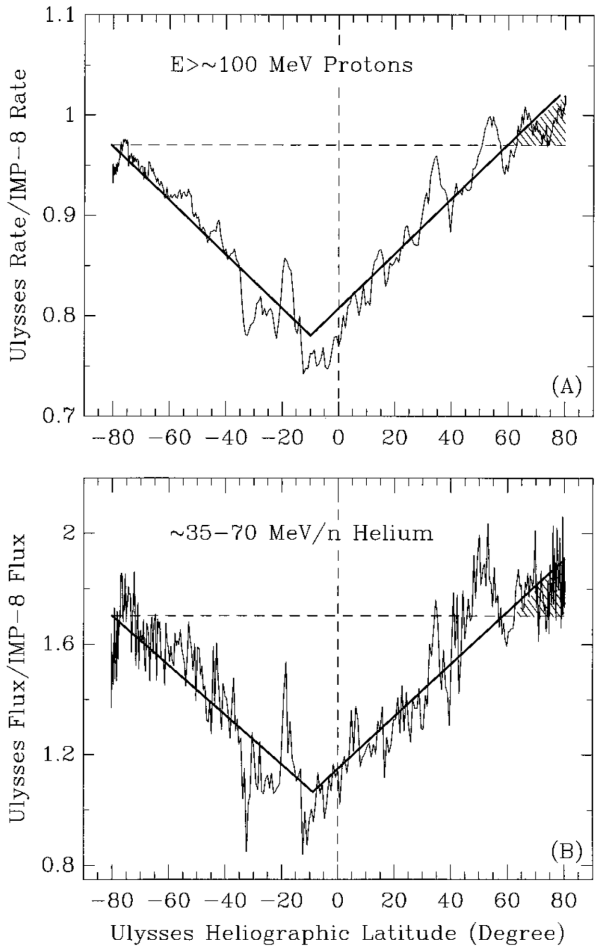

Figure 5.1: Daily average Ulysses/IMP 8 flux ratio of $E >\sim 100$ MeV galactic protons (a) and $\sim 35-70$ MeV/nuc anomalous Helium (b) as functions of Ulysses heliographic latitude in degrees. The straight lines are least-square fits to the flux ratio in the southern and northern hemispheres. The shaded area indicates an average flux excess in the north pole above the south pole flux. Adapted from *Simpson et al.* (1996).

The content of this chapter was published by *Ngobeni and Potgieter* (2012).

5.2 Evidence of inherent north-south asymmetric modulation conditions

The existence of inherent asymmetrical modulation conditions can also be related to the global structuring of the HMF. Ulysses observations of the HMF in the polar regions of the inner heliosphere indicated that it was stronger in the southern hemisphere than in the northern hemisphere (*Forsyth et al.*, 1996; *Smith et al.*, 2000; *Erdos and Balogh*, 2010). This north-south asymmetry was also clearly evident from cosmic ray observations by Ulysses (*Heber and Potgieter*, 2006; *Simpson et al.*, 1996), see also the discussion of this effect by *Potgieter* (2011). Figure 5.1 shows the daily average Ulysses/IMP 8 flux ratios of $E >\sim 100$ MeV galactic protons (a)

and $\sim 35 - 70$ MeV/nuc anomalous Helium (b) as functions of Ulysses heliographic latitude taken from *Simpson et al.* (1996). It is evident from this figure that higher intensities for both galactic proton and anomalous Helium in the inner heliosphere were observed in the northern hemisphere corresponding to the weaker HMF. In the outer heliosphere, *Manuel et al.* (2011a) have recently found that V1 and V2 GCR observations cannot be fitted with an identical set of transport parameters. This suggests also the existence of a possible inherent asymmetric modulation conditions in the outer heliosphere.

From MHD modeling point of view, the existence of an asymmetry in the magnetic structure between the northern and the southern hemispheres of the heliosheath was pointed out by *Opher et al.* (2011). The northern part of the hemisphere was found to be a region with more magnetic islands or holes. As a result diffusion of charged particles could be different in the two hemispheres. The geometrical alignment of the HMF and the ISMF at the HP only on one side of the heliosphere could easily enhance this asymmetry (e.g., *Opher et al.*, 2009; *Pogorelov et al.*, 2009; *Strauss et al.*, 2013a).

Changing solar activity, as the important driver of the heliospheric modulation of GCRs, exhibits also a north-south asymmetry (e.g., *Li et al.*, 2009; *Obridko et al.*, 2014). It is therefore possible that quite different levels of turbulence may occur between the northern and southern heliospheric hemispheres (e.g., *Efimov et al.*, 2008) thus causing what is referred to in this chapter as inherent asymmetric modulation conditions, in addition to the modulation effects of an asymmetrically structured heliosphere.

Since the HMF affects both particle drifts and diffusion, one is inclined to conclude that different modulation conditions of GCRs should exist between the north and south hemispheres.

5.3 The enhancement of perpendicular diffusion revisited

The following spatial dependences of $K_{\perp\theta}$ and $K_{\perp r}$, given by Equations 3.23 and 3.24, are extracted from *Burger et al.* (2000):

$$K_{\perp r} \propto K_{||} \frac{\delta B^2}{B_m^2}, \tag{5.1}$$

and

$$K_{\perp\theta} \propto F(\theta) K_{||} \frac{\delta B^2}{B_m^2}. \tag{5.2}$$

Note from Equation 5.1 that no explicit latitudinal dependence of $K_{\perp r}$ is assumed. However, it is evident that any change in the magnitudes of δB and B_m in Equations 5.1 and 5.2 between the north and the south hemispheres results in different values between the two hemispheres

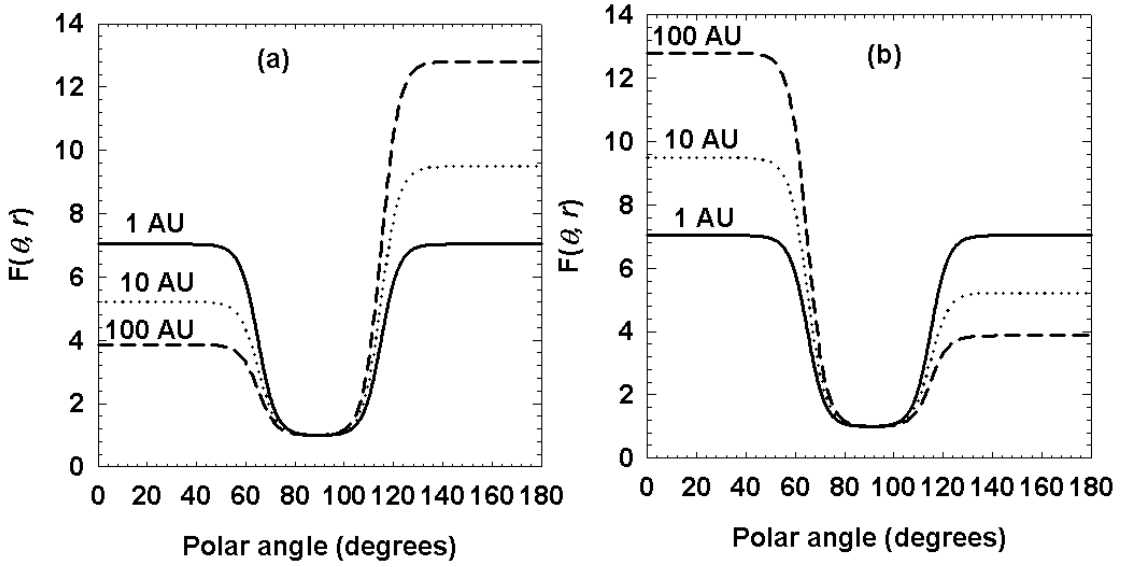

Figure 5.2: Enhancement of $K_{\perp\theta}$ described by the function $F(\theta, r)$ with respect to its value in the equatorial plane as a function of polar angle θ at different radial distances. In panel (a) it decreases with radial distance in the northern hemisphere while increasing in the southern hemisphere; in panel (b) it increases in the northern hemisphere but decreases in the southern hemisphere.

for both $K_{\perp\theta}$ and $K_{\perp r}$. In a modified HMF, while retaining the well-known expressions for the diffusion coefficients in spherical coordinates, an alternative would be to represent differences in $\dfrac{\delta B^2}{B_m^2}$ between the two hemispheres by spatial adjustments in $F(\theta)$. This allows for a study of latitudinal effects associated with the solar wind turbulence also in the outer heliosphere. The adjustment is accomplished with a more complicated spatial dependence,

$$F(\theta, r) = \left(\frac{d+1}{2}\right) \mp \left(\frac{d-1}{2}\right) \tanh\left[\frac{1}{\Delta\theta}(\theta - 90^o + \theta_F)\right], \tag{5.3}$$

with $\Delta\theta = \dfrac{1}{8}$ and $\theta_F = 25^o$. While for d the following radial dependences are studied: $d = 7.1r^{\mp 0.13}$ and $d = 7.1r^{\pm 0.13}$. Hence the difference between $F(\theta)$, given by Equation 3.25, and $F(\theta, r)$ is that d in $F(\theta)$ has a constant value of ~ 7. In all cases the upper signs are valid for $\theta \leq 90^o$ and lower signs for $\theta > 90^o$. The function $F(\theta, r)$ thus enhances $K_{\perp\theta}$ with respect to its value in the equatorial plane ($\theta = 90^o$) as a function of radial distance and polar angle as shown in Figure 5.2: in panel (a), $F(\theta, r)$ decreases from a factor of ~ 7 at 1 AU in the northern hemisphere to ~ 4 at 100 AU. In the southern hemisphere, it increases from ~ 7 at 1 AU to $\sim$ 13 at 100 AU. Panel (b) shows the opposite of panel (a), with the $F(\theta, r)$ increasing in the north and decreasing in the south hemisphere by similar values. For $K_{\perp r}$ the latitudinal dependence similar to that of $K_{\perp\theta}$ is assumed but the enhancement off the equatorial plane is a factor of 3.0 smaller than for $K_{\perp\theta}$. Both $K_{\perp\theta}$ and $K_{\perp r}$ are thus enhanced towards the poles with respect to their values in the equatorial plane but $K_{\perp\theta}$ by a factor 3.0 more than $K_{\perp r}$. This is done

to maintain congruence with Ulysses observations that the variance in the normal direction is more than in the radial direction over the solar poles (*Kóta and Jokipii*, 1995). In the equatorial plane, $K_{\perp\theta}$ and $K_{\perp r}$ remain equal as in previous modulation studies (*Ferreira et al.*, 2001b; *Langner et al.*, 2003; *Ngobeni and Potgieter*, 2011). The role of the latitude dependence of both $K_{\perp\theta}$ and $K_{\perp r}$ as represented in Figure 5.2 is the focus of this chapter and it is referred to as the north-south inherent asymmetric modulation conditions.

In what follows, the computed intensities of GCR Carbon with $\theta = 55^o$ obtained with the enhancement of $K_{\perp\theta}$ and $K_{\perp r}$ as in panels (a) and (b) of Figure 5.2 are compared to those with $\theta = 125^o$. This is done for the two drift cycles during both solar minimum and moderate solar maximum modulation conditions. What is shown below, from a modeling point of view, is the extent of the modulation differences of GCR Carbon between polar angles of $\theta = 55^o$ and $\theta = 125^o$ that can arise when the inherent asymmetry in modulation condition is combined with the heliosheath thickness that has a significant dependence on heliolatitude. The IS of *Webber and Higbie* (2009) is specified at the asymmetric HP.

5.3.1 Asymmetric modulation between Voyager 1 and Voyager 2 due to asymmetric enhancement of $K_{\perp\theta}$

5.3.1.1 Effects on GCR Carbon spectra

In Figure 5.3 the computed spectra of GCR Carbon as a function of kinetic energy/nuc at $\theta = 55^o$ (red lines) at radial distances of 1 AU, 60 AU and 100 AU are shown and compared to those at $\theta = 125^o$ (black lines). This is done for the enhancements of $K_{\perp\theta}$ as in panels (a) and (b) of Figure 5.2 and for the two drift cycles during solar minimum modulation conditions. The effects of the assumed asymmetric enhancement of $K_{\perp\theta}$ over the poles on differences between GCR Carbon modulation obtained at the Voyager latitudes are of interest. It can be seen from this figure that the differences between the two polar angles clearly become significant at lower energies and more so at a radial distance of 100 AU. At 1 AU the effects on the modulation of GCR Carbon subside completely at all energies for both drift cycles. What is interesting in this figure is that at a radial distance of 60 AU in the $A > 0$ cycle, intensities obtained at $\theta = 55^o$ are slightly larger than those at $\theta = 125^o$ at all energies when the enhancement of $K_{\perp\theta}$ increases towards the poles as in panel (b) of Figure 5.2. This is a clear manifestation of an intricate interplay that can exist between inherent asymmetric modulation conditions as represented by Figure 5.2 and the assumed north-south asymmetry in the geometry of the heliosphere as represented by Figure 4.2. For this case it seems that when the enhancement of $K_{\perp\theta}$ increases towards the poles as in panel (b) the consequent inherent asymmetric modulation is strong enough to even off-set the geometrical asymmetry at 60 AU, but only in the $A > 0$ magnetic cycle.

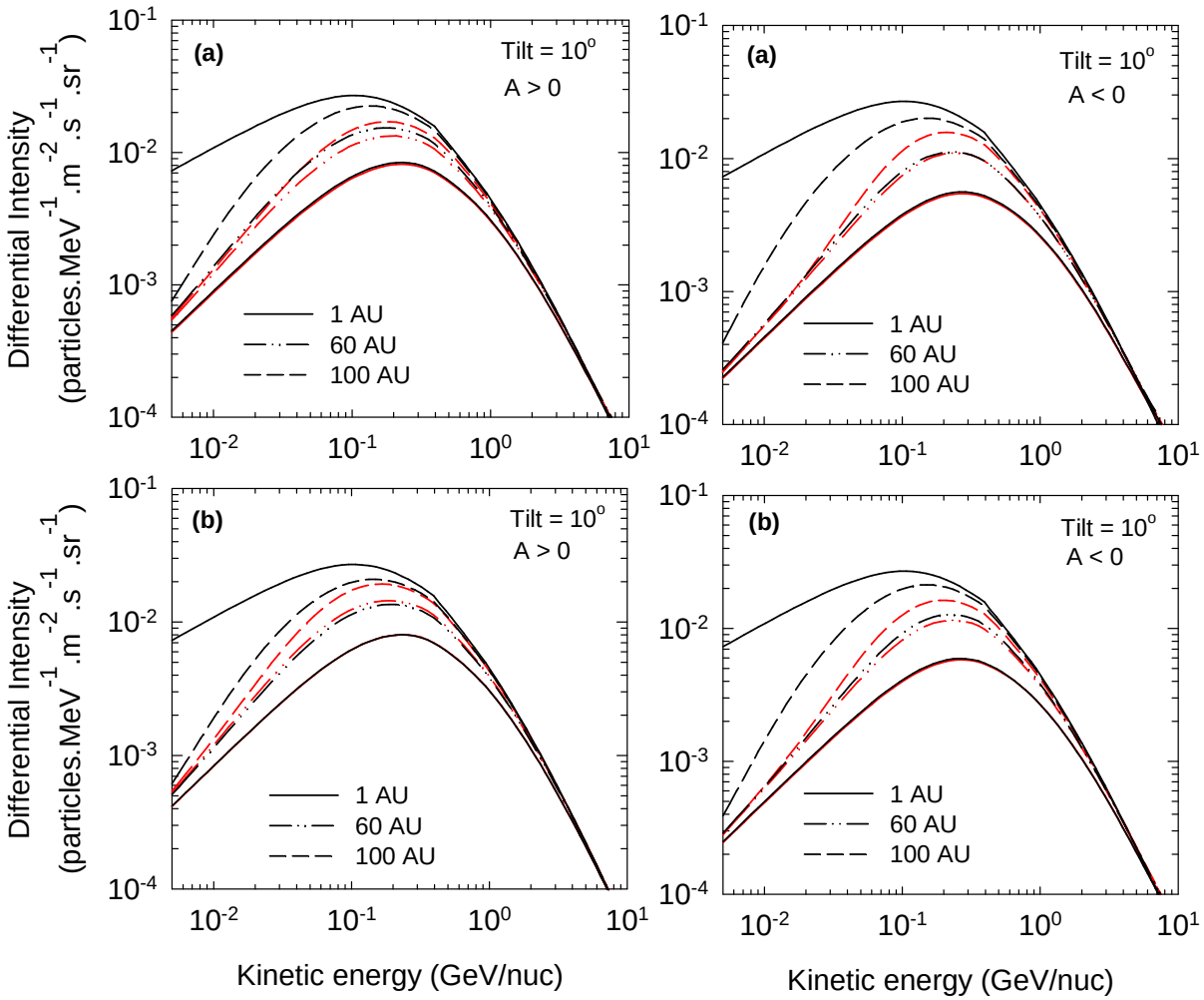

Figure 5.3: Computed differential intensities for GCR Carbon as a function of kinetic energy/nuc at radial distances of 1 AU, 60 AU and 100 AU for both polarity cycles (left panels for A $>$ 0, right panels for A $<$ 0) during solar minimum conditions ($\alpha = 10^o$). Top row represents solutions obtained with the enhancement of $K_{\perp\theta}$ increasing towards the poles as in panel (a) of Figure 5.2; bottom row with the enhancement as in panel (b) of Figure 5.2. For both rows $K_{\perp r}$ is assumed to be independent of latitude. Black lines represent solutions at $\theta = 125^o$ (with $r_{HP} = 109$ AU and $r_{TS} = 86$ AU) and red lines at $\theta = 55^o$ (with $r_{HP} = 131$ AU and $r_{TS} = 94$ AU).

Figure 5.4 shows the computed spectra at $\theta = 55^o$ and $\theta = 125^o$ at radial distances of 1 AU, 60 AU and 100 AU similar to Figure 5.3 but now for moderate solar maximum conditions. As noted before, the differences in spectra are larger at lower energies but now are even enhanced. Also that at 60 AU in the $A > 0$ cycle, the spectrum obtained at $\theta = 55^o$ is clearly larger than that at $\theta = 125^o$ at all energies when the enhancement of $K_{\perp\theta}$ increases towards the poles as in panel (b) of Figure 5.2. This effect is now clearly present for moderate solar maximum conditions and depends on the drift direction. At 100 AU, still in the same panel, the differences in spectra between the two polar angles are now reduced when compared to that obtained for solar minimum conditions.

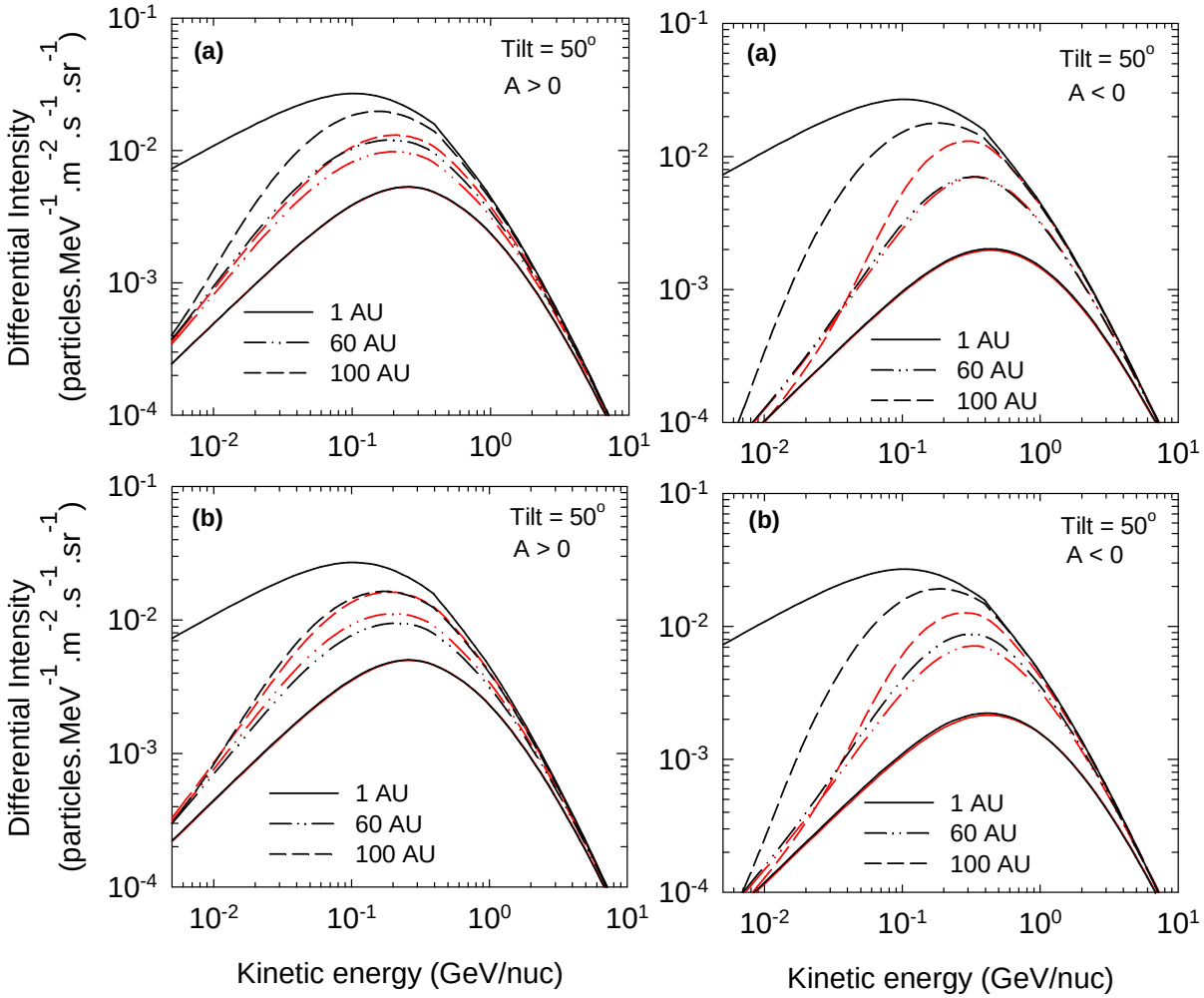

Figure 5.4: Similar to Figure 5.3 but for moderate solar maximum conditions ($\alpha = 50^o$).

5.3.1.2 Effects on GCR Carbon radial intensities

In Figure 5.5 the computed differential intensities for GCR Carbon as a function of radial distance r at kinetic energies of $E = 0.05$ GeV/nuc, 0.2 GeV/nuc and 1.0 GeV/nuc for both polarity cycles are shown with $\theta = 55^o$ (red lines) compared to those at $\theta = 125^o$ (black lines), during solar minimum. The top row shows the intensities computed with the enhancement of $K_{\perp\theta}$ as depicted in panel (a) of Figure 5.2, decreasing with r towards the direction of a wider heliosheath thickness (V1 direction) while increasing towards a narrower heliosheath thickness (V2 direction). (Take note that the assumed heliosheath is wider for $0^o < \theta < 90^o$ and narrower for $90^o \leq \theta < 180^o$.) The bottom row shows intensities computed with the enhancement of $K_{\perp\theta}$ increasing towards a wider heliosheath and decreasing towards a narrower heliosheath as in panel (b) in Figure 5.2. Essentially, Figure 5.5 shows the combined effects of both a geometrical asymmetry and an inherent asymmetry in modulation conditions, as a function of r. As explained before, the inherent asymmetric modulation conditions here are reflected by the enhancement of $K_{\perp\theta}$ off the ecliptic plane that differs from heliographic pole to pole while

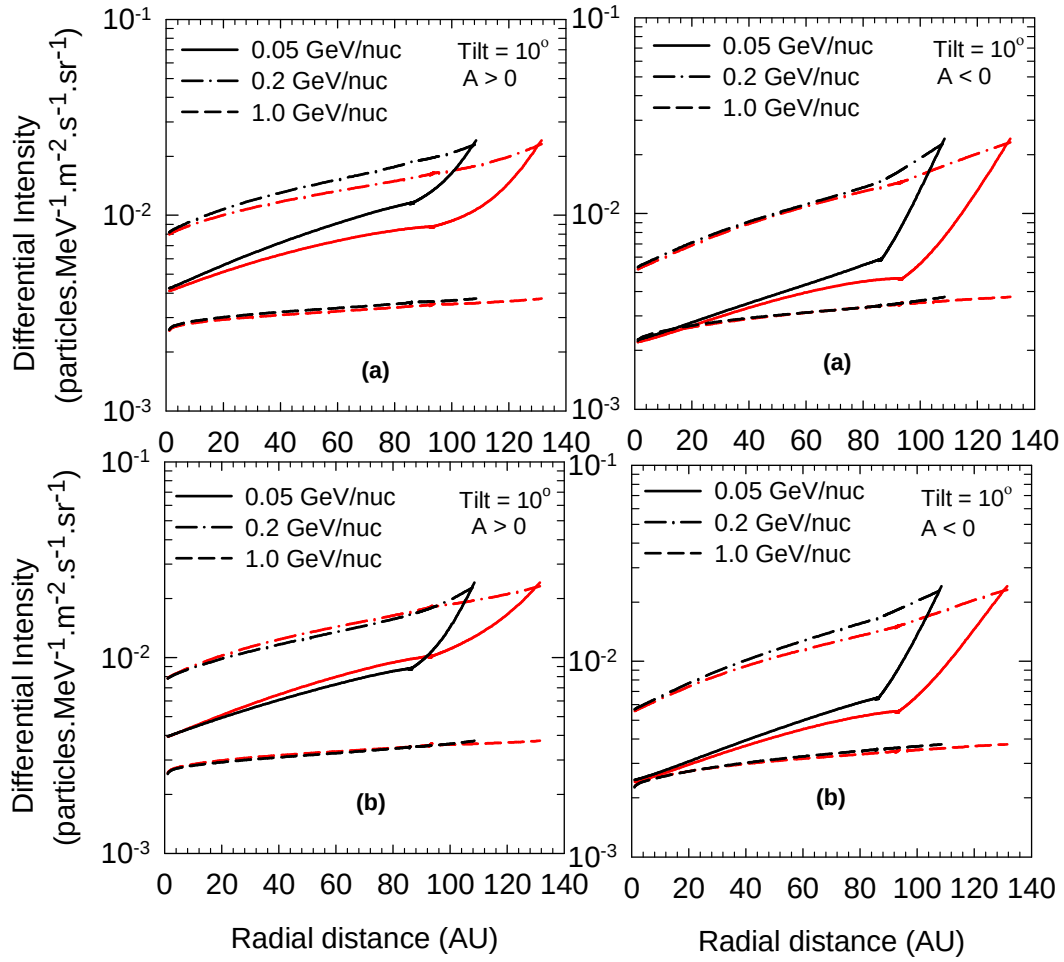

Figure 5.5: Computed differential intensity for GCR Carbon as a function of radial distance at $E = 0.05$ GeV/nuc, 0.2 GeV/nuc and 1.0 GeV/nuc for both polarity cycles (left panel is for $A > 0$ cycle; right panel for $A < 0$ cycle). Top row represents solutions obtained with the enhancement of $K_{\perp\theta}$ increasing towards the poles as in panel (a) of Figure 5.2; bottom row with the enhancement as in panel (b) of Figure 5.2. For both rows $K_{\perp r}$ is assumed to be independent of latitude. Black lines represent solutions at $\theta = 125^o$ ($r_{HP} = 109$ AU and $r_{TS} = 86$ AU) and red lines at $\theta = 55^o$ ($r_{HP} = 131$ AU and $r_{TS} = 94$ AU).

$K_{\perp r}$ remains latitude independent. It is noted that the effect of decreasing the enhancement of $K_{\perp\theta}$ towards the direction of a wider heliosheath thickness while simultaneously increasing it towards a narrower heliosheath thickness is to significantly enlarge the difference in the radial profiles between $\theta = 55^o$ and $\theta = 125^o$ in the $A > 0$ cycle throughout the heliosphere. While in the $A < 0$ cycle, the assumed inherent asymmetrical modulation decreases the difference modestly so that at 0.2 GeV/nuc the difference can only be noted in the heliosheath. This indicates that during this cycle and inside off the TS, the geometrically caused effects and the assumed asymmetric modulation effects are competing, with the geometric effects remaining dominant only at $E < 0.2$ GeV/nuc and in the heliosheath. However, when the enhancement of $K_{\perp\theta}$ increases as a function of r towards the direction of a wider heliosheath thickness but decreases towards the direction of a narrower heliosheath thickness, the GCR Carbon inten-

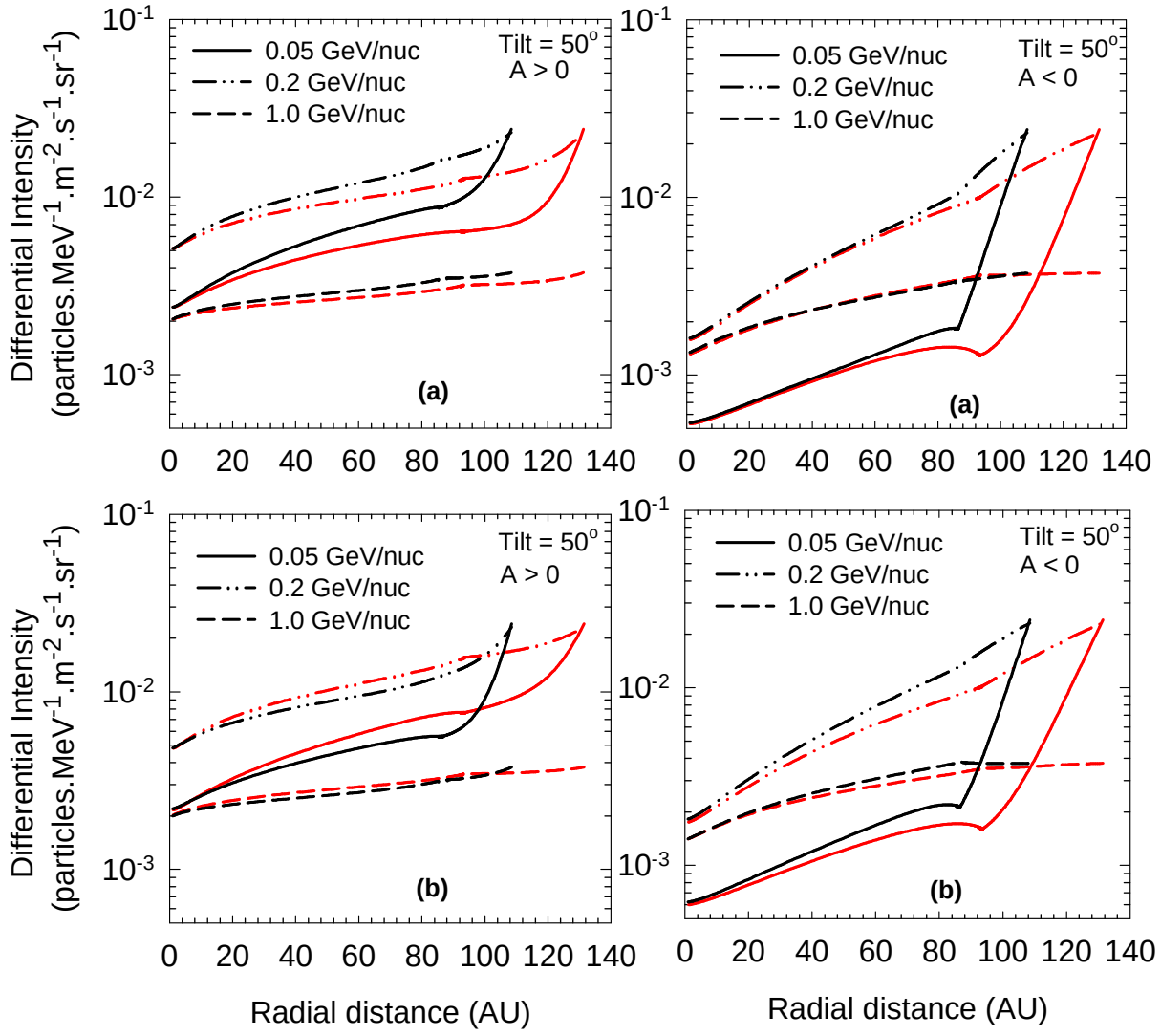

Figure 5.6: Similar to Figure 5.5 but for moderate solar maximum conditions ($\alpha = 50^o$).

sities at $\theta = 55^o$ are slightly larger than at $\theta = 125^o$ in the $A > 0$ cycle but only inside off the TS. This is quite interesting since both the TS and HP positions are ~ 8 AU and ~ 22 AU respectively closer to the Sun at 125^o, but not too surprising since geometric effects are wiped out by solar modulation inside off the TS. Therefore, in the $A > 0$ cycle the assumed inherent asymmetrical modulation effects off-set geometrical asymmetric effects completely inside off the TS. In the heliosheath the effects of the assumed asymmetry in the geometry of the heliospheric boundary remains dominant. In the $A < 0$ cycle, GCR Carbon intensity differences between the two polar directions slightly increase. The overall modulation feature in Figure 5.5 is that in the $A > 0$ cycle differences in intensities between $\theta = 55^o$ and $\theta = 125^o$ inside off the TS respond more significantly to the different values of the enhancement of $K_{\perp\theta}$ (inherent asymmetric modulation) than in the opposite drift cycle.

Figure 5.6 shows the computed radial intensities at $\theta = 55^o$ and $\theta = 125^o$ at energies of 0.05

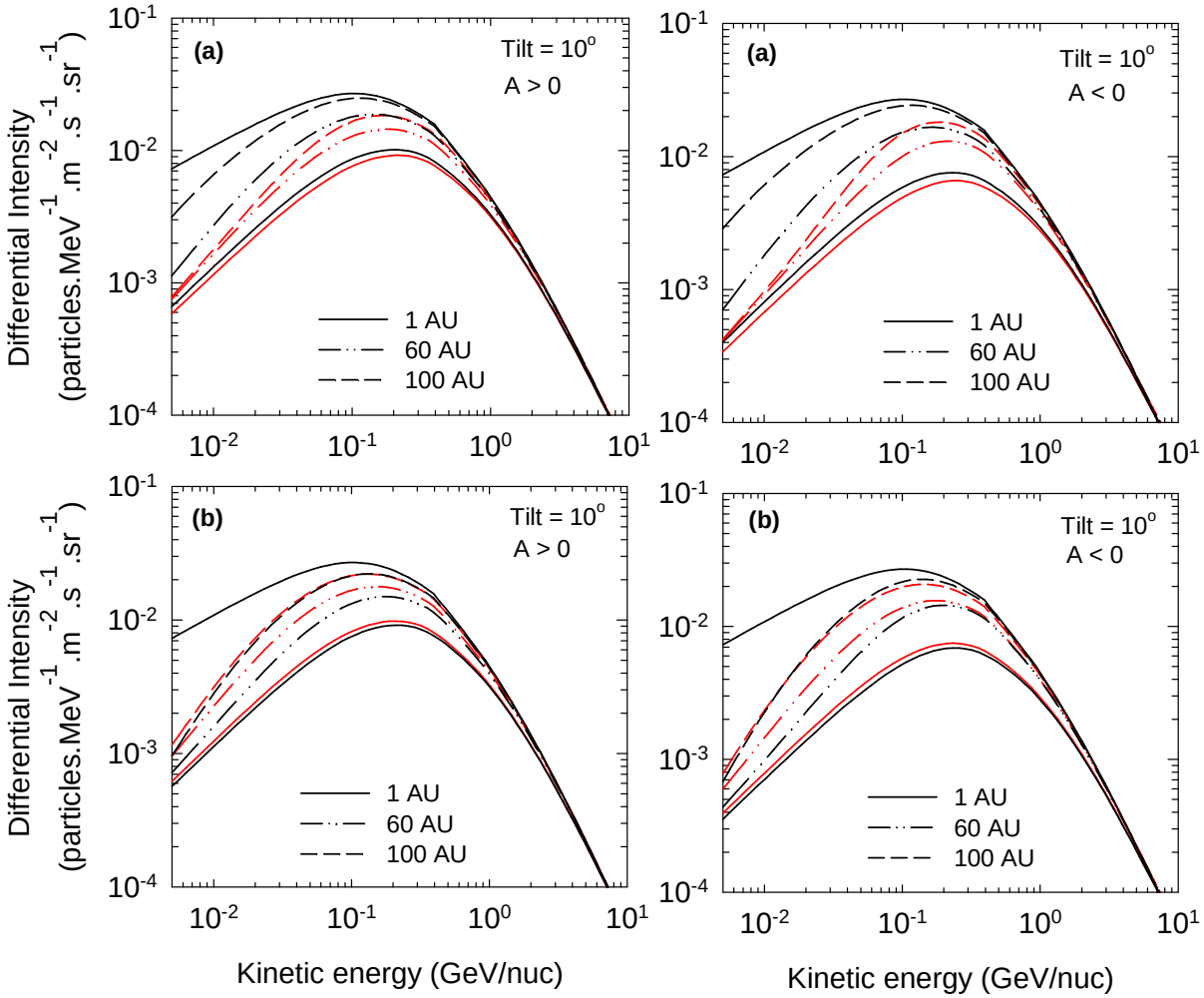

Figure 5.7: Similar to Figure 5.3, top row with both $K_{\perp\theta}$ and $K_{\perp r}$ increased towards the poles as in panel (a) in Figure 5.2; bottom row with both $K_{\perp\theta}$ and $K_{\perp r}$ increased towards the poles as in panel (b) in Figure 5.2. In both rows $K_{\perp\theta} = 3K_{\perp r}$ over the poles.

GeV/nuc, 0.2 GeV/nuc and 1.0 GeV/nuc similar to Figure 5.5 but now for moderate solar maximum conditions. Compared to Figure 5.5, the effects of inherent asymmetric modulation conditions as reflected by the enhancement of $K_{\perp\theta}$ towards the poles are now enhanced in both polarity cycles and differences in intensities between the two polar angles become noticeable at high energies in contrast to solar minimum conditions. Therefore the effects of the assumed asymmetric modulation become stronger with increasing solar activity.

5.3.2 Asymmetric modulation between Voyager 1 and Voyager 2 due to the combined asymmetric enhancement of $K_{\perp\theta}$ and $K_{\perp r}$

5.3.2.1 Effects on GCR Carbon spectra

Figure 5.7 is similar to Figure 5.3 but now the enhancement of both $K_{\perp\theta}$ and $K_{\perp r}$ is assumed. The top row depicts solutions obtained with both $K_{\perp\theta}$ and $K_{\perp r}$ increased towards the poles

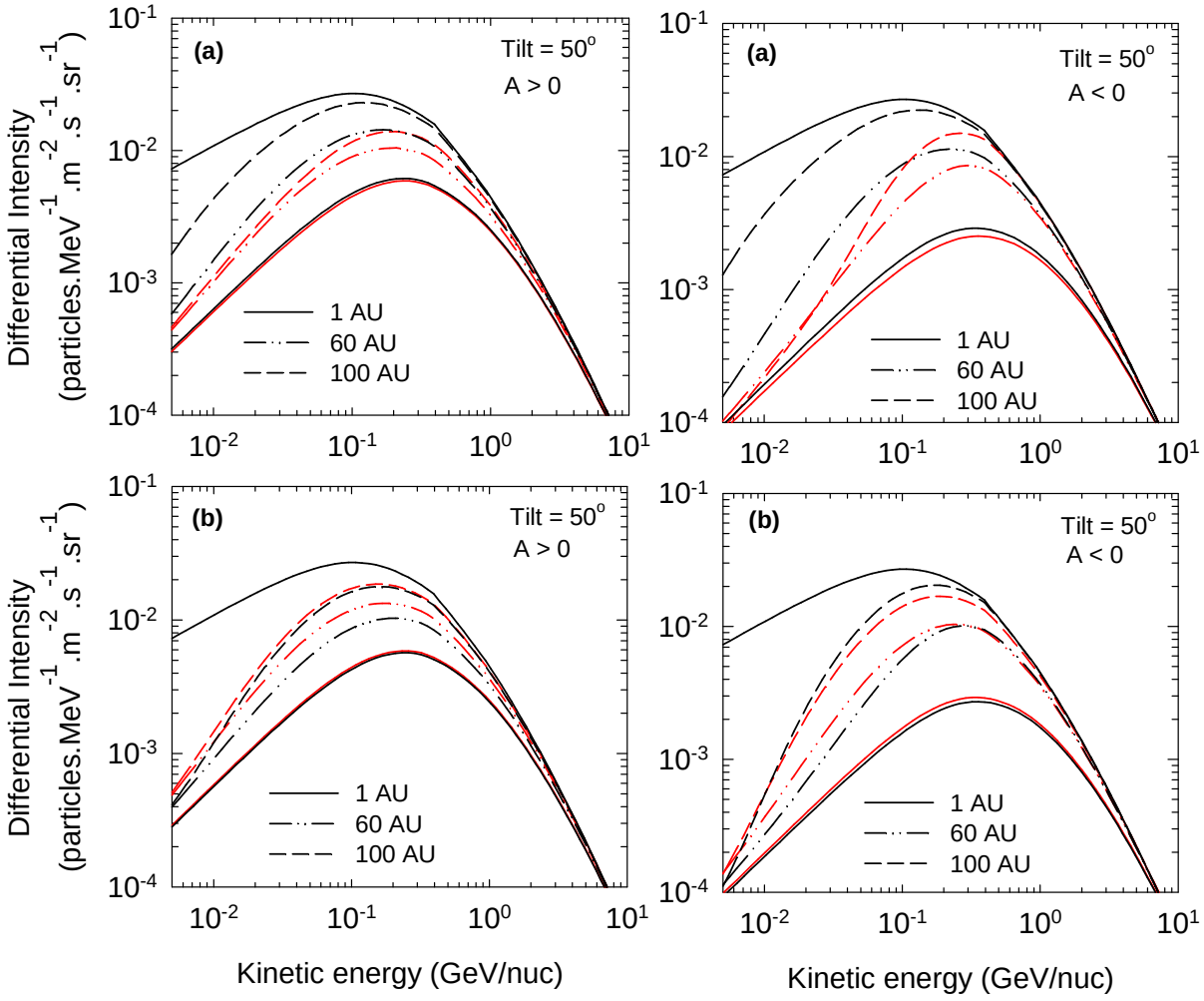

Figure 5.8: Similar to Figure 5.7 but for moderate solar maximum conditions ($\alpha = 50^0$).

as in panel (a) in Figure 5.2, while the bottom row is for solutions obtained with both $K_{\perp\theta}$ and $K_{\perp r}$ increased towards the poles as in panel (b) in Figure 5.2. Note that the enhancement of $K_{\perp r}$ over the poles is a factor 3 smaller than that of $K_{\perp\theta}$, as explained in section 5.3 above. While in the equatorial region $K_{\perp\theta} = K_{\perp r}$ is still the case. It can be noted from the top row that when compared to Figure 5.3, the differences are now very large at all radial distances including 1 AU and can also be clearly noted at higher energies in both polarity cycles. While in the bottom row large differences are only noted at 1 AU and 60 AU in both drift cycles. At 100 AU, still in the bottom row, no differences are noted between the two polar angles above $E > 30$ MeV/nuc for modulation in the $A > 0$ cycle, while in the $A < 0$ cycle the differences between the two solutions disappear below the same energy. The overall modulation picture in Figure 5.7 is that the top row illustrates that the combined effects on GCR Carbon spectra of geometrical asymmetry and inherent asymmetry in modulation conditions are reinforced for both polarity cycles. While in the bottom row, inherent asymmetric modulation effects cancel completely geometric asymmetric effects at all radial distances for modulation in the $A > 0$ cycle; in the $A < 0$ cycle this aspect is noticed at radial distances of 1 AU and 60 AU at all

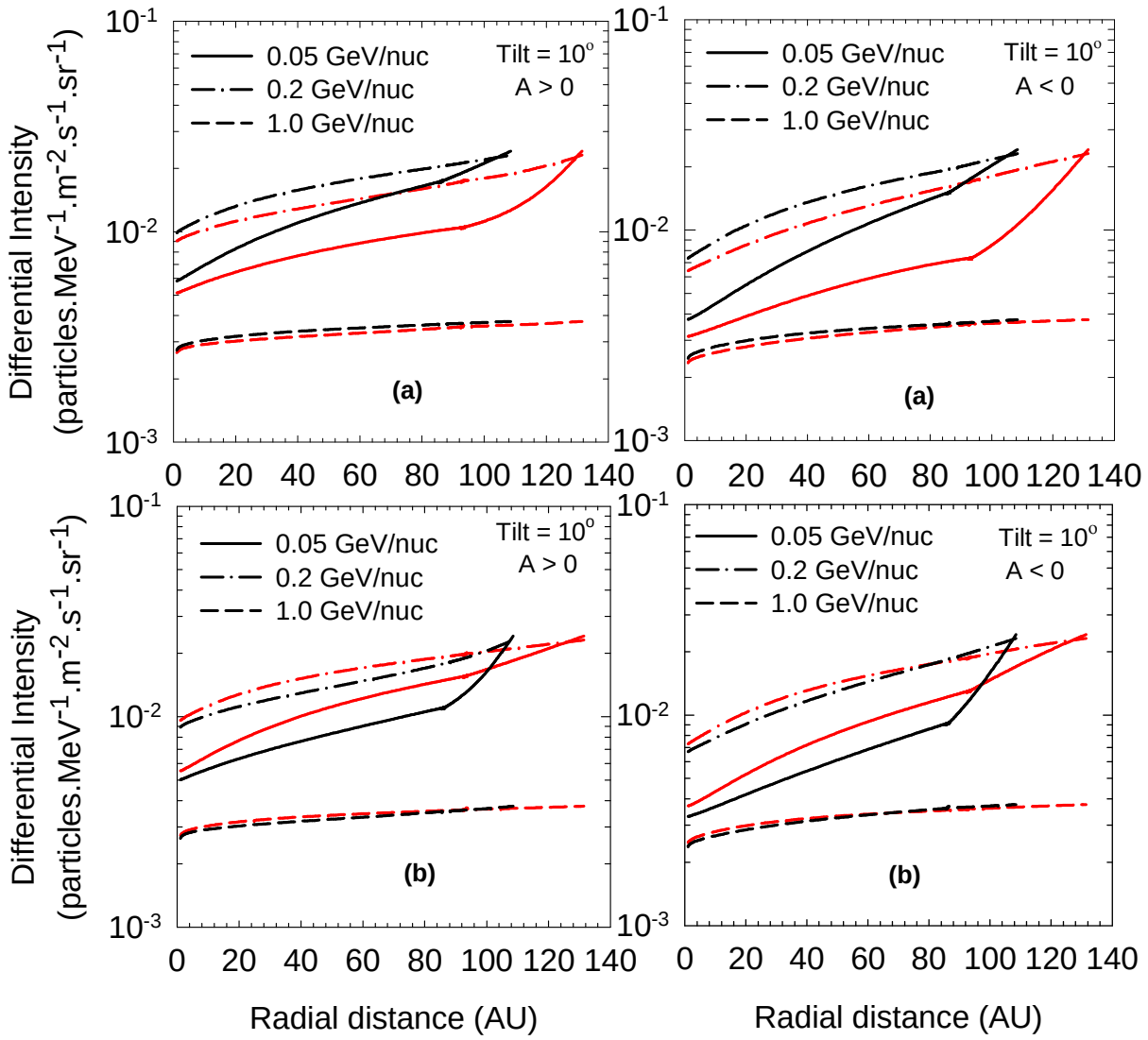

Figure 5.9: Similar to Figure 5.5, top row with both $K_{\perp\theta}$ and $K_{\perp r}$ increased towards the poles as in panel (a) in Figure 5.2; bottom row with both $K_{\perp\theta}$ and $K_{\perp r}$ increased towards the poles as in panel (b) in Figure 5.2. In both rows $K_{\perp\theta} = 3K_{\perp r}$ over the poles.

energies but only below ~ 20 MeV/nuc at 100 AU.

Figure 5.8 is similar to Figure 5.7 but now differences in GCR Carbon spectra between $\theta = 55^o$ and $\theta = 125^o$ are shown for modulation during increasing solar activity as represented by $\alpha = 50^o$. The modulational features discussed in Figure 5.7 are clearly present for moderate solar maximum conditions but more enhanced.

5.3.2.2 Effects on GCR Carbon radial intensities

The top row of Figure 5.9 is similar to what is shown in Figure 5.5 but now with the enhancement of both $K_{\perp\theta}$ and $K_{\perp r}$ decreasing as a function of r towards the direction of a wider heliosheath thickness but increasing towards a narrower heliosheath thickness as in panel (a) of

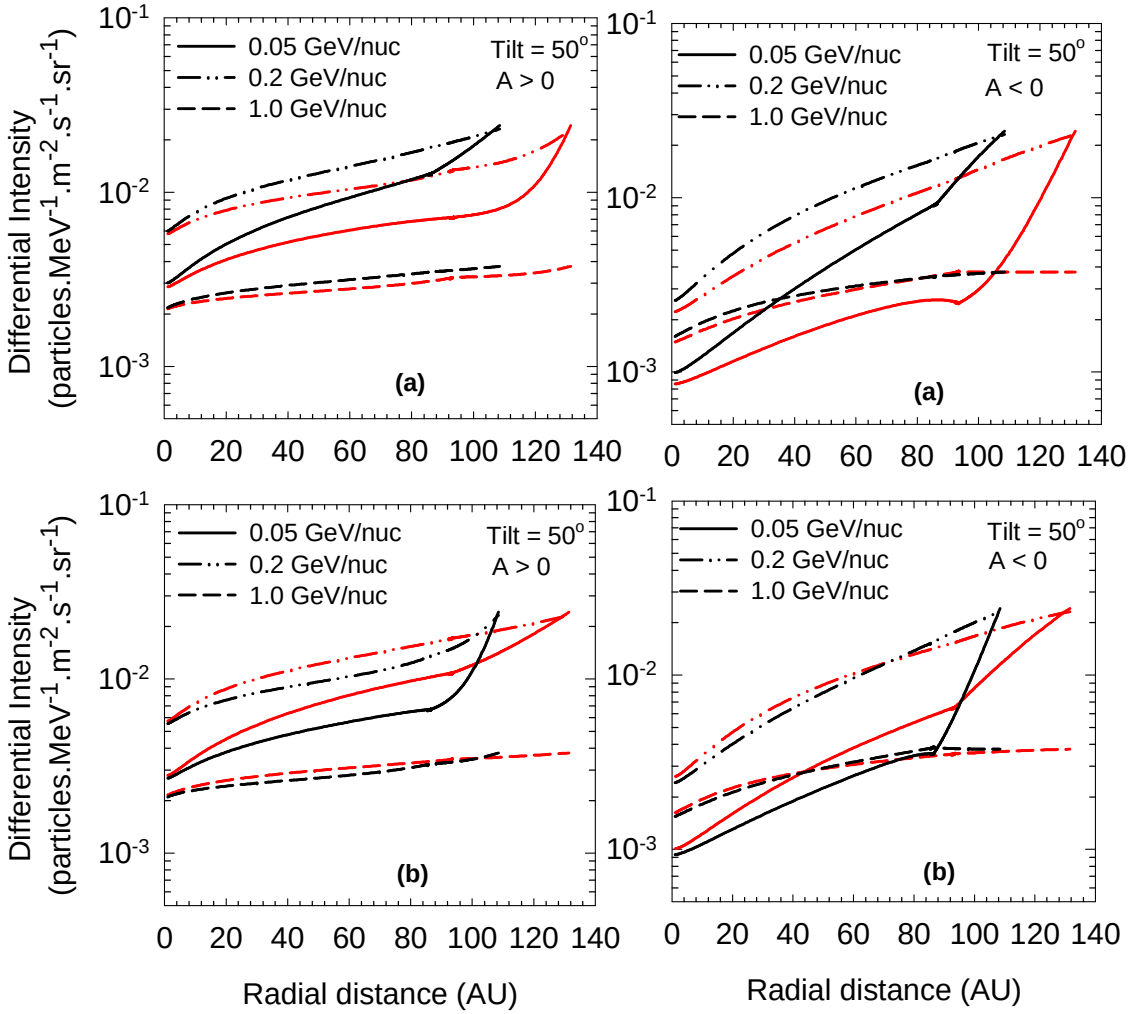

Figure 5.10: Similar to Figure 5.9 but for moderate solar maximum conditions ($\alpha = 50^0$).

Figure 5.2. The bottom row shows intensities obtained with the enhancement of both $K_{\perp\theta}$ and $K_{\perp r}$ increasing towards a wider heliosheath but decreasing towards a narrower heliosheath as in panel (b) of Figure 5.2. From the top row of Figure 5.9 follows that the differences for solar minimum conditions in the GCR Carbon intensities between the two polar angles are very large in both polarity cycles, even inside the TS and become also more noticeable at higher energies. In the bottom row the differences are less evident at higher energies. There is however a noteworthy large difference in the corresponding radial gradients at $E = 0.05$ GeV/nuc in the heliosheath between the two polar angles. For both drift cycles small radial gradients are obtained in the direction of increased latitudinal transport while large radial gradients are obtained in the direction of reduced latitudinal transport of GCRs in the heliosheath. This suggests that if the solar wind turbulence at and beyond the TS have a large latitudinal dependence, V1 and V2 will observe different radial gradients of GCR Carbon towards the asymmetric boundary. Therefore the latitudinal dependence of both perpendicular diffusion coefficients

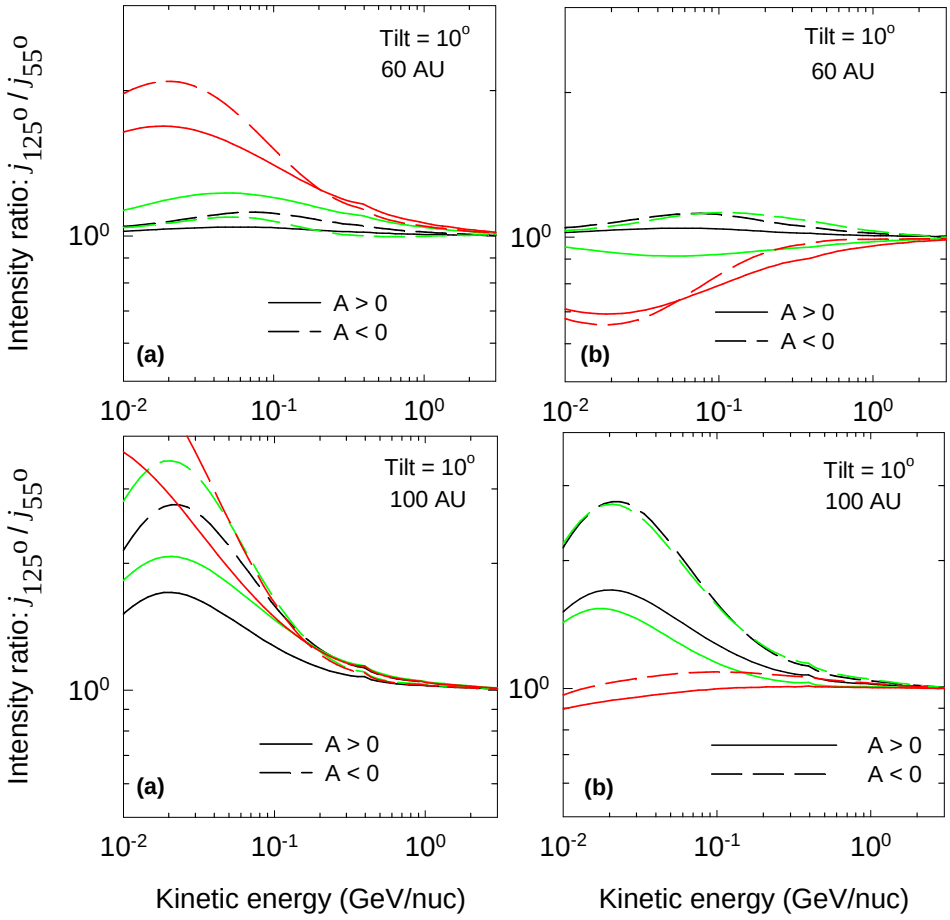

Figure 5.11: Computed intensity ratios (j_{125^o}/j_{55^o}) for GCR Carbon as a function of kinetic energy/nuc at radial distances of 60 AU (top row) and 100 AU (bottom row) for both polarity cycles (solid lines for $A > 0$, dashed lines for $A < 0$) during solar minimum conditions. Three sets of ratios are shown, first with only geometric asymmetry assumed (black lines), second with only the enhancement of $K_{\perp\theta}$ (green lines) as in Figure 5.2 and finally with the enhancement of both $K_{\perp\theta}$ and $K_{\perp r}$ (red lines) as in Figure 5.2. In the left panels both $K_{\perp\theta}$ and $K_{\perp r}$ are increased towards the poles as in panel (a) in Figure 5.2; right panels with both $K_{\perp\theta}$ and $K_{\perp r}$ increased towards the poles as in panel (b) in Figure 5.2.

combined with the asymmetric geometry of the heliosphere as illustrated in this chapter may be important for the understanding of modulation in the heliosheath between the two Voyager directions.

In Figure 5.10 the depicted computed radial intensities of GCR Carbon are similar to Figure 5.9 but this time with moderate solar maximum conditions assumed. As for solar minimum conditions, the differences in the top row are now very large below 1.0 GeV/nuc, even inside off the TS. Such large differences inside off the TS should have been observed easily, which seems not to be the case. In the bottom row the differences are modest with similar features as for solar minimum conditions but enhanced. This modeling scenario gives the GCR Carbon intensity in the V2 direction to become equal with the V1 intensities around 100 AU, but then increases sharply well above that of V1.

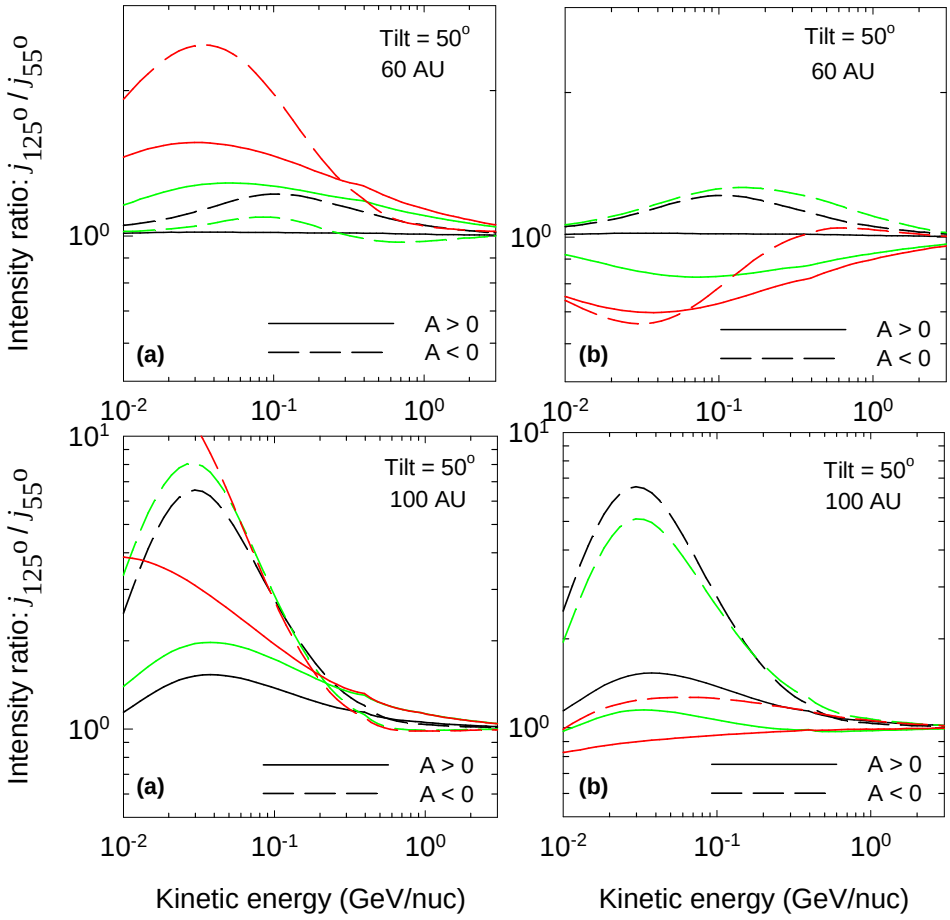

Figure 5.12: Similar to Figure 5.11 but for moderate solar maximum conditions ($\alpha = 50^o$).

5.4 The intensity ratios

Next, the role of the latitude dependence of both $K_{\perp\theta}$ and $K_{\perp r}$ in determining the intensity differences between $\theta = 55^o$ and $\theta = 125^o$ in the heliosphere is further illustrated. This is emphasized by showing in Figure 5.11 the intensity ratios j_{125^o}/j_{55^o} as a function of kinetic energy/nuc at radial distances of 60 AU and 100 AU for both polarity cycles and during solar minimum conditions. Two sets of ratios obtained for the assumed inherent asymmetry in modulation conditions (as indicated in Figure 5.2) are shown, first with only the enhancement of $K_{\perp\theta}$ (green lines) and then with the enhancement of both $K_{\perp\theta}$ and $K_{\perp r}$ (red lines). These ratios are compared to that obtained when only a geometric asymmetry is assumed (black lines, as reference solutions). In all cases the deviation from unity in Figure 5.11 is an indication of the contribution from both geometric asymmetry and inherent asymmetry in modulation condition to the differences in intensities between $\theta = 55^o$ and $\theta = 125^o$.

Note from the left panels in Figure 5.11, obtained with panel (a) in Figure 5.2, that for both polarity cycles the major deviation from unity is obtained when both $K_{\perp\theta}$ and $K_{\perp r}$ have a

significant latitude dependence. For this case, with $E = 0.05$ GeV/nuc, the intensity ratio increases from its maximum value of ~ 1.5 at 60 AU to ~ 2.0 at 100 AU in the A > 0 cycle and from ~ 1.8 to ~ 2.6 in the A < 0 cycle. While for $E < 0.05$ GeV/nuc the ratio increases significantly and becomes larger than 3.0 at 100 AU in the A < 0 cycle. For $E = 0.1$ GeV/nuc the ratio increases modestly from ~ 1.4 at 60 AU to a maximum of ~ 1.5 at 100 AU for both polarity cycles. However, when only $K_{\perp\theta}$ has a significant latitude dependence, the intensity ratios at all energies at 60 AU increase in the A > 0 cycle and decrease in the A < 0 cycle. But again a large increase in the intensity ratios is also noted at 100 AU especially at $E < 0.1$ GeV/nuc in both drift cycles. For all cases in the left panels of this figure the ratio is larger than a unity indicating that intensities at 125^o are larger than at 55^o at all radial distances as discussed above.

In the right panels of Figure 5.11, obtained with panel (b) in Figure 5.2, the major deviation from unity is also obtained when both $K_{\perp\theta}$ and $K_{\perp r}$ have significant latitude dependence similar to the left panels. At $E < 0.2$ GeV/nuc the intensity ratio remains less than unity at 60 AU but increases in the heliosheath and becomes larger than unity at 100 AU in the $A < 0$ cycle. At energies above 0.2 GeV/nuc the ratio becomes approximately unity at 100 AU in the A > 0 cycle. But when only $K_{\perp\theta}$ has a significant latitude dependence, the intensity ratio again changes modestly in the A < 0 cycle at all energies and remain more than unity at radial distance of 60 AU. While in the A > 0 cycle a decrease in intensity ratios below unity are noted at all energies inside the TS at 60 AU but larger values are again noted in the heliosheath at 100 AU.

Figure 5.12 is similar to Figure 5.11 but now the intensity ratios as a function of kinetic energy/nuc between $\theta = 55^o$ and $\theta = 125^o$ are shown for moderate solar maximum conditions. What is shown in the left panels of this figure obtained with panel (a) in Figure 5.2 is that, similar to the left panels of Figure 5.11, major deviation from unity is obtained when both $K_{\perp\theta}$ and $K_{\perp r}$ have a significant latitude dependence. For example, with $E = 0.05$ GeV/nuc, the intensity ratio increases from its maximum value of ~ 2.3 at 60 AU to ~ 7.0 at 100 AU in the A < 0 cycle. For modulation in the $A < 0$ cycle the intensity ratios for this scenario can be larger than a factor of 10 below ~ 40 MeV/nuc. In the right panels, similar features as in Figure 5.11 are also noted but are now clearly larger for moderate maximum conditions.

5.5 Summary and conclusions

The modulation of GCR Carbon was investigated with a modeled heliosheath thickness that has a significant dependence on heliolatitude combined with an enhancement of both $K_{\perp\theta}$ and $K_{\perp r}$ that is different in the two heliospheric hemispheres (in the meridional plane). This was done to establish to what extent increasing the enhancement of both perpendicular dif-

fusion coefficients as a function of radial distance r in one hemisphere while simultaneously decreasing it in the other hemisphere affects the GCR Carbon intensities between $\theta = 55^o$ and $\theta = 125^o$. This was done for both HMF polarity cycles, for solar minimum and for moderate maximum conditions. It was found that:

(1) Differences in intensities between $\theta = 55^o$ and $\theta = 125^o$ in the A > 0 cycle inside off the TS respond more significantly to the assumed inherent asymmetry as reflected by the enhancement of $K_{\perp\theta}$ towards the poles. Decreasing the enhancement of $K_{\perp\theta}$ towards the direction of a wider heliosheath and simultaneously increasing it towards a narrower heliosheath increases differences in the GCR intensities between $\theta = 55^o$ and $\theta = 125^o$. While increasing the enhancement of $K_{\perp\theta}$ towards the direction of a wider heliosheath and decreasing it towards a narrower heliosheath offset the geometric asymmetry completely inside off the TS, but more significantly for modulation in the A > 0 cycle. For increased solar activity these effects persist but become more enhanced.

(2) When $K_{\perp r}$ is also assumed to have a latitude dependence similar to $K_{\perp\theta}$, strong modulation differences between the two polar angles were indeed produced, even inside off the TS for both solar minimum and moderate maximum conditions. Such a scenario is more likely in the heliosheath and can thus be important in explaining modulation differences (apart from a possible time-dependence) between the two Voyager spacecraft.

(3) Significant differences in radial gradients between the two polar angles at lower energies ($E = 0.05$ GeV/nuc) occur in the heliosheath but only when both perpendicular diffusion coefficients have a latitude dependence and increasing in the direction of a wider heliosheath while decreasing in the direction of a narrower heliosheath. This may suggest that the latitude dependence of the solar wind turbulence may be larger in the heliosheath in the V1 direction than in the V2 direction.

It is concluded in this chapter that in addition to the asymmetry in the geometry of the heliosphere it is possible that an asymmetry in modulation conditions between the north and south hemispheres can also exist in the heliosheath. For example, the HMF turbulence could develop differently between the north and south hemispheres.

Chapter 6

The global heliospheric modulation of galactic cosmic ray Carbon

6.1 Introduction

Observations of GCR Carbon in the heliosphere provide a useful tool with which a comprehensive description of the global modulation of GCRs both inside and outside off the solar wind TS can be made. This is, in part, because GCR Carbon is not contaminated by ACRs as is the case for Oxygen, Helium and Protons. However, despite dramatic efforts made (see *Potgieter*, 2000; *Burger et al.*, 2000; *Potgieter and Ferreira*, 2002; *Heber and Potgieter*, 2006; *Potgieter*, 2008), a complete understanding of how GCRs are modulated from the time they enter the heliosphere to a point of observation, e.g. Earth, remains elusive (see also *Strauss et al.*, 2012). This is because a complete understanding of modulation in the heliosphere requires a detailed knowledge of the diffusion tensor, the heliospheric geometries and the HPS. Fortunately the HP location along the V1 direction and also the relevant HPS are fairly well known since 2012 (*Stone et al.*, 2013; *Krimigis et al.*, 2013; *Gurnett et al.*, 2013). The main setback and challenge remains insufficient knowledge about the spatial and rigidity dependence of the diffusion coefficients, especially beyond the Earth.

The availability of good observations of GCR Carbon at the Earth from ACE for the time period 1997-2010 (http://srl.caltech.edu/ACE/ASC/level2; *Webber*, 2006; *Lave et al.*, 2013; *Webber et al.*, 2012) and from the Voyager spacecraft for 1997-2010 (*Webber*, 2006; *Webber et al.*, 2012), when they were inside off the TS and in the heliosheath, together with the new HPS make it possible to evaluate the currently known modulation processes in order to illustrate their contributions, role and importance to modulation of GCRs in the heliosphere. In particular how these processes describe modulation from the Earth to beyond the TS on a global scale.

In this chapter the north-south asymmetrical model, the new HPS of GCR Carbon, the diffusion coefficients given in Chapter 3 and the observations of GCR Carbon from ACE, V1 and

V2 are used to study modulation of GCR Carbon in the heliosphere. First the model is applied to study modulation of GCR Carbon from solar minimum to moderate maximum activity at the Earth. Essentially, a modulation modeling investigation is made as to what adjustments should be made to the elements of the diffusion and drift tensors during increasing solar activity relative to their values during solar minimum conditions by establishing compatibility with ACE observations. Second the model is applied to study the contribution, role and significance of drifts and the enhancement of $K_{\perp\theta}$ in the heliosheath to GCR Carbon modulation.

The content of this chapter was published by *Ngobeni and Potgieter* (2014).

6.2 The new heliopause spectrum for galactic cosmic ray Carbon

GCR Carbon modulation in the heliosphere is very important since it provides a useful tool with which the global modulation of GCRs can be understood. This is, in part, because GCR Carbon is not contaminated by ACRs at lower energies ($<\sim 200$ MeV) as is the case for Oxygen, Helium and protons. Consequently, adequate knowledge about the GCR Carbon IS at lower energies, for both the intensity level and spectral shape is of significant importance for heliospheric modulation studies. From a solar modulation point of view, these IS's of GCRs should rather be called HPS's because they are specified at the HP. It is to be determined if they truly are identical to the LIS (see e.g. *Kóta and Jokipii*, 2014; *Strauss et al.*, 2013a; *Scherer et al.*, 2011). These HPS are then modulated throughout the heliosphere as a function of position, energy and time.

Before the recent V1 observations (*Stone et al.*, 2013; *Krimigis et al.*, 2013), the HPS at lower energies ($E < 500$ MeV/nuc) were simply estimated, or at best based on the computed results of galactic propagation models (GALPROP) (e.g. *Moskalenko et al.*, 2002). But GCRs experience large solar modulation at these corresponding energies and the nature of the heliospheric diffusion coefficients is not yet fully established. This has resulted in uncertainties in the modeling of the modulation of GCRs at lower energies because the total amount of modulation, including the heliosheath, depends on the assumed value of the relevant HPS. For example, if the location of the HP and TS is fixed, that is the width of the heliosheath prescribed, a higher IS for a given cosmic ray energy will result in more modulation and larger spatial gradients at a certain position in the heliosphere based on a given set of modulation parameters (e.g. *Potgieter and Ferreira*, 2002; *Langner et al.*, 2003; *Ngobeni and Potgieter*, 2010; *Nkosi et al.*, 2011). As long as these HPS were uncertain at lower energies, the actual total modulation between the HP and the Earth, for example, could not be determined, even with the most sophisticated global heliospheric models. Nonetheless the recent observation of the Voyager mission (*Stone et al.*, 2013; *Krimigis et al.*, 2013) is indeed a milestone and a giant step towards understanding the very local interstellar space, providing both the intensity and spectral shape of the HPS for

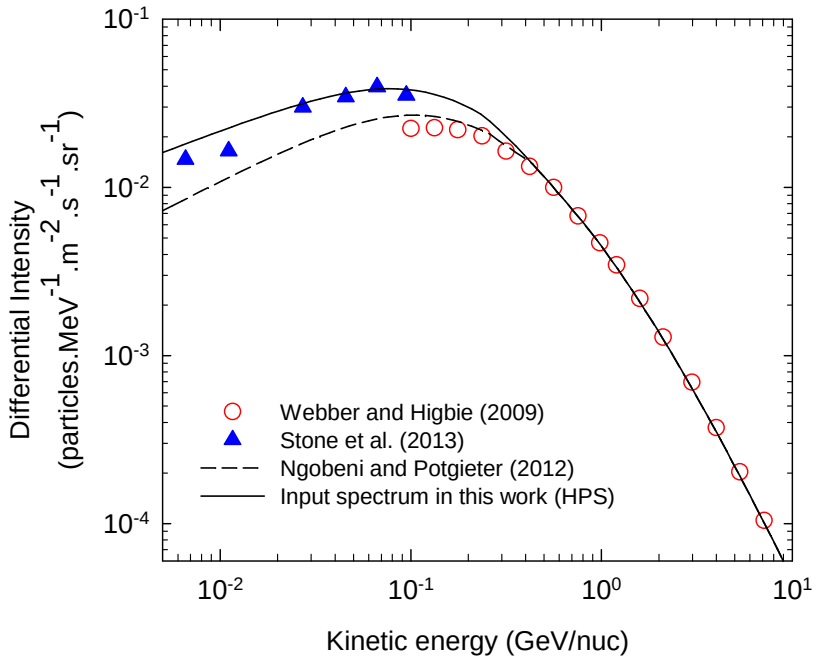

Figure 6.1: The new HPS for GCR Carbon is shown as a solid line together with V1 observations (filled triangles) at a radial distance of $\sim$ 122 AU from *Stone et al.* (2013). This HPS is compared to previous estimates (open circles) from *Webber and Higbie* (2009) and from *Ngobeni and Potgieter* (2012) (dashed line).

various species of GCRs, in particular GCR Carbon for this purpose, down to a few MeV/nuc. If this is indeed the case, V1 may now be measuring the HPS that can trustworthy be considered the lowest possible very LIS for GCRs. Clearly, the HPS plays a central role in the general understanding of how large GCR modulation is in the heliosphere, especially in the heliosheath.

Various methods based on different assumptions have been used to compute the LIS for different GCR species. For example the well-known GALPROP propagation model (*Moskalenko et al.*, 2002) and the Monte Carlo Diffusion (MCD) model (*Webber and Higbie*, 2009). However at $E <\sim 10$ GeV/nuc the galactic propagation processes are less precise (see e.g. *Webber and Higbie*, 2009; *Ptuskin et al.*, 2006).

In this chapter the HPS for GCR Carbon specified at the HP is based on what *Webber and Higbie* (2009) reported using the MCD model and is similar to that used in *Ngobeni and Potgieter* (2012) at higher energies ($E >$ 300 MeV/nuc). However, at lower energies a modification is made based on the recent V1 observations (*Stone et al.*, 2013). The parameterized form of this new HPS for GCR Carbon is given by

$$j_{HPS} = \frac{2.2}{26.91 + 455.16\left(\frac{E}{E_0}\right)\sqrt{\frac{E}{E_0}} + 0.55\left(\ln\frac{E}{E_0}\right)^2}\left[\frac{1}{0.65}\left(\frac{E}{E_0}\right)^{0.30}\right], \qquad (6.1)$$

when $E < 0.25$ GeV/nuc;

$$j_{HPS} = \frac{2.2}{26.91 + 455.16\left(\frac{E}{E_0}\right)\sqrt{\frac{E}{E_0}} + 0.55\left(\ln\frac{E}{E_0}\right)^2},$$

when 0.25 GeV/nuc $\leq E \leq 0.95$ GeV/nuc;

$$j_{HPS} = \frac{2.2}{66.64 + 305.48\left(\frac{E}{E_0}\right)\sqrt{\frac{E}{E_0}} + 115.58\left(\frac{E}{E_0}\right)},$$

when 0.95 GeV/nuc $< E < 13.0$ GeV/nuc;

$$j_{HPS} = 4.18\exp\left(-4.93 - 2.50\ln\left(\frac{E}{E_0}\right)\right),$$

when $E \geq 13.0$ GeV/nuc.

Here $E_0 = 1.0$ GeV/nuc. The new HPS for GCR Carbon as a function of kinetic energy/nuc is shown in Figure 6.1 as the solid line, in units of particles $\mathrm{m}^{-2}\ \mathrm{s}^{-1}\ \mathrm{sr}^{-1}\ \mathrm{MeV}^{-1}$. Also shown are the IS's from *Webber and Higbie* (2009) and *Ngobeni and Potgieter* (2012), as well as the recent V1 observations at ∼122 AU (*Stone et al.*, 2013). Because the IS of *Webber and Higbie* (2009) did not extend to lower energies ($E <\sim 100$ MeV/nuc), *Ngobeni and Potgieter* (2012) employed a phenomenological approach to extend the IS to lower energies of interest to modulation in the heliosphere. Clearly, their IS is well below the observed intensity at these low energies. For example, at $E = 10$ MeV/nuc and $E = 100$ MeV/nuc by a factor of ~ 2.0 and ~ 1.6 respectively. This contributes significantly at these lower energies to the total modulation as a function of position in the heliosphere.

6.3 The heliopause location along the Voyager 1 trajectory

The HPS for GCR Carbon, and for proton, Helium and Oxygen, together with the location of the HP along the V1 direction are fairly known and cannot be regarded as free parameters anymore. Before the recent V1 observations, the location of the HP has been based on HD and MHD model predictions (e.g. *Scherer and Ferreira*, 2005). Generally it was placed around ~ 140 AU in the nose region of the heliosphere, the direction in which the heliosphere is moving. Accurate information about the location of the HP is very important in global modeling of GCRs because it determines the size of the total modulation volume. The recent V1 observations (*Stone et al.*, 2013; *Krimigis et al.*, 2013; *Burlaga et al.*, 2013) indicate that it has encountered regions associated with what may be called a layered HP (*Swisdak et al.*, 2013) and crossed it into the very local interstellar medium at a radial distance of ~ 122 AU in August 2012 (*Gurnett et al.*, 2013). This provides accurate information about the location of the HP along the V1 direction. As yet, no observational evidence of the HP along the V2 direction exist. While for

the TS, its location has been fairly well-known in both hemispheres (*Stone et al.*, 2005; *Decker et al.*, 2005; *Stone et al.*, 2008; *Richardson et al.*, 2008). Based on this $in\ situ$ observation, the heliosheath thickness along the V1 direction can be estimated to be ~ 28 AU. Unfortunately this value changes over an 11-year solar cycle (*Snyman*, 2007; *Webber and Intriligator*, 2011), so that one must again rely on models to establish this dynamic behaviour.

The location of the HP is modified in the numerical model based on the V1 observations (*Stone et al.*, 2013), whereas the TS location is kept as in the previous chapters. Consequently, the TS and HP are respectively placed at $r_{HP} \sim 120$ AU and $r_{TS} \sim 90$ AU in the equatorial plane, at ~ 94 AU and ~ 122 AU with $\theta = 55^o$ (V1 trajectory) and ~ 86 AU and ~ 113 AU with $\theta = 125^o$ (V2 trajectory). It will be shown in Section 6.6 that constraints can be imposed on the location of the HP along the V2 direction.

Next the modulation of GCR Carbon at the Earth is studied from solar minimum to moderate maximum conditions.

6.4 Modulation of galactic cosmic ray Carbon in the inner heliosphere during increasing solar activity

Most of what has been learned in the inner heliosphere from the ecliptic plane to high heliolatitudes is from Ulysses observations. From a GCR modelling point of view, the observations that are of importance for this study are the north-south asymmetry in GCR modulation (this is discussed in Chapter 5) and the small latitudinal GCR gradients during solar minimum modulation conditions (see a detailed discussion by *Heber and Potgieter*, 2006; *Potgieter*, 2011). These observations were contrary to the predictions of the then drift models. It was soon realized that in order to produce the correct magnitude and rigidity dependence of the observed latitudinal gradients in the inner heliosphere, the rigidity dependence of the perpendicular diffusion coefficients ($K_{\perp r}$ and $K_{\perp \theta}$) must be different from that of the parallel diffusion coefficient ($K_{||}$) and also that an enhanced latitudinal transport is required (*Burger et al.*, 2000; *Potgieter*, 2000; *Ferreira*, 2002; *Heber and Potgieter*, 2006). The argument is based on Ulysses measurements that showed the variance in the transverse and normal directions of the HMF increasing more than in the radial direction (*Kóta and Jokipii*, 1995). Figure 6.2 shows an example of the computed latitudinal gradients for GCR protons between colatitudes 10^o and 90^o as a function of rigidity taken from *Langner* (2004); see also *Burger et al.* (2000). The enhanced latitudinal transport is represented by $K_{\perp \theta} > K_{\perp r}$ away from the equatorial regions by a factor of ~ 7 . Evidently the latitudinal gradient during solar minimum in the A > 0 cycle is small; it increases as a function of rigidity up to ~ 2 GV then decreases at higher rigidities. This observation in the inner heliosphere, concerning both the value of the latitudinal gradient and its rigidity dependence, put severe constraints on the model and requires that $K_{\perp \theta}$ must be enhanced in the polar direction.

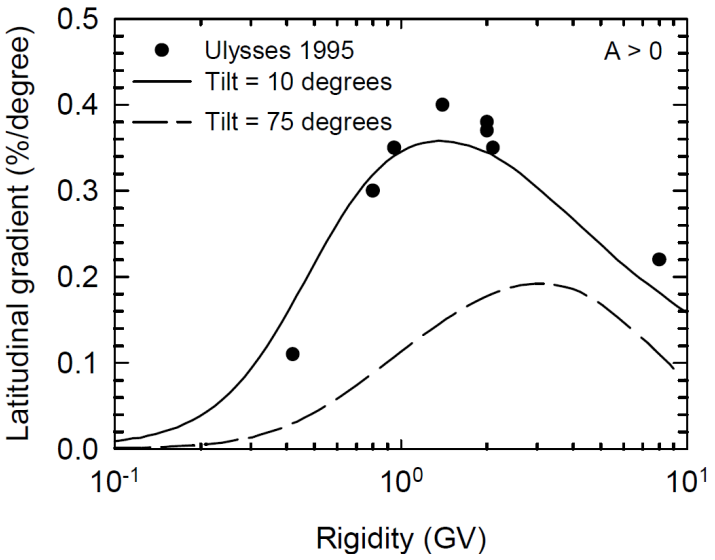

Figure 6.2: Modeled latitudinal gradients, in %/degrees, for the A > 0 polarity cycles at 3.0 AU for solar minimum (solid line) and solar maximum (dashed line) between colatitudes 10^o and 90^o. Observations are from Ulysses in 1995 (*Heber et al.*, 1996). Adapted from *Langner* (2004); see also *Burger et al.* (2000).

This constraint is incorporated in our numerical model as discussed in Chapter 3.

The computed differential intensity resulting from the new HPS of GCR Carbon is shown in Figure 6.3 as a function of kinetic energy/nuc at the Earth (1 AU in the equatorial plane) for an $A > 0$ polarity cycle assuming solar minimum conditions ($\alpha = 10^o$). The computed solution is shown in comparison with observations of GCR Carbon above ~2.0 GeV/nuc from a balloon experiment taken in 1976 (*Simon et al.*, 1980) and from ACE taken in 1997 (*Webber*, 2006) between 10 MeV/nuc and 1.0 GeV/nuc, observed in the $A > 0$ polarity cycles during minimum modulation periods. It follows from Figure 6.3 that these observations at the Earth are reasonably well reproduced by the modeled solution over this wide energy range. This provides a good reference solution for the total modulation between the HP and the Earth, and as such for the magnitude and rigidity dependence of the diffusion coefficients. As for this case the assumed rigidity dependence of $K_{||}$ is a combination of two power laws ($\sim P^{0.3}$ for $P < 5$ GV and $\sim P^2$ for $P \geq 5$ GV), whereas the rigidity dependence of $K_{\perp r}$ and $K_{\perp \theta}$ changes by $P^{-0.1}$ with respect to that of $K_{||}$ as given in Chapter 3. It can be noted from this figure that the total modulation between the HP and the Earth at 10 MeV/nuc for GCR Carbon causes a reduction in intensity of a factor of ~ 0.045, that is, the intensity at the Earth is only ~ 4.5 % of the HPS, whereas for 100 MeV/nuc it is ~ 17.5 %. Respectively, this means that the global radial gradient for GCR Carbon for this period was ~ 2.5 %/AU and ~ 1.4 %/AU, if the HP is taken at 122 AU. These aspects will be discussed further below.

For modulation at the Earth during the recent solar minimum in the $A < 0$ cycle, it was shown by *Potgieter et al.* (2013) that in order to reproduce proton observations with their numerical

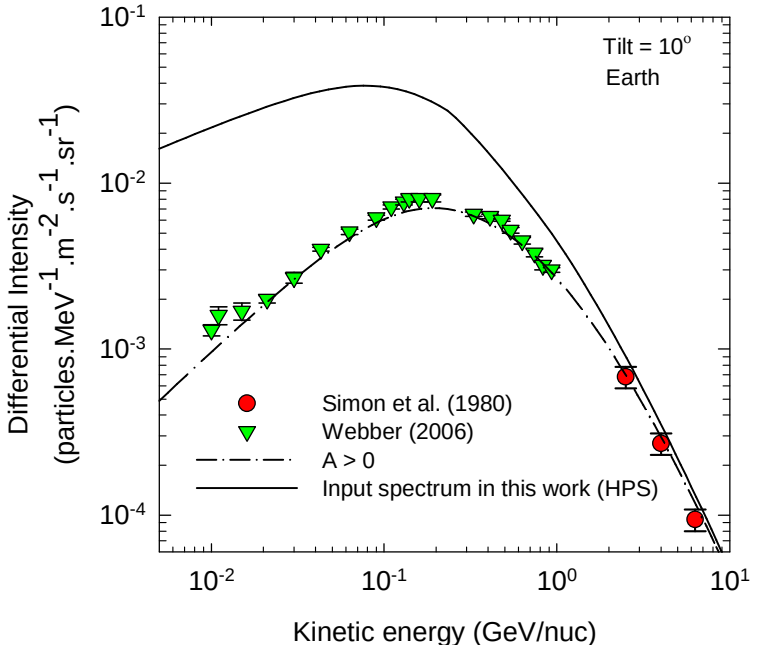

Figure 6.3: The computed differential intensities for GCR Carbon as a function of kinetic energy/nuc based on the new HPS shown in Figure 6.1. This is shown for solar minimum conditions ($\alpha = 10^o$) at Earth (1 AU in the equatorial plane, with $\theta = 90^o$) during an $A > 0$ polarity cycle. Also shown is the observed GCR Carbon intensity at Earth from *Simon et al.* (1980) (filled circles; taken in 1976) and *Webber* (2006) (filled triangles; taken in 1997-1998).

model, full drifts (100 % level) were required in addition to increasing the diffusion coefficients systematically from 2006 to 2009, with maximum intensities observed at the end of 2009. Hence in our model, in addition to the usual change in the sign of the HMF, and the subsequent reversal in the direction of drifts relative to the previous solar minimum, we assumed $k_A = 1.0$ in Equation 3.32, and that $\lambda_{||}$ in Equation 3.20 is increased by a factor of 1.4 for the recent solar minimum. The adjustment of $\lambda_{||}$ for modulation during increasing solar activity is given by Equation 4.30.

In this section the model is applied specifically to study GCR Carbon modulation at the Earth for the two previous solar minima epochs (1997-1998, an $A > 0$ cycle; and the recent $A < 0$ cycle around 2009) and the previous moderate solar maximum activity (2001-2003, $A < 0$ cycle) period. The solar minimum spectrum in the previous $A > 0$ cycle, as depicted in the right panel of Figure 6.3, is taken as the reference solution.

The computed spectra corresponding to the three different modulation conditions outlined above, are shown in the left panel of Figure 6.4 at the Earth; the solid line represents the previous solar minimum ($A > 0$), the dashed line for moderate solar maximum ($A < 0$) and dash-dot-dot line for the recent solar minimum ($A < 0$). The computed spectra are compared to the corresponding ACE observations of GCR Carbon measured during 1997-1998, 2001-2003 and 2009-2010 as reported by *Webber* (2006), *Lave et al.* (2013) and *Webber et al.* (2012) respec-

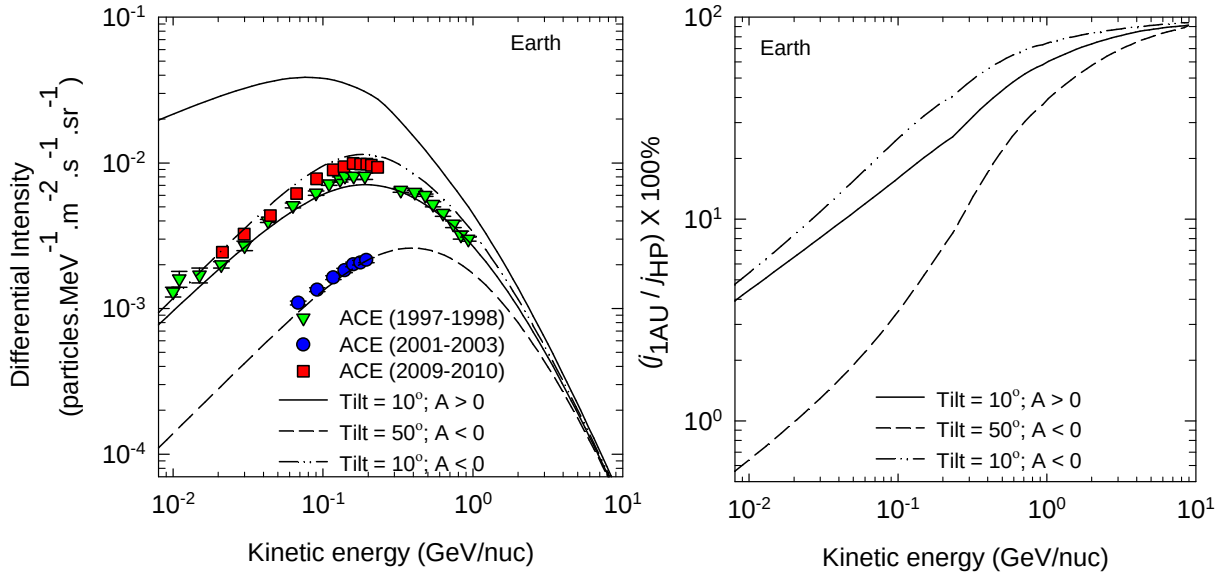

Figure 6.4: Modulated GCR Carbon spectra computed as a function of kinetic energy/nuc at the Earth (with polar angle of $\theta = 90^o$) for three different modulation conditions. Left panel: (1) The solid line for the previous $A > 0$ cycle solar minimum with $\alpha = 10^o$; (2) the dashed line for the previous $A < 0$ cycle moderate solar maximum with $\alpha = 50^o$; and (3) the dash-dot-dot line for the recent $A < 0$ cycle solar minimum with $\alpha = 10^o$. These modulated spectra are compared to ACE observations (green filled triangles for 1997-1998; blue filled circles, between 2001-2003; and red filled squares for 2009-2010) taken from *Webber* (2006), *Lave et al.* (2013) and *Webber et al.* (2012), respectively. The right panel shows the corresponding percentage ratio of the three modulated spectra at the Earth with respect to the HPS, as the IS.

tively. Clearly, from the left panel the Carbon spectrum observed at the Earth during the recent solar minimum in the $A < 0$ cycle is higher than during the $A > 0$ solar minimum cycle which was the first time it happened that an $A < 0$ spectrum exceeds an $A > 0$ spectrum at $E <$ 1.0 GeV/nuc. See also the discussion in this context by *Mewaldt et al.* (2010), *Bazilevskaya et al.* (2012) and *Potgieter et al.* (2013), particularly as emphasized by *Potgieter and Strauss* (2013). The observed high intensity during the recent solar minimum highlights that less modulation took place between the HP and the Earth when compared to the previous minima, despite the fact that it was an $A < 0$ cycle. It is also noted that the GCR Carbon intensities at the Earth decrease significantly at $E <$ ∼1.0 GeV/nuc from solar minimum to moderate solar maximum conditions. The computed spectra evidently produce reasonable compatibility with ACE observations for the two solar minima conditions as well as for the previous moderate solar maximum conditions. This indicates that the adjustments in the diffusion coefficients are reasonable for modulation at the Earth.

The compatibility of the model solutions, based on the new HPS at lower energies, with these observations provides a context within which the total amount of modulation that takes place between the HP and the Earth can be made reliably for the mentioned solar modulation conditions. This is done in the right panel of Figure 6.4 which shows the computed total modulation

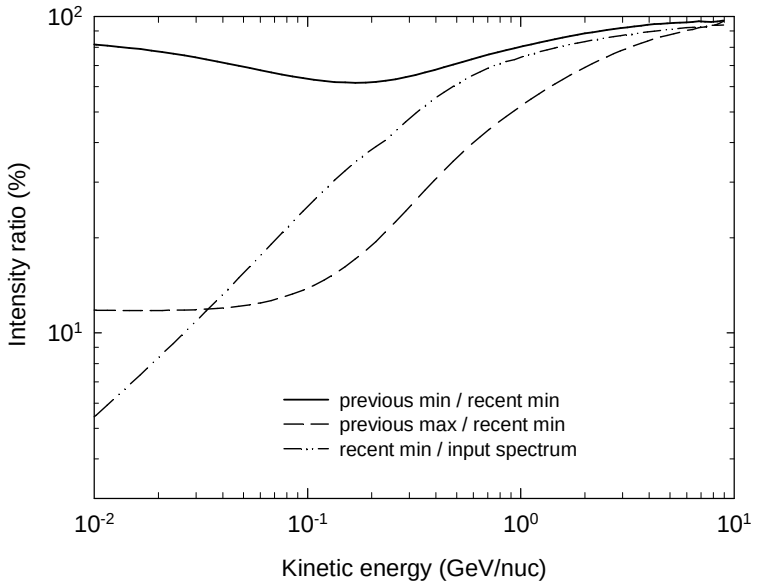

Figure 6.5: Computed percentage ratio of intensities as a function of kinetic energy/nuc at the Earth: (1) The solid line is for the ratio of the spectra from the previous solar minimum ($A > 0$, $\alpha = 10^o$) to the recent solar minimum ($A < 0$, $\alpha = 10^o$); (2) the dashed line for the ratio of the previous moderate maximum ($A < 0$, $\alpha = 50^o$) to the recent solar minimum; and (3) the dash-dot-dot line for the ratio of the spectrum in the recent solar minimum to the HPS.

as a percentage ratio in the equatorial plane. Depicted is the ratio, j_{1AU} / j_{HP} of the modulated spectra at the Earth (1 AU) to the HPS with the solid line representing the previous solar minimum, the dashed line for moderate solar maximum and the dash-dot-dot line for the recent solar minimum. It is evident that indeed the computed modulation between the HP and the Earth is the smallest for the recent solar minimum, and that the modulation of GCR Carbon between the Earth and the HP is getting increasingly larger the lower the kinetic energy becomes. For solar minimum conditions, between ∼4-6% of the HPS intensity at $E =$ 10 MeV/nuc is reaching the Earth, while at moderate solar maximum activity, ∼10 times less particles are reaching the Earth. Previously, only rough estimates could be made for the total modulation at these low energies. The convergence of the ratios at very high energies is caused by the energy limit of fading modulation at these high energies used as an initial condition in the numerical solutions, in this case 21 GeV/nuc.

In Figure 6.5 the interesting features, as shown above, are emphasized when the level of modulation between the HP and the Earth for the recent solar minimum is compared to that between the two previous solar activity periods and the recent solar minimum at the Earth. Again the percentage ratios are shown with the solid line representing the ratio of the previous solar minimum ($A > 0$) to the recent solar minimum ($A < 0$), the dashed line for the previous moderate maximum ($A < 0$) to the recent solar minimum, and the dash-dot-dot line for the ratio of the recent solar minimum to the HPS as done also in Figure 6.4. The solid line indicates that during the recent $A < 0$ cycle solar minimum more Carbon particles reached the Earth at all energies

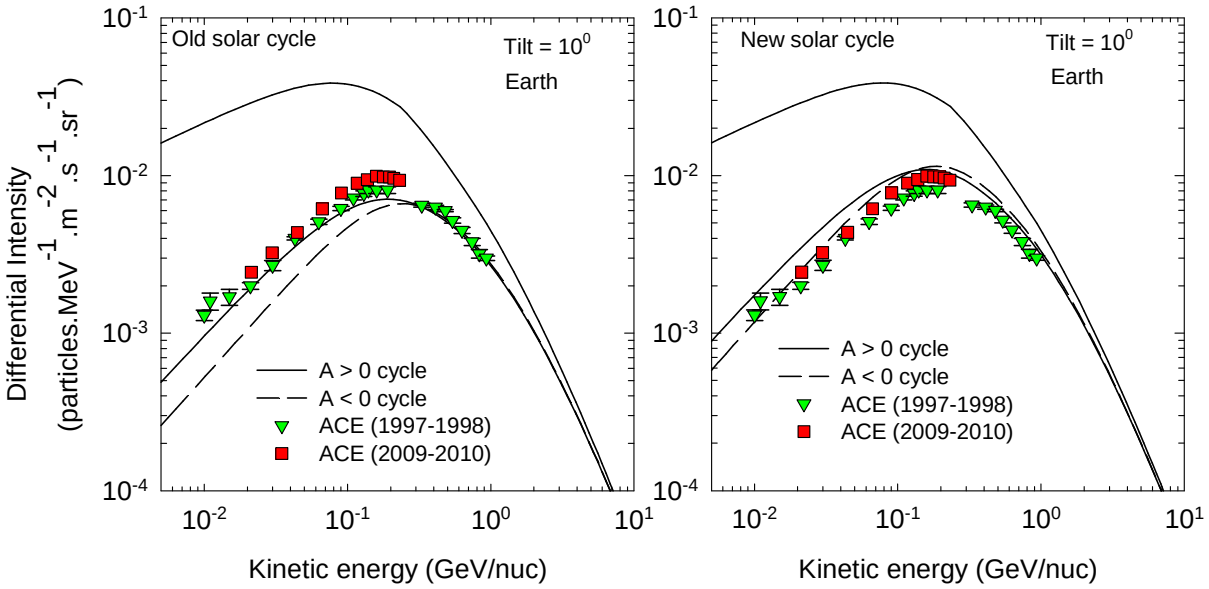

Figure 6.6: Modulated GCR Carbon spectra computed as a function of kinetic energy/nuc at the Earth (with polar angle of $\theta = 90^o$) for the usual solar minimum (left panel) and the unusual solar minimum modulation conditions (right panel). The solid lines represent solutions in the $A > 0$ cycle and the dashed lines for the $A < 0$ cycle. These modulated spectra are compared to ACE observations (green filled triangles for 1997-1998 and red filled squares for 2009-2010) taken from *Webber* (2006) and *Webber et al.* (2012), respectively.

than during the previous $A > 0$ cycle and that this modulation effect shows a local minimum around (150 $\pm$ 50) MeV/nuc. This implies that the observed spectra in 2009 were softer than previous minimum spectra; see also the discussion by *Potgieter and Strauss* (2013). The dashed line shows how the total modulation changes as a function of kinetic energy between moderate solar maximum and the recent solar minimum modulation; at 100 MeV/nuc it is almost a factor of ~ 10 whereas the ratio between the HPS and the recent solar minimum spectrum is a factor of ~ 25. It is evident that at energies $E > \sim 30$ MeV/nuc, the computed level of modulation between moderate solar maximum and the recent solar minimum exceeds the level of total modulation between the HP and the Earth for the recent solar minimum. This means that it is possible for the level of modulation at the Earth when solar activity changes from moderate maximum conditions to solar minimum conditions, to exceed the total modulation between the HP and the Earth.

It is evident in Figure 6.4 that by adjusting the set of diffusion coefficients the abnormally high intensities in the recent $A < 0$ cycle minimum conditions can be reproduced. Following *Strauss and Potgieter* (2014), similar predictions are made for the next solar minimum period in the $A > 0$ cycle using the adjusted modulation conditions. The computed differential intensities of GCR Carbon for the two solar cycles (left panel for the old solar cycle obtained with reference diffusion coefficients; right panel for the new solar cycle obtained with adjusted diffusion coefficients) assuming minimum modulation conditions are shown in Figure 6.6 as a function of kinetic energy/nuc at the Earth for both polarity cycles. The spectra are shown in

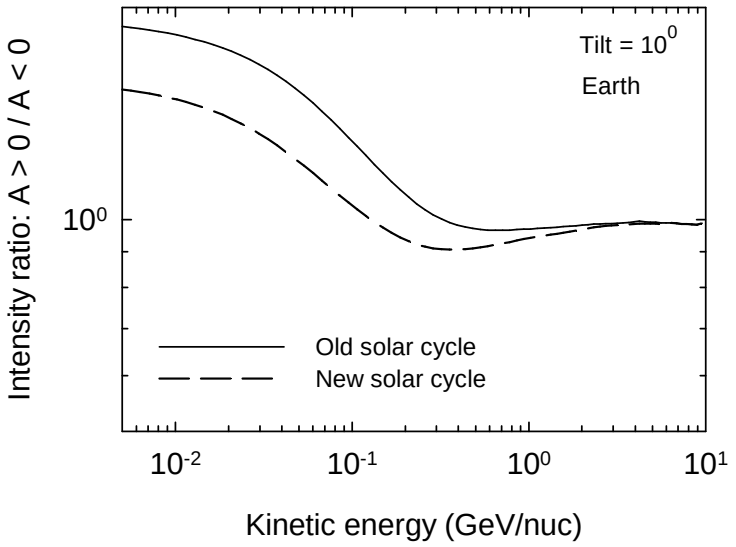

Figure 6.7: The computed ratio , $A > 0$ / $A < 0$, of the old (solid line) and the new solar cycles (dashed line) at the Earth as a function of kinetic energy/nuc during solar minimum modulation conditions.

comparison with GCR Carbon ACE observations (*Webber*, 2006; *Webber et al.*, 2012) from 1997 to 1998 during minimum periods in the $A > 0$ polarity cycle and also from 2009 to 2010 during minimum periods in the $A < 0$ cycle. Note that the computed spectra at the Earth in the $A > 0$ polarity cycle crosses that of the $A < 0$ cycle at ~ 300 MeV/nuc for modulation conditions representing the old solar cycle and at ~ 150 MeV/nuc for the new solar cycle. Such features have been reported previously (*Reinecke and Potgieter*, 1994; *Langner et al.*, 2003) and illustrate the significant role drifts play in the modulation of GCR in the inner heliosphere. The important point here is that the $A < 0$ spectrum is less than the $A > 0$ spectrum at these low energies primarily because of drifts in both solar cycles. This is taken to indicate that there is no contradictions between observations with drift models when the same modulation conditions are considered in the two polarity cycles. This implies that the highest GCR Carbon flux below ~ 150 MeV/nuc is yet to be observed if the same modulation conditions are to repeat in the next solar minimum. While at energies above 150 MeV/nuc, the highest GCR Carbon flux might have been observed. As one would expect, the computed spectra for the $A < 0$ cycle in the left panel tends to be too low compared to observations taken between 2009-2010, while in the right panel the computed spectra in the $A > 0$ cycle tends to be too high when compared to the ACE observation between 1997-1998.

Figure 6.7 shows the differences in the drift contributions (drift effects) for the old and the new cycles, as represented by the ratio in spectra of $A > 0$ and $A < 0$ cycles, as a function of kinetic energy/nuc during solar minimum conditions. For $E > 1.0$ GeV/nuc, differences between the two solutions for the two polarity cycles start to vanish with almost no difference when $E > 4.0$ GeV/nuc. What is striking in this figure is that the computed ratio decreases at

energies below ~ 2 GeV/nuc for the new solar cycle compared to the old cycle even though the level of drifts has been increased by a factor of 2.0 in the new cycle. Thus decreasing drift effects do not necessarily indicate decreasing levels of drift. Indeed the increasing level of drifts, as a result of the weakening HMF, has contributed significantly to the increased intensities of GCR Carbon at the Earth in the recent solar minimum (*Strauss and Potgieter*, 2014; *Potgieter et al.*, 2013).

Next, the north-south asymmetric model is applied to study modulation of GCR Carbon in the outer heliosphere and the computed solutions are compared to both V1 and V2 observations during solar minimum conditions. The reference parameters are again used unless otherwise stated. Hence the difference in the computed spectra between the $A > 0$ cycle and $A < 0$ cycle in the outer heliosphere is caused simply by the changing sign of the HMF and thus the subsequent changed direction of drifts.

6.5 Modulation of GCR Carbon in the outer heliosphere

It is important to note that modulation conditions in the outer regions of the heliosheath are not well known. When approaching the HP, the solar wind velocity is expected to bend from its original radial flow in the nose direction of the heliosphere and eventually to flow parallel to the interstellar flow, increasingly so towards the tail direction. Evidence from V2, with direct solar wind measurements, indicates that the radial flow inside the heliosheath is indeed slowly decreasing but much more slowly than reported for V1 (*Richardson and Wang*, 2011). In order to incorporate this detailed convection effect in a 2D shock acceleration model, as applied here, is not a trivial exercise, let alone doing it in a 3D shock acceleration model for GCRs, the reason why such an ADI model does not exist. Futhermore, it is also possible that the wavy HCS structure is not maintained throughout the outer regions of the turbulent heliosheath (*Pogorelov et al.*, 2013). According to *Florinski* (2011), when the solar wind slows down on approach to the HP the distance between folds of the current sheet decreases to a point where it becomes comparable to the cyclotron radius of a cosmic ray particle, definitely to that of GCR Carbon. As a result GCR particles should 'short-circuit' most of the waviness of the current sheet and actually have easy access out of the heliosheath into the outer heliosphere (inside off the TS). All these possibilities will add to the already complicated picture of modulation in the heliosheath. However, progress can be made based on the already generally known modulation processes.

The possibility of significant large modulation of GCRs in the distant heliosphere was addressed by *Webber and Lockwood* (2001) from an experimental point of view. A more comprehensive study of the importance of what happens at and beyond the TS from numerical modeling point of view has been done by *Langner* (2004) and *Langner et al.* (2003, 2004). From

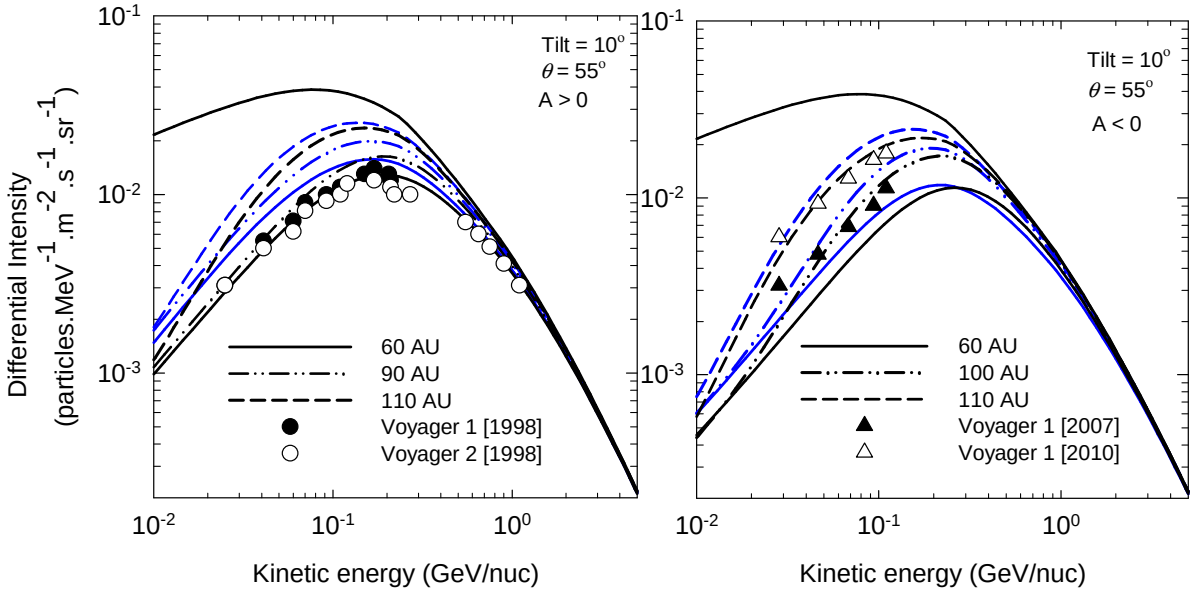

Figure 6.8: Computed differential intensity for GCR Carbon as a function of kinetic energy/nuc at radial distances of 60 AU, 90 AU (or 100 AU) and 110 AU for the two polarity cycles (left panel is for $A > 0$, right panel is for $A < 0$ cycles) during solar minimum modulation condition at $\theta = 55^o$. Two sets of solutions are shown in both panels: First, spectra without drifts in the heliosheath (black lines; $k_A = 0$ in Equation 3.32 for $r > r_{TS}$) and then the full model is assumed with drifts in the heliosheath (blue lines; $k_A = 0.5$ in Equation 3.32 throughout the heliosphere). Computed spectra are compared with observations of GCR Carbon in the outer heliosphere from V1 (filled circles for 1998 when it was at 72 AU; filled triangles for 2007 when it was at 104 AU; open triangles for 2010 when it was at 114 AU) and V2 (open circles for 1998 when it was at 56 AU) reported by *Webber* (2006) and *Webber et al.* (2012).

their studies, as do other authors (*Webber and Lockwood*, 2001; *McDonald et al.*, 2000, 2002), it has been established that the amount of modulation taking place in the heliosheath depends on energy as well as on solar activity with more than $\sim 80\%$ of the total modulation at lower energies (~ 200 MeV/nuc) occurring in the heliosheath (*Potgieter*, 2008). This prediction is indeed confirmed by V1 observations (*Webber et al.*, 2013).

However, it is not yet established as to what extent the various known modulation processes contribute to the total modulation in the heliosheath as a function of energy. The model is applied to study modulation in the outer heliosphere, in particular to investigate the relative importance of the role of drifts and the enhancement of polar perpendicular diffusion inside the heliosheath. The modeling solutions are compared with observations from V1 and V2 for both solar magnetic polarity cycles (two drift cycles) and during solar minimum conditions. GCR Carbon is most suitable for this kind of study because it is not contaminated by ACRs.

Modeling spectra for GCR Carbon at radial distances of 60 AU, 90 AU, 100 AU and 110 AU are compared to observations in the outer heliosphere as shown in Figure 6.8 for both polarity cycles (left panel for $A > 0$; right panel for $A < 0$) during solar minimum modulation condition and at $\theta = 55^o$ corresponding to the heliolatitude of V1. The observations are from V1,

when it was at 72 AU, 104 AU and 114 AU taken in 1998, 2007 and 2010, respectively, and also from V2 when it was positioned at 56 AU in 1998. This corresponds to the time periods when V1 was inside off the TS and in the heliosheath but respectively during two different magnetic cycles. At radial distances of 56 AU and 72 AU the modulation effects of an asymmetry in the geometry of the heliosphere is still negligible (see Chapter 4). In addition the contribution of drifts to modulation in the heliosheath is illustrated by neglecting drifts entirely in the heliosheath while keeping 50 percent drifts ($k_A = 0.5$ in Equation 3.32) at distances less than the TS position ($r < r_{TS}$). The results are compared to the reference spectra produced with drifts kept at a 50 percent level throughout the heliosphere, including the heliosheath. This modeling suggests that drifts should be scaled to zero in the heliosheath region as shown by the black lines in this figure in order to obtain reasonable compatibility with observations along the two Voyager heliolatitudes in the outer heliosphere, for both inside off the TS ($r < r_{TS}$) and in the heliosheath ($r > r_{TS}$). Making drifts zero in the heliosheath decreases intensities along the V1 direction at $E <$ ~1.0 GeV/nuc in the A > 0 cycle at all radial distances while in the A < 0 cycle the intensities increase slightly at $E >$ ~300 MeV/nuc. This feature is more noticeable at 60 AU. However, as follows from both panels, observations in the outer heliosphere in the two magnetic cycles seem to require that drifts be neglected in the heliosheath. This comparison between model solutions and observations in the outer heliosphere can improve our understanding of the relative importance of the role of drifts in the heliosheath, an issue which has remained ignored so far. It is evident from Figure 6.8 that drifts in the heliosheath play a less significant role along the V1 heliolatitude, but the question remains if this would also be true in the equatorial plane? This is further pursued below.

The focus on Figures 6.9 and 6.10 is on computing the radial intensities for GCR Carbon in the equatorial plane with $\theta = 90^o$ and at $\theta = 55^o$ which corresponds to the heliolatitude of V1. Two sets of radial intensities are shown, the reference intensities produced by the full model with all modulation effects taken into account compared to the radial intensities where certain modulation effects are neglected or switched off in the heliosheath in order to illustrate their contribution, role and importance.

Figure 6.9 shows the computed differential intensities as a function of radial distance, in AU, at energies of 0.05 GeV/nuc, 0.2 GeV/nuc and 1.0 GeV/nuc, respectively. The top row represents solutions at $\theta = 90^o$ and the bottom row at $\theta = 55^o$. Two sets of solutions are shown, without drifts in the heliosheath (represented by red lines; with $k_A = 0$ in Equation 3.32 for $r > r_{TS}$) compared to the reference solution (black lines; full model). All computations are done for the two magnetic field polarity cycles assuming solar minimum conditions. It can be seen that the polarity dependent differences, characteristic of drift models, are compelling in the equatorial plane. Differences between the computed results for the two polarity cycles, in particular the effect of the TS on GCR Carbon is more pronounced for the A < 0 cycle in the equatorial plane,

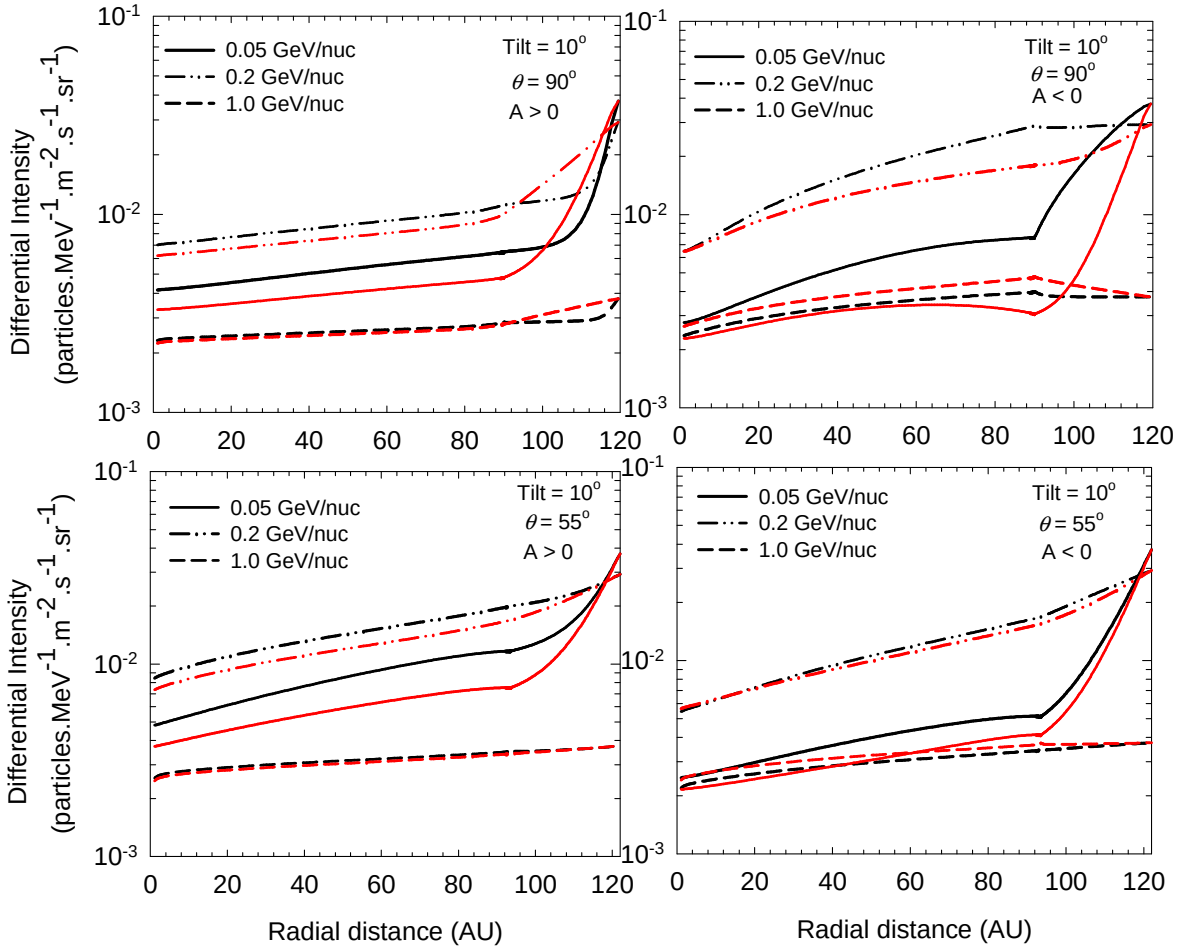

Figure 6.9: Computed differential intensity for GCR Carbon as a function of radial distance at energies of 0.05 GeV/nuc, 0.2 GeV/nuc and 1.0 GeV/nuc for both polarity cycles during solar minimum conditions ($\alpha = 10^o$). The top row is solutions at $\theta = 90^o$ (equatorial plane) and the bottom row at $\theta = 55^o$ (V1 heliolatitude). Two sets of solutions are shown in both panels: First, solutions produced when the full model is assumed with drifts in the heliosheath (black lines; $k_A = 0.5$ in Equation 3.32 throughout the heliosphere) and then without drifts in the heliosheath (red lines; $k_A = 0$ in Equation 3.32 for $r > r_{TS}$).

to the extent that the computed intensities at the TS position at 0.2 GeV/nuc and 1.0 GeV/nuc, actually exceeds the HPS value when drifts are taken into account in the heliosheath. However, when drifts are entirely neglected beyond the TS this effect is shifted to higher energies such that it disappears at 0.2 GeV/nuc. These general features are consistent with previous modeling studies done by *Langner* (2004); *Langner et al.* (2003); *Potgieter and Langner* (2004). In the equatorial plane, the differences between the two scenarios decrease with the decreasing radial distance. What is compelling in this region of the heliosphere is that in the A < 0 magnetic cycle the intensities at 0.05 GeV/nuc and 0.2 GeV/nuc obtained with no-drifts assumed in the heliosheath are lower than when drifts are assumed, whereas at 1.0 GeV/nuc the opposite occurs. This relates to the fact that more low energy particles are re-accelerated at the TS to higher energies and neglecting drifts in the heliosheath enhances this effect. This seems not possible during the A > 0 cycle because significant modulation is always predicted beyond

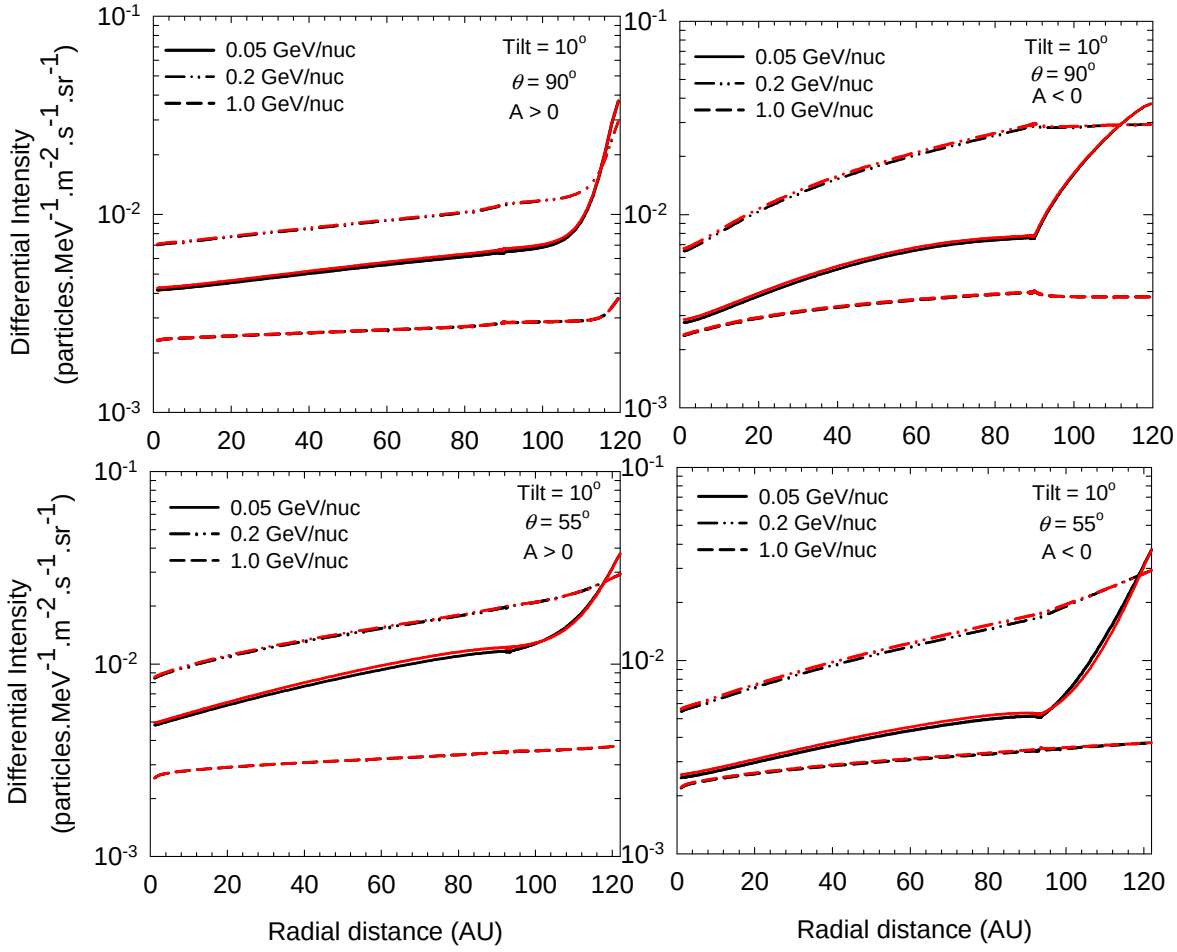

Figure 6.10: Computed differential intensity for GCR Carbon as a function of radial distance at energies of 0.05 GeV/nuc, 0.2 GeV/nuc and 1.0 GeV/nuc for both polarity cycles during solar minimum conditions ($\alpha = 10^o$). The top row are solutions at $\theta = 90^o$ (equatorial plane) and the bottom row at $\theta = 55^o$ (V1 heliolatitude). Two sets of solutions are shown in both panels: First, solutions produced when the full model is assumed with the enhancement of $K_{\perp\theta}$ throughout the heliosphere (black lines; $k_p > k_e$ in Equation 3.24) and then without any latitudinal enhancement in $K_{\perp\theta}$ in the heliosheath (red lines; $k_e = k_p$ in Equation 3.24 for $r > r_{TS}$)

the TS at all energies of interest for both scenarios. In the A > 0 cycle, computed intensities obtained without drifts in the heliosheath are lower inside off the TS but become large in the heliosheath. The effects of neglecting drifts in the heliosheath for equatorial plane modulation is that the large increase in the intensity close to the HP in the A > 0 cycle can be reduced significantly. However in the A < 0 cycle the increase can be made large at 0.05 GeV/nuc and 0.2 GeV/nuc.

Switching to the bottom panel, important is that at this heliolatitude the intensities at the TS for 0.2 GeV/nuc and 1 GeV/nuc in the A < 0 cycle no longer exceed the corresponding HPS values. It can be noted that at $\theta = 55^o$, differences between the two scenarios are more pronounced in the A > 0 cycle at 0.05 GeV/nuc and 0.2 GeV/nuc contrary to modulation in the equatorial plane. However at 1.0 GeV/nuc the differences are larger in the A < 0 cycle similar

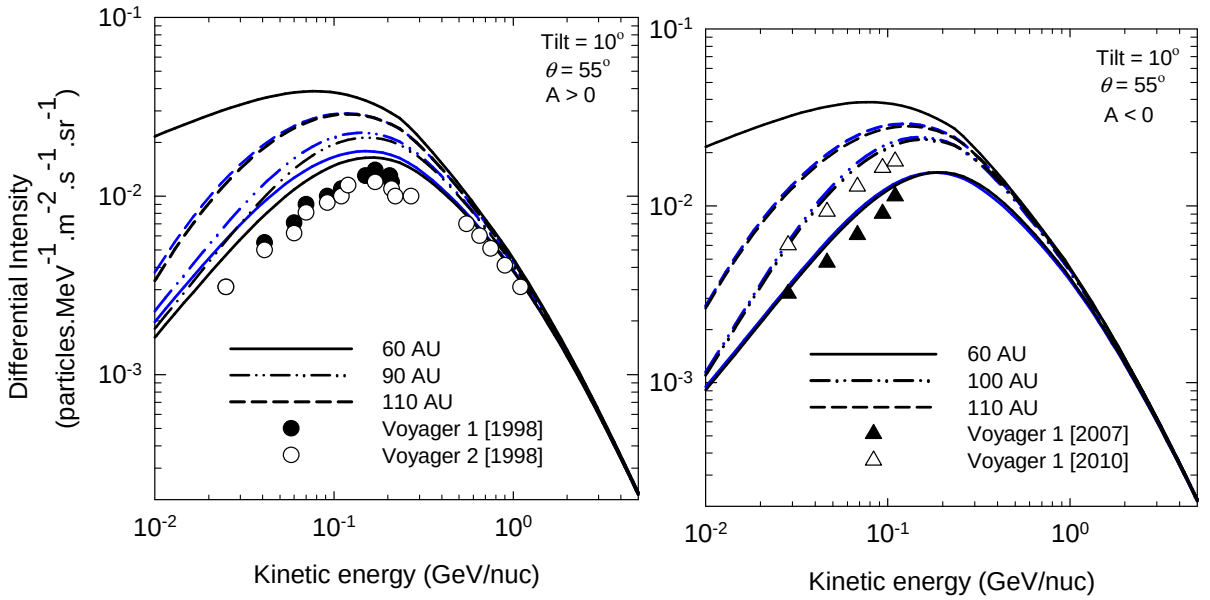

Figure 6.11: Similar to Figure 6.8 but with $k_e = 0.052$ in Equations 3.23 and 3.24 instead of $k_e = 0.026$. This means that the magnitudes of both $K_{\perp r}$ and $K_{\perp \theta}$ are increased by a factor of 2 in the equatorial plane while kept the same in the polar regions.

to what has been found in the equatorial plane. It is interesting to note in the bottom panel that for both scenarios the radial gradients in the heliosheath are generally similar and that the modulation difference between them is much reduced in the A < 0 cycle.

In Figure 6.10, the computed intensities obtained when the enhancement of $K_{\perp \theta}$ is neglected in the heliosheath ($k_e = k_p$ in Equation 3.24 for $r > r_{TS}$) but drifts are kept are shown as red lines. This will illustrate the relative importance of the enhancement of $K_{\perp \theta}$ in the heliosheath in relation to drifts. As before, the reference solution (black lines; full model) is compared with this scenario. The general feature in this figure is that the enhancement of $K_{\perp \theta}$ in the heliosheath has no significant effects on radial intensities of GCR Carbon at both heliolatitudes. This is because the latitudinal diffusive term in the TPE becomes increasingly dominant with decreasing radial distance ($r < 10$ AU). It is noted from the two figures that assumptions made about the effectiveness of drifts in the heliosheath have a more prominent effect on modulation of GCR Carbon than the enhancement of $K_{\perp \theta}$ in the heliosheath. This is in line with previous modulation studies done by *Potgieter and Langner* (2005) for GCR protons.

It is worth mentioning that the change in the radial gradients at the TS is abrupt because in this type of numerical model the TS is specified over a single grid point whereas in reality the TS is spread over a relatively large region (easily 300,000 km according to *Richardson et al.* (2008)) over which the radial gradient can undergo these changes. This implies that our model predicts upper limits for this type of GCR Carbon re-acceleration effects at the TS. These computed radial intensities should therefore be viewed as what can be expected from a standard global modulation approach of GCR Carbon in the heliosphere when drifts and the enhancement of

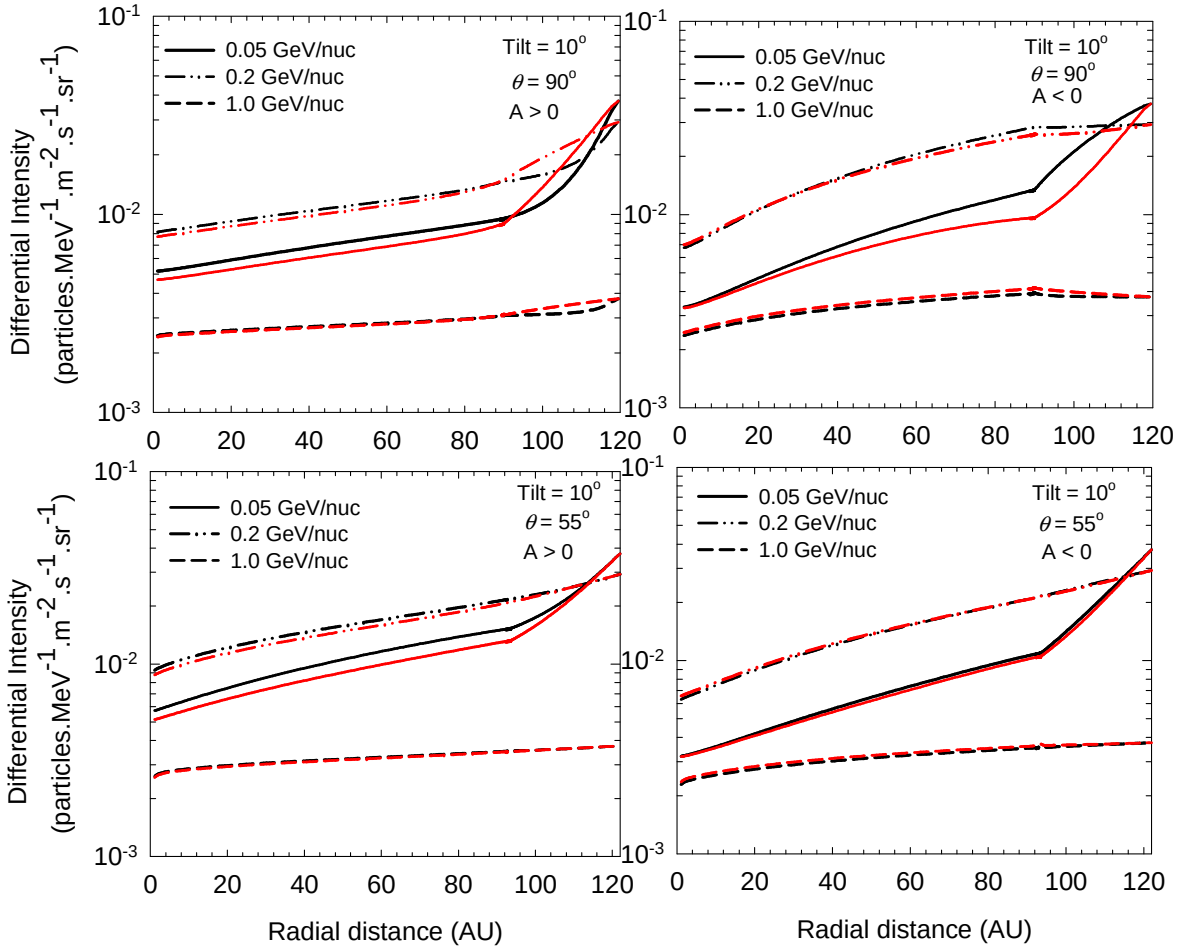

Figure 6.12: Similar fo Figure 6.9 but solutions now obtained with $k_e = 0.052$ in Equations 3.23 and 3.24 instead of $k_e = 0.026$.

$K_{\perp\theta}$ are respectively neglected in the heliosheath.

To further clarify the role of drifts and the enhancement of $K_{\perp\theta}$ in the heliosheath on radial intensities of GCR Carbon in the heliosphere, Figures 6.8, 6.9 and 6.10 are repeated but now with $k_e = 0.052$ assumed in Equations 3.23 and 3.24 instead of $k_e = 0.026$. Consequently, as noted from Equations 3.23 and 3.24, the magnitudes of both $K_{\perp r}$ and $K_{\perp\theta}$ are increased by a factor of 2 in the equatorial plane while kept the same in the polar regions. It must be borne in mind that this assumption also increases the effective radial diffusion coefficient in the equatorial plane in the outer heliosphere thus producing less efficient shock acceleration effects. Figure 6.11 is similar to Figure 6.8 except that $k_e = 0.052$. It follows from this figure that the reasonable fit to observations along the two Voyager directions at the corresponding radial distances both inside off the TS and in the heliosheath is lost in both magnetic cycles. In the left panel the corresponding computed modulated intensities as represented by the solid lines for 60 AU are both above the observations, while the right panel indicates that the dashed lines for 110 AU are above the open triangles and also that the dash-dot-dot lines for 100 AU fit

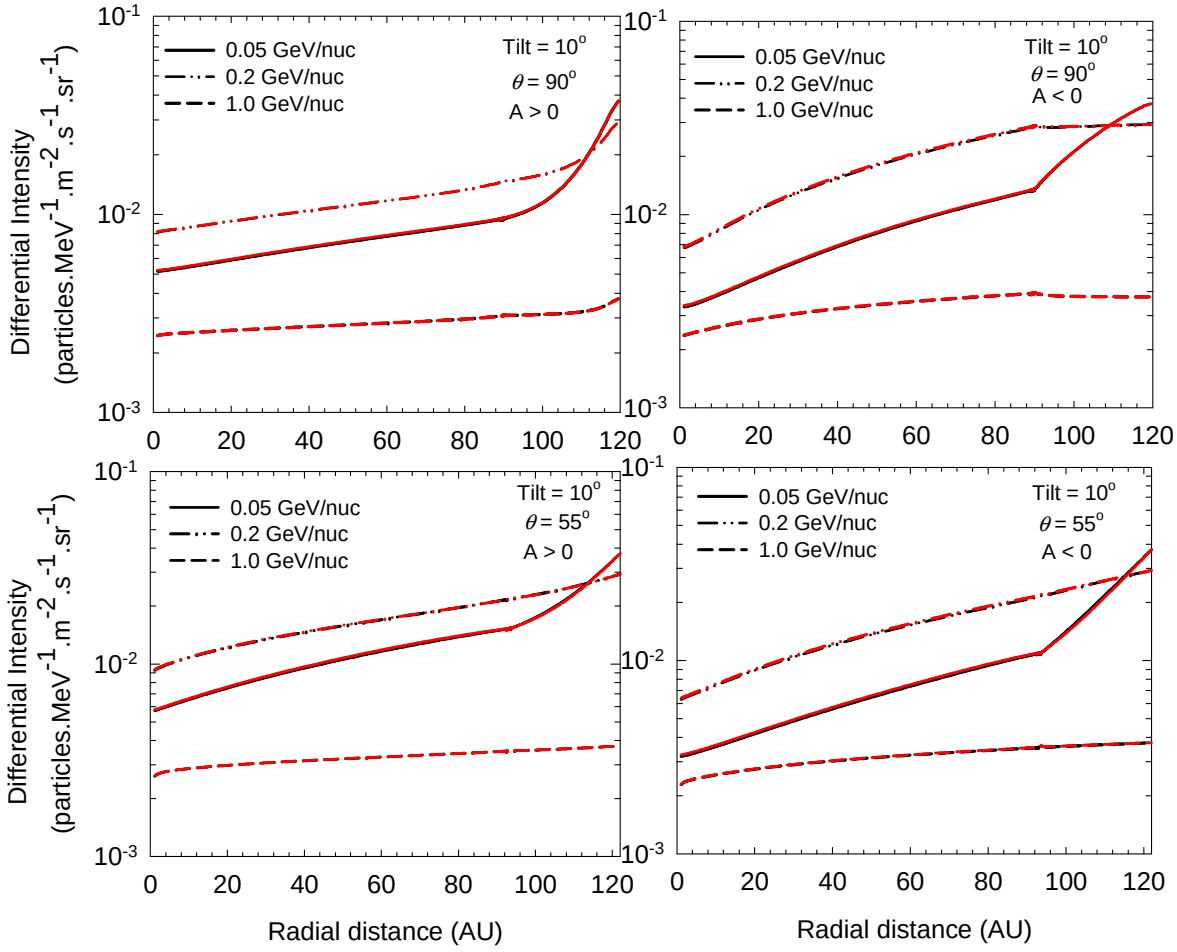

Figure 6.13: Similar fo Figure 6.10 but solutions now obtained with $k_e = 0.052$ in Equations 3.23 and 3.24 instead of $k_e = 0.026$.

the open triangles rather than the filled triangles. What is interesting is that for the A < 0 cycle differences between the two scenarios are now not obviously noticeable, indicating decreasing drift effects.

In Figure 6.12 the computed radial intensities are again shown with drifts neglected in the heliosheath (as in Figure 6.9 but now with $k_e = 0.052$ in Equations 3.23 and 3.24 instead of $k_e = 0.026$) but still maintaining the enhancement of $K_{\perp\theta}$ compared to the reference solution. It can be noted that the large differences between the two scenarios, as seen before, are now relatively small also in the equatorial plane. What is more interesting is that the differences between the two scenarios have been wiped out almost completely at all energies in the inner heliosphere for the modulation in the equatorial plane in the A < 0 cycle, whereas for the A > 0 cycle differences can be noted but only at energies of 0.05 GeV/nuc and 0.2 GeV/nuc. Whereas, at $\theta = 55^o$ differences are only noticeable in the A > 0 cycle and at lower energies; in the A < 0 differences are almost completely wiped out in the whole heliosphere. This can be taken to indicate that the subsequent effects of neglecting drifts completely in the heliosheath

may not be evident on the corresponding computed intensities along the V1 heliolatitude in the A < 0 cycle when k_e in Equations 3.23 and 3.24 is made large.

In Figure 6.13 $K_{\perp\theta}$ is assumed independent of polar angle in the heliosheath ($k_e = k_p$ in Equation 3.24 for $r > r_{TS}$) similar to Figure 6.10. As before, the effects of the enhancement of $K_{\perp\theta}$ in the heliosheath are disappointingly absent from the computed intensities at both heliolatitudes.

However it should be noted that this approach, where the observations at different radial distances are related to the computed intensities, is relevant to the understanding of the radial dependence of $K_{||}$ in the outer heliosphere.

6.5.1 Comparison of modulation in the heliosheath to the total modulation

In the next three figures the intensity differences between the spectrum at the HP (indicated as j_{HP}) and the modulated spectrum at the TS (indicated as j_{TS}) are compared to the differences between j_{HP} and the modulated spectrum at 1 AU (indicated as j_{1AU}). The results are shown as the percentage ratio $(j_{HP} - j_{TS})/(j_{HP} - j_{1AU})$ for a wide range of kinetic energy, first at $\theta = 55^o$, then for $\theta = 90^o$, all for solar minimum conditions ($\alpha = 10^o$) and for both drift cycles. This ratio is less than 100 % but when it becomes negative it means the incoming GCR Carbon particles have been re-accelerated at the TS so that the intensity at the TS is higher than the HPS.

In Figure 6.14, this ratio is depicted for $\theta = 55^o$ with solid lines giving solutions with the full model, that is with drifts present throughout the whole heliosphere; the dotted lines for solutions without any drifts in the heliosheath ($k_A = 0$ in Equation 3.32 for $r > r_{TS}$) and the dashed lines for solutions without any latitudinal enhancement in $K_{\perp\theta}$ ($k_e = k_p$ in Equation 3.24 for $r > r_{TS}$) in the heliosheath. The top row shows solutions obtained with $k_e = 0.026$ and the bottom row with $k_e = 0.052$ in Equations 3.23 and 3.24, with k_p unchanged as specified in Chapter 3. It follows from the top row that neglecting drifts in the heliosheath increases the modulation in the heliosheath along the V1 heliolatitude, at all energies in the $A > 0$ cycle, while in the $A < 0$ cycle a similar effect occurs only at $E <\sim 400$ MeV/nuc, because above this energy the effects of neglecting drifts in the heliosheath is to decrease the total modulation in the heliosheath. It is also evident that the contributions of the enhancement of $K_{\perp\theta}$ to the total modulation in the heliosheath is negligible in the $A > 0$ cycle, while in the $A < 0$ cycle it is only noticeable at $E >\sim 100$ MeV/nuc but quite small.

The bottom panel of Figure 6.14 shows that the contributions of drifts and enhanced $K_{\perp\theta}$ to the total modulation in the heliosheath along the V1 heliolatitude can be made less significant in both magnetic polarity cycles by simply increasing the magnitude of k_e. Increasing

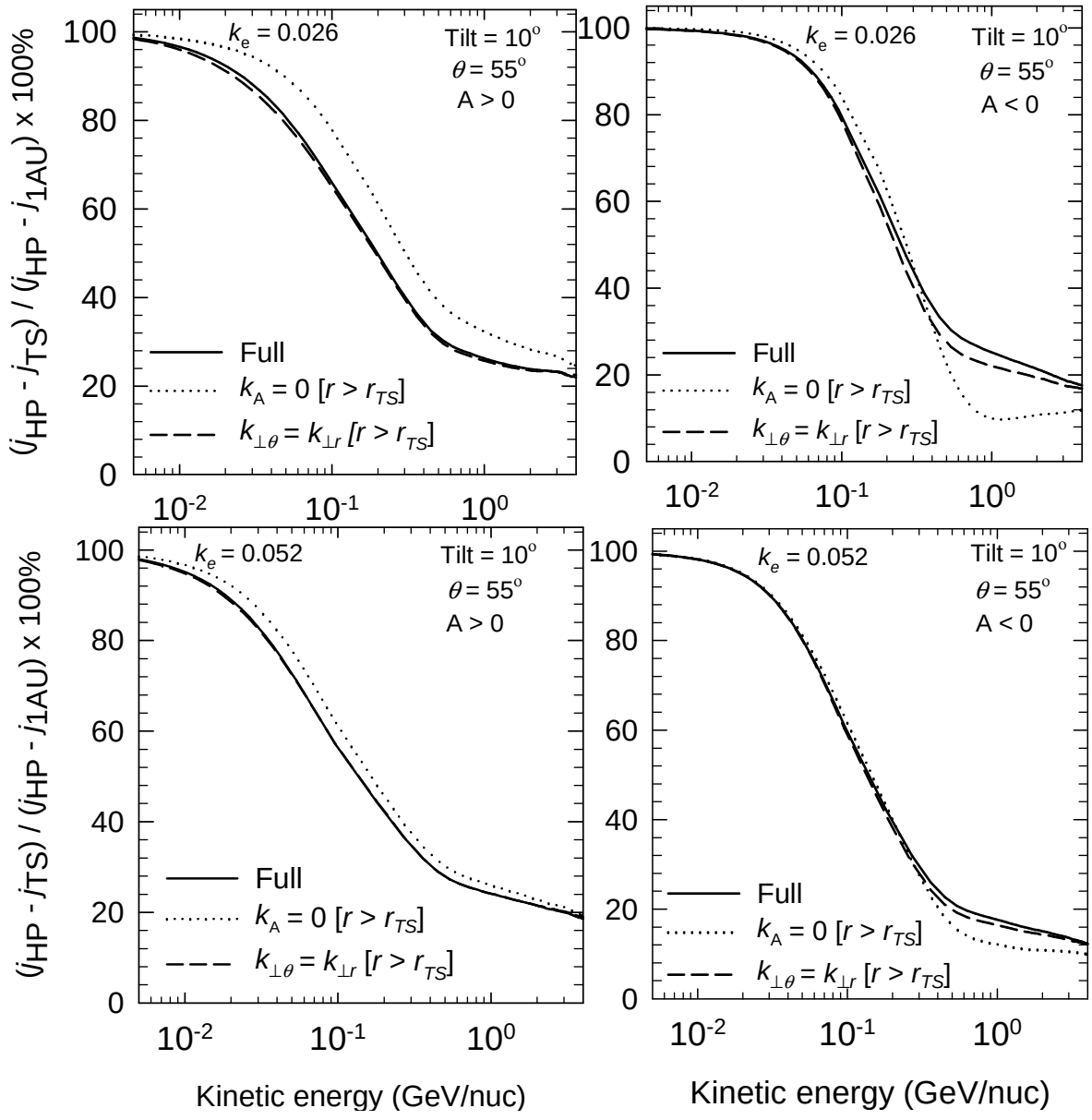

Figure 6.14: Computed ratio of GCR Carbon modulation in the heliosheath to the total modulation between the HP and 1 AU as a function of kinetic energy/nuc for both polarity cycles ($A > 0$ on the left; $A < 0$ on the right) at $\theta = 55^o$ and for solar minimum conditions ($\alpha = 10^o$). The solid lines correspond to solutions produced when the full model is assumed; the dotted lines without any drifts in the heliosheath ($k_A = 0$ in Equation 3.32 when $r > r_{TS}$); the dashed lines without any latitudinal enhancement in polar perpendicular diffusion in the heliosheath ($k_e = k_p$ in Equation 3.24 when $r > r_{TS}$). The top row shows solutions obtained with $k_e = 0.026$ and the bottom row with $k_e = 0.052$ in Equations 3.23 and 3.24.

this parameter is causing shock re-acceleration of GCRs to be less effective, without changing the shock's properties through its compression ratio (see also *Potgieter and Langner*, 2005). Thus, the bottom panel of this figure demonstrates that the total modulation in the heliosheath seems less sensitive to the variation in the modulation processes in the heliosheath when shock acceleration becomes insignificant.

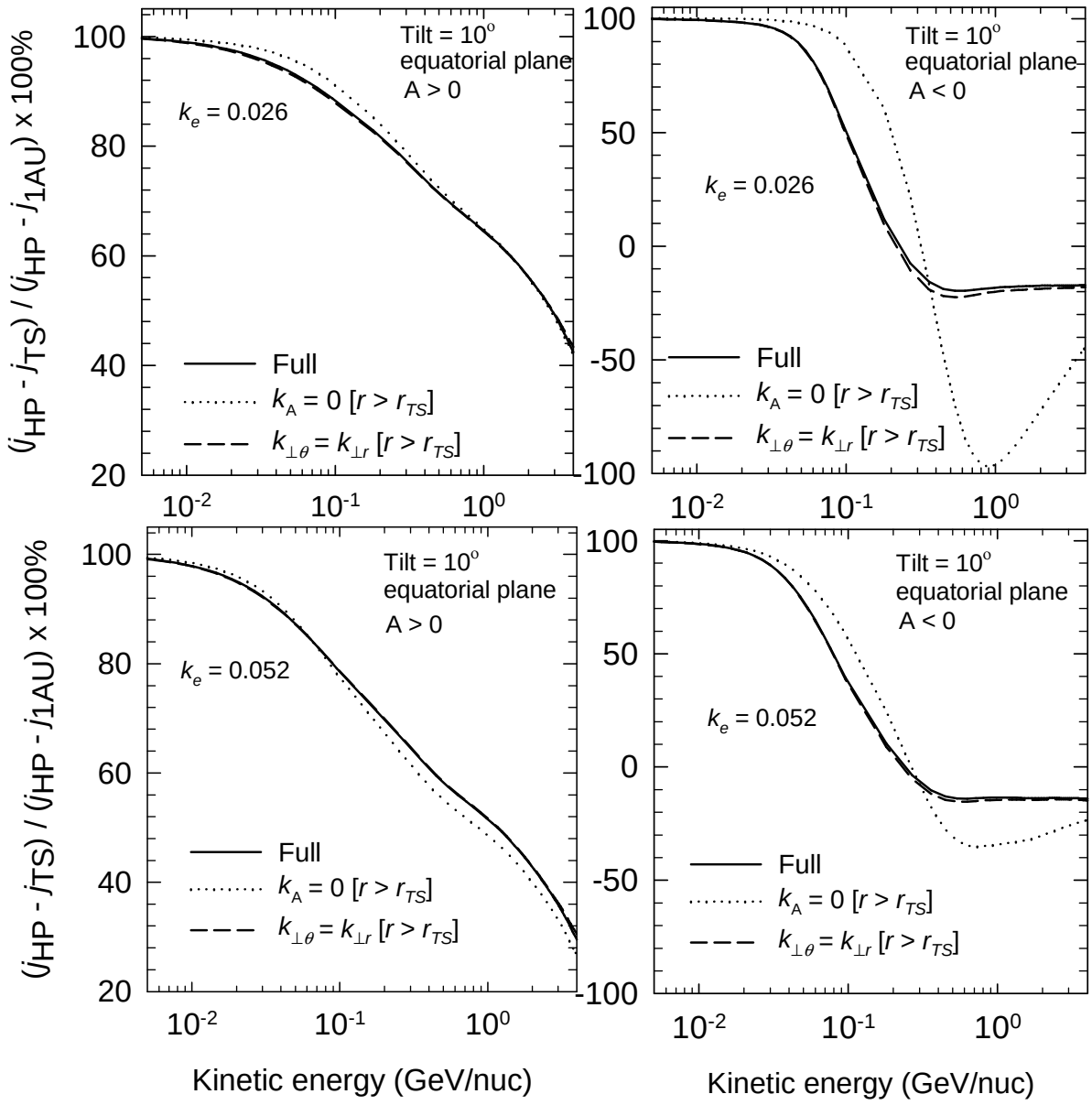

Figure 6.15: Similar to Figure 6.14 but now shown in the equatorial plane ($\theta = 90^o$).

Figure 6.15 is similar to Figure 6.14, but the modulation effects are now illustrated in the equatorial plane. The top panel indicates that in the $A > 0$ cycle the total modulation for the three scenarios are the same above ~ 1.0 GeV/nuc and only slightly different below this value. The effects of neglecting drifts in the heliosheath are most spectacular in the equatorial plane in the $A < 0$ cycle at $E >\sim 400$ MeV/nuc. As mentioned, the negative percentages present in Figure 6.15, especially for the $A < 0$ cycles, indicate that the Carbon intensities at the TS are higher than at the HP. This feature becomes even more enhanced, apparently unrealistically, when drifts are entirely neglected in the heliosheath, but less so when $k_e = 0.052$. This could indicate that neglecting drifts completely in the heliosheath is an oversimplification for the modulation in the equatorial plane in the $A < 0$ magnetic cycle. Hence, Figure 6.8 and Figure

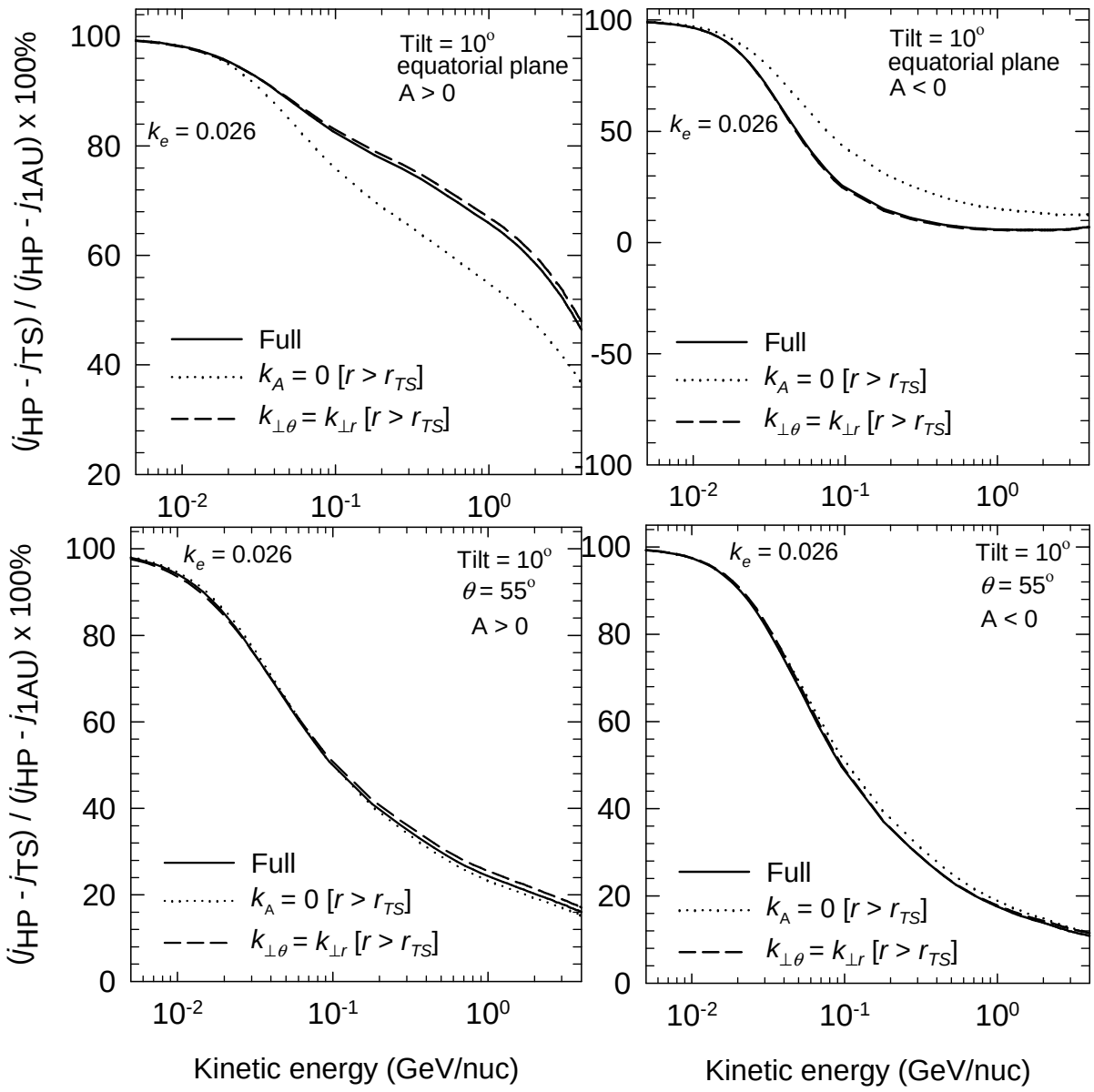

Figure 6.16: Similar to Figure 6.14 but now shown in the equatorial plane (top row) and at $\theta = 55^o$ (bottom row) without any re-acceleration of GCR Carbon at the TS ($s_k = 1.0$).

6.15 taken together, indicate that the drift reduction function as used in Equation 3.32 should also include a spatial dependence in the heliosheath that decreases towards the polar regions, that is, apart from the already implemented reduction in the rigidity dependence. To improve the understanding of drifts in the heliosheath, further advances in the effects of diffusive scattering on the drift coefficient, similar to the approach of *Burger and Visser* (2010), are needed to derive a self-consistent drift reduction function for the modulation of GCRs in the outer heliosphere. This avenue will be explored in the next chapter.

The compression ratio of the solar wind TS is an important parameter in modulation studies (see *Ngobeni and Potgieter*, 2008, 2010), affecting GCRs when they enter the heliospheric mod-

ulation region because with $s_k > 1.0$ they can experience re-acceleration at the TS. In Figure 6.16, the contribution of drifts and the enhancement of $K_{\perp\theta}$ in the heliosheath are illustrated for modulation that occurs in the heliosheath without the re-acceleration of GCRs at the TS (that is, with $s_k = 1.0$). In essence the only difference with Figure 6.14 and Figure 6.15 is that the TS does not re-accelerate GCRs anymore. The large negative percentage ratios as in the previous figure are therefore no longer present. The computed ratios in the top panels are for the equatorial plane whereas the bottoms panels are for $\theta = 55^o$. The solid lines correspond to solutions produced when the full model is used, the dotted lines without any drifts in the heliosheath ($k_A = 0$ in Equation 3.32 when $r > r_{TS}$) and the dashed lines without any latitudinal enhancement of $K_{\perp\theta}$ in the heliosheath ($k_e = k_p$ in Equation 3.24 when $r > r_{TS}$). Only the case with $k_e = 0.026$ in Equations 3.23 and 3.24 is shown. First, note that the effects of neglecting drifts in the heliosheath in determining the total modulation in the heliosheath become insignificant at $\theta = 55^o$ when no re-acceleration of GCR occurs at the TS for both drift cycles. In the equatorial plane the effects of neglecting drifts is to decrease the total modulation in the heliosheath in the $A > 0$ cycle at $E >\sim 20$ MeV/nuc, while in the $A < 0$ cycle the modulation increases in the heliosheath at roughly the same energy. The last two figures essentially demonstrate the interesting interplay between the re-acceleration of GCRs at the TS and drifts; see also the discussion of these aspects by *Potgieter and Langner* (2005) and *Langner and Potgieter* (2008).

The analysis above indicates that a more fundamental investigation into the importance and how much drifts occur in the outer heliosphere especially in the heliosheath is most relevant.

6.6 Global radial gradients

Two alternative ways of computing the radial gradients exist, namely a local and a non-local gradient (see e.g., *Potgieter et al.*, 1989). The local gradient is defined as the variation of the differential intensity Δj with the corresponding variation in radial distance Δr, and is simply given by

$$G_r = \frac{1}{j}\frac{\Delta j}{\Delta r}, \tag{6.2}$$

expressed in %/AU and can easily be computed at various energies and different positions with a numerical model. This local radial gradient is computed by *Ngobeni and Potgieter* (2010), approximating the theoretical expressions given as

$$g_r = \frac{1}{f}\frac{\partial f}{\partial r}. \tag{6.3}$$

Here f is the distribution function as defined in Chapter 3. The accuracy with which g_r is computed is determined by the spatial grid size used in the numerical model ($\Delta r \rightarrow 0 \Rightarrow G_r \rightarrow g_r$). This local radial gradient is unpractical to measure (one needs two closely spaced spacecraft at the same heliolatitude), so that a non-local or global radial gradient is calculated when a comparison with observed intensities by spacecraft probes is planned. (Spacecraft are separated by large spatial differences, e.g., V1, V2 and ACE.) This non-local radial gradient at position $r_2 > r_1$ with corresponding intensities j_2 and j_1 is defined as:

$$G_r^* = \frac{\Delta \ln j}{\Delta r} = \ln(\frac{j_2}{j_1})\frac{100\%}{r_2 - r_1}. \tag{6.4}$$

This form of radial gradient may also be calculated from differential intensities for a particular energy bin (instead of being integrated over an energy range), then called the non-local differential gradient. Since the calculation of observational spatial gradients is tricky, care must always be exercised how these observational gradients (e.g. *De Simone et al.*, 2011) are interpreted and when compared to modeling results.

Many authors reported on the observed radial gradients and their time variation based on direct observations (e.g., *Heber et al.*, 1993; *Fujii and McDonald*, 1999, 2001; *Webber and Lockwood*, 2004). Numerical calculations of these gradients have also been extensively illustrated (e.g., *Potgieter*, 1984; *Potgieter et al.*, 1989; *Ndiitwani*, 2005; *Ngobeni and Potgieter*, 2010; *Strauss and Potgieter*, 2010) and can explain the basic and prominent features of the observations.

It is shown next that it is possible to estimate the position of the HP along the V2 direction using the global radial gradient for GCR Carbon along the V1 direction observed between 110 AU and the HP. Because GCR Carbon is not contaminated by the ACRs, then gradients at lower energies (< 100 MeV/nuc) where the evolution of the global radial gradient changes largely beyond 110 AU can be used to undertake this kind of study. This study would not be possible for GCR Helium, Hydrogen and Oxygen due to severe contamination by the ACR components at these corresponding energies.

6.6.1 Inferring the heliopause position along the Voyager 2 direction using the observed global radial gradient along the Voyager 1 direction

Webber and Intriligator (2014) used the ratio of the observed TS crossings distances (of ~ 1.125) between the north and the south hemispheres to estimate the HP position along the V2 direction to be 108.2 ± 2.5 AU ($\sim 122 AU/1.125$). This implies that V2 should cross the HP between about the middle of 2014 to the end of 2015, which is conceivable if the motion of the HP is relatively small. The HP should not move too much because that would require motion of large volume of plasma, since it separates the solar and interstellar medium (see a discussion by *Washimi et al.*, 2011). From cosmic ray point of view, *Manuel* (2013) estimated the position

of the HP along V2 by using a time dependence in both the TS and the HP positions in their model to reproduce GCR proton intensities observed by V1 and V2 at $E > 70$ MeV/nuc (corresponding to a rigidity of 2.5 GV in their model) from 2002 to 2012. They found that reasonable compatibility between model solution and observations could be established when the HP distance along the V2 direction is placed at 100 ± 3 AU. It is noted that at $E > 70$ MeV/nuc there may still be significant contamination of GCR protons by the ACR components. Also that the HPS of GCR species as observed by V1 were not yet available. Since GCR Carbon is clean of anomalous components, the position of the HP along the V2 direction can be estimated using GCR Carbon global radial gradients measured by V1 from 2010 till 2012 when it observed the HP.

Equation 6.4 can be re-arranged to calculate the position of r_2 in terms of r_1, j_1, j_2 and G_r^* as

$$r_2 = \ln\left[\frac{j_2}{j_1}\right]\frac{100\%}{G_r^*} + r_1. \tag{6.5}$$

Since information about the GCR Carbon intensities in 2010, positions of V1, V2 and the HP position along the V1 (r_{HP1}) direction together with the HPS (j_{HPS}) is available, the HP position along the V2 direction (r_{HP2}) can be estimated from Equation 6.5 as follows

$$r_{HP2} = \ln\left[\frac{j_{HPS}}{j_{2010}^{v2}}\right]\frac{100\%}{G_r^{*,v2}} + r_{v2,2010}, \tag{6.6}$$

where j_{2010}^{v2} and $r_{v2,2010} = 92$AU are respectively the GCR Carbon intensity observed by V2 and its radial position in 2010, while $G_r^{*,v2}$ is the global radial gradient along the V2 direction between 2010 and r_{HP2}. Unfortunately, $G_r^{*,v2}$ is not yet available and then one should rely on the global radial gradient along the V1 direction, $G_r^{*,v1}$, to estimate the position of the HP along the V2 direction making this approach highly idealized but still interesting and informative.

Shown in Table 6.1 is the calculated HP position along the V2 direction using the global radial gradient observed by V1 from 2010 till it observed the HP at ∼122 AU. Here j_{2010}^{v1} represents GCR Carbon intensities observed by V1 in 2010 at a radial distance of ∼114 AU; j_{2010}^{v1}, j_{2010}^{v2} and j_{HPS} are in units of particles m^{-2} s^{-1} sr^{-1} MeV^{-1}.

Table 6.1: Estimation of the HP position along the V2 direction using the global radial gradients observed by V1 between 2010 and 2012 ($G_r^{*v1} = G_r^{*v2}$ is assumed).

Energy (GeV/nuc)	j_{2010}^{v1} ($r = 114$ AU)	j_{2010}^{v2} ($r = 92$ AU)	j_{HPS}	G_r^{*v1}(%/AU)	r_{HP2} (AU)
0.029	0.00615	0.004	0.0300	17.6	103.4
0.047	0.00942	0.00538	0.0345	14.4	104.9
0.070	0.0129	0.0085	0.0397	12.5	104.3
0.095	0.0168	0.0110	0.0353	8.3	106.1

As indicated in Table 6.1, the average calculated HP distance along the V2 direction is ~ 104.6 AU if it were to observe the same global radial gradient as V1 did from 2010 up to the HP.

However, it is noted that V2's radial position is already at $\sim$ 104.6 AU in mid 2014 and its solar wind radial velocity component is still large indicating that it is not yet close to the HP (*Richardson*, 2013).

In Table 6.2 the estimated HP distance along the V2 direction together with the heliosheath width (HS) and the expected time of crossing are shown based on the assumption that V2 will observe global radial gradients for GCR Carbon that are smaller than those observed by V1 ($G_r^{*v1} > G_r^{*v2}$) by a factor ranging from 0.5 to 0.9. It can be seen in this table that when the

Table 6.2: Estimated HP position along the V2 direction together with the heliosheath width (HS) and the expected time of crossing.

$G_r^{*v2}(\%/\text{AU})$	r_{HP2} (AU)	HS width (AU)	Year of HP crossing
$0.9G_r^{*v1}$	106	22	end 2014/beginning 2015
$0.8G_r^{*v1}$	108	24	mid 2015
$0.7G_r^{*v1}$	110	26	end 2015/ beginning 2016
$0.6G_r^{*v1}$	113	29	beginning 2017
$0.5G_r^{*v1}$	117	33	mid 2018

difference in global radial gradients between V1 and V2 at lower energies is $<\sim 30\%$, then V2 is expected to cross the HP not later than the year 2016. Otherwise it would imply that the observed heliosheath width is wider in the south than in the north hemisphere contrary to MHD modeling results (see *Opher et al.*, 2009; *Pogorelov et al.*, 2009). Or, alternatively, that the HPS is non-isotropic and higher in the direction of V2. From this analysis it appears that a reasonable position of the HP along the V2 direction is at $r = 108 \pm 2$ AU, consistent with the prediction of *Webber and Intriligator* (2014).

6.7 Summary and conclusion

In this chapter, the modulation of GCR Carbon at the Earth was investigated with a 2D numerical model that contains a termination shock, a heliosheath, the re-acceleration of GCRs at the TS and drifts. GCR Carbon has the advantage that it is not contaminated by the anomalous component which is not the case for protons and Helium. For the first time a new HPS (as unmodulated input spectrum) for low energies (~ 5 MeV/nuc $> E <\sim 300$ MeV/nuc) is used. This HPS was observed by V1 at $\sim$ 122 AU for $E < 200$ MeV/nuc and is found to be significantly higher than previous estimates of *Webber and Higbie* (2009), for example, at $E = 10$ MeV/nuc and $E = 100$ MeV/nuc by a factor of ~ 2.0 and ~ 1.6 respectively. This contributes significantly at these lower energies to the total modulation as a function of position in the heliosphere. The new HPS for GCR Carbon is given by Equation 6.1. It was found that the total modulation between the HP and the Earth during solar minimum in the $A > 0$ cycle at 10 MeV/nuc amounts to $\sim$ 4.5% of the HPS, whereas for 100 MeV/nuc it is $\sim$ 17.5%. Respectively,

this means that the global radial gradient between the HP and the Earth for GCR Carbon for this period was $\sim 2.5\%/\text{AU}$ and $\sim 1.4\%/\text{AU}$, if the HP is taken at 122 AU.

Modeling results were shown at the Earth for the previous solar minimum, an $A > 0$ cycle with $\alpha = 10^o$, for a moderate solar maximum in an $A < 0$ cycle with $\alpha = 50^o$, and for the recent solar minimum, an $A < 0$ cycle, also with $\alpha = 10^o$. For moderate solar maximum conditions, adjustment of $K_{||}$ by a factor of 0.6 and for both perpendicular diffusion coefficients, $K_{\perp r}$ and $K_{\perp \theta}$, by a factor of 1.5 with respect to their assumed previous solar minimum values were found to be optimal to establish compatibility with ACE observations. While for the recent solar minimum (around 2009) reasonable compatibility with observations is obtained only when $K_{||}$ is increased by a factor of 1.4 and with full drifts assumed relative to their previous solar minimum values. The change in modulated spectra at the Earth from solar maximum (2001-2003) to the recent minimum was found to exceed the difference between the HPS and the modulated spectrum at the Earth during the recent solar minimum at $E >\sim 30$ MeV/nuc.

The numerical model was also applied to study modulation in the outer heliosphere, especially inside the heliosheath. The computed spectra were shown for solar minimum conditions ($\alpha = 10^o$) at radial distances of 60 AU, 90 AU, 100 AU and 110 AU and were compared to observations taken inside off the TS ($r < r_{TS}$) in the $A > 0$ cycle, and inside the heliosheath ($r > r_{TS}$) in the $A < 0$ cycle. Reasonable compatibility with corresponding Voyager observations in both polarity cycles was established when drifts were scaled to zero in the heliosheath and $k_e = 0.026$ in Equations 3.23 and 3.24. This can be interpreted to indicate that drifts in the heliosheath play a less important role at these (Voyager) heliolatitudes, but it is not to say that drifts do not occur at all in the heliosheath.

In addition, the contribution of drifts and the enhancement of $K_{\perp \theta}$ in the heliosheath were investigated and illustrated by computing the ratio of the modulation in the heliosheath to the total modulation between the HP and 1 AU: $(j_{HP} - j_{TS})/(j_{HP} - j_{1AU})$. This was done for three scenarios, the full model with all its assumptions, then for drifts scaled to zero in the heliosheath ($k_A = 0$ in Equation 3.32 when $r > r_{TS}$) and for the enhancement of $K_{\perp \theta}$ neglected in the heliosheath ($k_e = k_p$ in Equation 3.24 when $r > r_{TS}$). A general result is that the effect of neglecting drifts in the heliosheath is more significant than neglecting the enhancement of $K_{\perp \theta}$, which is important in the inner heliosphere e.g. to explain the small latitudinal gradients observed by Ulysses. When drifts were entirely neglected in the heliosheath, the intensities in the equatorial plane close to the TS, where GCRs are re-accelerated, became spectacularly larger than the HPS values in the $A < 0$ cycle, resulting in unrealistic large percentage ratios (shown in Figure 6.15). This means that drifts are needed to transport particles away from the TS (in the nose direction of the heliosphere) during this cycle otherwise it would be a very effective and evident source of re-accelerated GCRs and even ACRs. Since there is a complex

interplay between drifts and the re-acceleration of GCRs at the TS, this may indicate that drifts cannot be neglected in the heliosheath, so that further investigation is need.

It was found that the drift reduction function as used in this chapter, and the previous chapters, should also include a spatial dependence in the heliosheath that decreases towards the polar regions, apart from the already implemented reduction in the rigidity dependence.

Finally, the global radial gradients of GCR Carbon along the V1 direction at low energies ($E < 100$ MeV/nuc) were used to estimate the position of the HP along the V2 direction. It is predicted that V2 could observe the HP at $r = (108 \pm 2)$ AU sometime between the end of 2014 and the beginning of the year 2016, consistent with the prediction of *Webber and Intriligator* (2014).

In the next chapter further advances of the effects of scattering on the drift coefficient are studied.

Chapter 7

Drift reduction in the heliosphere

7.1 Introduction

It is well known that particle drift motions are suppressed by diffusive scattering as established by direct numerical simulations (*Giacalone et al.*, 1999; *Minnie et al.*, 2007; *Tautz and Shalchi*, 2012). The effect of constant scattering on the drift velocities of charged particles has always been included in numerical modulation models provided that the weak scattering drift velocity is scaled down in magnitude, although in a phenomenological manner as comparisons between drift models and observations required or in an $ad\ hoc$ theoretical manner, as discussed in Chapter 3. Progress has been made especially concerning the rigidity dependence of the drift coefficient close to the Earth. What has not yet been established is the spatial dependence of the scattering parameter, $\omega\tau$, as will be defined below but progress has been made (see e.g. *Burger and Visser*, 2010).

In this chapter what is currently known about the spatial and rigidity dependence of the scattering parameter $\omega\tau$ is used to illustrate, evaluate and discuss its effects on the drift coefficient for the modulation of GCR Carbon in the heliosphere.

7.2 Drift coefficient

Following on the introductory discussion in Chapter 3, in the general case the average drift velocity caused by the gradient and curvature in the HMF is given by

$$\langle \mathbf{v}_d \rangle = \nabla \times K_T \frac{\mathbf{B}}{B_m}, \tag{7.1}$$

with K_T the generalized drift coefficient, $\mathbf{B}$ the HMF vector with magnitude B_m. The generalized drift coefficient based on assuming weak scattering with $\omega\tau \gg 1.0$ is then given as

$$K_T = \frac{\beta P}{3B_m} f_s, \tag{7.2}$$

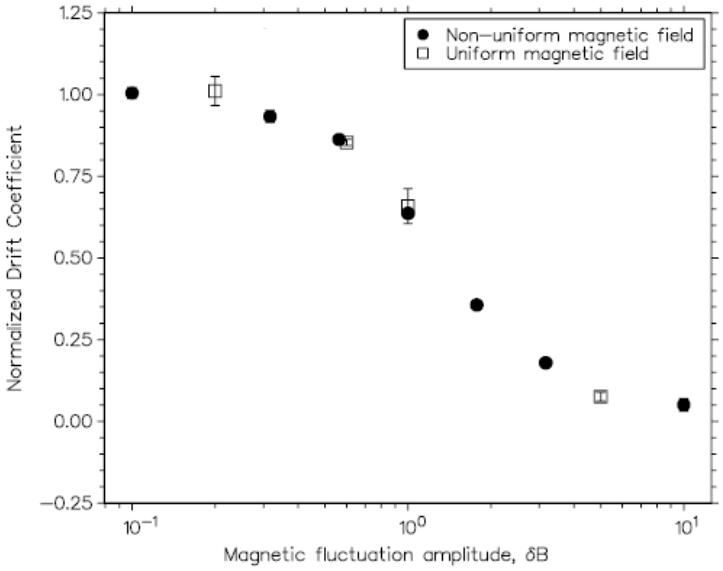

Figure 7.1: Drift coefficient, normalized to the weak scattering value, as a function of magnetic fluctuation amplitude δB. Adapted from *Minnie et al.* (2007).

where f_s is the drift reduction function due to diffusive scattering, with P the particle rigidity and β the ratio of the particle speed to the speed of light as in Chapter 3. It follows from Equation 7.2 that when $f_s = 0$ drift velocities become zero and when $f_s = 1.0$ drift velocities become maximal when weak scattering is assumed. The expression for f_s is given by *Bieber and Matthaeus* (1997) as

$$f_s = \frac{(\omega\tau)^2}{1 + (\omega\tau)^2}, \tag{7.3}$$

where ω is the gyro-frequency and τ represent some time scale defined by scattering. As a result Equation 7.1 can be re-written as

$$\langle \mathbf{v}_d \rangle = \frac{\beta P}{3} \left[f_s \nabla \times \frac{\mathbf{B}}{B_m^2} + \nabla f_s \times \frac{\mathbf{B}}{B_m^2} \right]. \tag{7.4}$$

It follows from Equation 7.4 that when f_s is constant, meaning no spatial dependence in $\omega\tau$, the term $\nabla f_s = 0$. As a result the effect of particle scattering on the drift velocity is to reduce its magnitude by a constant factor f_s (see also *Jokipii*, 1993). In this case the spatial dependence of the HMF remains the only driver of the gradient and curvature drifts. However, when $\omega\tau$ has a spatial dependence $\nabla f_s \neq 0$ and the second term on the right hand side of Equation 7.4 can have significant effects on the drift coefficient.

Interest in the effects of turbulent magnetic fields on the weak scattering drift coefficient has increased (see *Giacalone et al.*, 1999; *Minnie et al.*, 2007; *Burger and Visser*, 2010; *Tautz and Shalchi*, 2012). An example is shown in Figure 7.1 of the drift coefficient, normalized to the weak scattering value, as a function of magnetic fluctuation amplitude δB calculated from the numerical simulations of *Minnie et al.* (2007). It is evident from this figure that for sufficiently strong turbulence ($\delta B > 4$), the maximal weak scattering drift coefficient is significantly suppressed.

7.3 Drift reduction caused by a constant $\omega\tau$

In the past it became apparent that drift models often describe observations of CRs better when drifts are reduced, meaning when $f_s < 1.0$ in Equation 7.4 (see *Potgieter et al.*, 1989; *Ferreira*, 2002; *Ndiitwani et al.*, 2005; *Langner*, 2004). This indicates that maximal weak scattering drifts result in excessive drift effects. See e.g. *Jokipii and Kopriva* (1979) as an example of such effects.

From Equation 7.3 three scenarios of f_s are trivially distinguishable depending on the value of $\omega\tau$:

- for $\omega\tau \longrightarrow 0 \Longrightarrow f_s \longrightarrow 0$, no particle drifts present.
- for $\omega\tau = 1.0 \Longrightarrow f_s = 0.5$, particle drifts are present but reduced by half compared to the maximal weak scattering value.
- for $10 \leq \omega\tau \leq \infty \Longrightarrow f_s \longrightarrow 1.0$, the particle drift assumes its maximal weak scattering value.

The three scenarios above can be used as a starting point to gain insight into the range of magnitudes of the parameter $\omega\tau$ reasonable for CR modulation studies. The question to ask is what information can be gained from other values of $\omega\tau$ in addition to the above mentioned three scenarios? In answering this question, the first step to be taken is to link the scaling down of the weak scattering drift velocities to different values of $\omega\tau$. This is shown in Table 7.1 with $\langle \mathbf{v}_d \rangle^{ws}$ denoting the maximal weak scattering drifts velocity. Note that when $f_s = 1.0, 0.5,$ and 0 respectively, Equation 7.4 describes what *Potgieter et al.* (1989) called 100% (full drifts), 50% (half drifts) and no-drifts. It follows from Table 7.1 that, for example, when $\omega\tau = \frac{1}{3}$ particle drifts are scaled down to 10% of the weak scattering values. Also that when $\omega\tau = \frac{1}{2}$ only 20% particle drifts are assumed in the heliosphere. Thus, the effects of constant $\omega\tau$ on the drift coefficient have always been implicitly included in numerical modulation models. What has not yet been established is the effects of the spatial dependence of $\omega\tau$.

It can also be easily noted in Table 7.1 that all values of $\omega\tau$ between 5 and ∞ contribute to only $<\sim 4\%$ reduction of $\langle \mathbf{v}_d \rangle^{ws}$. Evidently, $\sim 96\%$ reduction in $\langle \mathbf{v}_d \rangle^{ws}$ is contained in values of $\omega\tau$ that are ≤ 5. This clearly indicates that values of $\omega\tau$ that can result in reasonable drift reduction for CR modulation in the heliosphere range from $0 \leq \omega\tau \leq 5$. However it is noteworthy to mention that when $\omega\tau$ has a constant value, particle drift speeds at all rigidities are scaled down by the same magnitude, which is not necessarily the case since particles of different rigidities are scattered differently by the HMF. The important point here is that from the analyses made it is found that $\omega\tau \leq 5$ to achieve reasonable drift reduction. Next the rigidity dependence of $\omega\tau$ is evaluated from what is currently known to further gain insight into a plausible range of values of this parameter.

Table 7.1: Estimation of the range of values of $\omega\tau$ reasonable for drift reduction in the heliosphere.

$\omega\tau$	f_s	$\langle \mathbf{v}_d \rangle$	level of drifts
0	0	0	0%
$\frac{1}{3}$	$\frac{1}{10}$	$\left[\frac{1}{10}\right] \langle \mathbf{v}_d \rangle^{ws}$	10%
$\frac{1}{2}$	$\frac{2}{10}$	$\left[\frac{2}{10}\right] \langle \mathbf{v}_d \rangle^{ws}$	20%
1	$\frac{5}{10}$	$\left[\frac{5}{10}\right] \langle \mathbf{v}_d \rangle^{ws}$	50%
2	$\frac{8}{10}$	$\left[\frac{8}{10}\right] \langle \mathbf{v}_d \rangle^{ws}$	80%
3	$\frac{9}{10}$	$\left[\frac{9}{10}\right] \langle \mathbf{v}_d \rangle^{ws}$	90%
5	$\frac{25}{26}$	$\left[\frac{9.62}{10}\right] \langle \mathbf{v}_d \rangle^{ws}$	96.2%
10	$\frac{100}{101}$	$\left[\frac{9.9}{10}\right] \langle \mathbf{v}_d \rangle^{ws}$	99%
$\rightarrow \infty$	$\frac{10}{10}$	$\left[\frac{10}{10}\right] \langle \mathbf{v}_d \rangle^{ws}$	100%

7.4 Rigidity dependence of $\omega\tau$

A relatively simple functional form of $\omega\tau$ that depends only on rigidity can be constructed easily from studies done by *Burger et al.* (2000) and is written as:

$$\omega\tau = \sqrt{k_A \frac{\left(P/P_0^{'}\right)^2}{1 + (1 - k_A)\left(P/P_0^{'}\right)^2}}, \tag{7.5}$$

with P the rigidity, k_A a dimensionless constant ranging from 0 to 1.0 and $P_0^{'} = \frac{1}{\sqrt{10}}$ GV as in Chapter 3. Following Equation 7.3 the corresponding drift reduction function and drift coefficient respectively become

$$f_s = k_A \frac{\left(P/P_0^{'}\right)^2}{1 + \left(P/P_0^{'}\right)^2}. \tag{7.6}$$

and

$$K_T = k_A \frac{\beta P}{3B_m} \frac{\left(P/P_0^{'}\right)^2}{1 + \left(P/P_0^{'}\right)^2}. \tag{7.7}$$

It is easy to note that Equation 7.7 is the same as Equation 3.32. The essence of Equation 7.7 is that below ~ 1.0 GV drifts are reduced with respect to the weak scattering case when $k_A = 1.0$. Take note that for $k_A = 1.0$, $\omega\tau$ reduces to $P/P_0^{'}$ which is the assumption made by *Burger et al.* (2000). However, when $k_A < 1.0$ drifts are also reduced at rigidities above 1.0 GV. Thus any value $k_A < 1.0$ specifies the amount of drifts allowed above 1.0 GV with respect to the weak scattering case. It must be noted that $\omega\tau$ in Equation 7.5 has no spatial dependence,$\nabla f_s =$

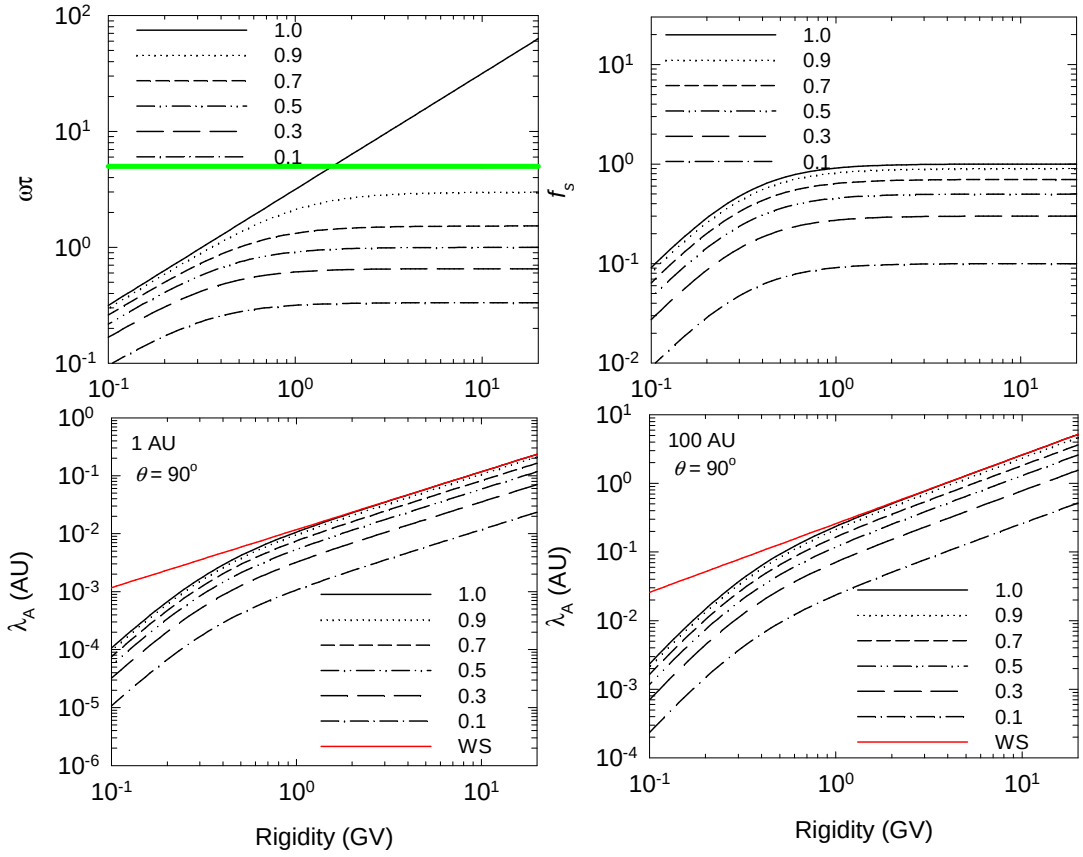

Figure 7.2: The top row shows the scattering parameter $\omega\tau$ (left panel), as given by Equation 7.5, and the drift reduction function (right panel), as given by Equation 7.6, as a function of rigidity in GV for different values of k_A. In the bottom row the corresponding drift scales λ_A, in AU, together with their weak scattering values (represented by red lines and denoted WS) are shown at radial distances of 1 AU (left panel) and 100 AU (right panel) in the equatorial plane with $\theta = 90^o$. The green horizontal line in the top row represents $\omega\tau = 5$.

0 also in this case. Equation 7.7 has been used in many modulation models but assuming different values for k_A (*Burger et al.*, 2000; *Ferreira*, 2002; *Langner*, 2004; *Ndiitwani*, 2005; *Ngobeni and Potgieter*, 2011). In the previous chapter it was shown that $k_A = 0.5$ is reasonable for modulation inside off the TS ($r < r_{TS}$), while $k_A = 0$ in the heliosheath ($r > r_{TS}$) is required to fit observations in the outer heliosphere. It was also shown that to fit observations at the Earth in the recent (new) solar cycle in the $A < 0$, $k_A = 1.0$ is required (see also a detailed discussion by *Potgieter et al.*, 2013).

The top row in Figure 7.2 shows $\omega\tau$ (left panel), as given by Equation 7.5, and f_s (right panel), as given by Equation 7.6, as a function of rigidity for different values of k_A. The green horizontal line is drawn at $\omega\tau = 5$ for comparison. It is striking to note that $\omega\tau$ changes dramatically above 1.0 GV when k_A is decreased from 1.0 to 0.9, e.g., at a rigidity of 20 GV $\omega\tau$ decreases from a magnitude of ~ 65 to ~ 3. However, the change in f_s is not as nearly as large. In essence above 1.0 GV, f_s is ~ 1.0 when $k_A = 1.0$ and ~ 0.9 when $k_A = 0.9$. What can also be noted is that for any value of $\omega\tau > 5$, f_s remains ~ 1.0. This indeed confirms the earlier prediction that

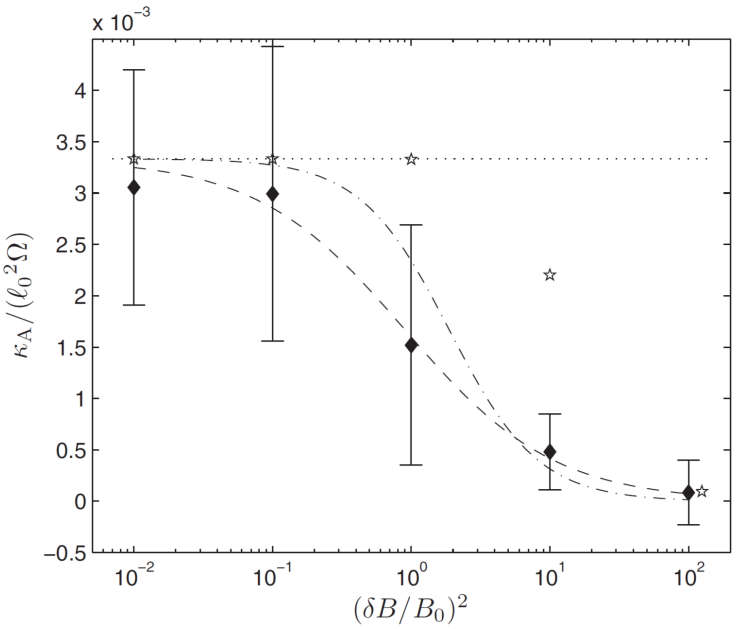

Figure 7.3: Simulated drift coefficient, indicated as diamonds with error bars, for 15% slab and 85% 2D turbulence for different values of the turbulent magnetic field strength, δB, normalized to the background magnetic field, B_0. The dotted line denotes the weak scattering limit whereas the stars illustrate the classical scattering results. The dashed line and dash-dot lines illustrate results from the analytical expression given by Equation 7.8 for different values of a and b. Note that κ_A in the figure denotes K_T. Adapted from *Tautz and Shalchi* (2012).

effective drift reduction takes place when $\omega\tau \leq 5$. This is clearly articulated in the bottom row of this figure.

The bottom row of Figure 7.2 shows the drift scale λ_A, given by Equation 3.33, as a function of rigidity for different values of k_A at radial distances of 1 AU and 100 AU in the equatorial plane ($\theta = 90^o$). Also shown for comparison, represented by red lines, is the maximal weak scattering drift scale. It can be noted that for $k_A = 1.0$ the drift scale is the same as the weak scattering value above 1.0 GV and this occurs only when $\omega\tau > 5$. It is also clearly seen that when $k_A < 1.0$ the maximal weak scattering drift scale is also reduced at rigidities > 1.0 GV by the magnitude of k_A. In the next section attention is switched to the spatial dependence of $\omega\tau$.

7.5 Spatial dependence of $\omega\tau$

Recently, *Tautz and Shalchi* (2012) used a numerical Monte Carlo test-particle simulation code to calculate the drift coefficient by integrating the trajectories of charged particles that are scattered in the turbulent magnetic fields. Figure 7.3 shows their normalized K_T as a function of the average turbulence strength normalized to the background field magnitude for composite turbulence. As before K_T is evidently suppressed when the relative turbulence strength is

increased. The best fit to the simulated K_T in Figure 7.3 is given by the following analytical expression:

$$K_T = \frac{\beta P}{3B_m} \frac{1}{1 + a\left[\frac{\delta B}{B_m}\right]^{2b}}. \tag{7.8}$$

Where for a composite turbulence model with 15% slab and 85% 2D they achieved good correlation between numerical simulations and Equation 7.8 when $a = 1.09 \pm 0.52$ and $b = 0.81 \pm 0.35$ as seen in Figure 7.3 and represented by the dashed line. Following Equation 7.2, the corresponding f_s can be written as

$$f_s = \frac{1}{1 + a\left[\frac{\delta B}{B_m}\right]^{2b}}. \tag{7.9}$$

It thus become possible to relate f_s in Equation 7.9 to $\omega\tau$. Following *Bieber and Matthaeus* (1997), although the turbulence models are different, the corresponding $\omega\tau$ can be approximated as

$$\omega\tau = \frac{1}{\sqrt{a}\left[\frac{\delta B}{B_m}\right]^{b}}. \tag{7.10}$$

Clearly, f_s given by Equation 7.9 has no rigidity dependence but $\nabla f_s \neq 0$. Equations 7.9 and

Table 7.2: Estimation of the range of values of $\omega\tau$ reasonable for drift reduction in the heliosphere from Tautz and Shalshi (2012).

	$\delta B/B_m$	$\omega\tau$	f_s	level of drifts
$a = 0.57$ and $b = 0.46$	0.01	11	0.99	99%
	0.1	3.82	0.94	94%
	0.5	1.82	0.77	77%
	1	1.33	0.64	64%
	2	0.96	0.48	48%
$a = 1.61$ and $b = 1.16$	0.01	164.65	1.0	100%
	0.1	11.39	0.99	99%
	0.5	1.76	0.76	76%
	1	0.79	0.38	38%
	2	0.35	0.11	11%

7.10 can be useful to estimate plausible values of $\omega\tau$ similar to what has been done in Table 7.1. This is shown in Table 7.2 for different levels of turbulence, as denoted by the ratio $\delta B/B_m$, and different values of both a and b. It is evident from this table that for values of $\omega\tau > 5$ there is no substantive drift reduction, confirming the earlier argument that $\omega\tau \leq 5$ to achieve reasonable drift reduction in the heliosphere. It can also be noted that when the ratio $\delta B/B_m$ increases drift reduction becomes strong (*Minnie et al.*, 2007). Unfortunately, Equations 7.9 and 7.10 have no rigidity dependences. Furthermore, the value of drift reduction as calculated in Table 7.2 will be altered by $\nabla f_s \neq 0$ as required by Equation 7.9, which is not included for this simple analysis. Thus, the values in Table 7.2 should be viewed as a first order estimate of $\omega\tau$.

The values of $\omega\tau$ that contain both rigidity and spatial dependences are given by *Bieber and Matthaeus* (1997) and written as

$$\omega\tau = \frac{2}{3}\frac{R_L}{D_\perp}, \tag{7.11}$$

where R_L is the particle gyro-radius and $D_\perp$ is the field line diffusion coefficient describing the perpendicular de-correlation of the magnetic field lines. The expression for $D_\perp$ is taken from *Matthaeus et al.* (1995) and is given by

$$D_\perp = \frac{1}{2}\left[D_{slab} + \sqrt{D_{slab}^2 + 4D_{2D}^2}\right]. \tag{7.12}$$

D_{slab} represents the field line diffusion coefficient due to slab fluctuations and D_{2D} due to 2D fluctuations. The expressions for both D_{slab} and D_{2D} are given in *Matthaeus et al.* (2007) as

$$D_{slab} = \frac{1}{2}\frac{\delta B_{slab}^2}{B_m^2}\lambda_{slab} \tag{7.13}$$

and

$$D_{2D} = \frac{\sqrt{\delta B_{2D}^2/2}}{B_m}\lambda_{ultra} \tag{7.14}$$

where λ_{slab} and λ_{ultra} denotes the slab correlation length and 2D turbulence ultrascale respectively. The expression for λ_{slab} is given by *Burger et al.* (2008) as

$$\lambda_{slab} = \frac{1}{k_{min}}, \tag{7.15}$$

with the analytical expression for k_{min} given by Equation 3.21.

Burger and Visser (2010) pointed out that Equation 7.11 results in large drift reduction and as such does not fit direct numerical simulations of *Minnie et al.* (2007). They parameterized Equation 7.11 to become:

$$\omega\tau = \frac{11}{3}\frac{\sqrt{R_L/\lambda_{slab}}}{[D_\perp/\lambda_{slab}]^g}, \tag{7.16}$$

where

$$g = 0.3\log_{10}\left[\frac{R_L}{\lambda_{slab}}\right] + 1.0. \tag{7.17}$$

Because as of yet no measurements of λ_{ultra} is available, *Burger and Visser* (2010) used an $ad\ hoc$ function of this turbulence parameter by assuming that it depends only on radial distance and has a magnitude of 0.3 AU at the Earth. Their analytical expression for λ_{ultra} is given by the following equation:

$$\lambda_{ultra} = 0.3\left[\frac{r}{r_0}\right]^{0.4} AU. \tag{7.18}$$

Here r is in AU and r_0 is a constant with a magnitude of 1.0 AU. They came to the conclusion that an $ab\ initio$ calculation of the λ_{ultra} is required, but then both the perpendicular and the parallel mean free paths will change if the 2D ultrascale changes due to a different choice for the turbulence spectrum. The values of λ_{ultra} by *Burger and Visser* (2010) are directly implemented in our numerical model and the results will be shown. Next, an attempt is made to

use the turbulence model of *Engelbrecht and Burger* (2013) to calculate the ultrascale driven by turbulence spectra rather than an *ad hoc* assumption as done by *Burger and Visser* (2010).

A more fundamental expression of λ_{ultra} is given by *Engelbrecht and Burger* (2013) based on studies done by *Matthaeus et al.* (2007) as

$$\lambda_{ultra} = \sqrt{C_0 \lambda_{2D} \left[\left(\frac{1}{q-1} + 1 \right) \lambda_{out} + \left(\frac{1}{s+1} - 1 \right) \lambda_{2D} \right]}, \tag{7.19}$$

where

$$C_0 = \left[1 + \left(\frac{1}{q+1} - 1 \right) \frac{\lambda_{2D}}{\lambda_{out}} + \left(\frac{1}{s-1} \right) \right]^{-1}, \tag{7.20}$$

with $s = 5/3$ the spectral index in the inertial range and q the spectral index in the "outer range" which is set to 3. Here, λ_{2D} and λ_{out} denote the 2D bend over scale and the outer scale respectively. It was further assumed in their model that:

$$\lambda_{out} = 12.5 \lambda_{c,2D}, \tag{7.21}$$

where $\lambda_{c,2D}$ is the 2D correlation scale length.

To calculate $\omega\tau$ similar to that of *Engelbrecht and Burger* (2013), information about $\lambda_{c,2D}$ is needed. Unfortunately, the model used in this study does not calculate the turbulence quantities from the fundamental theory as done by *Engelbrecht and Burger* (2013). However, further improvements can be made, in the context of the model used, to calculate different scenarios of how $\lambda_{c,2D}$ changes with radial distance and with latitude. To establish reasonable scenarios, values of $\lambda_{c,2D}$ as a function of latitude from *Engelbrecht and Burger* (2013) model based on the turbulence model of *Oughton et al.* (2011) were obtained at radial distances of 1 AU and 100 AU for a rigidity of 0.5 GV. To obtain an analytical expression that represents both the radial and latitude dependence of $\lambda_{c,2D}$, the following expression is used to approximate the predicted values of the results of *Engelbrecht and Burger* (2013):

$$\lambda_{c,2D} = \varrho \left[\frac{r}{r_0} \right]^{\sigma} \Gamma(\theta) AU, \tag{7.22}$$

where $\varrho = 0.006$ and $\sigma = 0.4$ are dimensionless quantities, whereas $\Gamma(\theta)$ is a function that enhances $\lambda_{c,2D}$ towards the poles with respect to its value in the equatorial plane. From Equation 7.22, two different scenarios for $\lambda_{c,2D}$ were obtained that are used to calculate λ_{ultra} and the corresponding $\omega\tau$ in the model. The two scenarios of $\lambda_{c,2D}$ are shown in Figure 7.4 as a function of polar angle at radial distances of 1 AU and 100 AU in comparison with results from the turbulence model of *Engelbrecht and Burger* (2013). Scenario (a) corresponds to the assumption that $\lambda_{c,2D}$ increases by a factor of 2.3 over the poles with respect to its value in the equatorial plane; for scenario (b) $\lambda_{c,2D}$ enhances by a factor of 6 over the poles. From these fits it follows that at 1 AU $\lambda_{c,2D}$ from *Engelbrecht and Burger* (2013) enhances by a factor of ~ 2.3 from the equatorial plane towards the poles, whereas at 100 AU it has a very strong increase towards the

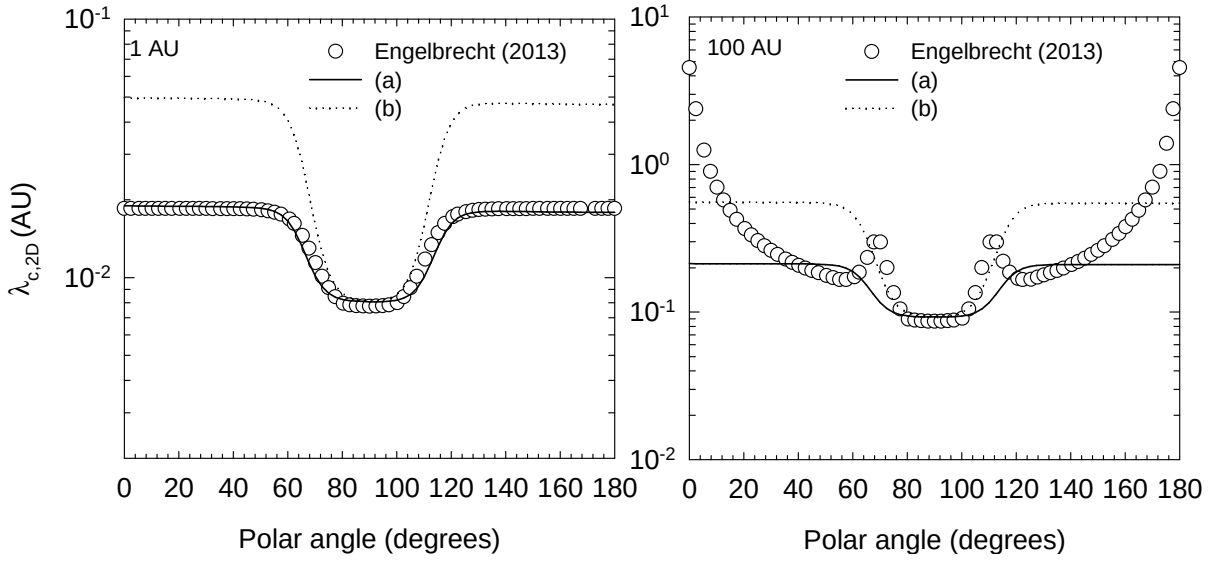

Figure 7.4: The 2D correlation scale length, $\lambda_{c,2D}$, as a function of polar angle at radial distances of 1 AU (left panel) and 100 AU (right panel) for rigidity of 0.5 GV (open circles) from *Engelbrecht and Burger* (2013). Also shown are two different scenarios of $\lambda_{c,2D}$ as used in the model; scenario (a) (solid lines) $\lambda_{c,2D}$ enhances by a factor of 2.3 over the poles and scenario (b) (dotted lines) by factor of 6.

polar regions. Note that scenario (a) gives a good fit of the results from the turbulence model for all latitudes at 1 AU, whereas at 100 AU a good fit is only obtained close to the equatorial plane. Scenario (b) becomes very large at 1 AU over the poles but still small at 100 AU over the poles. Clearly, the turbulence model predicts very large values of $\lambda_{c,2D}$ over the poles at 100 AU.

Figure 7.5 shows four scenarios of $\omega\tau$ and f_s studied in this chapter which differ markedly as a function of polar angle. Here, B2000 denotes $\omega\tau$ from *Burger et al.* (2000), given by Equation 7.5 for $k_A = 0.5$, and shown as the solid line. The dotted line represent $\omega\tau$ from *Burger and Visser* (2010), given by Equation 7.16 with λ_{ultra} given by Equation 7.18, indicated as BV2010. The two $\omega\tau$ scenarios from *Engelbrecht and Burger* (2013) are respectively the dashed line indicated as EB2013(a), with λ_{ultra} given by Equation 7.19 and $\lambda_{c,2D}$ denoted by (a) in Figure 7.4, and the dash-dot-dot line indicated as EB2013(b) with $\lambda_{c,2D}$ denoted by (b) in Figure 7.4. Note that $\omega\tau$ from *Burger et al.* (2000) has no spatial dependence and that the corresponding drift reduction function f_s is largest at the poles but smallest at the equatorial plane. It can be clearly seen that the assumed spatial dependence of $\omega\tau$ produces dramatic decreases of this parameter towards the poles at larger radial distances, especially when λ_{ultra} from *Engelbrecht and Burger* (2013) is assumed. At a radial distance of 100 AU, $f_s \ll 1.0$ at the poles whereas it remains ~ 1.0 in the equatorial plane. This provides the context to study the effects associated with scaling down drifts as a function of latitude.

Figure 7.6 shows four scenarios of $\omega\tau$ and f_s as a function of rigidity at radial distances of 1 AU and 100 AU in the equatorial plane. It is noted that both $\omega\tau$ and f_s from *Burger et al.* (2000)

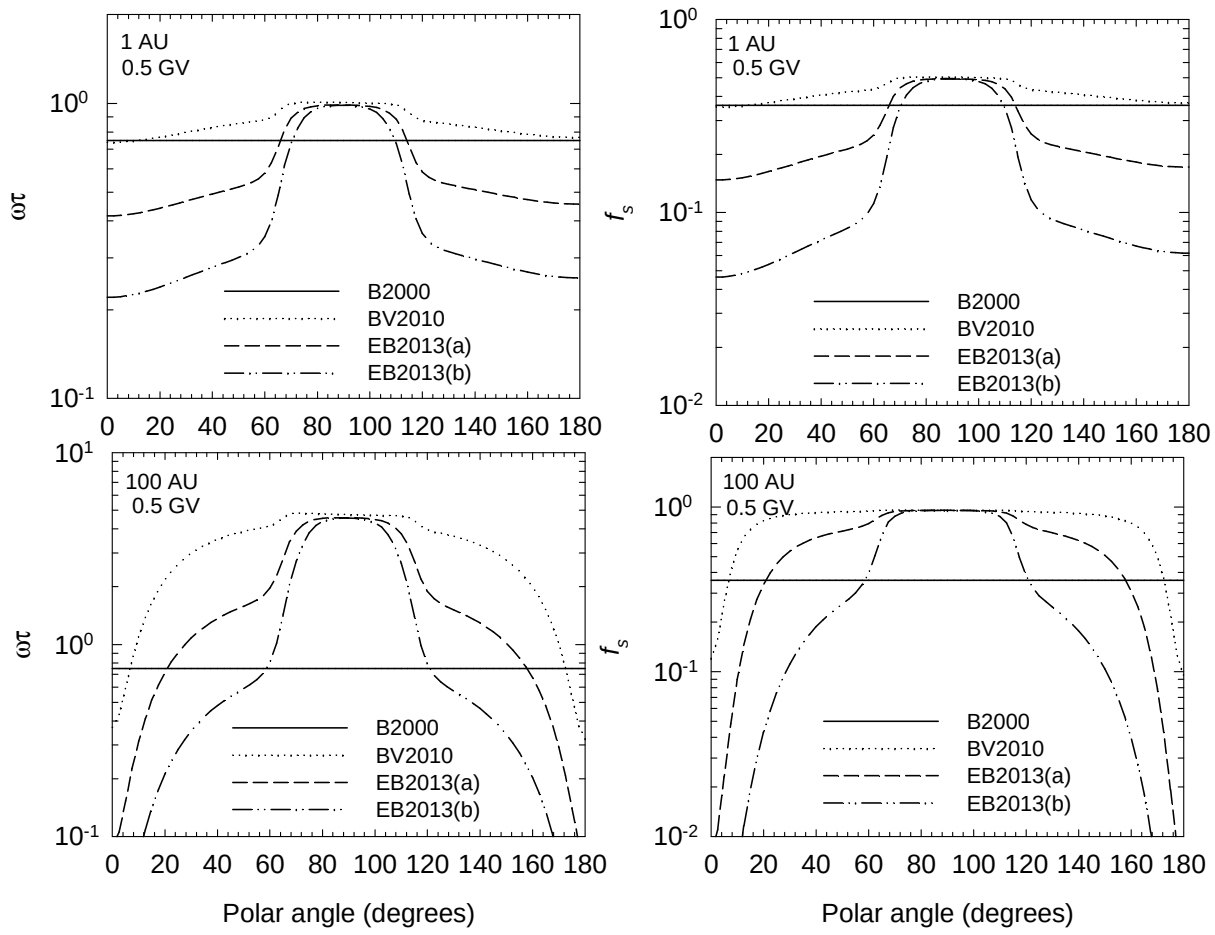

Figure 7.5: Four scenarios of the scattering parameter $\omega\tau$ (left panel) and the corresponding drift reduction function f_s (right panel) as a function of polar angle at radial distances of 1 AU (top row) and 100 AU (bottom row) for a rigidity of 0.5 GV. B2000 is $\omega\tau$ from *Burger et al.* (2000), given by Equation 7.5 for $k_A = 0.5$, is shown as the solid lines; The dotted lines BV2010 is $\omega\tau$ from *Burger and Visser* (2010), given by Equation 7.16 with λ_{ultra} given by Equation 7.18; The dashed lines EB2013(a) is $\omega\tau$ from *Engelbrecht and Burger* (2013), given by Equation 7.16 with λ_{ultra} given by Equation 7.19 and $\lambda_{c,2D}$ represented by scenario (a) in Figure 7.4, and the dash-dot-dot lines EB2013(b) is $\omega\tau$ also from *Engelbrecht and Burger* (2013), given by Equation 7.16 with $\lambda_{c,2D}$ represented by (b) in Figure 7.4.

remain small compared to the other three scenarios for all rigidities. Furthermore, the other three scenarios remain approximately equal for all rigidities in the equatorial plane.

Figure 7.7 shows four scenarios of λ_A, given by Equation 3.33, as a function of rigidity at radial distances of 1 AU and 100 AU in the equatorial plane (top row) and as a function of polar angle (bottom row) for 0.5 GV. These values correspond to the four scenarios of $\omega\tau$ and f_s shown in Figures 7.5 and 7.6. Also shown as the red solid lines and denoted WS in each of the panels is the drift scale when weak scattering is assumed. Effectively, WS correponds to the assumption that there is no drift reduction in the heliosphere ($f_s = 1.0$); for the B2000 scenario, drift reduction is present but $\nabla f_s = 0$ and for scenarios BV2010, EB2013(a) and EB2013(b) drift reduction is also present and $\nabla f_s \neq 0$. In essence the three scenarios BV2010, EB2013(a) and EB2013(b) illustrate differences that arise in the drift reduction function when different assumptions are

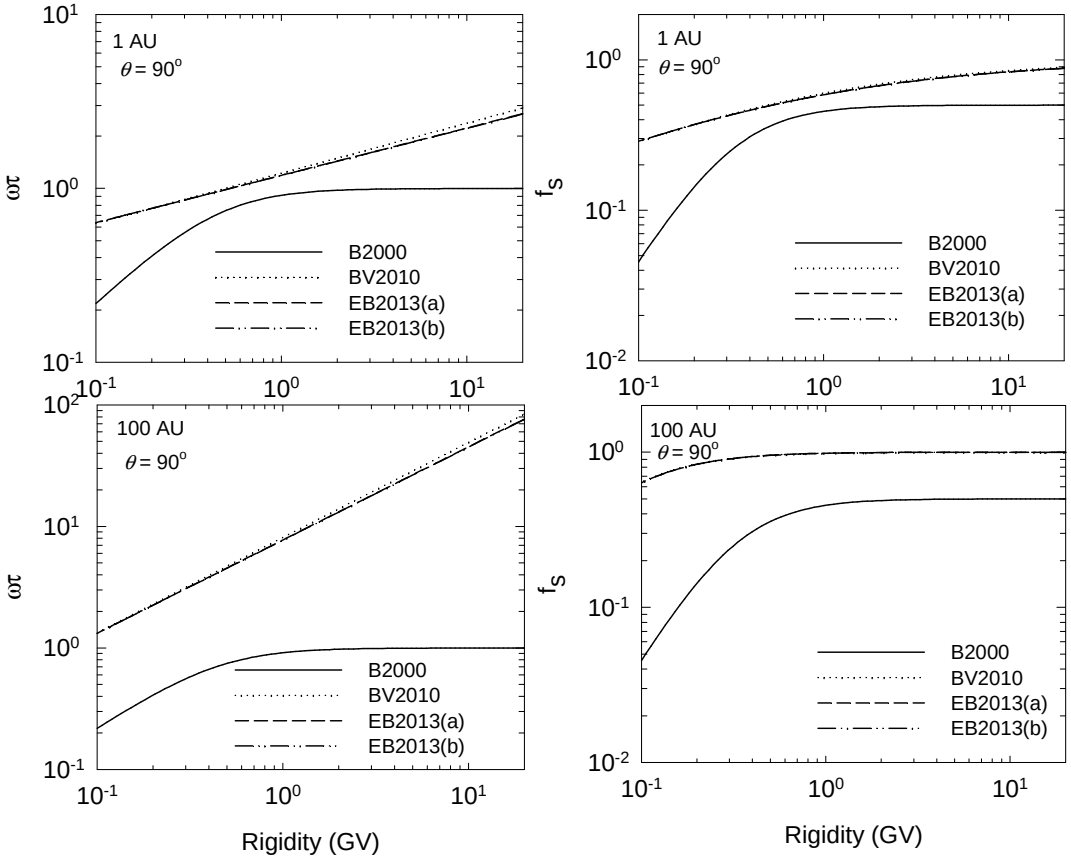

Figure 7.6: Similar to Figure 7.5 but $\omega\tau$ and f_s are shown as a function of rigidity in the equatorial plane with $\theta = 90^0$.

made about λ_{ultra}. Evidently, the four scenarios result in a drift reduction of the maximal weak scattering drift coefficient at all rigidities at the Earth. However at 100 AU in the equatorial plane, substantive drift reduction at all rigidities is only noted for the B2000 scenario. For the scenarios BV2010, EB2013(a) and EB2013(b) drift reduction is only noted at $P < 0.3$ GV. A significant result is noted in the bottom panel of Figure 7.7 at 1 AU, scenarios B2000 and BV2010 follow the latitudinal dependence of the maximal weak scattering drift scale; characterized by large values of λ_A at the poles and smaller values in the equatorial plane. Whereas for scenarios EB2013(a) and EB2013(b) drifts scales are clearly larger in the equatorial plane than over the poles. At 100 AU drift scales for scenarios BV2010, EB2013(a) and EB2013(b) become significantly smaller than WS over the polar regions. How small λ_A becomes over the poles depends on the latitude dependence of λ_{ultra}. It can be noted that scenario B2000 offers notable drift reduction in the equatorial plane even at a radial distance of 100 AU. From this figure it can be noted that, by and large, assuming the latitudinal dependence of λ_{ultra} as done by *Engelbrecht and Burger* (2013) alters the long held picture of the polar dependence of drifts at 1 AU.

In what follows, the 2D shock acceleration model described by *Ngobeni and Potgieter* (2011, 2012, 2014) and in this work is applied to study the effects of different drift reduction scenar-

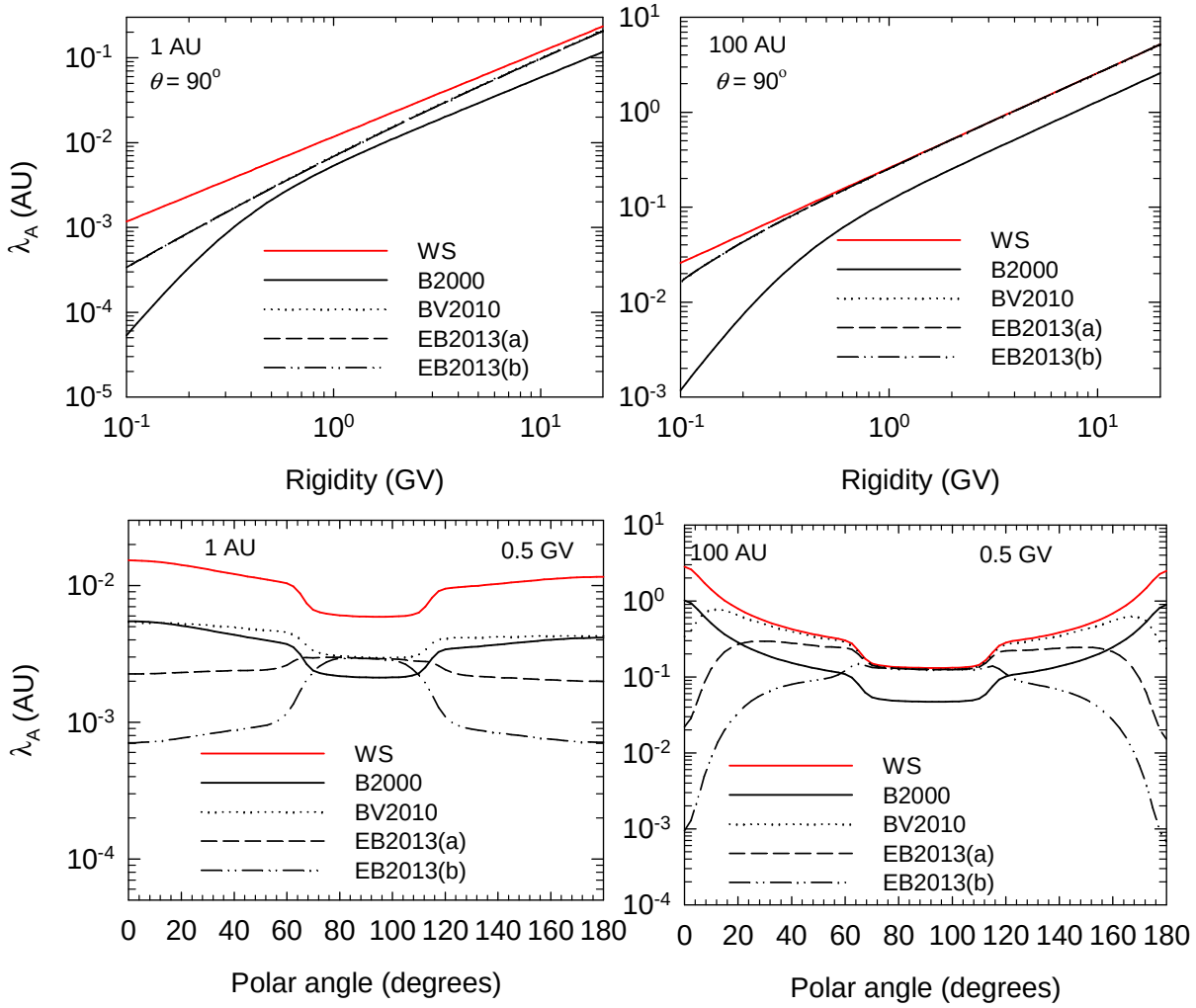

Figure 7.7: Top row: Drift scale λ_A, in AU, corresponding to the four scenarios of $\omega\tau$ and f_s in Figures 7.5 and 7.6 as a function of rigidity at radial distances of 1 AU and 100 AU in the equatorial plane (left to right panels). Bottom row: Corresponding drift scale as a function of polar angle for 0.5 GV. The red solid lines WS represent the drift scale when weak scattering is assumed.

ios, as illustrated in Figures 7.5, 7.6 and 7.7, on the computed GCR Carbon intensities in the heliosphere.

7.5.1 Effects of drift reduction on GCR Carbon spectra

The results shown in this section are focused mainly on the four different scenarios of $\omega\tau$ that were used to calculate the reduction in the maximal weak scattering drift coefficient and their subsequent effects on modulation of GCR Carbon at radial distances of 1 AU, 60 AU and 110 AU in the equatorial plane and at a polar angle $\theta = 55^o$ for the $A > 0$ cycle and $A < 0$ cycle during solar minimum conditions.

In Figure 7.8 the computed modulation for GCR Carbon in the equatorial plane at radial distances of 1 AU, 60 AU and 110 AU, respectively, is shown as spectra for the $A > 0$ polarity

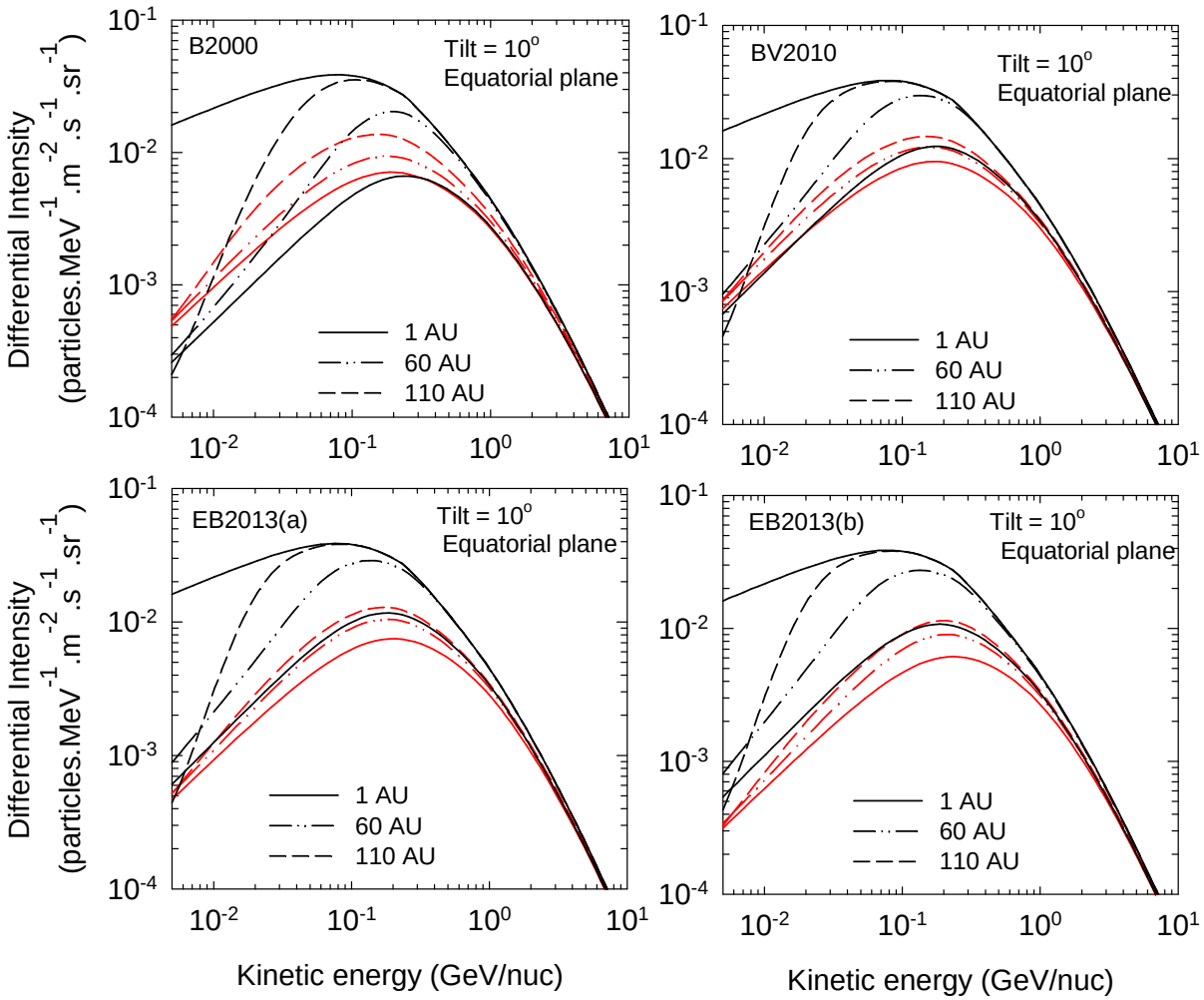

Figure 7.8: The computed differential intensity for GCR Carbon as a function of kinetic energy/nuc for the $A > 0$ polarity cycle (red lines) and $A < 0$ polarity cycle (black lines) in the equatorial plane at radial distances of 1 AU, 60 AU and 110 AU during solar minimum modulation conditions ($\alpha = 10^o$). Four different computed intensities are shown which correspond to the four scenarios of λ_A as shown in Figure 7.7; panel B2000 represents solutions obtained when $\omega\tau$ from *Burger et al.* (2000) is used, panel BV2010 $\omega\tau$ is taken from *Burger and Visser* (2010), and panels EB2013(a) and EB2013(b) are from *Engelbrecht and Burger* (2013) with $\lambda_{c,2D}$ represented by (a) and (b) in Figure 7.4 respectively.

cycle (red lines) and $A < 0$ polarity cycle (black lines) during solar minimum conditions. The four panels correspond to the four scenarios of λ_A given in Figure 7.7. Here the effects of $\omega\tau$ are illustrated with emphasis on the resulting differences in modulation between the two drift cycles. Comparing the four panels illustrates that when $\omega\tau$ decreases from large values in the equatorial plane to very small values over the poles, the intensities become unexpected. As seen in panels EB2013(a) and EB2013(b), the intensities in the $A < 0$ cycles become larger than in the $A > 0$ cycle at all energies primarily because of drifts. This effect is even more pronounced in panel EB2013(b) where $\lambda_{c,2D}$ increases by a factor of 6 over the polar regions. This demonstrates that assuming λ_A as represented by the dash and dash-dot-dot lines in Figure 7.7 combined with the elements of the diffusion tensor assumed for this work produces unrealistic maximum effects in the equatorial plane. However, Panels B2000 and BV2010 are consistent

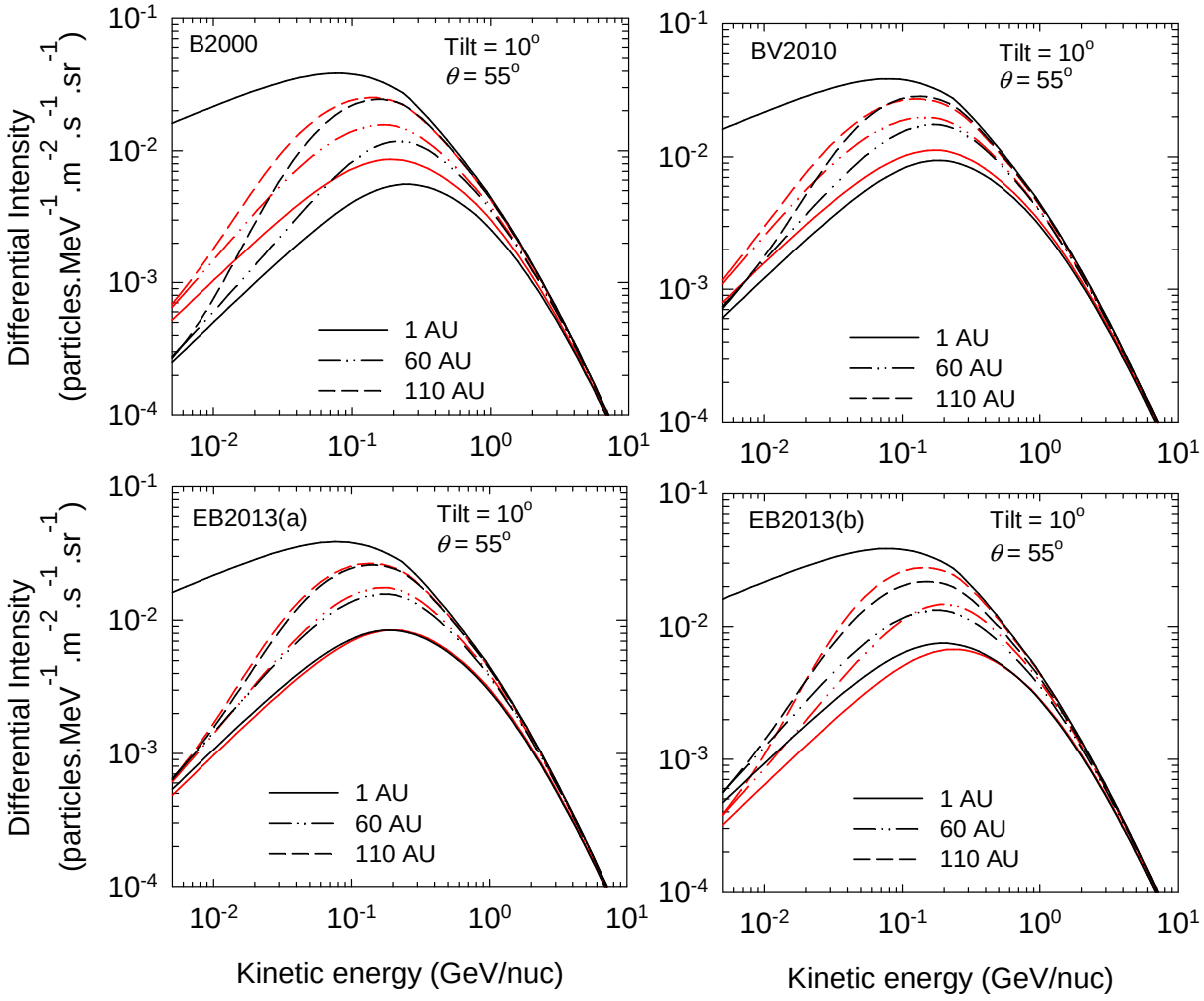

Figure 7.9: Similar to Figure 7.8 but shown at $\theta = 55^o$ (heliolatitude of V1).

with the expected drift effects at the Earth; spectra in the $A > 0$ polarity cycle cross that of the $A < 0$ cycle at low energies (see also *Ngobeni and Potgieter*, 2008).

Figure 7.9 is similar to Figure 7.8 but the effects of $\omega\tau$ on the drift coefficient in the modulation of GCR Carbon are now illustrated at $\theta = 55^o$. What is readily seen in this figure is that for panels BV2010, EB2013(a) and EB2013(b) the differences between $A > 0$ and $A < 0$ spectra are quite reduced when compared to panel B2000; more so for panel EB2013(a). This is because the enhancement of $K_{\perp\theta}$ is now combined with λ_A that is small over the polar regions and as such drifts are suppressed even more at this latitude. What is peculiar in this figure is that for panel EB2013(b) the spectra in the $A > 0$ are lower than in the $A < 0$ at lower energies at all radial distances. This effect is also noticeable in panel EB2013(a) at 1 AU but to a lesser extent; this is discussed further below. These effects are illustrated clearly below as the ratio of intensities between the two cycles is shown.

Figure 7.10 shows the differences in the drifts contribution, as represented by the ratio of spectra of $A > 0$ and $A < 0$ cycles, as a function of kinetic energy/nuc at radial distances of 1

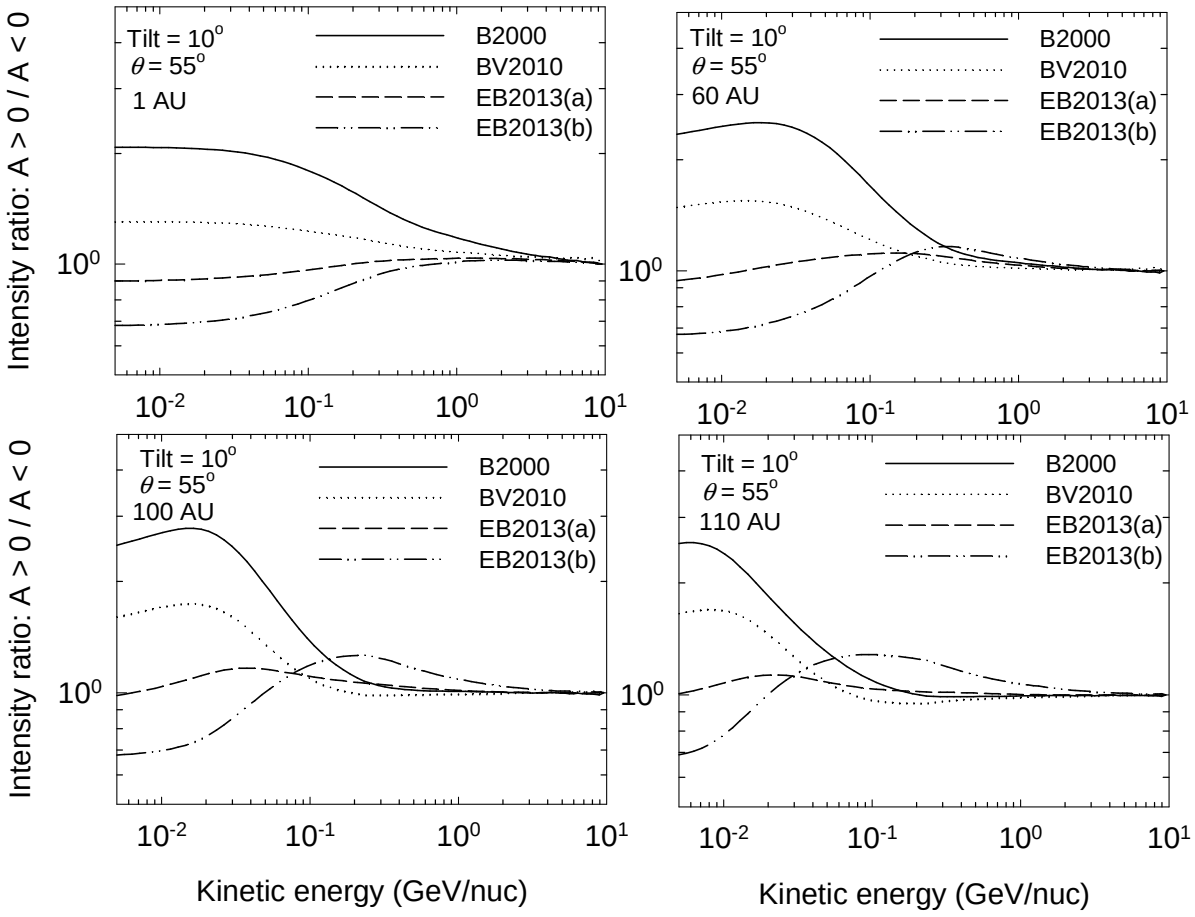

Figure 7.10: The computed ratio , $A > 0$ / $A < 0$, as a function of kinetic energy/nuc at radial distances of 1 AU, 60 AU, 100 AU and 110 AU during solar minimum modulation conditions at $\theta = 55^o$. Four sets of solutions are shown in each panel corresponding to four scenarios of λ_A as shown in Figure 7.7: solid lines represent solutions for B2000, the dotted line for BV2010, the dashed line for EB2013(a) and the dash-dot-dot line for EB2013(b).

AU, 60 AU, 100 AU and 110 AU during solar minimum conditions at a polar angle $\theta = 55^o$. The computed intensity ratios correspond to four scenarios of λ_A as given in Figure 7.7. It is evident that for $E > 1.0$ GeV/nuc, differences between the four scenarios of λ_A start to vanish with almost no difference when $E > 4.0$ GeV/nuc. Furthermore, it can be clearly seen that differences between spectra in the $A > 0$ and $A < 0$ cycle are larger at $E <\sim$100 MeV/nuc when the *ad hoc* drift reduction of *Burger et al.* (2000) as represented by B2000 is utilised. What is striking in this figure is the behaviour of the ratio of spectra for scenario EB2013(b) in the outer heliosphere, it becomes smaller than 1.0 below ∼100 MeV/nuc and larger than 1.0 above this energy. This can be taken to illustrate the point that such large drift reduction over the poles as represented by scenario EB2013(b) in Figure 7.7 is not suitable inside off the TS for the elements of the diffusion tensor assumed in this study.

Figure 7.11 is similar to Figure 7.10 but shown in the equatorial plane. It is evident that at 1 AU the drift reduction from *Burger and Visser* (2010) as represented by BV2010 produces

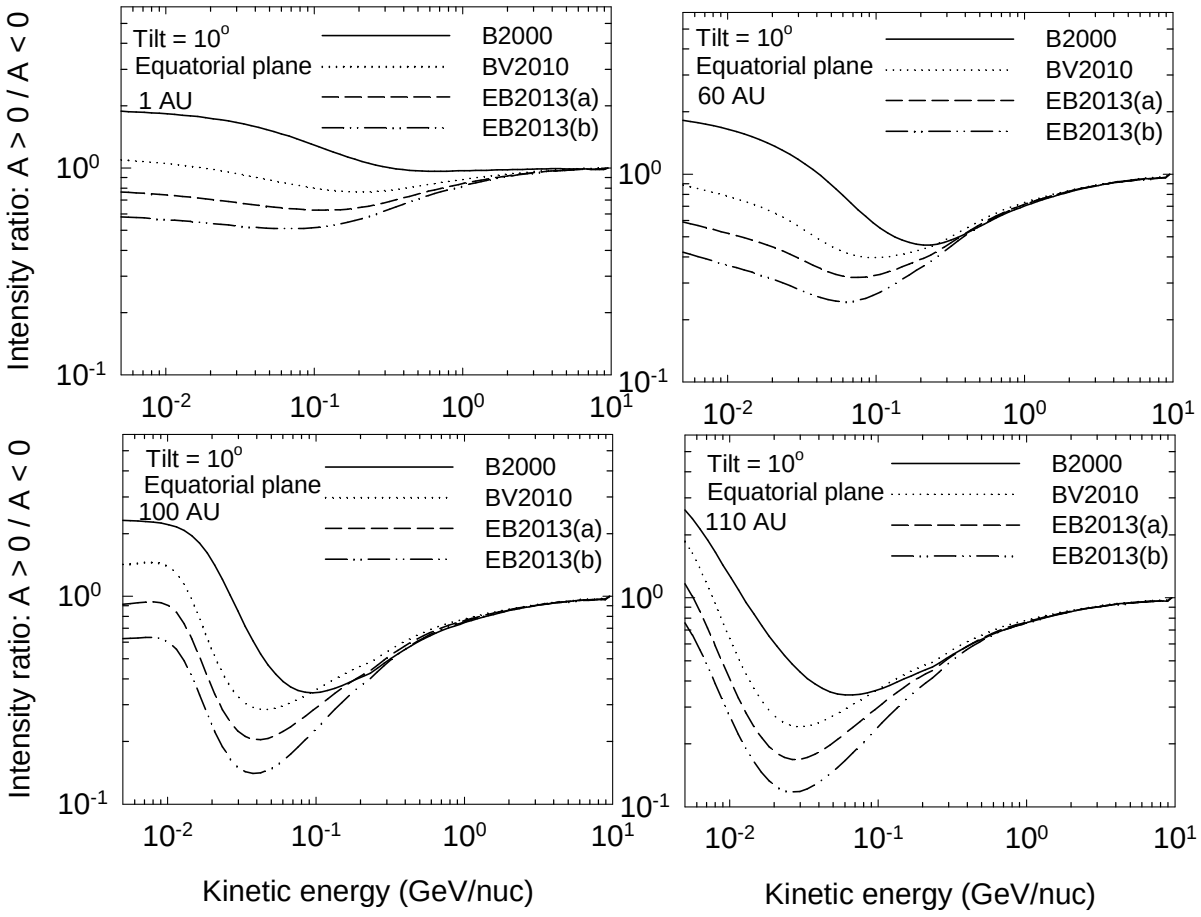

Figure 7.11: Similar to Figure 7.10 but shown in the equatorial plane ($\theta = 90^o$).

the smallest differences in intensities for the two polarity cycles below ∼100 MeV/nuc. The approach of *Burger et al.* (2000) as represented by B2000 remains larger than the other scenarios at $E <$∼30 MeV/nuc at the Earth. However, in the outer heliosphere B2000 offers better drift reduction (corresponding ratio is closest to 1.0) between energies of ∼30-100 MeV/nuc when compared to the other scenarios, while EB2013(b) produces the largest ratio at the same energy range. Above ∼200 MeV/nuc the four scenarios converge in the outer heliosphere. Take note that the intensity ratios obtained from the four scenarios have similar energy dependences in the equatorial plane contrary to $\theta = 55^o$. In what follows the relation between the four scenarios of $\omega\tau$ and $K_{\perp\theta}$ is illustrated by switching off the enhancement of $K_{\perp\theta}$ ($k_e = k_p$ in Equation 3.24 throughout the heliosphere).

Figure 7.12 is similar to Figure 7.8 but the enhancement of $K_{\perp\theta}$ in the polar direction is not used, that is, $K_{\perp\theta}$ is assumed independent of polar angle. This illustrates what contributions the four scenarios of the drift reduction make to the GCR Carbon spectra when there is no additional drift reduction due to the enhancement of $K_{\perp\theta}$ over the poles. It can be seen in this figure that the computed tendencies of $A > 0$ cycle and $A < 0$ cycle spectra are similar to Figure 7.8 but the features are, however, more enhanced when $K_{\perp\theta}$ has no latitude dependence.

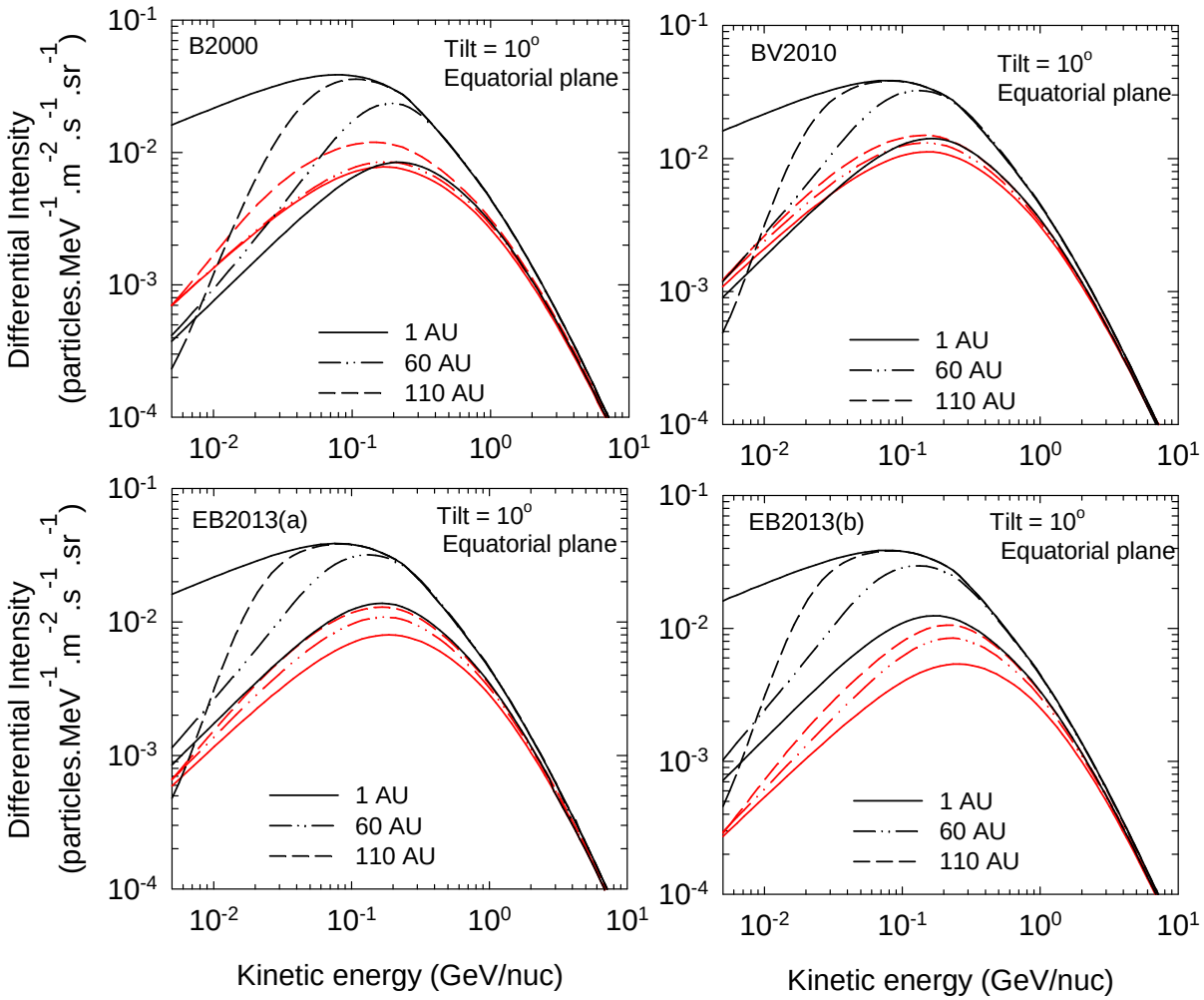

Figure 7.12: Similar to Figure 7.8 but without the enhancement of $K_{\perp\theta}$ ($k_e = k_p$ in Equation 3.24 throughout the heliosphere).

Compared to Figure 7.8 the difference between the $A > 0$ and $A < 0$ spectra is now larger.

Figure 7.13 is similar to Figure 7.9 but the enhancement of $K_{\perp\theta}$ is not assumed. For panels B2000, BV2010 and EB2013(b) similar features as in Figure 7.9 are noted but enhanced. What is interesting is that for panel EB2013(a), as expected, the spectra in the $A > 0$ are now larger than in the $A < 0$ at lower energies at all radial distances. This is contrary to Figure 7.9.

From Figures 7.12 and 7.13 it is evident that for panel B2000 the omission of the enhancement of $K_{\perp\theta}$ towards the poles in the whole heliosphere is an oversimplification because then drift effects become very large at both latitudes. While for panels BV2010 and EB2013(a) $K_{\perp\theta}$ that is independent of polar angle become a reasonable assumption at $\theta = 55^o$. In the equatorial plane, however, drift effects remain large and unexpected in panels BV2010 and EB2013(a) respectively. Panel EB2013(b) again seems by far the most removed from reality, illustrating that the drift reduction as is done in this panel represents an extreme scenario for the elements of the diffusion tensor assumed in this work.

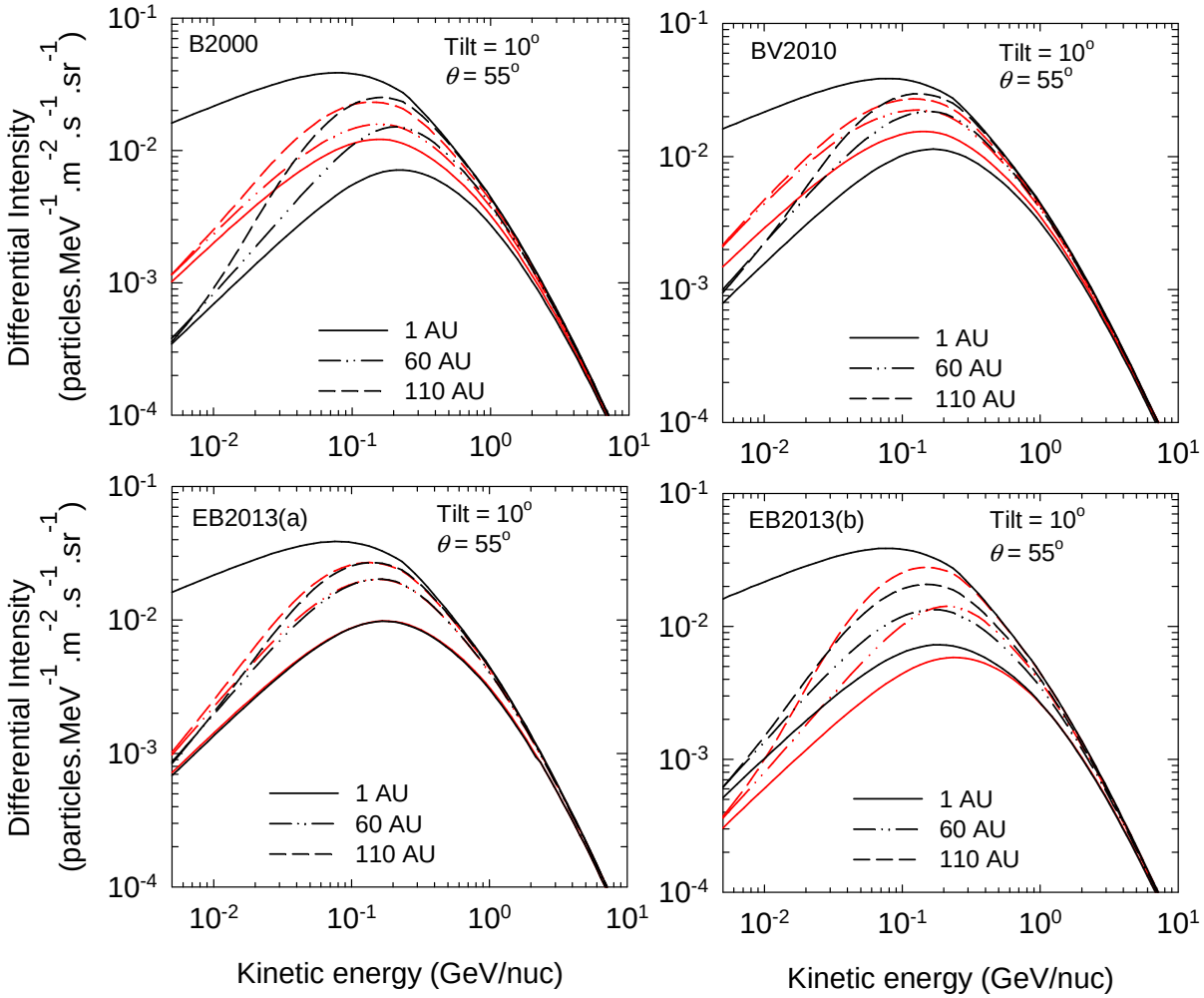

Figure 7.13: Similar to Figure 7.9 but without the enhancement of $K_{\perp\theta}$ ($k_e = k_p$ in Equation 3.24 throughout the heliosphere).

Figure 7.14 is similar to Figure 7.10 but without the enhancement of $K_{\perp\theta}$. Larger drift effects are predicted for all scenarios when compared to Figure 7.10. What is interesting in this Figure is that for scenario EB2013(a) the predicted increase in drift effects is in the right direction because the ratio of $A > 0$ to $A < 0$ spectra is larger than 1.0 at lower energies and remains $\sim$1.0 at higher energies.

Figure 7.15 is similar to Figure 7.11 but without the enhancement of $K_{\perp\theta}$. The tendency is the same as in the intensities ratios in Figure 7.11 but the effects are stronger.

7.6 Summary and conclusions

In this chapter, first, reasonable values of $\omega\tau$ that can be considered to represent drift reduction for modulation in the heliosphere were estimated based on the available knowledge. It was found that $\omega\tau$ ranges from 0 to 5. However these values should be viewed as first order

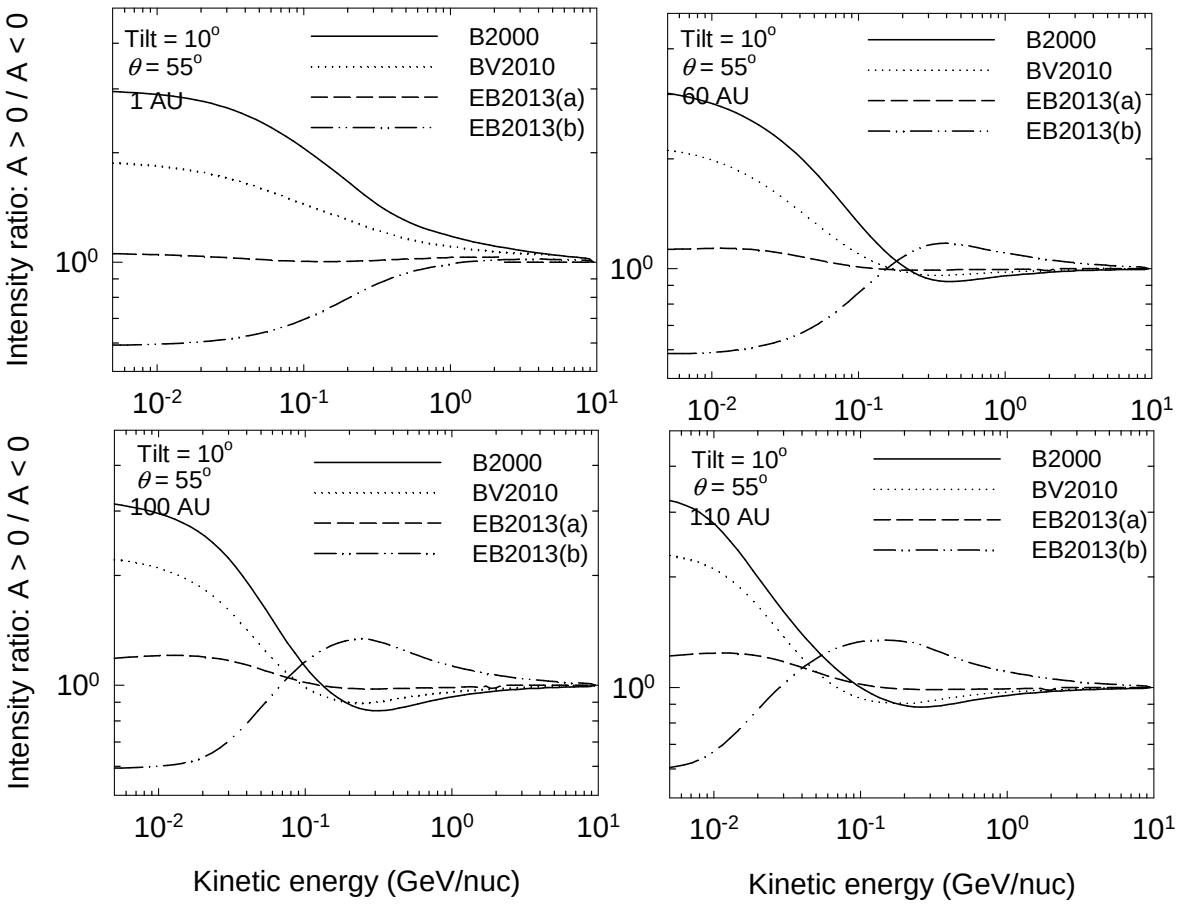

Figure 7.14: Similar to Figure 7.10 but without the enhancement of $K_{\perp\theta}$ ($k_e = k_p$ in Equation 3.24 throughout the heliosphere).

estimates of $\omega\tau$.

Second, the north-south asymmetrical TS model as described by *Ngobeni and Potgieter* (2011, 2012, 2014) and in Chapter 4 was used to study the effects of four different scenarios of $\omega\tau$, as given in Figure 7.5, on the drift coefficient, represented as a drift scale λ_A in Figure 7.7, in the modulation of GCR Carbon in the heliosphere. This was illustrated with and without the enhancement of $K_{\perp\theta}$ for the two solar magnetic field polarities during solar minimum conditions. Of particular interest is how the relation between the four scenarios of λ_A and $K_{\perp\theta}$ influences differences in spectra between the $A > 0$ cycle and $A < 0$ cycles for modulation in the equatorial plane and at a polar angle of $\theta = 55^o$. To get a fundamentally based expression (not *ad hoc* or pure phenomenological) for $\omega\tau$ for a fundamental reduction of the weak scattering drift coefficient, the model also incorporates predictions for the 2D correlation scale length, $\lambda_{c,2D}$, based on the turbulence model of *Engelbrecht and Burger* (2013) for the calculation of plausible profiles for the 2D turbulence ultrascale, λ_{ultra}. The four scenarios of $\omega\tau$ were taken from *Burger et al.* (2000), *Burger and Visser* (2010) and *Engelbrecht and Burger* (2013).

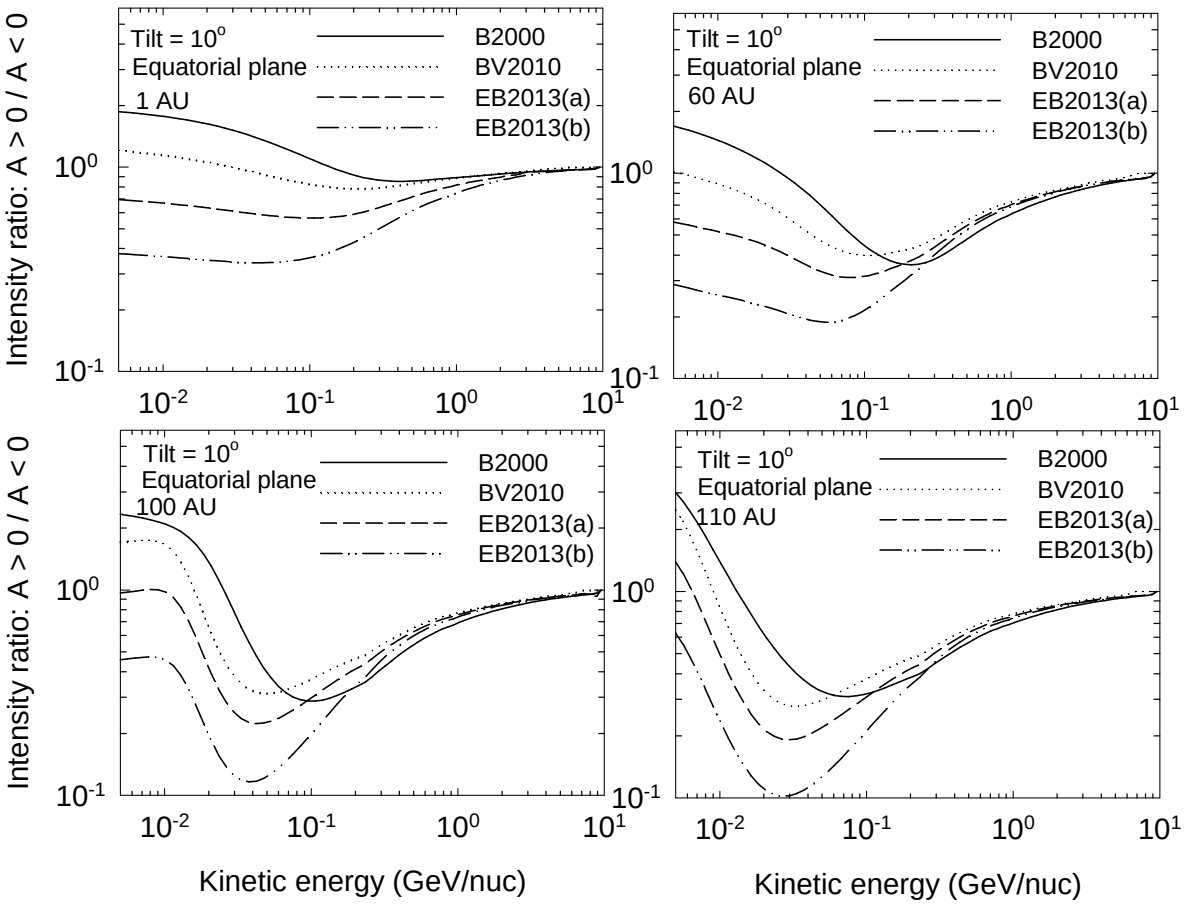

Figure 7.15: Similar to Figure 7.11 but but without the enhancement of $K_{\perp\theta}$ ($k_e = k_p$ in Equation 3.24 throughout the heliosphere).

The considered different scenarios for $\omega\tau$ have significant effects on the weak scattering drift coefficient and as such on the subsequent computed differential intensities in both polarity cycles. At 1 AU it was found that when $\omega\tau$ decreases rapidly over the polar regions, λ_A becomes very small at the poles compared to its value in the equatorial plane. This is contrary to the generally assumed spatial dependence of the maximal weak scattering drift scale. The consequent effect is that in the equatorial plane the $A < 0$ spectra are higher than the $A > 0$ spectra at all energies primarily because of drifts; which is unexpected from a 'classical' drift modelling point of view, and contrary to observations (see *Strauss and Potgieter*, 2014; *Langner*, 2004). This feature persists for the equatorial plane modulation even when the enhancement of $K_{\perp\theta}$ is neglected as long as $\omega\tau$ has a strong latitude dependence. This is taken to indicate that the interplay between drifts and $K_{\perp\theta}$ in determining the total drift effects depends also on the chosen scenario of $\omega\tau$.

At a polar angle of $\theta = 55^o$, drift effects almost disappear for the scenario of $\omega\tau$ from *Engelbrecht and Burger* (2013) that is represented by the enhancement of $\lambda_{c,2D}$ by a factor of 2 over the

poles. This is also the case when the enhancement of $K_{\perp\theta}$ is neglected but even better. While for the scenario of $\omega\tau$ where the enhancement of $\lambda_{c,2D}$ is a factor of 6 over the poles, the $A > 0$ spectra are lower than the $A < 0$ at lower energies which is inconsistent with V1 observations. The latter approach to the enhancement of $\lambda_{c,2D}$ gives the largest unexpected drift effects at $\theta = 55^o$, as well as in the equatorial plane, even when $K_{\perp\theta}$ does not depend on a polar angle. This scenario is important because it puts a limit as to what can be the expected latitudinal dependence of the turbulence parameter $\lambda_{c,2D}$ in the outer heliosphere.

It was found that a very strong decrease of $\omega\tau$ over the poles result in a drift coefficient that is very small over the poles and as such the qualitative subsequent modulated intensities are inconsistent with observations in the equatorial plane for the assumed elements of the diffusion tensor used for this work. Furthermore, of the four scenarios of $\omega\tau$ that were studied, the $ad\ hoc$ scenario of *Burger et al.* (2000), given by Equation 7.7 with $k_A = 0.5$, is consistent with the predicted $\omega\tau < 5$ at all rigidities. It is concluded that upstream of the TS, expressions for the diffusive scattering parameter $\omega\tau$ derived from fundamental theory that can be utilized in the modulation model to study their qualitative and quantitative effects on the drift coefficient in the modulation of GCRs depend also on assumptions made about the latitudinal dependence of the elements of the diffusion tensor. For the elements of the diffusion tensor assumed in this study, scenarios of $\omega\tau$ with strong decreases towards the poles are realistic at and beyond the TS where the solar wind turbulence must have a larger latitudinal dependence.

Chapter 8

Summary and conclusions

This work focussed on illustrating how the north-south asymmetrical geometry of the heliosphere as suggested by MHD models (*Opher et al.*, 2009; *Pogorelov et al.*, 2009; *Strauss*, 2013; *Luo et al.*, 2013) alters the distribution of GCRs, in particular Carbon, between the north and south hemispheres. To achieve this objective, the 2D shock acceleration model developed by *Langner* (2004) based on Parker's transport equation (*Parker*, 1965) was used and modified to include the north-south asymmetry in the geometry of the heliosphere. This asymmetry was incorporated in the model by assuming a significant dependence for the heliolatitude of the thickness of the heliosheath. Then an investigative study was done to establish the inherent asymmetrical modulation that arose when different enhancements for both perpendicular diffusion coefficients between the two hemispheres were assumed in a simulated heliosphere that already contained a north-south asymmetrical geometry. The model was further improved to incorporate recent V1 observations of the HP location and the relevant HPS for GCR Carbon. Comparing the modeled results with various spacecraft observations led to the study of the effects of diffusive scattering on the drift coefficient in the modulation of GCRs in the heliosphere. The different conclusions are summarised next:

After introducing the reader to the study of modulation of CRs in the heliosphere and the thesis overview in **Chapter 1**, an overview was given in **Chapter 2** of the Sun, the solar wind, the HMF, the HCS, solar cycle variations, the heliosphere and its geometry and charged particles in the heliosphere. A concise discussion was also given about selected spacecraft missions.

In **Chapter 3**, a discussion of the major modulation transport processes combined in the transport equation (*Parker*, 1965) was given. Only four elements of the diffusion tensor are of special interest in a 2D modulation model, namely $K_{||}$, $K_{\perp r}$, $K_{\perp \theta}$ and K_T, the diffusion coefficient parallel to the heliospheric magnetic field, perpendicular to the heliospheric magnetic field in the radial direction, perpendicular to the heliospheric magnetic field in the polar direction and the drift coefficient respectively. The expression for $K_{||}$ used in this work was taken from *Burger et al.* (2008) and *Engelbrecht* (2008) based on expressions derived by *Teufel and Schlickeiser* (2003) using quasilinear theory and a random sweeping model for composite dynamical turbulence.

The effects of the dissipation range were neglected similar to the approach of *Engelbrecht and Burger* (2013) and *Engelbrecht* (2013), whereas the expressions for the rigidity and spatial dependences of $K_{\perp r}$, $K_{\perp\theta}$ and K_T were based on a steady state model derived by *Burger et al.* (2000). A reasonable phenomenological consensus for the global description of cosmic rays modulation in the heliosphere was reached, i.e., $K_{\perp\theta} > K_{\perp r}$ away from the equatorial region and $K_{\perp\theta} = K_{\perp r}$ in the equatorial region (*Potgieter*, 1996, 2000; *Burger et al.*, 2000; *Ferreira*, 2002; *Langner*, 2004; *Moeketsi*, 2004; *Ngobeni*, 2006; *Strauss*, 2010). The mathematical formalism of incorporating diffusive shock re-acceleration of GCRs into the modulation model was also given and discussed.

In **Chapter 4** the TS numerical model developed by *Langner* (2004) was extended to compute the modulation effects caused by a north-south asymmetry in the geometry of the heliosphere. A study was then made of the modulation differences between solutions in the north and south hemispheres using two IS's for GCR Carbon at the HP, one from *Webber and Higbie* (2009) as the lowest option, and the other one as the highest option from *Moskalenko et al.* (2002). This was done for both HMF polarity cycles and for solar minimum, with tilt angle $\alpha = 10^o$, and moderate solar maximum conditions with $\alpha = 50^o$. The effects of this asymmetry on the modulated GCR Carbon spectrum and its radial dependence were studied at 1 AU, 60 AU and 100 AU and at polar angles of $\theta = 55^o$ and $\theta = 125^o$, corresponding to the trajectories of V1 and V2, respectively. The effects of this type of asymmetry on GCR Carbon modulation were found to be insignificant in the inner heliosphere ($r < 40$ AU) but become increasingly important with increasing distance to reach a maximum effect beyond the TS but only for energies below a few-hundred MeV/nuc. It was also found that increasing the IS at $E <\sim 300$ MeV/nuc enhances asymmetric modulation effects for a given polar angle dependence of the width of the heliosheath. This chapter illustrates that the effects of meridional asymmetry in the width of the heliosheath between the two Voyager positions on GCR Carbon intensities depend on the position of the observer in the heliosphere, the particle energy, solar activity and the assumed IS. Also that this asymmetric modulation can be made large by assuming: (1) A significantly larger meridional asymmetry. (2) A much higher IS at low energies. (3) A non-isotropic IS and (4) modulation conditions that are globally different between the northern and southern regions of the heliosphere.

In **Chapter 5**, the effects of the inherent asymmetrical modulation conditions that arise when different enhancements for $K_{\perp\theta}$ and $K_{\perp r}$ between the two hemispheres are assumed were investigated. This was modeled with a simulated heliosphere that already contained a heliosheath thickness that has a significant dependence on heliolatitude described in **Chapter 4**. The modulated spectra and radial intensities of GCR Carbon between polar angles $\theta = 55^o$ and $\theta = 125^o$ were compared. This was done for both HMF polarity cycles during solar minimum and moderate solar maximum conditions. It was found that in the $A > 0$ cycle these

differences in intensity between 55^o and 125^o change both quantitatively and qualitatively for the assumed asymmetrical modulation condition as reflected by $K_{\perp\theta}$, while in the $A < 0$ cycle, minute quantitative differences were obtained. However, when both $K_{\perp\theta}$ and $K_{\perp r}$ have significant latitude dependences, major differences in intensities between the two polar angles were obtained in both polarity cycles. The radial gradients of GCR Carbon at lower energies ($E = 0.05$ MeV/nuc) between the two polar angles were found to be significantly different in the heliosheath. This can be taken to indicate that the latitude dependence of the solar wind turbulence in the heliosheath is different between the two Voyager directions. Thus, this chapter illustrates that in addition to the asymmetry in the geometry of the heliosphere it is possible that an asymmetry in modulation conditions between the north and south hemispheres could also exist in the heliosheath.

In **Chapter 6**, the asymmetric modulation model described in **Chapter 4** was improved by incorporating accurate information about the HP location and the relevant HPS for GCR Carbon based on the recent V1 observations. For the first time a new HPS (as unmodulated input spectrum) for low energies (~ 5 MeV/nuc $> E <\sim 300$ MeV/nuc) was used. This HPS was observed by V1 at ~ 122 AU for $E < 200$ MeV/nuc and was found to be significantly higher than previous estimates of *Webber and Higbie* (2009), for example, at $E = 10$ MeV/nuc and $E = 100$ MeV/nuc by a factor of ~ 2.0 and ~ 1.6 respectively. This contributes significantly at these lower energies to the total modulation as a function of position in the heliosphere. Modeling results were shown at the Earth for the previous solar minimum, an $A > 0$ cycle with $\alpha = 10^o$, for a moderate solar maximum in an $A < 0$ cycle with $\alpha = 50^o$, and for the recent solar minimum, an $A < 0$ cycle, also with $\alpha = 10^o$. For moderate solar maximum conditions, adjustment of $K_{||}$ by a factor of 0.6 and for both perpendicular diffusion coefficients, $K_{\perp r}$ and $K_{\perp\theta}$, by a factor of 1.5 with respect to their assumed previous solar minimum values were found to be optimal to establish compatibility with ACE observations. While for the recent solar minimum (around 2009) reasonable compatibility with observations was obtained only when $K_{||}$ was increased by a factor of 1.4 and with full drifts assumed ($k_A = 1.0$) relative to their previous solar minimum values. The change in modulated spectra at the Earth from solar maximum (2001-2003) to the recent minimum was found to exceed the difference between the HPS and the modulated spectrum at the Earth during the recent solar minimum at $E >\sim 30$ MeV/nuc. The numerical model was also applied to study modulation in the outer heliosphere, especially inside the heliosheath. Modeled spectra were shown for solar minimum conditions at radial distances of 60 AU, 90 AU, 100 AU and 110 AU and were compared to observations taken inside off the TS ($r < r_{TS}$) in the $A > 0$ cycle, and inside the heliosheath ($r > r_{TS}$) in the $A < 0$ cycle. It was found that reasonable compatibility with corresponding Voyager observations in both polarity cycles was established when drifts were scaled down to zero in the heliosheath. Lastly, the contribution of drifts and the enhancement of $K_{\perp\theta}$ in the heliosheath were investigated and illustrated by computing the ratio of the modulation in the

heliosheath to the total modulation between the HP and 1 AU: $(j_{HP} - j_{TS})/(j_{HP} - j_{1AU})$. This was done for three scenarios, the full model with all its assumptions, then for drifts scaled to zero in the heliosheath ($k_A = 0$ when $r > r_{TS}$) and for the enhancement of $K_{\perp\theta}$ neglected in the heliosheath ($k_e = k_p$ when $r > r_{TS}$). A general result found was that the effect of neglecting drifts in the heliosheath is more significant than neglecting the enhancement of $K_{\perp\theta}$. This chapter illustrates that the drift reduction function given in **Chapter 3** should also include a spatial dependence apart from the already implemented reduction in the rigidity dependence. This is taken to indicate that further advances in the effects of diffusive scattering on the drift coefficient are needed to derive a self-consistent drift reduction function suitable for modulation in the heliosphere.

In **Chapter 7**, available knowledge about the spatial and rigidity dependence of the scattering parameter $\omega\tau$ was used to study its effects on the drift coefficient for the modulation of GCR Carbon in the heliosphere. As a first step, reasonable values of $\omega\tau$ that can be considered to represent drift reduction for modulation in the heliosphere were estimated and found to range from 0 to 5. However these values should be viewed as first order estimates of $\omega\tau$. Second, the asymmetric model was used to study the effects of four different scenarios of $\omega\tau$ on the drift coefficient, represented as drift scale λ_A, in the modulation of GCR Carbon in the heliosphere. This was illustrated with and without the enhancement of $K_{\perp\theta}$ for the two solar magnetic field polarities during solar minimum conditions. Of particular interest was how the relation between the four scenarios of λ_A and $K_{\perp\theta}$ influenced differences in spectra between the $A > 0$ cycle and $A < 0$ cycles for modulation in the equatorial plane and at a polar angle of $\theta = 55^o$. To get a fundamentally based expression (not $ad\ hoc$ or pure phenomenological) for $\omega\tau$ for a fundamental reduction of the weak scattering drift coefficient, the model also incorporates predictions for the 2D correlation scale length, $\lambda_{c,2D}$, based on the turbulence model of *Engelbrecht and Burger* (2013) for the calculation of plausible profiles for the 2D turbulence ultrascale, λ_{ultra}. The four scenarios of $\omega\tau$ were taken from *Burger et al.* (2000), *Burger and Visser* (2010) and *Engelbrecht and Burger* (2013). It was shown that at 1 AU, when $\omega\tau$ decreased rapidly over the polar regions, λ_A became very small at the poles compared to its value in the equatorial plane. This was found to be contrary to the generally assumed spatial dependence of the maximal weak scattering drift scale. The consequent effect was that in the equatorial plane the $A < 0$ spectra were higher than the $A > 0$ spectra at all energies primarily because of drifts; which was unexpected from a 'classical' drift modeling point of view (see *Langner*, 2004; *Strauss and Potgieter*, 2014). This feature was found to persist for the equatorial plane modulation even when the enhancement of $K_{\perp\theta}$ was neglected. This was taken to indicate that a very strong decrease of $\omega\tau$ over the poles result in a drift coefficient that is very small over the poles and as such the qualitative subsequent modulated intensities are inconsistent with observations in the equatorial plane for the assumed elements of the diffusion tensor used for this work. It is concluded in this chapter that upstream of the TS, expressions for the diffusive scattering

parameter $\omega\tau$ derived from fundamental theory that can be utilized in the modulation model to study their qualitative and quantitative effects on the drift coefficient in the modulation of GCRs depend also on assumptions made about the latitudinal dependence of the elements of the diffusion tensor. For the elements of the diffusion tensor assumed in this study, scenarios of $\omega\tau$ with strong decreases towards the poles are realistic at and beyond the TS where the solar wind turbulence must have a larger latitudinal dependence.

Recommendations for future research:

- To extend the study to include other species of GCRs e.g. Hydrogen, Helium and Oxygen.
- To investigate the effects of the diffusive scattering parameter required for the reduction of the drift coefficient in modulation studies with a pure Parker field.
- To couple the model with MHD models to provide a more realistic solar wind profile associated with the heliosheath.
- To investigate the modulation effects of GCRs caused by a 3D non-spherical heliosphere using a non-Parkerian geometry of the HMF.

Extracts from this thesis were published in four peer reviewed journals:

- Ngobeni, M.D., and Potgieter, M. S.: *A study of the global heliospheric modulation of galactic carbon*, Advances in Space Research, 53:1634-1646, 2014.
- Ngobeni, M.D., and Potgieter, M. S.: *Modelling of galactic carbon in an asymmetrical heliosphere: Effects of asymmetrical modulation conditions*, Advances in Space Research, 49:1660-1669, 2012.
- Ngobeni, M.D., and Potgieter, M. S.: *Modulation of galactic cosmic rays in a north-south asymmetrical heliosphere*, Advances in Space Research, 48:300-307, 2011.
- Ngobeni, M.D., and Potgieter, M. S.: *The heliospheric modulation of cosmic rays: Effects of a latitude dependent solar wind termination shock*, Advances in Space Research, 46:391-401, 2010.

Two articles were published in conference proceedings:

- Ngobeni, M.D., and Potgieter, M. S.:*Modelling of galactic carbon in an asymmetrical heliosphere: Effects of asymmetrical modulation conditions due to solar activity*, in Proc. 32nd Inter. Cosmic Ray Conf. (Beijing), 2011.
- Ngobeni, M.D., and Potgieter, M. S.:*Modulation of galactic cosmic rays in a north-south asymmetrical heliosphere*, in Proc. 32nd Inter. Cosmic Ray Conf. (Beijing), 2011.

Bibliography

Axford, W. I., E. Leer, and G. Skadron, The acceleration of cosmic rays by shock waves, in *Proc. 15th Inter. Cosmic Ray Conf. (Plovdiv)*, vol. 11, pp. 132–137, 1977.

Balogh, A., E. J. Smith, B. T. Tsurutani, D. J. Southwood, R. J. Forsyth, and T. S. Horbury, The heliospheric magnetic field over the south polar region of the Sun, *Science*, *268*, 1007–1010, 1995.

Bazilevskaya, G. A., M. B. Krainev, V. S. Makhmutov, Y. I. Stozhkov, A. K. Svirzhevskaya, and N. S. Svirzhevsky, Change in the rigidity depence of the galactic cosmic ray modulation in 2008-2009, *Adv. Space Res.*, *49*, 784–790, 2012.

Bell, A. R., The acceleration of cosmic rays in shock fronts - I, *Mon. Not. R. astr. Soc.*, *182*, 147–156, 1978a.

Bell, A. R., The acceleration of cosmic rays in shock fronts - II, *Mon. Not. R. astr. Soc.*, *182*, 443–455, 1978b.

Bieber, J. W., and W. H. Matthaeus, Cosmic ray pitch angle scattering in dynamical magnetic turbulence, in *Proc. 22nd Inter. Cosmic Ray Conf. (Dublin)*, vol. 3, pp. 248–251, 1991.

Bieber, J. W., and W. H. Matthaeus, Perpendicular diffusion and drift at intermediate cosmic-ray energies, *Astrophys. J.*, *485*, 655–659, 1997.

Bieber, J. W., W. H. Matthaeus, C. W. Smith, W. Wanner, M.-B. Kallenrode, and G. Wibberenz, Proton and electron mean free paths: The Palmer consensus revisited, *Astrophys. J.*, *420*, 294–306, 1994.

Bieber, J. W., W. Wanner, and W. H. Matthaeus, Dominant two-dimensional solar wind turbulence with implications for cosmic ray transport, *J. Geophys. Res.*, *101*, 2511–2522, 1996.

Biermann, L., Kometenschweife und solare Korpuskularstrahlung, *Zs. f. Ap.*, *29*, 274–286, 1951.

Biermann, L., Solar corpuscular radiation and the interplanetary gas, *The Observatory*, *77*, 109–110, 1957.

Burger, R. A., On the theory and application of drift motion of charged particles in inhomogeneous magnetic field, Ph.D. thesis, Potchefstroom University for CHE, South Africa, 1987.

Burger, R. A., and M. Hattingh, Steady-state drift-dominated modulation models for galactic cosmic rays, *Astrophys. and Space Sc.*, *230*, 375–382, 1995.

Burger, R. A., and M. Hattingh, Effect of Fisk type heliospheric magnetic fields on the latitudinal transport of cosmic rays, in *Proc. 27th Inter. Cosmic Ray Conf. (Hamburg)*, vol. 9, pp. 3698–3701, 2001.

Burger, R. A., and M. Hitge, The effect of a Fisk-type heliospheric magnetic field on cosmic-ray modulation, *Astrophys. J.*, *617*, L73–L76, 2004.

Burger, R. A., and M. S. Potgieter, The calculation of neutral sheet drift in two-dimensional cosmic-ray modulation models, *Astrophys. J.*, *339*, 501–511, 1989.

Burger, R. A., and D. J. Visser, Reduction of drifts effects due to solar wind turbulrnce, *Astrophys. J.*, *725*, 1366–1372, 2010.

Burger, R. A., M. S. Potgieter, and B. Heber, Rigidity dependence of cosmic ray proton latitudinal gradients measured by the Ulysses spacecraft: Implications for the diffusion tensor, *J. Geophys. Res.*, *105*, 27,447–27,455, 2000.

Burger, R. A., T. P. J. Krüger, M. Hitge, and N. E. Engelbrecht, A Fisk-Parker hybrid heliospheric magnetic field with a solar-cycle dependence, *Astrophys. J.*, *674*, 511–519, 2008.

Burlaga, L. F., N. F. Ness, and E. C. Stone, Magnetic field observations as Voyager 1 entered the heliosheath depletion region, *Science*, *341*, 147–150, 2013.

Caballero-Lopez, R. A., H. Moraal, and F. B. McDonald, The modulation of galactic cosmic-ray electrons in the heliosheath., *Astrophys. J.*, *725*, 121–127, 2010.

Carlson, P., A centuary of cosmic rays, *Phys. Today*, *65*, 30–36, 2012.

Casadei, D., and V. Bindi, The origin of cosmic ray protons and electrons, *Astrophys. J.*, *612*, 262, 2004.

Cliver, E. W., History of research on solar energetic particle (SEP) events: the evolving paradigm, in *Universal heliophysical processes*, *Proc. IAU Symp.*, vol. 257, edited by N. Gopalswamy and D. F. Webb, pp. 401–412, 2008.

De Simone, N., V. Di Felice, J. Gieseler, M. Boezio, M. Casolino, P. Picozza, and B. Heber, Latitudinal and radial gradients of galactic cosmic ray protons in the inner heliosphere - PAMELA and Ulysses observations, *ASTRA*, *7*, 425–434, 2011.

Decker, R. B., S. M. Krimigis, E. C. Roelof, M. E. Hill, T. P. Armstrong, G. Gloeckler, D. C. Hamilton, and L. J. Lanzerotti, Voyager 1 in the foreshock, termination shock and heliosheath, *Science*, *309*, 2020–2024, 2005.

Douglas, J., On the numerical integration of $\frac{\partial^2 u}{\partial x^2} + \frac{\partial^2 u}{\partial y^2} = \frac{\partial u}{\partial t}$ by implicit methods, *J. Soc. Indust. Appl. Math.*, *3*(1), 42–65, 1955.

Drury, L. O., An introduction to the theory of diffusive shock acceleration of energetic particles in tenuous plasmas, *Rep. Prog. Phys.*, *46*, 973–1027, 1983.

Earl, J. A., The diffusive idealization of charged-particle transport in random magnetic fields, *Astrophys. J.*, *193*, 231–242, 1974.

Effenberger, F., H. Fichtner, K. Scherer, S. Barra, J. Kleimann, and R. D. Strauss, A generalized diffusion tensor for fully anisotropic diffusion of energetic particles in the heliospheric magnetic field, *Astrophys. J.*, *750*(108), 1–8, 2012.

Efimov, A. I., L. N. Samoznaev, M. K. Bird, I. V. Chashei, and D. Plettemeir, Solar wind turbulence during the solar cycle deduced from Galileo coronal radio-sounding eexperiment., *Adv. Space Res.*, *42*, 117–123, 2008.

Engelbrecht, N. E., On the heliospheric diffusion tensor and its effect on 26-day recurrent cosmic ray variations., Master's thesis, North-West University (Potchefstroom Campus), South Africa, 2008.

Engelbrecht, N. E., On the development and applications of a three-dimensional ab initio cosmic-ray modulation model, Ph.D. thesis, North-West University (Potchefstroom campus), South Africa, 2013.

Engelbrecht, N. E., and R. A. Burger, An ab initio model for cosmic ray modulation, *Astrophys. J.*, *772*, 46–57, 2013.

Erdos, G., and A. Balogh, North-south asymmetry of the location of the heliospheric current sheet revisited., *J. Geophys. Res.*, *115*(A01105), 1–8, 2010.

Fahr, H. J., T. Kausch, and H. Scherer, A 5-fluid hydrodynamic approach to model the solar system-interstellar medium interaction, *Astron. Astrophys.*, *357*, 268–282, 2000.

Ferreira, S. E. S., A study of the modulation of cosmic ray electrons in the heliosphere, Master's thesis, Potchefstroom University for CHE, South Africa, 1998.

Ferreira, S. E. S., The heliospheric transport of galactic cosmic rays and Jovian electrons, Ph.D. thesis, Potchefstroom University for CHE, South Africa, 2002.

Ferreira, S. E. S., and M. S. Potgieter, Long-term cosmic-ray modulation in the heliosphere, *Astrophys. J.*, *603*, 744–752, 2004.

Ferreira, S. E. S., M. S. Potgieter, R. A. Burger, and B. Heber, Modulation effects of anisotropic perpendicular diffusion on cosmic ray electron intensities in the heliosphere, *J. Geophys. Res.*, *105*, 18,305–18,314, 2000.

Ferreira, S. E. S., M. S. Potgieter, R. A. Burger, H. Fichtner, and C. Lopate, Modulation of Jovian and galactic electrons in the heliosphere: 2. Radial transport of a few MeV electrons, *J. Geophys. Res.*, *106, 29*, 313–322, 2001a.

Ferreira, S. E. S., M. S. Potgieter, R. A. Burger, B. Heber, and H. Fichtner, Modulation of Jovian and galactic electrons in the heliosphere: 1. Latitudinal transport of a few MeV electrons, *J. Geophys. Res.*, *106*, 24,979–24,987, 2001b.

Ferreira, S. E. S., M. S. Potgieter, and K. Scherer, Transport and acceleration of anomalous cosmic rays in the inner heliosheath, *J. Geophys. Res.*, *112*(A11101), 1–11, 2007.

Fichtner, H., Anomalous cosmic rays: Messengers from the outer heliosphere, *Space Sci. Rev.*, *95*, 639–754, 2001.

Fisk, L. A., Solar modulation of galactic cosmic rays, 2., *J. Geophys. Res.*, *76*, 221–226, 1971.

Fisk, L. A., Possible evidence for latitude-dependent cosmic-ray modulation, in *Proc. 14th Inter. Cosmic Ray Conf. (Munich)*, vol. 3, pp. 905–909, 1975.

Fisk, L. A., Solar modulation of galactic cosmic rays, 4. Latitude-dependent modulation, *J. Geophys. Res.*, *81*, 4646–4650, 1976.

Fisk, L. A., Motion of the footpoints of heliospheric magnetic field lines at the Sun: Implications for recurrent energetic particle events at high heliographic latitudes, *J. Geophys. Res.*, *101*, 15,547–15,553, 1996.

Fisk, L. A., and G. Gloeckler, The acceleration of anomalous cosmic rays by stochastic acceleration in the heliosheath, *Adv. Space Res.*, *43*, 1471–1478, 2009.

Fisk, L. A., B. Kozlovsky, and R. Ramaty, An interpretation of the observed oxygen and nitrogen enhancements in low-energy cosmic rays, *Astrophys. J.*, *190*, L35–L37, 1974.

Florinski, V., On the transport of cosmic rays in the distant heliosheath, *Adv. Space Res.*, *48*, 308–313, 2011.

Florinski, V., and N. V. Pogorelov, Four-dimensional transport of galactic cosmic rays in the outer heliosphere and heliosheath, *Astrophys. J.*, *701*, 642–651, 2009.

Forsyth, R. J., A. Balogh, E. J. Smith, G. Erdos, and D. J. McComas, The underlying Parker spiral structure in the Ulysses magnetic field observations, 1990-1994, *J. Geophys. Res.*, *101*, 395–403, 1996.

Fujii, Z., and F. B. McDonald, The radial intensity gradients of galactic and anomalous cosmic rays., *Adv. Space Res.*, *23*, 437–441, 1999.

Fujii, Z., and F. B. McDonald, Radial diffusion coefficients and the distance to the modulation boundary for galactic and anomalous cosmic rays., *Adv. Space Res.*, *27*, 559–564, 2001.

Garcia-Munoz, M., G. M. Mason, and J. A. Simpson, A new test for solar modulation theory: the 1972 May-July low-energy galactic cosmic-ray proton and Helium spectra, *Astrophys. J.*, *182*, L81–L84, 1973.

Giacalone, J., The efficient acceleration of thermal protons by perpendicular shocks, *Astrophys. J.*, *628*, L37–L40, 2005.

Giacalone, J., and J. R. Jokipii, The transport of cosmic rays across a turbulent magnetic field, *Astrophys. J.*, *520*, 204–214, 1999.

Giacalone, J., J. R. Jokipii, and J. Kota, Particle drifts in a fluctuating magnetic field, in *Proc. 26th Inter. Cosmic Ray Conf. (Salt Lake City)*, vol. 7, pp. 37–40, 1999.

Giacalone, J., J. F. Drake, and J. R. Jokipii, The acceleration mechanism of anomalous cosmic rays, *Space Sci. Rev*, *173*, 283–307, 2012.

Gleeson, L. J., and W. I. Axford, The Compton-Getting effect, *Astrophys. and Space Sc.*, *2*(4), 431–437, 1968.

Goldstein, M. L., D. A. Roberts, and W. H. Matthaeus, Magnetohydrodynamic turbulence in the solar wind, *Annu. Rev. Astron. Astrophys.*, *33*, 283–325, 1995.

Guo, X., and V. Florinski, Galactic cosmic–ray modulation near the heliopause, *Astrophys. J.*, *793*, 1–18, 2014.

Gurnett, D. A., W. S. Kurth, L. F. Burlaga, and N. F. Ness, In situ observations of interstellar plasma with Voyager 1, *Science*, *341*, 1489–1491, 2013.

Haasbroek, L. J., The transport and acceleration of charged particles in the heliosphere, Ph.D. thesis, Potchefstroom University for CHE, South Africa, 1997.

Hansteen, V. H., and E. Leer, Coronal heating, densities, and temperatres and solar wind, *J. Geophys. Res.*, *100*, 21,577–21,593, 1995.

Hasselmann, K., and G. Wibberenz, A note on the parallel diffusion coefficient, *Astrophys. J.*, *162*, 1049–1051, 1970.

Hathaway, D. H., The solar cycle, *Liv. Rev. Solar Phys.*, *7*, 1–65, 2010.

Hattingh, M., The modulaion of galactic cosmic rays in a three-dimensional heliosphere, Ph.D. thesis, Potchefstroom University for CHE, South Africa, 1998.

Hattingh, M., and R. A. Burger, A new simulated wavy neutral sheet drift model, *Adv. Space Res.*, *16*, 213–216, 1995.

Heber, B., Cosmic rays through the solar hale cycle, *Space Sci. Rev.*, *176*, 265–278, 2011.

Heber, B., and M. S. Potgieter, Cosmic rays at high heliolatitudes, *Space Sci. Rev.*, *127*, 117–194, 2006.

Heber, B., A. Raviart, C. Paizis, M. Bailk, W. Droge, and R. Ducros, Modulation of galactic cosmic ray particles observed onboard Ulysses spacecraft., in *Proc. 23rd Inter. Cosmic Ray Conf. (Calgary)*, vol. 461, 1993.

Heber, B., W. Droge, P. Ferrando, L. J. Haasbroek, H. Kunow, R. Müller-Mellin, C. Paizis, M. S. Potgieter, A. Raviart, and G. Wibberenz, Spatial variation of > 40MeV/n nuclei fluxes observed during the Ulysses rapid latitude scan., *Astron. Astrophys.*, *316*, 538–546, 1996.

Hoeksema, J. T., Large-scale structure of the heliospheric magnetic field: 1976-1991, *in Solar Wind Seven Colloquium*, pp. 191–196, 1992.

Horbury, T. S., A. Balogh, R. J. Forsyth, and E. J. Smith, The rate of turbulent evolution over the Sun's poles, *Astron. Astrophys.*, *316*, 333–341, 1996.

Jokipii, J. R., Cosmic-ray propagation. I. Charged particles in a random magnetic field, *Astrophys. J.*, *146*, 480–487, 1966.

Jokipii, J. R., Particle acceleration at a termination shock 1. Application to the solar wind and the anomalous component, *J. Geophys. Res.*, *91*, 2929–2932, 1986.

Jokipii, J. R., Particle drifts for finite scattering rate, in *Proc. 23rd Inter. Cosmic Ray Conf. (Calgary)*, vol. 3, pp. 497–500, 1993.

Jokipii, J. R., and D. A. Kopriva, Effects of particle drift on the transport of cosmic rays. III. Numerical model of galactic cosmic-ray modulation, *Astrophys. J.*, *234*, 384–392, 1979.

Jokipii, J. R., and J. Kóta, The polar heliospheric magnetic field, *Geophys. Res. Lett.*, *16*, 1–4, 1989.

Jokipii, J. R., and B. T. Thomas, Effects of drift on the transport of cosmic rays IV. Modulation by a wavy interplanetary current sheet, *Astrophys. J.*, *243*, 1115–1122, 1981.

Jokipii, J. R., E. H. Levy, and W. B. Hubbard, Effects of particle drift on cosmic-ray transport. I. General properties, application to solar modulation, *Astrophys. J.*, *213*, 861–868, 1977.

Jokipii, J. R., J. Kota, and E. Merenyi, The gradient of galactic cosmic rays at the solar wind termination shock, *Astrophys. J.*, *405*, 782–786, 1993.

Jones, F. C., and D. C. Ellison, The plasma physics of shock acceleration, *Space Sci. Rev.*, *58*, 259–346, 1991.

Kobayashi, T., Y. Komori, K. Yoshida, and J. Nishimura, The most likely source of high-energy cosmic-ray electron in supernova remnants, *Astrophys. J.*, *601*, 340–351, 2004.

Kojima, M., A. R. Breen, K. Fujiki, K. Hayashi, T. Ohmi, and M. Tokumaru, Fast solar wind after the rapid acceleration, *J. Geophys. Res.*, *109*(A04103), 1–10, 2004.

Kopp, A., I. Busching, M. S. Potgieter, and R. D. Strauss, A stochastic approach to galactic proton propagation: Influence of the spiral arm structure, *New Astron.*, *30*, 32–37, 2014.

Kóta, J., and J. R. Jokipii, Effects of drift on the transport of cosmic rays. VI - A three-dimensional model including diffusion, *Astrophys. J.*, *265*, 573–581, 1983.

Kóta, J., and J. R. Jokipii, 3-D distribution of cosmic rays in the outer heliosphere, in *Proc. 24th Inter. Cosmic Ray Conf. (Rome)*, vol. 4, pp. 680–683, 1995.

Kóta, J., and J. R. Jokipii, 3-D simulations of heliospheric transport: A comparison of models, in *Proc. 25th Inter. Cosmic Ray Conf. (Durban)*, vol. 2, pp. 25–29, 1997.

Kóta, J., and J. R. Jokipii, Are cosmic rays modulated beyond the heliopause?, *Astrophys. J.*, *782*, 24–29, 2014.

Krieger, A. S., A. F. Timothy, and E. C. Roelof, A coronal hole and its identification as the source of a high velocity solar wind stream, *Solar Phys.*, *29*, 505–525, 1973.

Krimigis, S. M., R. B. Decker, E. C. Roelof, M. E. Hill, T. P. Armstrong, G. Gloeckler, D. C. Hamilton, and L. J. Lanzerotti, Search for the exit: Voyager 1 at heliosphere's border with the Galaxy, *Science*, *341*, 144–147, 2013.

Krüger, T. P. J., The effect of a Fisk-Parker hybrid magnetic field on cosmic rays in the heliosphere, Master's thesis, North–West University (Potchefstroom Campus), South Africa, 2005.

Krymski, G. F., A regular mechanism for the acceleration of charged particles on the front of a shock wave., *Dokl. Akad. Nauk. SSR.*, *234*, 1306–1308, 1977.

Langner, U. W., Effects of termination shock acceleration on cosmic rays in the heliosphere, Ph.D. thesis, Potchefstroom University for CHE, South Africa, 2004.

Langner, U. W., and M. S. Potgieter, Solar wind termination shock and heliosheath effects on the modulation of protons and anti-protons., *J. Geophys. Res.*, *109*, 1–12, 2004.

Langner, U. W., and M. S. Potgieter, The heliospheric modulation of cosmic ray protons during increased solar ativity: Effects of the position of the solar wind termination shock and of the heliopause, *Ann. Geophys.*, *23*, 1–6, 2005.

Langner, U. W., and M. S. Potgieter, The role of radial perpendicular diffusion and latitude dependent acceleration along the solar wind termination shock, *Adv. Space Res.*, *41*, 368–372, 2008.

Langner, U. W., M. S. Potgieter, and W. R. Webber, Modulation of cosmic ray protons in the heliosheath, *J. Geophys. Res.*, *108*(A10), 1–9, 2003.

Langner, U. W., M. S. Potgieter, and W. R. Webber, Modelling of 'barrier' modulation for cosmic ray protons in the outer heliosphere, *Adv. Space Res.*, *34*, 138–143, 2004.

Langner, U. W., M. S. Potgieter, H. Fichtner, and T. Borrmann, Effects of different solar wind speed profiles in the heliosheath on the modulation of cosmic-ray protons, *Astrophys. J.*, *640*, 1119–1134, 2006.

Lave, K. A., M. E. Wiedenbeck, W. R. Binns, E. R. Christian, A. C. Cummings, A. J. Davis, G. A. de Nolfo, M. H. Israel, R. A. Leske, R. A. Mewaldt, E. C. Stone, and T. T. von Rosenvinge, Galactic cosmic-ray energy spectra and composition during the 2009-2010 solar minimum period, *Astrophys.J.*, *770*, 117–132, 2013.

le Roux, J. A., The solar modulation of galactic cosmic rays as described by a time-dependent drift model, Ph.D. thesis, Potchefstroom University for CHE, South Africa, 1990.

le Roux, J. A., M. S. Potgieter, and V. S. Ptuskin, A transport model for the diffusive shock acceleration and modulation of anomalous cosmic rays in the heliosphere, *J. Geophys. Res.*, *101*, 4791–4803, 1996.

Li, K. J., P. X. Gao, L. S. Zhan, X. J. Shi, and W. W. Zhu, The north-south asymmetry of solar activity at high latitude., *Mon. Not. R. Astron. Soc.*, *394*, 231–238, 2009.

Luo, X., M. Zhang, H. K. Rassoul, N. V. Pogorelov, and J. Heerikhuisen, Galactic cosmic-ray modulation in a realistic global magnetohydrodynamic heliosphere, *Astrophys. J.*, *764*, 85, 2013.

Manuel, R., Time-dependent modulation of cosmic rays in the outer heliosphere., Ph.D. thesis, North-West University (Potchefstroom Campus), South Africa, 2013.

Manuel, R., S. E. S. Ferreira, and M. S. Potgieter, Cosmic ray modulation in the outer heliosphere: Predictions for cosmic ray intensities up to the heliopause along Voyager 1 and 2 trajectories, *Adv. Space Res.*, *48*, 874–883, 2011a.

Manuel, R., S. E. S. Ferreira, and M. S. Potgieter, Cosmic ray modulation along Voyager 1 and 2 trajectories, in *Proc. 32nd Inter. Cosmic Ray Conf. (Beijing)*, vol. 11, pp. 19–22, 2011b.

Marsch, E., Kinetic physics of the solar wind plasma, *in Physics of the Inner Heliosphere, edited by Schwenn, R. and Marsch, E., Springer-Verlag, Berlin*, *45*, 45–133, 1991.

Marsden, R. G., The heliosphere after Ulysses, *Astrophys. Space Sc.*, *277*, 337–347, 2001.

Matthaeus, W. H., P. C. Gray, J. Pontius, and J. W. Bieber, Spatial structure and field-line diffusion in transverse magnetic turbulence, *Phys. Rev. Let.*, *75*, 2136–2139, 1995.

Matthaeus, W. H., G. Qin, J. W. Bieber, and G. P. Zank, Nonlinear collisionless perpendicular diffusion of charged particles, *Astrophys. J.*, *590*, L53–L56, 2003.

Matthaeus, W. H., J. W. Bieber, D. Ruffolo, P. Chuychai, and J. Minnie, Spectral properties and length scales of two-dimensional magnetic field models, *Astrophys. J.*, *667*, 956–962, 2007.

McComas, D. J., H. A. Elliot, J. T. Gosling, D. B. Reisenfield, R. M. Skoung, B. E. Goldstein, M. Neugebauer, and A. Balogh, Ulysses' second fast latitude scan: Complexity near solar maximum and the reformation of polar coronal holes, *Geophys. Res. Lett.*, *29*, 1–4, 2002.

McComas, D. J., D. Alexashov, M. Bzowski, H. J. Fahr, J. Heerikhuisen, V. V. Izmodenov, M. A. Lee, E. Mobius, N. V. Pogorelov, N. A. Schwadron, and G. P. Zank, The heliosphere's interstellar interaction: No bow shock, *Science*, *336*, 1291–1293, 2012.

McDonald, F. B., B. Heikkila, N. Lal, and E. C. Stone, The relative recovery of galactic and anomalous cosmic rays in the distant heliosphere: Evidence for modulation in the heliosheath., *J. Geophys. Res.*, *105*(A1), 1–8, 2000.

McDonald, F. B., B. Klecker, R. E. McGuire, and D. V. Reames, Relative recovery of galactic and anomalous cosmic rays at 1 AU: Further evidence for modulation in the heliosheath., *J. Geophys. Res.*, *107*(A8), 2–9, 2002.

Mewaldt, R. A., A. J. Davis, K. A. Lave, R. A. Leske, E. C. Stone, M. E. Wiedenbeck, W. R. Binns, E. R. Christian, A. C. Cummings, G. A. De Nolfo, M. H. Israel, A. W. Labrador, and T. T. von Rosenvinge, Record-setting cosmic-ray intensities in 2009 and 2010, *Astrophys. J. Lett.*, *723*, L1–L6, 2010.

Minnie, J., J. W. Bieber, W. H. Matthaeus, and R. A. Burger, Suppression of particle drifts by turbulence, *Astrophys. J.*, *670*, 1149–1158, 2007.

Moeketsi, D. M., Modelling of galactic and Jovian electrons in the heliosphere., Master's thesis, North-West University (Potchefstroom Campus), South Africa, 2004.

Moraal, H., Proton modulation near solar minimum periods in consecutive solar cycles, in *Proc. 21th Inter. Cosmic Ray Conf. (Adelaide)*, vol. 6, pp. 140–143, 1990.

Moraal, H., R. A. Caballero-Lopez, K. G. McCracken, F. B. McDonald, R. A. Mewaldt, V. S. Ptuskin, and M. E. Wiedenbeck, Cosmic ray energy changes at the termination shock and in the heliosheath, in *AIP Conf. Proc. : Physics of the Inner Heliosheath*, vol. 858, edited by J. Heerikhuisen, V. Florinski, G. P. Zank, and N. V. Pogorelov, pp. 219–225, 2006.

Moskalenko, I. V., A. W. Strong, J. F. Ormes, and M. S. Potgieter, Secondary antiprotons and propagation of cosmic rays in the galaxy and heliosphere, *Astrophys. J.*, *565*, 280–296, 2002.

Ndiitwani, D. C., A study of the time-dependent modulation of galactic cosmic rays in the heliosphere., Master's thesis, North–West University (Potchefstroom Campus), South Africa, 2005.

Ndiitwani, D. C., S. E. S. Ferreira, M. S. Potgieter, and B. Heber, Modelling cosmic ray intensities along the Ulysses trajectory, *Ann. Geophys.*, *23*, 1061–1070, 2005.

Ngobeni, M. D., Aspects of the modulation of cosmic rays in the outer heliosphere, Master's thesis, North-West University (Potchefstroom Campus), South Africa, 2006.

Ngobeni, M. D., and M. S. Potgieter, Cosmic ray anisotropies in the outer heliosphere, *Adv. Space Res.*, *41*, 373–380, 2008.

Ngobeni, M. D., and M. S. Potgieter, The heliospheric modulation of cosmic rays: Effects of a latitude dependent solar wind termination shock, *Adv. Space Res.*, *46*, 391–401, 2010.

Ngobeni, M. D., and M. S. Potgieter, Modulation of galactic cosmic rays in a north-south asymmetrical heliosphere, *Adv. Space Res.*, *48*, 300–307, 2011.

Ngobeni, M. D., and M. S. Potgieter, Modelling of galactic carbon in an asymmetrical heliosphere: Effects of asymmetrical modulation conditions, *Adv. Space Res.*, *49*, 1660–1669, 2012.

Ngobeni, M. D., and M. S. Potgieter, A study of the global heliospheric modulation of galactic carbon, *Adv. Space Res.*, *53*, 1634–1646, 2014.

Nkosi, G. S., M. S. Potgieter, and W. R. Webber, Modelling of low-energy galactic electrons in the heliosheath, *Adv. Space Res.*, *48*, 1480–1489, 2011.

Obridko, V. N., V. E. Chertoprud, and K. M. Kuzanyan, North-south asymmetry in the distribution of solar background magnetic field, *Solar Phys.*, *289*, 2867–2878, 2014.

Opher, M., E. C. Stone, and P. C. Liewer, The effects of a local interstellar magnetic field on Voyager 1 and 2 observations, *Astrophys. J.*, *640*, L71–L74, 2006.

Opher, M., J. D. Richardson, G. Toth, and T. I. Gombosi, Confronting observations and modeling: The role of the interstellar magnetic field in Voyager 1 and 2 asymmetries, *Space Sci. Rev.*, *143*, 43–55, 2009.

Opher, M., J. F. Drake, M. Swisdak, K. M. Schoeffler, J. D. Richardson, R. B. Decker, and G. Toth, Is the magnetic field in the heliosheath laminar or a turbulent sea of bbubles?, *Astrophys. J.*, *734*, 71–81, 2011.

Oughton, S., W. H. Matthaeus, C. W. Smith, B. Breech, and P. A. Isenberg, Transport of solar wind fluctuations: A two-component model, *J. Geophys. Res.*, *116*, 8105–8118, 2011.

Palmer, I. D., Transport coefficients of low-energy cosmic rays in interplanetary space, *Rev. Geophys. Space Phys.*, *20*, 335–351, 1982.

Parker, E. N., Dynamics of the interplanetary gas and magnetic fields, *Astrophys. J.*, *128*, 664–676, 1958.

Parker, E. N., Sudden expansion of the corona follow a large solar flare and the attendant magnetic field and cosmic effects, *Astrophys. J.*, *133*, 1033–1014, 1961.

Parker, E. N., The passage of energetic charged particles through interplanetary space, *Planet. Space Sci.*, *13*, 9–49, 1965.

Peaceman, D. W., and H. H. Rachford, The numerical solution of parabolic and elliptic differential equations, *J. Soc. Indust. Appl. Math.*, *3*(1), 28–41, 1955.

Pei, C., J. W. Bieber, R. A. Burger, and J. Clem, A general time-dependent stochastic method for solving Parker's transport equation in spherical coordinates, *J. Geophys. Res.*, *115*(A12107), 1–12, 2010.

Perri, S., V. Carbone, and P. Veltri, Where does fluid-like turbulence break down in the solar wind?, *Astrophys. J. Lett.*, *725*, L52–L55, 2010.

Phillips, J. L., A. Balogh, S. J. Bame, B. E. Goldstein, J. T. Gosling, J. T. Hoeksema, D. J. McComas, M. Neugebauer, N. R. Sheeley, and Y. M. Wang, Ulysses at 50^o south: constant immersion in the high-speed solar wind, *Geophys. Res. Lett.*, *21*, 1105–1108, 1994.

Phillips, J. L., S. J. Bame, A. Barnes, B. L. Barraclough, W. C. Feldman, B. E. Goldstein, J. T. Gosling, G. W. Hoogeveen, D. J. McComas, M. Neugebauer, and S. T. Suess, Ulysses solar wind plasma observations from pole to pole, *Geophys. Res. Lett.*, *22*, 3301–3304, 1995.

Pogorelov, N. V., J. Heerikhuisen, G. P. Zank, J. J. Mitchell, and I. H. Cairns, Heliospheric asymmetries due to the action of the interstellar magnetic field, *Adv. Space Res.*, *44*, 1337–1344, 2009.

Pogorelov, N. V., S. T. Suess, S. N. Borovikov, R. W. Ebert, D. J. McComas, and G. P. Zank, Three-dimensional features of the oute heliosphere due to coupling between the interstellar and interplanetary magnetic fields. IV. solar cycle model based on Ulusses observations., *Astrophys.J.*, *772*, 2, 2013.

Potgieter, M. S., The modulaion of galactic cosmic rays as described by a three-dimensional drift model, Ph.D. thesis, Potchefstroom University for CHE, South Africa, 1984.

Potgieter, M. S., Heliospheric modulation of galactic electrons: Consequences of new calculations for the mean free path of electrons between 1 MeV and $\sim$10 GeV, *J. Geophys. Res.*, *101*(A11), 24,411–24,422, 1996.

Potgieter, M. S., Heliospheric modulation of cosmic ray protons: Role of enhanced perpendicular diffusion during periods of minimum solar modulation, *J. Geophys. Res.*, *105*(A8), 18,295–18,303, 2000.

Potgieter, M. S., Challenges to cosmic ray modelling: From beyond the solar wind termination shock, *Adv. Space Res.*, *41*, 245–258, 2008.

Potgieter, M. S., The dynamic heliosphere, solar activity, and cosmic rays, *Adv. Space Res.*, *46*, 402–412, 2010.

Potgieter, M. S., Cosmic rays in the inner heliosphere: Insight from observations, theory and models., *Space Sci. Rev.*, *176*, 165–176, 2011.

Potgieter, M. S., Solar modulation of cosmic rays, *Liv. Rev. Solar Phys.*, *10*, 1–66, 2013.

Potgieter, M. S., and S. E. S. Ferreira, Effects of solar wind termination shock on the modulation of Jovian and galactic electrons in the heliosphere, *J. Geophys. Res.*, *107*, 1–9, 2002.

Potgieter, M. S., and U. W. Langner, The heliospheric modulation of cosmic ray boron and carbon, *Ann. Geophys.*, *22*, 3729–3740, 2004.

Potgieter, M. S., and U. W. Langner, Modulation of cosmic rays: Perpendicular diffusion and drifts in a heliosphere with a solar wind termination shock, *Adv. Space Res.*, *35*, 554–561, 2005.

Potgieter, M. S., and H. Moraal, A drift model for the modulation of galactic cosmic rays, *Astrophys. J.*, *294*, 425–440, 1985.

Potgieter, M. S., and H. Moraal, Acceleration of cosmic rays in the solar wind termination shock. I. A steady state technique in a spherically symmetric model, *Astrophys. J.*, *330*, 445–455, 1988.

Potgieter, M. S., and R. R. Nndanganeni, The solar modulation of electrons in the heliosphere, *Astrophys. Space Scie.*, *345*, 33–40, 2013.

Potgieter, M. S., and R. D. Strauss, The highest recorded proton spectrum at Earth since the beginning of the space age, in *Proc. 33th Inter. Cosmic Ray Conf. (Rio De Janeiro)*, 2013.

Potgieter, M. S., J. A. le Roux, and R. A. Burger, Interpanetary cosmic ray radial gradients with steady-state modulation models, *J. Geophys. Res.*, *94*, 2323–2332, 1989.

Potgieter, M. S., L. J. Haasbroek, P. Ferrando, and B. Heber, The modelling of the latitude dependence of cosmic ray protons and electrons in the inner heliosphere, *Adv. Space Res.*, *19*, 917–920, 1997.

Potgieter, M. S., E. E. Vos, M. Boezio, N. De Simone, V. Di Felice, and V. Formanto, Modulation of galactic protons in the heliosphere during the unusual solar minimum of 2006 to 2009, *Solar Phys.*, *281*, 391–406, 2013.

Ptuskin, V. S., I. V. Moskalenko, F. C. Jones, A. W. Strong, and V. N. Zirakashvili, Dissipation of magnetohydrodynamic waves on energetic particles: Impact on interstellar turbulence and cosmic-ray transport, *Astrophys. J.*, *642*, 902–916, 2006.

Raath, J. L., A comparative study of cosmic ray modulation models, Master's thesis, North–West University (Potchefstroom Campus), South Africa, 2014.

Reinecke, J. P. L., and M. S. Potgieter, An explanation for the difference in cosmic ray modulation at low and neutron monitor energies during consecutive solar minimum periods., *J. Geophys. Res.*, *99*, 14,761–14,767, 1994.

Richardson, J. D., Voyager observations of the interaction of the heliosphere with the interstellar medium., *J. Adv. Res.*, *4*, 229–233, 2013.

Richardson, J. D., and C. Wang, Plasma in the heliosheath: 3.5 years of observations, *Astrophys. J. Lett.*, *734*(L21), 1–5, 2011.

Richardson, J. D., C. Wang, and K. I. Paularena, The solar wind: From solar minimum to solar maximum, *Adv. Space Res.*, *27*, 427–479, 2001.

Richardson, J. D., J. C. Kasper, C. Wang, J. W. Belcher, and A. J. Lazarus, Cool heliosheath plasma and deceleration of the upstream solar wind at the termination shock, *Nature*, *454*, 63–66, 2008.

Schatten, K. H., J. M. Wilcox, and N. F. Ness, A model of interplanetary and coronal magnetic fields, *Solar Phys.*, *6*, 442–455, 1969.

Scherer, K., and H. J. Fahr, Solar cycle induced variation of the outer heliospheric structure, *Geophys. Res. Lett.*, *30(17)*, 1–4, 2003.

Scherer, K., and S. E. S. Ferreira, A heliospheric hybrid model: hydrodynamic plasma flow and kinetic cosmic ray transport, *ASTRA*, *1*, 17–27, 2005.

Scherer, K., and H. Fichtner, The return of the bow shock, *Astrophys. J.*, *782*, 25, 2014.

Scherer, K., H. Fichtner, R. D. Strauss, S. E. S. Ferreira, M. S. Potgieter, and H. J. Fahr, On cosmic ray modulation beyond the heliopause: Where is the modulation boundary?, *Astrophys. J.*, *735*, 1–5, 2011.

Schlickeiser, R., On the interplanetary transport of solar cosmic rays, *J. Geophys. Res.*, *93*, 2725–2729, 1988.

Schwenn, R., The average solar wind in the inner heliosphere: Structure and slow variations, *Proc. NASA Conf. Publication*, *2280*, 489–507, 1983.

Schwenn, R., Solar wind sources and their variations over the solar cycle, *Space Sci. Rev.*, *124*, 51–76, 2006.

Shalchi, A., A unified particle diffusion theory for cross-field scattering: Subdiffusion, recovery of diffusion, and diffusion in three-dimensional turbulence, *Astrophys. J. Lett.*, *720*, L127–L130, 2010.

Sheeley, N. R., Y. M. Wang, S. H. Hawley, G. E. Brueckner, K. P. Dere, et al., Measurements of flow speeds in the corona between 2 and 30 $R_{\odot}$, *Astrophys. J.*, *484*, 472–478, 1997.

Simon, M., H. Spiegelhauer, W. K. H. Schmidt, F. Siohan, J. F. Ormes, V. K. Balasubrahmanyan, and J. F. Arens, Energy spectra of cosmic-ray nuclei to above 100 GeV per nucleon, *Astrophys. J.*, *239*, 712–724, 1980.

Simpson, J. A., D. Hamilton, G. Lentz, R. B. McKibben, A. Mogro-Campero, M. Perkins, K. R. Pyle, A. J. Tuzzolini, and J. J. O'Gallagher, Proton and electrons in Jupiters's magnetic field : Results from the university of Chicago experiment on Pioneer 10, *Science*, *183*, 306–309, 1974.

Simpson, J. A., M. Zhang, and S. Bame, A solar polar north-south asymmetry for cosmic-ray propagation in the heliosphere: The Ulysses pole-to-pole rapid transit, *Astrophys. J.*, *465*, L69–L72, 1996.

Smith, C. W., and J. W. Bieber, Solar cycle variation of the interplanetary magnetic field spiral, *Astrophys. J.*, *370*, 435–441, 1991.

Smith, E. J., The heliospheric current sheet, *J. Geophys. Res.*, *106*, 15,819–15,831, 2001.

Smith, E. J., Solar cycle evolution of the heliospheric magnetic field: The Ulysses legacy, *J. Atmos. Solar-Terrestrial Phys.*, *73*, 277–289, 2011.

Smith, E. J., J. R. Jokipii, J. Kota, R. P. Lepping, and A. Szabo, Evidence of a north-south asymmetry in the heliosphere associated with a southward displacement of the heliospheric current sheet, *Astrophys. J.*, *533*, 1084–1089, 2000.

Snodgrass, H. B., Magnetic rotation of the solar photosphere, *Astrophys. J.*, *270*, 288–299, 1983.

Snyman, J. L., Modelling of the heliosphere and cosmic ray transport, Master's thesis, North–West University (Potchefstroom Campus), South Africa, 2007.

Stawicki, O., Quasi-linear drift of cosmic rays in weak turbulent electromagnetic fields, *Astrophys. J.*, *624*, 178–188, 2005a.

Stawicki, O., Nonlinear perpendicular diffusion in strong turbulent electromagnetic fields, *Adv. Space Res.*, *35*, 547–553, 2005b.

Steenberg, C. D., Modelling of anomalous and galactic cosmic ray modulation in the outer heliosphere, Ph.D. thesis, Potchefstroom University for CHE, South Africa, 1998.

Steenberg, C. D., and H. Moraal, An acceleration/modulation model for anomalous cosmic ray hydrogen in the heliosphere, *Astrophys. J.*, *463*, 776–783, 1996.

Steenkamp, R., Shock acceleration as source of the anomalous component of cosmic rays in the heliosphere, Ph.D. thesis, Potchefstroom University for CHE, South Africa, 1995.

Sternal, O., N. E. Engelbrecht, R. A. Burger, S. E. S. Ferreira, H. Fichtner, B. Heber, A. Kopp, M. S. Potgieter, and K. Scherer, Possible evidence for a Fisk-type heliospheric magnetic field. I. Analyzing Ulysses/KET electron observations, *Astrophys. J.*, *741*, 1–12, 2011.

Stone, E. C., A. C. Cummings, F. B. McDonald, B. C. Heikkila, N. Lal, and W. R. Webber, Voyager 1 explores the termination shock region and the heliosheath beyond, *Science*, *309*, 2017–2020, 2005.

Stone, E. C., A. C. Cummings, F. B. McDonald, B. C. Heikkila, N. Lal, and W. R. Webber, An asymmetric solar wind termination shock, *Nature*, *454*, 71–74, 2008.

Stone, E. C., A. C. Cummings, F. B. McDonald, B. C. Heikkila, N. Lal, and W. R. Webber, Voyager 1 observes low-energy galactic cosmic rays in a region depleted of heliospheric ions, *Science*, *341*, 150–153, 2013.

Strauss, R. D., Modelling of anomalous cosmic rays, Master's thesis, North–West University (Potchefstroom Campus), South Africa, 2010.

Strauss, R. D., Modeling of cosmic rays in the heliosphere by stochastic processes, Ph.D. thesis, North–West University (Potchefstroom Campus), South Africa, 2013.

Strauss, R. D., and M. S. Potgieter, Modeling anomalous cosmic ray oxygen gradients over successive solar cycles, *J. Geophys. Res.*, *115*(A12111), 1–13, 2010.

Strauss, R. D., and M. S. Potgieter, Is the highest cosmic-ray flux yet to come?, *Solar Phys.*, *289*, 3197–3205, 2014.

Strauss, R. D., M. S. Potgieter, and S. E. S. Ferreira, The heliospheric transport and modulation of multiple charged anomalous oxygen revisited, *Astron. Astrophys.*, *513*(A24), 1–6, 2010a.

Strauss, R. D., M. S. Potgieter, S. E. S. Ferreira, and M. E. Hill, Modelling anomalous cosmic ray oxygen in the heliosheath, *Astron. Astrophys.*, *522*(A35), 1–8, 2010b.

Strauss, R. D., M. S. Potgieter, I. Busching, and A. Kopp, Modeling the modulation of galactic and jovian electrons by stochastic processes, *Astrophys. J.*, *735*, 1–13, 2011.

Strauss, R. D., M. S. Potgieter, I. Busching, and A. Kopp, Modelling heliospheric current sheet drift in stochastic cosmic ray transport models, *Astrophys. and Space Sc.*, *339*, 223–236, 2012.

Strauss, R. D., M. S. Potgieter, and S. E. S. Ferreira, Cosmic ray modulation beyond the heliopause: A hybrid modelling approach, *Astrophys. J.*, *765*, 1–6, 2013a.

Strauss, R. D., M. S. Potgieter, and S. E. S. Ferreira, Modelling and observing Jovian electron propagation ttime in the inner heliosphere, *Adv. Space Res.*, *51*, 339–349, 2013b.

Swisdak, M., J. F. Drake, and M. Opher, A porous, layered heliopause, *Astrophys. J.*, *774*, L8–L13, 2013.

Tautz, R. C., and A. Shalchi, Drift coefficient of charged particles in turbulent magnetic fields, *Astrophys.J.*, *125*, 744–751, 2012.

Teufel, A., and R. Schlickeiser, Analytic calculation of the parallel mean free path of heliospheric cosmic rays. I. Dynamical magnetic slab turbulence and random sweeping slab turbulence, *Astron. Astrophys.*, *393*, 703–715, 2002.

Teufel, A., and R. Schlickeiser, Analytic calculation of the parallel mean free path of heliospheric cosmic rays. II. Dynamical magnetic slab turbulence and random sweeping slab turbulence with finite wave power at small wavenumbers, *Astron. Astrophys.*, *397*, 15–25, 2003.

Usoskin, I. G., History of solar activity over millennia, *Liv. Rev. Solar Phys.*, *10*, 1–94, 2013.

Wang, Y. M., Semiempirical models of the slow and fast solar wind, *Space Sci. Rev.*, *172*, 123–143, 2011.

Washimi, H., and T. Tanaka, MHD structure of the heliosphere and its response to the 11 -year solar cycle variations, *Adv. Space Res.*, *23*, 551–560, 1999.

Washimi, H., G. P. Zank, Q. Hu, T. Tanaka, K. Munakata, and H. Shinagawa, Realistic and time-varying outer heliospheric modelling, *Mon. Not. R. Astron. Soc.*, *416*, 1475–1485, 2011.

Webber, W. R., Voyager measurements of galactic cosmic rays and implications for modulation in the heliosheath and beyond, in *Physics of the inner Heliosheath, AIP Conf. Proc. 858*, 2006.

Webber, W. R., and P. R. Higbie, Galactic propagation of cosmic ray nuclei in a model with an increasing diffusion coefficient at low rigidities: A comparison of the new interstellar spectra with Voyager data in the outer heliosphere, *J. Geophys. Res.*, *114*(A02103), 1–6, 2009.

Webber, W. R., and D. S. Intriligator, Voyagers 1 and 2 in a shrunken and squashed heliosphere, *J. Geophys. Res.*, *116*(A06105), 1–8, 2011.

Webber, W. R., and D. S. Intriligator, Voyager 1 and 2 observations of cosmic ray intensities in the north-south heliosheath - Implications for the latitude extent of the heliospheric current sheet and radial structure in the heliosheath., in *arXiv:1403.3322*, 2014.

Webber, W. R., and J. A. Lockwood, Voyager and Pioneer spacecraft measurements of cosmic ray intensities in the outer heliosphere: Toward a new paradigm for understanding the global solar modulation process 1. Minimum solar modulation (1987 and 1997), *J. Geophys. Res.*, *106*, 29,323–29,331, 2001.

Webber, W. R., and J. A. Lockwood, onset and amplitude of the 11-year solar modulation of cosmic ray intensities at Earth and at Voyager 1 and 2 during the period 1997 to 2003., *J. Geophys. Res.*, *109*, 11,101–11,107, 2004.

Webber, W. R., A. C. Cummings, F. B. McDonald, E. C. Stone, B. C. Heikkila, and N. Lal, Transient intensity changes of cosmic rays beyond the heliospheric termination shock observed at Voyager 1., *J. Geophys. Res.*, *114*(A07108), 1–6, 2009.

Webber, W. R., F. B. McDonald, P. R. Higbie, and B. C. Heikkila, Recovery of 150-250 MeV/nuc cosmic ray helium nuclei intensities between 2004-2010 near the earth, at Voyager 2 and at Voyager 1 in the heliosheath- a two zone heliosphere., in *arXiv:1109.1810*, 2011.

Webber, W. R., F. B. McDonald, P. R. Higbie, and B. C. Heikkila, Recovery of 150-250 MeV/nuc cosmic ray helium nuclei intensities between 2004-2010 near the earth, at Voyager 2 and at Voyager 1 in the heliosheath- a two zone heliosphere, in *arXiv:1109.1810*, 2012.

Webber, W. R., P. R. Higbie, and F. B. McDonald, A Comparison of galactic cosmic ray H, He and C/O Spectra measured between $\sim$5 and 500 MeV/nuc beyond 122 AU at Voyager 1 with the predictions of a diffusion model for propagation in the Galaxy, in *arXiV:1308.4426*, 2013.

Zank, G. M., and H. R. Muller, The dynamical heliosphere, *J. Geophys. Res.*, *108*, 1240–1248, 2003.

Zhang, M., A Markov stochastic process theory of cosmic-ray modulation, *Astrophys. J.*, *513*, 409–420, 1999.

Zurbuchen, T. H., N. A. Schwadron, and L. A. Fisk, Direct observational evidence for a heliospheric magnetic field with large excursions in latitude, *J. Geophys. Res.*, *102*, 24,175–24,181, 1997.

Acknowledgements

I would like to express my gratitude to the following people and institutions in no particular order:

- Heavenly Father for having given me this few and far between opportunity to comprehend a small portion of his splendid creation.
- Prof. Marius Potgieter, my supervisor, for his splendid guidance, suggestions, explanations and motivation.
- Mr Sibusiso Nkosi for his friendship, advice and modulation discussions
- Dr Rex Manuel, for his friendship, motivation, discussions and making LATEX available.
- Mr Matthew Holleran for his unwavering assistance with computer related problems and queries
- The Centre for Space Research at the North-West University (Potchefstroom Campus) for the use of their facilities.
- The South African National Research Foundation for partial financial support for my sabbatical leave and staff bursaries as well as the full financial support for attending the COSPAR conferences.
- Mrs. Petro Sieberhagen, Mrs. Elanie van Rooyan and Mrs. Lee-Ann van Wyk for their administrative assistance.
- Ms Christa van Wyk for proof reading the thesis.
- My friends, Isak Davids, Chris Ndiitwani, Rendani, Sungulani Shivambu and Standley Ngobeni.
- My brothers Thomas Ngobeni and Richard Khazamula Ngobeni

Finally, I wish to thank my parents Mbhazima Xiteveteve Ngobeni and Florah Tsakani Ntsumele-Ngobeni for their support and sacrifice throughout my study.